Unveiling Failure Mechanisms of Harsh Environment Ceramic Materials

---

A

Dissertation

Presented to

the faculty of the School of Engineering and Applied Science

University of Virginia

---

in partial fulfillment

of the requirements for the degree

Doctor of Philosophy

by

Clifton H. Bumgardner

December 2020

APPROVAL SHEET

This

Dissertation

is submitted in partial fulfillment of the requirements
for the degree of

Doctor of Philosophy

Author: Clifton H. Bumgardner

This Dissertation has been read and approved by the examing committee:

Advisor: Xiaodong Li

Advisor:

Committee Member: Xiaodong Li

Committee Member: Baoxing Xu

Committee Member: Elizabeth Opila

Committee Member: Osman Ozbulut

Committee Member: Peng Xu

Committee Member:

Accepted for the School of Engineering and Applied Science:

Craig H. Benson, School of Engineering and Applied Science

December 2020

ABSTRACT

As sources of energy have expanded from burning wood and coal to a diverse assortment of modern renewable and nonrenewable sources, including hydrothermal, ultra-high temperature combustion, and nuclear, more robust, structural and protective materials are urgently needed to harness this energy. These materials often require excellent thermal stability, must be chemically inert, and must demonstrate reliable mechanical performance to withstand harsh conditions within many energy generation systems, like a nuclear reactor or combustion engine. Here, thermal barrier coatings (TBCs) and silicon carbide fiber / silicon carbide matrix composites (SiC/SiC CMCs) are considered for their wide suitability for multiple extreme environment energy applications. Both materials have been extensively studied within the last few decades, yet there remain many critical questions about their failure mechanisms in relevant environments and loading modes, which represent barriers to their widespread adoption.

This dissertation elucidates these critical failure mechanisms via digital image correlation (DIC) - enabled mechanical testing of TBC and CMC material systems under relevant environmental conditions up to 1200 °C and loading modes via indentation, wear, and flexural testing. DIC techniques enable quantitative measurements of deformation and strain, which provide boundary conditions for predictive analytical models of material stress state and creep response. Material degradation is further characterized via electron microscopy and acoustic emission monitoring. Importantly, both TBCs and CMCs are multi-component systems composed of high temperature ceramic materials, and their failure mechanisms reflect a complicated accumulation of properties of their individual constituents. Thus, it is critical to characterize and quantify the multiscale thermomechanical properties and multi-component interactions inherent in these hierarchically structured material systems, such as thermal property and residual stress mismatch between coating layers or material constituents, which can exacerbate local stress concentrations and promote degradation. DIC techniques are fully capable of quantifying and tracking this degradation to its source.

Through this work, new materials design paradigms are revealed, which support superior performance within these harsh environments. Key findings relating to the TBC system include the need (i) to minimize

thermal property mismatch between coating layers, which exacerbate residual stresses within each layer and promote delamination, and (ii) to optimize the coating deposition methodology to reduce instances of porosity, pre-existing cracks, and solid particles, which can serve as fracture initiation sites. Key findings relating to the CMC system include (i) the need for optimization of the fiber tow architecture to create non-uniform microstructure to disrupt crack growth and (ii) the development of a rule-of-mixtures materials model to describe the nanoscale CMC creep response.

TABLE OF CONTENTS

ACKNOWLEDGEMENTS

There are many people who I would like to thank for their support and encouragement. First, I would like to thank my advisor, Prof. Xiaodong "Chris" Li, who has been a steady source of motivation and guidance. His mentorship and example as a leader, teacher, and scientist have challenged me to continuously push myself beyond perceived limits, to "strain harden" but never break. I also would like to thank my committee members, Profs. Baoxing Xu, Elizabeth Opila, and Osman Ozbulut, and Dr. Peng Xu for their support and constructive guidance. Dr. Peng Xu has been a steady source of encouragement over several years of collaborative research into accident tolerant nuclear fuel claddings.

Throughout my graduate experience, I have been fortunate to know and work with a highly talented group of student researchers. Together, we have completed numerous federally-sponsored and industry-sponsored research projects, drafted many publications, and spent many long hours in the laboratory. I am pleased to thank and acknowledge the support of my friends and colleagues: Dr. Yellapu Murty, Dr. Zan Gao, Dr. Brendan Croom, Dr. Ningning Song, Dr. Yunya Zhang, Dr. Jiadeng Zhu, Dr. F. Michael Heim, Dr. Liwen Zhang, Dr. Timothy Harrell, Alex Jarama, David Roache, Ryan Cordier, J. Tyler Daspit, Morgan Price, Oliver Holzmond, Jamison Bartlett, Victor Shen, Cole Love-Baker, Yosyp Schwab, Kenneth Brown, Diana Burden, Yucheng Zhou, Jiajun He, Rouxi Chen, Zhijing Xue, Andre Sushenko, Alex Schershel, and Hans Hudyncia.

My friends and family have been strong supporters of my ambitions throughout my academic career. My parents, Fred and Kathy Bumgardner, saw, perhaps quicker than I did at first, that the University of Virginia would be a new home where I could grow to accomplish more than I thought myself possible. My brother, J. Coleman Bumgardner, could always be counted on to keep me grounded and remind me to laugh with his quick wit and clever puns. My grandmother, Kathryn Moore, was always there to share a supportive ear and kind word. My closest friends, Justin and Monica Pierce and Patrick and Alexandra Bailey, provided warm support and many weekends of welcome distraction. Lastly, I must acknowledge those close family members no longer present but who nonetheless contributed to my success: my uncle James Moore, Jr.; my grandfather James Moore, Sr., whose example is the one I judge myself against every day; and my

grandparents Fred and Colleen Bumgardner, who always wanted me to become a doctor (though this is not quite the doctorate they had in mind!).

My research has been supported with guidance and funding from numerous sources. Specific research activities were funded by Westinghouse Electric Company (Chapter 5), the Department of Energy Nuclear Energy University Program (DE-NE0008706, Chapters 5 & 6), and Rolls-Royce Corporation (Chapter 7). I would also like to thank Dr. Peng Xu (currently of Idaho National Laboratory), Dr. Roger Lu, and Ed Lahoda of Westinghouse Electric Company, Dr. Christian Deck of General Atomics, and Dr. Andrew Ritchey and Dr. Jason Baker of Rolls-Royce for providing materials and critical insight for this research. Richard White, Joe Thompson, and the Nanoscale Materials Characterization Facility have provided training on the scanning electron microscope and energy dispersive X-ray spectrometer at the University of Virginia, which were used in the completion of this research.

LIST OF FIGURES

LIST OF TABLES

COMMON ABBREVIATIONS AND ACRONYMS

AE – acoustic energy

AFM – atomic force microscopy

APS – air plasma spray

BC – bond coat layer

BN – boron nitride

CMC – ceramic matrix composite

COD – crack opening displacement

COF – coefficient of friction

CVD – chemical vapor deposition

CVI – chemical vapor infiltration

DFL – deviation from linearity

DIC – digital image correlation

DVC – dense vertical cracks

EDS – energy dispersive X-ray spectroscopy

ERR – Energy release rate

FE – finite element model

F_f – force of friction

He - helium

NC-AE – normalized cumulative acoustic energy

pc – poly crystal

PL – proportional limit

PyC – pyrolytic carbon

rb – reaction bonded

sc – single crystal

SiC – silicon carbide

SEM – scanning electron microscopy

SMI – silicon melt infiltration

TBC – thermal barrier coating

TC – top coat layer

TGO – thermally grown oxide

XCT – X-ray computed tomography

XRD – X-ray diffraction

YSZ – yttria stabilized zirconia

CHAPTER 1: INTRODUCTION

1. The Role of Harsh Environment Ceramic Materials

As sources of energy have expanded from burning wood and coal to a diverse assortment of modern renewable and nonrenewable sources, including hydrothermal, ultra-high temperature combustion, and nuclear, more robust, structural and protective materials are urgently needed to enable next-generation technologies to harness this energy. This need is readily apparent within aircraft jet engines, where greater fuel efficiency demands higher operating temperature, often in excess of 1300 °C. To withstand these temperatures, many engine components require an active or passive cooling system, protective thermal coating system, or both [1,2]. Another salient energy materials need is nuclear fuel cladding, which must possess good irradiation resistance, chemical stability, and thermomechanical durability. The nuclear industry is currently investigating next-generation accident tolerant fuel systems to extend reactor design safety to include extreme, non-ideal conditions, driven by industry demand for greater efficiency and by safety concerns following the Fukushima incident [3–6]. Across these different examples from multiple industries, common trends link the material needs: high thermal stability, corrosion resistance, and mechanical durability.

This dissertation is focused on an investigation of thermal barrier coatings (TBCs) and silicon carbide fiber / silicon carbide matrix composites (SiC/SiC CMCs), which are energy materials of key scientific and industry interest due to their wide suitability for multiple extreme environment energy applications. Both materials have been extensively studied within the last few decades, yet there remain many critical questions about their failure mechanisms in relevant environments and loading modes, which represent key barriers to their widespread adoption.

2. Overview of Thermal Barrier Coatings

TBCs are widely used to provide thermal insulation to an underlying substrate within high temperature environments, most commonly the extreme environment within a gas turbine engine [7]. These

environments are characterized by temperatures as high as 1400 °C and a mix of superheated air and combusted fuel, which can generate pressures up to 3.5 MPa. As such, TBCs are applied across multiple components within a gas turbine engine, including the compressor blades, compressor seals, turbine blades, turbine seals, and burner [2,8,9]. The durability of these coatings is highly dependent on many parameters: coating thickness, roughness, porosity, residual stress, and pre-existing defects (cracks, voids) [10–12]. Remarkable work has been performed and is well documented in the literature of the failure mechanisms within TBCs, predominately coating delamination, using numerical methods and post-failure microscopy, but these studies assume a homogeneous ceramic coating without the microstructural variation seen in actual coatings [13–16]. Furthermore, much of this work provides only a piecemeal examination of the properties of TBCs, from their mechanical performance under flexure or tension [17], their thermomechanical fatigue response [18–20], to their phase stability and residual stress state [21]. While the current literature provides a good fundamental understanding of TBC failure, these failure mechanisms cannot be separated from the many microstructural variations and asperities, loading mode, and inherent residual stress state.

TBC systems may be multilayered; each layer can possess distinct thermomechanical properties, which results in a complex stress state during high temperature operation or during large mechanical deformations. The properties of each layer are also highly dependent on the methodology by which they were deposited: commonly air plasma spray, chemical vapor deposition, or physical vapor deposition. Air plasma spray, or thermal spray, processes involve passing fine ceramic powders through a plasma arc and onto the substrate. The plasma arc melts the powders, which land randomly as splats and cool on the substrate into a hard, porous coating layer [22,23]. In a chemical vapor deposition process, reactive gas precursors are fed into a chamber around the substrate; a reaction is initiated at a controlled temperature, and the gases decompose to form the coating atop the substrate. Physical vapor deposition processes use electron beams to melt the coating precursor into a vapor, which then decomposes onto the substrate. Vapor deposition coatings are typically characterized by a columnar coating microstructure, formed from the decomposing gases. While air plasma sprayed coatings typically have higher porosity (10 to 20 %), both processes leave a coating

microstructure with voids and cracks, which may contribute to failure [9,24,25]. Furthermore, the actual materials for each coating layer may vary. The TBC itself is commonly a zirconia or silicate material, which is deposited on a bond coat, usually a nickel or chromium alloy, with the substrate [9,23,25,26].

The variety of coating deposition techniques and material choices itself imposes limitations on the practicality of holistic research into TBC failure mechanisms. Thus, this dissertation focuses on TBCs composed of a yttria-stabilized zirconia (YSZ) top coat deposited via an air plasma spray methodology [27]. In this air plasma spray process, the plasma arc melts the particles, so they will flatten and solidify on the substrate in the form of splats. These splats build up during spraying as the plasma arc passes up and down the substrate. This process can deposit coatings of variable thickness, material, and consistency across flat or complex geometric surfaces and can be automated to enable cost-effective manufacturing; however, air plasma sprayed coatings are also prone to inherent defects [7] and significant residual stress due to large thermal gradients during deposition and in use [28,29].

Figure 1.1 presents a representative micrograph of the YSZ TBC system manufactured via air plasma spraying used in this dissertation and showcases frequently seen inherent defects. At a glance, the microstructure is not homogeneous; there are varying concentrations of pores, voids, and pre-existing cracks. These features form as splats during deposition. Much like pebbles in a jar, the splats do not always fill all the available space and leave voids as they solidify. Lateral, inter-splat cracks tend to form as a layer of molten splats are deposited on already cooling splats and cannot sufficiently solidify together. Not all ceramic particles are fully melted by the plasma arc, so some solid particles may be included within the coating [7,30]. Another notable feature is the coating layer interface; it is rough and uneven, which can promote stress concentrations, poor bonding, and localized oxidation. Thermally grown oxide (TGO) layers are frequently observed along coating interfaces over repeat thermal cycling, which can alter the layer adhesion strength [27,31]. Not shown in Figure 1.1, periodically spaced surface cracks have been observed within the top coating, often penetrating as far as the TGO layer. These cracks, referred to as dense vertical cracks (DVCs) have been documented to increase coating compliance and enhance interfacial durability [32,33], but their effect on TBC failure mechanisms have not been well documented.

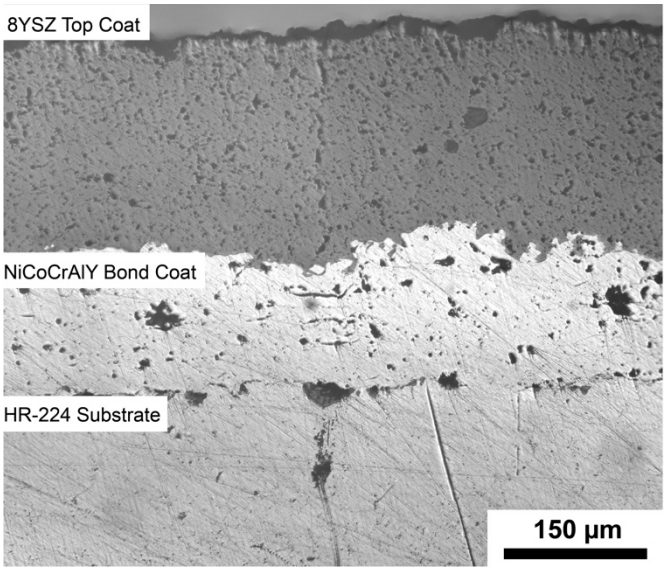

Figure 1.1. A micrograph of the YSZ TBC system deposited via air plasma spraying and characterized in this dissertation, showing inter-splat voids, uneven coating interfaces, and heterogeneous microstructure.

There is little available research to quantitatively correlate fracture with coating microstructure, but it is hypothesized that the TBC failure mechanisms are directly governed by the aggregate effect of the full heterogeneous microstructure. Thus, it is critical to experimentally study the TBC system and use computational solutions, like finite element simulations, to strengthen and explain results rather than to rely on numerical approaches alone. It is difficult for numerical approaches to integrate all of these parameters to accurately describe the failure mechanisms of these coatings, so this dissertation applies a series of *in-situ* experimental testing techniques to elucidate the fracture and failure mechanisms to address the following technical questions:

i. How can we accurately quantify the residual stress within TBC coating layers? What is the role of the coating layer stress state on fracture? Mechanical properties of individual coating layers (*i.e.*, modulus, thermal expansion coefficient) will affect the local stress state, but it is also important to investigate the aggregate effect of multiple layers (such as the bond coat and top coat), each with disparate thermomechanical properties. As these coating systems cool, heat up, and cool in many cycles during

spraying and over time, the contrast in properties across the system can contribute to significant residual stress within the coating, which can promote cracking [20,34].

ii. How do pre-existing defects contribute to the mechanical durability and failure of the coating? These defects will likely serve as crack initiation sites and promote rapid crack growth, leading to coating delamination and failure.

iii. How are these mechanisms affected by high temperature effects (*i.e.*, material softening, oxidation)? High temperatures will promote oxidation, which is documented to most afflict coating layer interfaces and through-thickness cracks [27]. The growth of oxidation layers will add localized stress concentrations, which may reduce the activation barrier to delamination cracking. Furthermore, material softening at high temperatures (>1000 °C) may complicate the coating system stress state as layers relax and soften.

3. Overview of SiC/SiC Ceramic Matrix Composites

Ceramic materials are attractive materials for high temperature applications (up to 1500 °C); however, their brittle and catastrophic failure modes are highly problematic in aerospace and nuclear applications where safety is a mission-critical consideration. Ceramic fiber / ceramic matrix composites represent a potential solution where the fiber / matrix architecture can enable higher strength and toughness because individual constituents may fail, but the load can be redistributed to remaining fibers [35]. There are numerous technical questions, which must be addressed before CMCs are ready for implementation in mission-critical structural roles. These questions include unveiling the architecture, load, and environment dependent failure mechanisms, thermomechanical properties, oxidation effects, among many others.

In this dissertation, the research focus is on SiC fiber /SiC matrix CMCs, which are prime candidates to replace conventional alloy materials in aerospace and nuclear energy applications due to their excellent strength and corrosion resistance even at temperatures above the operating limits of most superalloys and due to the stability of SiC thermomechanical properties even under neutron irradiation [36,37]. It is

commonly understood that the properties and failure mechanisms of CMCs are highly dependent on the loading orientation and CMC architecture [38–40]; this effect can be attributed to the hierarchical structure of the CMC (Figure 1.2) [41] and the resulting impact on load distribution. The SiC fibers are the prominent load-bearing feature of the CMC, and hundreds of individual fibers bundled together in tows can be woven or braided forming complex structures to distribute loading. The fibers are coated with a thin boron nitride or pyrolytic carbon coating and then coated with a SiC matrix interphase via either a chemical vapor infiltration or chemical vapor deposition process [42,43].

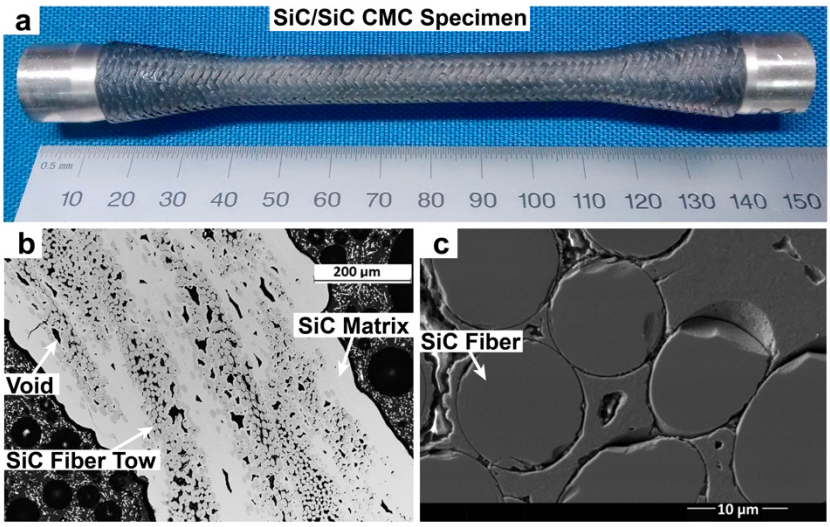

Figure 1.2. An example of a typical SiC/SiC CMC. (a) A hollow, CMC tube prepared as a tensile specimen. (bc) SEM micrographs showing the fiber microstructure. Adapted from Singh, *et al*. (2018) [41].

The resulting CMC architecture is very complicated, and thus, there are many necessary avenues of research. Much work has been done to examine the conventional tensile properties of CMCs [40,44,45] and even properties under off-axis loading (*i.e*., loading along an off-axis orientation to the fiber tow architecture) [40,46]. This testing has uncovered the fundamental fracture mechanisms of CMC for the conventional tensile load orientation; it has been demonstrated that the onset of matrix microcracking under load relieves stresses and transfers load from the matrix to the fibers. Proper tailoring of the fiber / matrix interface with a thin coating (pyrolytic carbon or boron nitride) helps to arrest or deflect cracks from

propagating from the matrix through the fibers [35]. This mechanism enables the CMC to accommodate higher strains and achieve greater strength than monolith ceramic materials [47–49]. CMCs with both pyrolytic carbon (PyC / Chapters 5 and 6) and boron nitride (BN / Chapter 7) fiber coatings are examined in this dissertation.

This prior work has demonstrated the mechanical performance of the CMCs is dependent on load orientation and load distribution mechanisms distinct for different two-dimensional and three-dimensional tow weave or braid architectures. Furthermore, the specific choice of material constituents, most prominently, the fiber / matrix coating, can have significant implications for CMC performance. Pyrolytic carbon interfaces are used to maintain the irradiation resistance of nuclear fuel materials [50] but are limited to low temperatures (<500 °C); in contrast, boron nitride coatings can withstand much higher temperatures and are more suitable for gas turbine applications [51]. Several different types of SiC fibers are also used, such as Nicalon, Tyranno, and Sylramic SiC fibers, which have significant variations in modulus and strength [52,53]. The methodology of matrix infiltration can also change the composite microstructure and mechanical performance. Matrix infiltration techniques include polymer infiltration and pyrolysis, chemical vapor infiltration, reactive and silicon melt infiltration, and slurry infiltration [51,54,55]. There are advantages and disadvantages to each method; and manufacturers must strike a balance between factors, such as mechanical properties, low residual stresses, and good creep and oxidation resistance, and limitations, such as a proclivity to matrix cracking due to shrinkage, the presence of pores and residual materials (like silicon), and large production costs [51].

For all this material complexity, there remain many areas in need of continued investigation, such as the load distribution mechanisms within nonconventional mission loading modes, anisotropy of thermomechanical properties, CMC constituent bonding and contact interactions, CMC porosity implications for fracture resistance, and thermal expansion mismatch between constituents. This dissertation addresses the following technical questions to provide a fundamental scientific understanding of CMC failure mechanisms in areas not addressed by the current literature:

i. What are the failure mechanisms of CMC nuclear fuel cladding? How are these mechanisms dependent on the loading mode and CMC architecture? The failure mechanisms of CMCs in nonconventional or multiaxial loading modes are less understood, owing to the lack of test methodologies beyond tension and compression testing. For example, nuclear fuel claddings are unlikely to be loaded in either tension or compression; instead, the 4 m long tubes must accommodate moderate bending strains and expansion of the fuel pellets during burnup [56]. Thus, new test methodologies are necessary to evaluate failure mechanisms attributed to the relevant loading modes.

ii. How do the failure mechanisms of the CMC affect the hermeticity, or gas tightness, of the nuclear fuel cladding? Cladding hermeticity is necessary to ensure radioactive gas remain contained within the fuel rod, so a critical question is the load and deformation limit of the cladding before gas escapes. Even at relatively low loads, matrix microcracking may be extensive enough to open channels through the cladding. Typically, hermeticity testing occurs without any concurrent loading or deformation, so it is not currently feasible to relate deformation with the gas tightness of the cladding. A new, coupled hermeticity / mechanical test rig is necessary to investigate this mission-critical quality.

iii. How is creep response governed by CMC microstructure? Can this response be isolated to identify contributions from individual features (grain boundaries, materials phases, CMC constituents, *etc.*)? How does this response scale from individual constituents to bulk composite response? The creep properties of CMCs are also poorly understood, but creep, even of this generally thermally stable material system, cannot be ignored when it may be exposed to high operating temperatures above 1200 °C for aerospace applications. The bulk composite creep behavior may be investigated via conventional tensile creep experiments [45,57], but it is critical to resolve the contribution of individual CMC constituents to the bulk composite deformation. Individual constituent properties are known to regulate mechanical properties, so it is only reasonable to assume they have equal importance to the composite creep response.

4. Statement of Research Objectives

This dissertation seeks to address critical technical questions regarding the fracture and failure mechanisms of TBC and CMC materials with focused emphasis on relevant loading mode and environment conditions. The work related to zirconia-based TBCs elucidates the microstructural, environment, and load-dependent factors critical to the failure of these coatings. This insight informs the manufacturing and future application of protective thermal coatings. This work includes:

i. High temperature wear experiments to unveil the damage mechanisms of TBCs in a gas turbine environment. Wear within a simulated turbine environment (at 1000 °C) evokes the stresses and fracture mechanisms experienced by TBCs in operation. Friction and wear rate data provide *in-situ* indicators of coating degradation. Post-experiment characterization via digital image correlation and electron microscopy qualify the extent of degradation while finite element simulations predict the accumulation of stresses within the coating.

ii. The development of a curvature-based TBC residual stress model. Pre-existing stress states within the coating can either contribute to early fracture or delay fracture. Thus, it is important to develop robust methodologies to quantify the residual stress. Here, a digital image correlation-enabled technique provides non-contact curvature measurements, which are converted into stress measurements via a Euler Bernoulli beam-in-bending model. Residual stresses are typically measured by hole drilling [58], Raman spectroscopy [59], or X-ray diffraction [60,61], but these techniques are not practical in a manufacturing environment. Digital image correlation techniques have been shown by others to provide accurate and reliable surface profile measurements [62,63], which are conducive to curvature measurements for stress calculations. Thus, this non-contact technique could be advantageous to in-process stress measurement during coating deposition to tailor the deposition to optimize the stress to delay fracture.

iii. Thermal cycling experiments to unveil the temperature-dependent and microstructure-dependent degradation mechanisms of TBCs. Thermal cycling experiments were conducted within an optical microscope heating stage, which has temperature capabilities up to 1200 °C. *In-situ* optical microscopy

image correlation was used to resolve the thermal expansion of the coating layers during repeated cycling and elucidate crack initiation and propagation. Importantly, this experimental study reflects the influence of the complex, heterogeneous TBC microstructure on crack propagation.

The work related to SiC/SiC CMCs investigates the failure mechanisms leading to loss of hermeticity, or gas tightness, and probe the low-temperature (<1000 °C) creep response of individual CMC constituents. This insight will inform the manufacturing and future application of protective thermal coatings. This work includes:

i. An investigation of the coupled fracture and hermeticity of CMC nuclear fuel claddings. Nuclear fuel claddings are anticipated to experience primarily bending and expansion loading modes in application. In contrast to tension testing, there are relatively few documented bending and expanding plug experiments, and none of those incorporate a consideration for the gas tightness of the CMC [64,65]. A new, *in-situ* hermeticity testing rig was developed to correlate leak detection with deformation. The new test rig was validated through four-point bending of steel, alumina, and borosilicate glass specimens; thus, it was possible to assess the limitations of the proposed test rig over a range of material response from brittle fracture to ductile deformation.
ii. An investigation of the environment dependent fracture of CMCs. Building on the effort of the previous investigation of CMC fracture and hermeticity, in-process crack detection and crack opening displacement measurements were performed via full-field digital image correlation analysis of CMC specimens in bending. Thus, crack properties can be correlated with flexural strain during loading to understand the progression of fracture damage. Furthermore, in recognition of the harsh operating environments of these CMCs, select specimens were subjected to high temperature (1200 °C) treatments in open air, inert (helium), and vacuum environments to elucidate environment-dependent fracture mechanisms.
iii. An investigation of the CMC constituent-level creep response. In nuclear energy and aerospace applications, CMCs are expected to withstand high temperature environments. Within jet engines,

operating temperatures may be as high as, or even greater, than 1300 °C [2,8]. While nuclear applications will not typically approach those temperatures (the typical reactor operating temperature is between 280 and 320 °C) [66], under abnormal conditions, such as fuel meltdown, temperatures may exceed 2000 °C [67]. In both aerospace and nuclear energy applications, where tight tolerances are necessary for safe operation, material deformation due to creep poses a critical challenge, and it is essential to understand and quantify the creep response. Numerous studies have aimed to address this need with tensile creep and fatigue testing of CMCs at elevated temperatures [57,68,69]. These studies focus on the aggregate CMC creep response, but as CMC architecture and composition can vary from application to application, it is also important to investigate how the creep of individual constituents contributes to the aggregate response. Thus, targeted indentation creep measurements were used to probe the constituent creep response with increasing temperature.

5. Experimental Methods Enhanced with In-Situ Digital Image Correlation

This dissertation presents experimental and computational work relating to the failure mechanisms of TBCs and CMCs, including mechanical testing (wear/fretting, flexural), thermal cycling, nanoindentation, and finite element simulations. However, the foundation of this work is digital image correlation (DIC) - enhanced experimentation. DIC measurements are performed using one or more cameras, or other imaging instrument, to track the displacement of a detectable, high contrast speckle pattern. This speckle pattern is typically applied with paint, but in some applications, the object of interest may have a high contrast surface texture or microstructure, which can serve as a substitute speckle pattern. A high resolution, gray-scale imaging source works best to maximize contrast and to allow for finer speckles, ideally about four pixels per speckle, in order to derive more accurate deformation calculations. Quantitative deformation and strain measurements are calculated based on the pixel displacement of points or speckles within the full field of view [70]. Compared to conventional deformation measurement techniques, like strain gauges or an extensometer, DIC is advantageous for providing full-field measurements rather than being limited to point

measurements and for being a non-contact technique, making it highly suitable for high temperature applications.

There are different iterations of DIC; DIC is highly versatile and can be performed with multiscale imaging techniques, such as everyday digital cameras [71,72], scanning and transmission electron microscopy [73–75], atomic force microscopy [76], and X-ray tomography [64,77]. Depending on the imaging technique, DIC calculations can be performed to characterize two-dimensional and three-dimensional surface deformations or volumetric internal microstructural deformation [70]. DIC within this dissertation is limited to two-dimensional and three-dimensional surface characterization, performed with one to two cameras, respectively. All image correlation was performed using commercial DIC software (Correlated Solutions Vic-2D and Vic-3D).

In any iteration of DIC, deformation measurements are made by quantifying the displacement of pixels within each collected image from some reference image, usually but not always the first image collected. This calculation is performed by tracking distinguishable groups of speckles within a subset. These subsets must contain enough speckles to be distinct, so they can be tracked from image to image and can be discernable from potentially dozens to hundreds of subsets within an image. The DIC algorithms quantify the pixel displacement vector of each subset to generate a full-field displacement map with a theoretical accuracy better than 0.01 pixels (Figure 1.3). These algorithms can isolate contributions to deformation from translation, rotation, shear, and rigid body motion. The subsets are spaced across the field of view and spaced from subset center to subset center by some step distance, typically a third of the subset size [70]. It is up to the operator to specify the subset size and step size and to find a balance between a tool large subset with less spatial resolution yet speedy computation time and a subset too small, which may fail to correlate from image to image.

The basis for much of this dissertation is three-dimensional DIC (3D-DIC), in which a pair of cameras are positioned around the object of interest with overlapping fields of view. The two cameras are calibrated using a grid with a known speckle pattern to establish the angle and distance of the cameras relative to each other. Thus, the in-plane and out-of-plane coordinates of the object surface can be triangulated between

images captured from both cameras, providing stereoscopic image correlation for three-dimensional measurements.

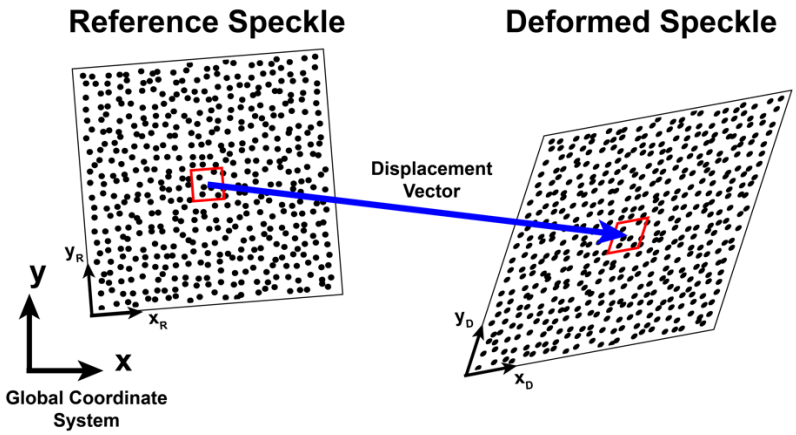

Figure 1.3. A graphical representation of the displacement from reference to deformed speckle pattern. A red box denotes an individual subset of a few speckles. Adapted from [70].

Regardless of the specific configuration, DIC typically requires uniform illumination and good contrast; insufficient lighting, oversaturation, lack of focus, and lack of contrast can all contribute to measurement error. A study conducted by Sandia National Laboratory explored in detail the different sources of DIC variation, noise, and error, categorizing error as either random (noise) or systematic (bias). A graphical representation of their analysis is presented in Figure 1.4 [78]. Subtle variations in these factors between every test necessitate quantifying the measurement error before each test; this error is reported in the following chapters. However, a standard procedure for measuring the error was used, where the surface of interest was imaged while unloaded and/or at a stable temperature. Artificial spatial and temporal deformation in those images would constitute error, and a singular value of this error was typically determined by averaging this variation. This approach captures systematic error and random error. Systematic bias in DIC profiles can be corrected and subtracted from the analyses, but random error is quantified and listed alongside the analyses. Specific contributing factors and accommodations for DIC error are discussed in the context of each test in the following chapters.

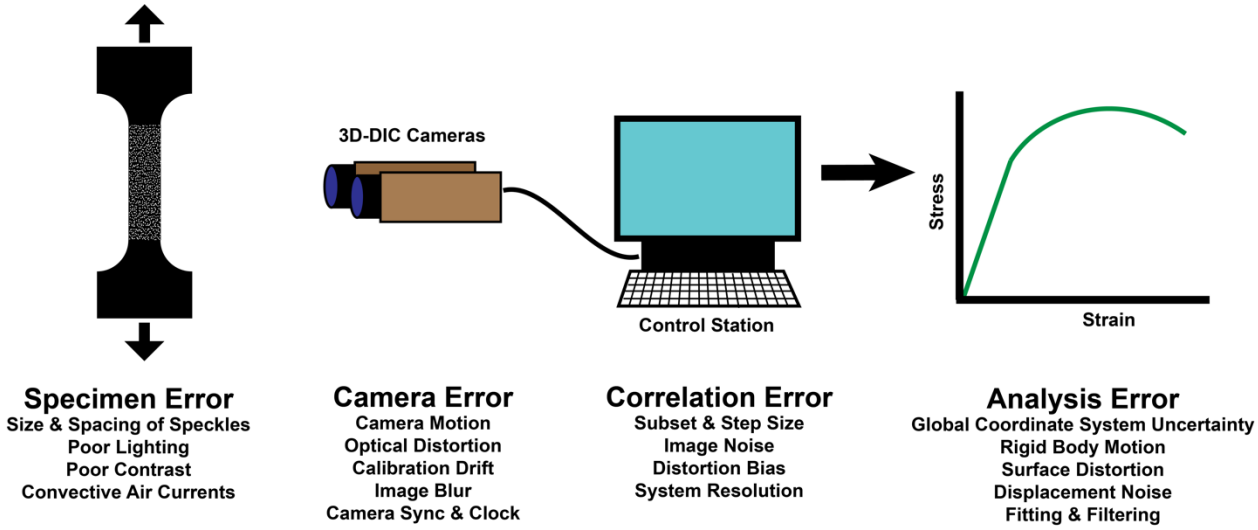

Figure 1.4. A graphical representation of the sources of DIC error associated with the specimen, cameras, correlation calculations, and analysis and quantification of strain. Adapted from [78].

6. References

[1] E.O. Ezugwu, Key improvements in the machining of difficult-to-cut aerospace superalloys, Int. J. Mach. Tools Manuf. 45 (2005) 1353–1367. doi:10.1016/j.ijmachtools.2005.02.003.

[2] R.K. Mishra, C. Beura, Life consumption assessment of a large jet engine, J. Fail. Anal. Prev. 14 (2014) 519–529. doi:10.1007/s11668-014-9842-2.

[3] M. Hirano, T. Yonomoto, M. Ishigaki, N. Watanabe, Y. Maruyama, Y. Sibamoto, T. Watanabe, K. Moriyama, Insights from review and analysis of the Fukushima Dai-ichi accident, J. Nucl. Sci. Technol. 49 (2012) 1–17. doi:10.1080/18811248.2011.636538.

[4] Z. Karoutas, J. Brown, A. Atwood, L. Hallstadius, E. Lahoda, S. Ray, J. Bradfute, The maturing of nuclear fuel: Past to Accident Tolerant Fuel, Prog. Nucl. Energy. 102 (2018) 68–78. doi:10.1016/j.pnucene.2017.07.016.

[5] M. Kurata, Research and development methodology for practical use of accident tolerant fuel in light water reactors, Nucl. Eng. Technol. 48 (2016) 26–32. doi:10.1016/j.net.2015.12.004.

[6] P. Yvon, F. Carré, Structural materials challenges for advanced reactor systems, J. Nucl. Mater. 385 (2009) 217–222. doi:10.1016/j.jnucmat.2008.11.026.

[7] P. Fauchais, Understanding plasma spraying, J. Phys. D. Appl. Phys. 37 (2004) R86–R108. doi:10.1088/0022-3727/37/9/R02.

[8] C.B. Meher-Homji, G. Gabriles, Gas turbine blade failures - causes, avoidance, and troubleshooting, in: Proc. 27th Turbomach. Symp., 1998: pp. 129–179. http://citeseerx.ist.psu.edu/viewdoc/download?doi=10.1.1.462.4970&rep=rep1&type=pdf (accessed May 18, 2016).

[9] J.T. DeMasi-Marcin, D.K. Gupta, Protective coatings in the gas turbine engine, Surf. Coatings Technol. 68–69 (1994) 1–9. doi:10.1016/S0043-1648(03)00446-0.

[10] J.R. Fincke, W.D. Swank, R.L. Bewley, D.C. Haggard, M. Gevelber, D. Wroblewski, Diagnostics and control in the thermal spray process, Surf. Coatings Technol. 146–147 (2001) 537–543. doi:10.1016/S0257-8972(01)01432-3.

[11] P. Fauchais, M. Vardelle, A. Vardelle, Reliability of plasma-sprayed coatings: monitoring the plasma spray process and improving the quality of coatings, J. Phys. D. Appl. Phys. 46 (2013) 224016. doi:10.1088/0022-3727/46/22/224016.

[12] C. Lamuta, G. Di Girolamo, L. Pagnotta, Microstructural, mechanical and tribological properties of nanostructured YSZ coatings produced with different APS process parameters, Ceram. Int. 41 (2015) 8904–8914. doi:10.1016/j.ceramint.2015.03.148.

[13] S.R. Choi, J.W. Hutchinson, A.G. Evans, Delamination of multilayer thermal barrier coatings, Mech. Mater. 31 (1999) 431–447. doi:10.1016/S0167-6636(99)00016-2.

[14] R.W. Jackson, M.R. Begley, Critical cooling rates to avoid transient-driven cracking in thermal barrier coating (TBC) systems, Int. J. Solids Struct. 51 (2014) 1364–1374. doi:10.1016/j.ijsolstr.2013.12.029.

[15] A.G. Evans, J.W. Hutchinson, The mechanics of coating delamination in thermal gradients, Surf. Coatings Technol. 201 (2007) 7905–7916. doi:10.1016/j.surfcoat.2007.03.029.

[16] J.W. Hutchinson, A.G. Evans, On the delamination of thermal barrier coatings in a thermal gradient, Surf. Coatings Technol. 149 (2002) 179–184. doi:10.1016/S0257-8972(01)01451-7.

[17] Y.C. Zhou, T. Tonomori, A. Yoshida, L. Liu, G. Bignall, T. Hashida, Fracture characteristics of thermal barrier coatings after tensile and bending tests, Surf. Coatings Technol. 157 (2002) 118–127. doi:10.1016/S0257-8972(02)00154-8.

[18] R. Eriksson, S. Sjöström, H. Brodin, S. Johansson, L. Östergren, X.H. Li, TBC bond coat–top coat interface roughness: Influence on fatigue life and modelling aspects, Surf. Coatings Technol. 236 (2013) 230–238. doi:10.1016/j.surfcoat.2013.09.051.

[19] A. Moridi, M. Azadi, G.H. Farrahi, Thermo-mechanical stress analysis of thermal barrier coating system considering thickness and roughness effects, Surf. Coatings Technol. 243 (2014) 91–99. doi:10.1016/j.surfcoat.2012.02.019.

[20] Z. Lu, S.W. Myoung, Y.G. Jung, G. Balakrishnan, J. Lee, U. Paik, Thermal fatigue behavior of air-plasma sprayed thermal barrier coating with bond coat species in cyclic thermal exposure, Mater. 6 (2013) 3387–3403. doi:10.3390/ma6083387.

[21] P. Scardi, M. Leoni, L. Bertamini, Influence of phase stability on the residual stress in partially stabilized zirconia TBC produced by plasma spray, Surf. Coatings Technol. 76–77 (1995) 106–112. doi:10.1016/0257-8972(95)02496-4.

[22] Y. Niu, X. Zheng, X. Liu, H. Ji, C. Ding, Influence of powder size on characteristics of air plasma sprayed silicon coatings, Ceram. Int. 38 (2012) 5897–5905. doi:10.1016/j.ceramint.2012.03.080.

[23] B.T. Richards, H.N.G. Wadley, Plasma spray deposition of tri-layer environmental barrier coatings, J. Eur. Ceram. Soc. 34 (2014) 3069–3083. doi:10.1016/j.jeurceramsoc.2014.04.027.

[24] W. Beele, G. Marijnissen, A. Van Lieshout, The evolution of thermal barrier coatings - Status and upcoming solutions for today's key issues, Surf. Coatings Technol. 120–121 (1999) 61–67. doi:10.1016/S0257-8972(99)00342-4.

[25] A. Feuerstein, J. Knapp, T. Taylor, A. Ashary, A. Bolcavage, N. Hitchman, Technical and economical aspects of current thermal barrier coating systems for gas turbine engines by thermal spray and EBPVD: A review, J. Therm. Spray Technol. 17 (2008) 199–213. doi:10.1007/s11666-007-9148-y.

[26] Z.H. Xu, Y. Yang, P. Huang, X. Li, Determination of interfacial properties of thermal barrier coatings by shear test and inverse finite element method, Acta Mater. 58 (2010) 5972–5979. doi:10.1016/j.actamat.2010.07.013.

[27] A. Rabiei, A.G. Evans, Failure mechanisms associated with the thermally grown oxide in plasma-sprayed thermal barrier coatings, Acta Mater. 48 (2000) 3963–3976. doi:10.1016/S1359-6454(00)00171-3.

[28] S. Krämer, S. Faulhaber, M. Chambers, D.R. Clarke, C.G. Levi, J.W. Hutchinson, A.G. Evans, Mechanisms of cracking and delamination within thick thermal barrier systems in aero-engines subject to calcium-magnesium-alumino-silicate (CMAS) penetration, Mater. Sci. Eng. A. 490 (2008) 26–35. doi:10.1016/j.msea.2008.01.006.

[29] S.S. Panwar, T.U. Patro, K. Balasubramanian, B. Venkataraman, High-temperature stability of yttria-stabilized zirconia thermal barrier coating on niobium alloy—C-103, Bull. Mater. Sci. 39 (2016) 321–329. doi:10.1007/s12034-015-1140-4.

[30] A.A. Kulkarni, A. Goland, H. Herman, A.J. Allen, J. Ilavsky, G.G. Long, F. De Carlo, Advanced microstructural characterization of plasma-sprayed zirconia coatings over extended length scales, J. Therm. Spray Technol. 14 (2005) 239–250. doi:10.1361/10599630523818.

[31] M.Y. He, J.W. Hutchinson, A.G. Evans, Simulation of stresses and delamination in a plasma-sprayed thermal barrier system upon thermal cycling, Mater. Sci. Eng. A. 345 (2003) 172–178. doi:10.1016/S0921-5093(02)00458-6.

[32] X.L. Fan, R. Xu, W.X. Zhang, T.J. Wang, Effect of periodic surface cracks on the interfacial fracture of thermal barrier coating system, Appl. Surf. Sci. 258 (2012) 9816–9823. doi:10.1016/j.apsusc.2012.06.036.

[33] H. Guo, H. Murakami, S. Kuroda, Thermal cycling behavior of plasma sprayed segmented thermal barrier coatings, Mater. Trans. 47 (2006) 306–309. doi:10.2320/matertrans.47.306.

[34] Y.C. Zhou, T. Hashida, Thermal fatigue failure induced by delamination in thermal barrier coating, Int. J. Fatigue. 24 (2002) 407–417. doi:10.1016/S0142-1123(01)00096-2.

[35] R. Naslain, Design, preparation and properties of non-oxide CMCs for application in engines and nuclear reactors: an overview, Compos. Sci. Technol. 64 (2004) 155–170. doi:10.1016/S0266-3538(03)00230-6.

[36] R.J. Price, Properties of silicon carbide for nuclear fuel particle coatings, Nucl. Technol. 35 (1977) 320–336. doi:10.13182/NT77-A31892.

[37] Y. Katoh, L.L. Snead, T. Nozawa, T. Hinoki, A. Kohyama, N. Igawa, T. Taguchi, Mechanical properties of chemically vapor-infiltrated silicon carbide structural composites with thin carbon interphases for fusion and advanced fission applications, Mater. Trans. 46 (2005) 527–535.

[38] M.Z. Berbon, K.L. Rugg, M.S. Dadkhah, D.B. Marshall, Effect of weave architecture on tensile properties and local strain heterogeneity in thin-sheet C-SiC composites, J. Am. Ceram. Soc. 85 (2002) 2039–2048. doi:10.1111/j.1151-2916.2002.tb00401.x.

[39] M.N. Rossol, V.P. Rajan, F.W. Zok, Effects of weave architecture on mechanical response of 2D ceramic composites, Compos. Part A Appl. Sci. Manuf. 74 (2015) 141–152. doi:10.1016/j.compositesa.2015.04.003.

[40] G.N. Morscher, H.M. Yun, J.A. Dicarlo, In-plane cracking behavior and ultimate strength for 2D woven and braided melt-infiltrated SiC/SiC composites tensile loaded in off-axis fiber directions, J. Am. Ceram. Soc. 90 (2007) 3185–3193. doi:10.1111/j.1551-2916.2007.01887.x.

[41] G. Singh, S.T. Gonczy, C.P. Deck, E. Lara-Curzio, Y. Katoh, Interlaboratory round robin study on axial tensile properties of SiC-SiC CMC tubular test specimens, Int. J. Appl. Ceram. Technol. (2018) 1–16. doi:10.1111/ijac.13010.

[42] Y. Gowayed, G. Ojard, R. Miller, U. Santhosh, J. Ahmad, R. John, Mechanical Properties of MI SiC/SiC Composites and Their Constituents, 2007. http://oai.dtic.mil/oai/oai?verb=getRecord&metadataPrefix=html&identifier=ADA471472 (accessed May 18, 2016).

[43] C.P. Deck, H.E. Khalifa, B. Sammuli, T. Hilsabeck, C.A. Back, Fabrication of SiC–SiC composites for fuel cladding in advanced reactor designs, Prog. Nucl. Energy. 57 (2012) 38–45. doi:10.1016/J.PNUCENE.2011.10.002.

[44] S.R. Choi, N.P. Bansal, M.J. Verrilli, Delayed failure of ceramic matrix composites in tension at elevated temperatures, J. Eur. Ceram. Soc. 25 (2005) 1629–1636. doi:10.1016/j.jeurceramsoc.2004.05.024.

[45] G.N. Morscher, V. V. Pujar, Design guidelines for in-plane mechanical properties of SiC fiber-reinforced melt-infiltrated SiC composites, Int. J. Appl. Ceram. Technol. 6 (2009) 151–163. doi:10.1111/j.1744-7402.2008.02331.x.

[46] C.S. Lynch, A.G. Evans, Effects of off-axis loading on the tensile behavior of a Ceramic-Matrix Composite, J. Am. Ceram. Soc. 79 (1996) 3113–23. doi:10.1111/j.1151-2916.1996.tb08085.x.

[47] C. Cady, A.G. Evans, K.E. Perry, Stress redistribution around mechanical attachments in ceramic matrix composites, Composites. 26 (1995) 683–690. https://ac.els-cdn.com/001043619591134Q/1-s2.0-001043619591134Q-main.pdf?_tid=4a24cf2c-cafa-11e7-800f-00000aacb35e&acdnat=1510856379_d3635520f9c97814588bb24dfbfb732b (accessed November 16, 2017).

[48] G. Morscher, J. Gyekenyesi, Room temperature tensile behavior and damage accumulation of Hi-Nicalon reinforced SiC matrix composites, 22nd Annu. Conf. Compos. Adv. Ceram. Mater. Struct. (2009). https://ntrs.nasa.gov/archive/nasa/casi.ntrs.nasa.gov/19980237335.pdf (accessed November 9, 2017).

[49] G.N. Morscher, H.M. Yun, J.A. DiCarlo, Matrix cracking in 3D orthogonal melt-infiltrated SiC/SiC composites with various z-fiber types, J. Am. Ceram. Soc. 88 (2004) 146–153. doi:10.1111/j.1551-2916.2004.00029.x.

[50] S. Agarwal, G. Duscher, Y. Zhao, M.L. Crespillo, Y. Katoh, W.J. Weber, Multiscale characterization of irradiation behaviour of ion-irradiated SiC/SiC composites, Acta Mater. 161 (2018) 207–220. doi:10.1016/j.actamat.2018.09.012.

[51] D. Kopeliovich, Advances in ceramic matrix composites using infiltration techniques, in: Adv. Ceram. Matrix Compos., Elsevier, 2014: pp. 79–108. doi:10.1533/9780857098825.1.79.

[52] T. Hinoki, E. Lara-Curzio, L.L. Snead, Mechanical properties of high purity SiC fiber-reinforced CVI-SiC matrix composites, Fusion Sci. Technol. 44 (2003). http://citeseerx.ist.psu.edu/viewdoc/download?doi=10.1.1.550.1651&rep=rep1&type=pdf (accessed January 13, 2017).

[53] H.M. Yun, J.Z. Gyekenyesi, Y.L. Chen, D.R. Wheeler, J.A. Dicarlo, Tensile behavior of SiC/SiC composites reinforced by treated Sylramic SiC fibers, Ceram. Eng. Sci. Proc. (2001) 521–531. http://onlinelibrary.wiley.com/store/10.1002/9780470294680.ch60/asset/ch60.pdf?v=1&t=ja1et44c&s=ce79b0421089ac5ed8ee192361d317a2f1bcc654 (accessed November 6, 2017).

[54] G.S. Corman, A.J. Dean, S. Brabetz, M.K. Brun, K.L. Luthra, L. Tognarelli, M. Pecchioli, Rig and engine testing of melt infiltrated ceramic composites for combustor and shroud applications, J. Eng. Gas Turbines Power. 124 (2002) 459–464. doi:10.1115/1.1455637.

[55] L.A. Timms, W. Westby, C. Prentice, D. Jaglin, R.A. Shatwell, J.G.P. Binner, Reducing chemical vapour infiltration time for ceramic matrix composites., J. Microsc. 201 (2001) 316–323. doi:10.1046/j.1365-2818.2001.00840.x.

[56] J.S. Cheon, B.H. Lee, Y.H. Koo, J.Y. Oh, D.S. Sohn, Evaluation of a pellet-clad mechanical interaction in mixed oxide fuels during power transients by using axisymmetric finite element modeling, Nucl. Eng. Des. 231 (2004) 39–50. doi:10.1016/j.nucengdes.2004.02.009.

[57] G.N. Morscher, G. Ojard, R. Miller, Y. Gowayed, U. Santhosh, J. Ahmad, R. John, Tensile creep and fatigue of Sylramic-iBN melt-infiltrated SiC matrix composites: Retained properties, damage development, and failure mechanisms, Compos. Sci. Technol. 68 (2008) 3305–3313. doi:10.1016/j.compscitech.2008.08.028.

[58] G.S. Schajer, Hole-drilling residual stress profiling with automated smoothing, J. Eng. Mater. Technol. 129 (2007) 440–445.

[59] Y. Kang, Y. Qiu, Z. Lei, M. Hu, An application of Raman spectroscopy on the measurement of residual stress in porous silicon, Opt. Lasers Eng. 43 (2005) 847–855. doi:10.1016/j.optlaseng.2004.09.005.

[60] J.L. Bartlett, B.P. Croom, J. Burdick, D. Henkel, X. Li, Revealing mechanisms of residual stress development in additive manufacturing via digital image correlation, Addit. Manuf. 22 (2018) 1–12. doi:10.1016/j.addma.2018.04.025.

[61] P.S. Prevéy, X-ray Diffraction Residual Stress Techniques, in: Met. Handb., Metals Park: American Society for Metals, 1986: pp. 380–392. https://mme.iitm.ac.in/vsarma/mm3320/ResidualStress.pdf (accessed April 23, 2017).

[62] S.R. McNeill, M.A. Sutton, Z. Miao, J. Ma, Measurement of surface profile using digital image correlation, Exp. Mech. 37 (1997) 13–20. doi:10.1007/BF02328744.

[63] J.D. Helm, S.R. McNeill, M.A. Sutton, Improved three-dimensional image correlation for surface displacement measurement, Opt. Eng. 35 (1996) 1911–1920. doi:10.1117/1.600624.

[64] B.P. Croom, P. Xu, E.J. Lahoda, C.P. Deck, X. Li, Quantifying the three-dimensional damage and stress redistribution mechanisms of braided SiC/SiC composites by in situ volumetric digital image correlation, Scr. Mater. 130 (2017) 238–241. doi:10.1016/j.scriptamat.2016.12.021.

[65] I.J. van Rooyen, W.R. Lloyd, T.L. Trowbridge, S.R. Novascone, K.J. Wendt, I.J. Van Rooyen, T.L. Trowbridge, S.R. Novascone, K.J. Wendt, S.M. Bragg-Sitton, SiC-CMC-Zircaloy-4 Nuclear Fuel Cladding Performance During 4- Point Tubular Bend Testing, LWR Fuel Perform. Meet. Fuel 2013. (2013).

[66] T. Allen, J. Busby, M. Meyer, D. Petti, Materials challenges for nuclear systems, Mater. Today. 13 (2010) 14–23. doi:10.1016/S1369-7021(10)70220-0.

[67] M. Mochizuki, T. Nguyen, K. Mashiko, Y. Saito, R. Singh, T. Nguyen, V. Wuttijumnong, Prevention possibility of nuclear power reactor meltdown by use of heat pipes for passive cooling of spent fuel, Front. Heat Pipes. 4 (2013) 13001. doi:10.5098/fhp.v4.1.3001.

[68] J.-L. Chermant, G. Farizy, G. Boitier, S. Darzens, J. Vicens, J.-C. Sangleboeuf, Creep Behavior and Mechanism for CMCs with Continuous Ceramic Fibers, in: R.C. Bradt, D. Munz, M. Sakai, K.W. White (Eds.), Springer US, 2005: pp. 203–219. http://link.springer.com/chapter/10.1007/978-0-387-28920-5_16 (accessed April 27, 2016).

[69] G.N. Morscher, V. V. Pujar, Creep and Stress-Strain Behavior after Creep for SiC Fiber Reinforced, Melt-Infiltrated SiC Matrix Composites, J. Am. Ceram. Soc. 89 (2006) 1652–1658. doi:10.1111/j.1551-2916.2006.00939.x.

[70] M.A. Sutton, J.-J. Orteu, H.W. Schreier, Image Correlation for Shape, Motion and Deformation Measurements, 1st ed., New York, 2009.

[71] M. Malesa, D. Szczepanek, M. Kujawiska, A. Wiercz, P. Koakowski, Monitoring of civil engineering structures using digital image correlation technique, 14th Int. Conf. Exp. Mech. 6 (2010) 31014. doi:10.1051/epjconf/20100631014.

[72] T. Ramos, A. Furtado, S. Eslami, S. Alves, H. Rodrigues, A. Arêde, P.J. Tavares, P.M.G.P. Moreira, 2D and 3D digital image correlation in civil engineering - measurements in a masonry wall, Procedia Eng. 114 (2015) 215–222. doi:10.1016/j.proeng.2015.08.061.

[73] S. Guo, M. Sutton, X. Li, N. Li, L. Wang, SEM-DIC based nanoscale thermal deformation studies of heterogeneous material, Conf. Proc. Soc. Exp. Mech. Ser. 3 (2014) 145–150. doi:10.1007/978-3-319-00768-7_17.

[74] M.A. Sutton, N. Li, D.C. Joy, A.P. Reynolds, X. Li, Scanning electron microscopy for quantitative small and large deformation measurements part I: SEM imaging at magnifications from 200 to 10,000, Exp. Mech. 47 (2007) 775–787. doi:10.1007/s11340-007-9042-z.

[75] Y. Zhang, N. Song, J. He, R. Chen, X. Li, Lithiation-aided conversion of end-of-life lithium-ion battery anodes to high-quality graphene and graphene oxide, Nano Lett. 19 (2019) 512–519. doi:10.1021/acs.nanolett.8b04410.

[76] Z.H. Xu, M.A. Sutton, X. Li, Mapping nanoscale wear field by combined atomic force microscopy and digital image correlation techniques, Acta Mater. 56 (2008) 6304–6309. doi:10.1016/j.actamat.2008.08.044.

[77] B. Croom, W.-M. Wang, J. Li, X. Li, Unveiling 3D deformations in polymer composites by coupled micro X-ray computed tomography and volumetric digital image correlation, Exp. Mech. 56 (2016) 999–1016. doi:10.1007/s11340-016-0140-7.

[78] P.L. Reu, T.J. Miller, DIC uncertainty quantification for large scale outdoor testing, in: Soc. Exp. Mech., Greenville, SC, 2014.

CHAPTER 2: HIGH TEMPERATURE WEAR AND INDENTATION DAMAGE MECHANISMS OF THERMAL BARRIER COATINGS

1. Introduction

Thermal barrier coatings (TBCs) are multilayered ceramic coating systems frequently used, especially in the aviation industry, for thermal protection of metal alloy components [1], but they can also provide some wear protection of aerospace and automotive engine components [2,3]. In particular, jet engine turbine blades can be exposed to temperatures as high as 1300 °C, and the force of superheated air passing out of the turbine compressor into the combustion chamber can generate pressures up to 3.5 MPa [4,5]. For many metal alloys, the operating temperature is near or even beyond their melting points, requiring the coating to serve as a thermal barrier between the extreme heat and the substrate alloy. If the coating is unable to sustain the pressure, it may fail, break off, and expose the metal [5]. For this reason, turbine blade failure in a jet airliner, especially a passenger airliner, can have disastrous effects.

In response, a high temperature wear and mechanical damage study was conducted to probe the damage mechanisms of TBCs in a relevant operating environment. Previous studies have examined the effect of sliding contact, coating thickness, and friction coefficient on the stresses within TBCs [6,7]. Others have focused on particle impingement on TBCs to observe the impact on internal stresses and cracking [3]. Further research has targeted the residual stresses of yttria stabilized zirconia using Raman spectroscopy after heat treatments to 1150 °C [8]. However, TBC failure can be attributed to many factors (like residual stress, wear, and other thermomechanical mechanisms) acting in concert. Thus, an in-depth understanding of the coupled mechanisms leading to coating failure is required. From this understanding, it may be possible to identify material properties of coating layers that require improvements to prevent or delay failure.

This study built upon substantial prior work in the literature by incorporating analysis of coating properties and failure behavior at temperatures of 1000 °C within an experimental framework to replicate the operating temperature for many applications of ceramic coatings. In keeping with prior examinations of TBC wear mechanisms, this study used tribological testing to wear a sample of thermal barrier coating

to simulate conditions within a jet engine and to determine when failure will occur [9,10]. Furthermore, a control test was performed at room temperature, 23 °C, for a comparison analysis to evaluate the impact of thermal expansion on the failure mechanisms. Microscopy imaging and energy dispersive X-ray spectroscopy also provided detailed images of wear damage and layer delamination as successfully demonstrated by previous research [11,12]. Thus, a holistic inspection of TBC failure is presented in relevant turbine environments to elucidate the primary contributing factors to failure.

2. Experimental Methods

All wear and indentation tests were conducted on a specimen of a nickel-based superalloy, Haynes HR-224, composed of Ni-27.5Fe-20Cr-3.8Al [13]. This nickel alloy substrate was chosen as the substrate material due to its high temperature strength and oxidation resistance, factors determined by previous studies to be critical for operation within a turbine engine [14,15]. A ~250 μm thick top coat of yttria-stabilized zirconia (8YSZ) and a ~150 μm thick bond coat of NiCoCrAlY were applied to the specimen using an air plasma spray deposition process, layered as shown in Figure 2.1. Both coating materials were selected due to their wide use in industry and in research analysis [8,9,12].

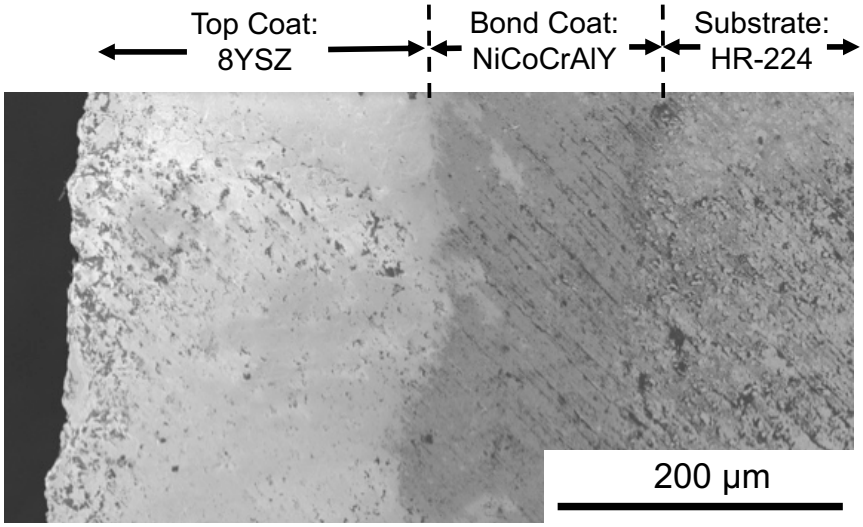

Figure 2.1. A micrograph of a TBC specimen used in this study, showing the thickness of the layers: TC, BC, and substrate.

Wear and indentation analyses of the sample were conducted using a Bruker UMT-3 tribometer (Bruker Nano Inc. Campbell, CA, USA), which was capable of measuring normal and lateral forces as well as the displacement of the indenter. Wear testing was performed in a pin-on-disk configuration as specified by ASTM G99-17. All wear tests were conducted within a furnace chamber in air, either heated to a high temperature (1000 °C) to experimentally approach the inlet temperature of a turbine or to room temperature (23 °C) as a baseline. Actual turbine temperatures will be much higher, but this experiment at 1000 °C may demonstrate the significant role of temperature in the degradation mechanisms of TBCs. Under applied loads ranging incrementally from 3 to 5 N (corresponding to 3.8 to 6.4 MPa), the oscillation tests were run for one hour each at both room and high temperatures, which corresponded to 19,098 cycles where each cycle was a 2 mm oscillation. During the tests, the tribometer collected measurements of normal (N) and lateral forces, frictional force (F_f), and used these measurements to calculate the coefficient of friction (μ), using the following equation: $F_f = \mu * N$ [16]. A 6.3mm diameter alumina ball was used as the indenter for wear tests, where the ball was oscillated with a frequency of 33.3 Hz.

Indentation hardness tests were conducted with a sapphire Vickers indenter at both room and high temperatures using the Oliver-Pharr methodology [17]. Indentations were made into a TBC cross section sufficiently thick to prevent any influence from the mounting device and with indentations spaced 5 mm apart. The cross-section was mechanically polished and at least ten indentations were made per layer to reduce any adverse effect of surface roughness on the hardness measurement [18].

3. Results and Discussion

3.1. Results of Experimental Wear Testing

Figure 2.2 presents the coefficient of friction over the hour-long tests for each applied load at 23 and 1000 ºC. At first glance, the friction exhibited a typical response: an initial period of increasing wear and unstable coefficient of friction followed by a prolonged period of stable wear and kinetic coefficient of friction. However, the initial friction response between the testing at 23 and 1000 °C was very distinct

within the first 2,500 cycles. At room temperature, the initial or static coefficient of friction was low and increased to a stable kinetic coefficient of friction. In contrast, at 1000 °C, the initial static coefficient of friction started high and decreased to a stable kinetic coefficient of friction. Furthermore, there was a significant 24.7 % decrease between the kinetic coefficients of friction at 23 and 1000 °C, which averaged to 0.37 and 0.28, respectively.

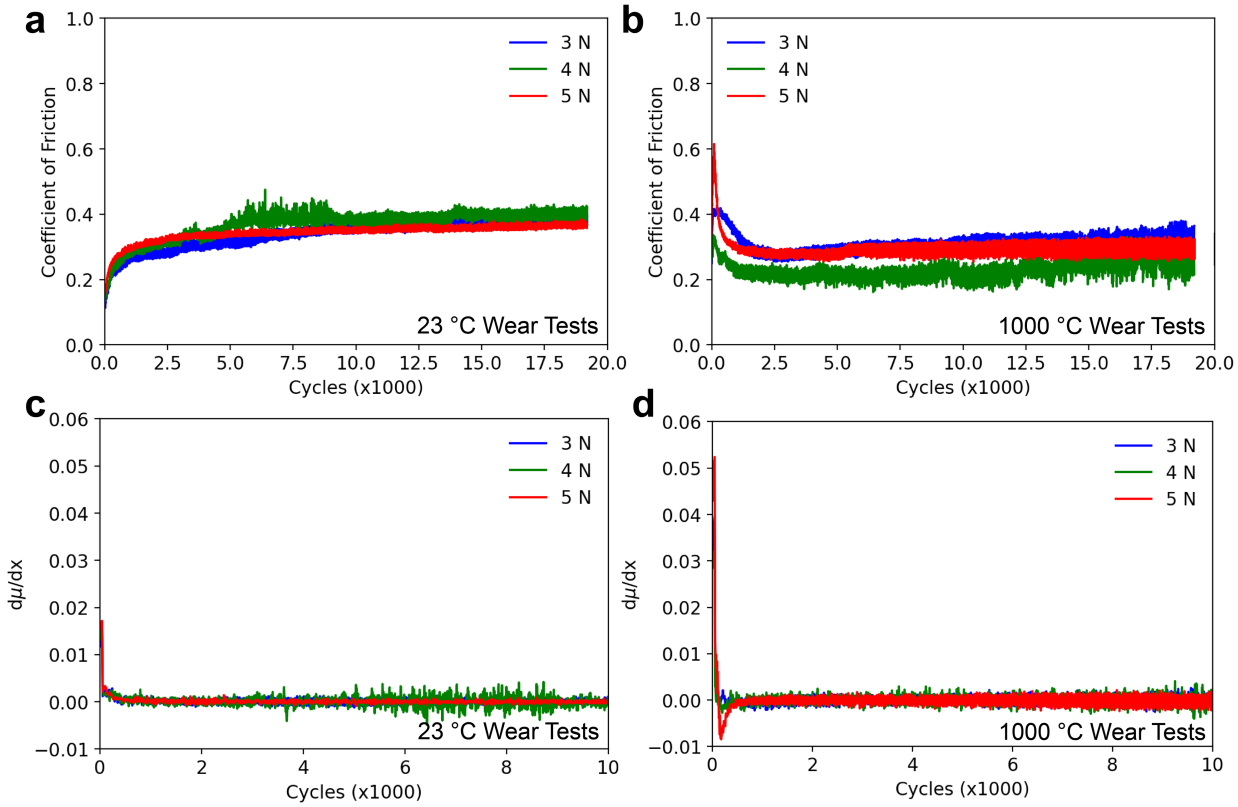

Figure 2.2. The *in-situ* coefficient of friction of the 8YSZ top coat is presented for each test at (a) 23 and (b) 1000 °C. The derivative of the coefficient of friction ($d\mu/dx$) is also presented at (c) 23 and (d) 1000 °C over the initial 10,000 cycles.

Table 2.1 lists the recorded values of friction force and coefficient of friction taken at the start and end of testing. The initial values represent both the friction of the 8YSZ top coat and the impact of stiction, the necessary force required to overcome static friction and allow motion [13]; the reported values correspond to the first 50 cycles. This initial disparity between the frictional response at the two test temperatures was best represented by Figures 2.2c,d, in which the slope, or derivative of the coefficient of friction $d\mu/dx$,

was plotted. These figures clearly show the change from an initial static friction state occurs much more dramatically over a few hundred cycles at 1000 °C, where the magnitude of the slopes was much greater. In both sets of tests at 23 and 1000 °C, the stable regions of kinetic coefficient of friction do not suggest any sudden delamination event; such an event would register a step change in friction. Instead, the friction plots would present two possibilities: (i) either delamination occurred rapidly within the first 1000 cycles or (ii) delamination did not occur and coating wear was a gradual process.

Table 2.1. Initial and final friction, coefficient of friction, wear depth (calculated based on the change in the measured height of the indenter), and wear rate (calculated by wear depth, dimension of the indenter, and time) for the 8YSZ top coat.

Room Temperature (23 ºC) Wear Testing						
Normal Force (N)	**Initial F_f (N)**	**Initial COF**	**Final F_f (N)**	**Final COF**	**Depth (µm)**	**Wear Rate (10^{-7} mm^3/min)**
3	0.42 ± 0.06	0.17 ± 0.03	1.14 ± 0.13	0.36 ± 0.05	8.10 ± 0.41	4.88 ± 0.17
4	0.62 ± 0.11	0.18 ± 0.02	1.66 ± 0.23	0.39 ± 0.05	9.30 ± 0.66	8.49 ± 0.22
5	0.83 ± 0.13	0.21 ± 0.03	1.81 ± 0.13	0.37 ± 0.03	6.87 ± 0.40	4.39 ± 0.06
High Temperature (1000 ºC) Wear Testing						
Normal Force (N)	**Initial F_f (N)**	**Initial COF**	**Final F_f (N)**	**Final COF**	**Depth (µm)**	**Wear Rate (10^{-5} mm^3/min)**
3	1.11 ± 0.16	0.39 ± 0.03	0.91 ± 0.11	0.31 ± 0.03	224 ± 4	3.99 ± 0.32
4	1.18 ± 0.35	0.30 ± 0.02	1.01 ± 0.18	0.23 ± 0.03	213 ± 6	5.55 ± 0.46
5	2.36 ± 0.27	0.48 ± 0.06	1.53 ± 0.15	0.29 ± 0.03	226 ± 10	10.31 ± 0.64

Furthermore, it is reasonable to assume the kinetic coefficient of friction will be consistent for each TBC layer, so if the final coefficients of friction were fairly comparable across individual tests at the same temperature, the wear likely progressed through the same coating layer. Variation of the coefficient of friction values would be indicative of penetration of the indenter tip into different coating layers or significant alteration of the contact surface, such as the generation of significant wear debris. Indeed, at 23 °C, the kinetic friction coefficient values featured a standard deviation of 2 % and a percent difference between the largest and smallest values of over 6 %. Coupled with the lack of a step change within the plots

in Figure 2.2a, it was clear that frictional properties measured at room temperature may be considered representative of this particular 8YSZ system. However, at 1000 °C, while the standard deviation of kinetic friction coefficients was only 3%, the percent difference between the largest and smallest values were over 25 %, significant enough to possibly indicate breakthrough into another coating layer or significant alteration of the contact surface.

To elucidate these trends further, Figure 2.3 displays the wear depth and wear rates at high and room temperature. The wear depth, *d,* was measured as the displacement of the indenter tip. The wear rate (Figure 2.3c) was calculated as the slope of the volume of material removed per min. The volume of material removed was quantified as follows:

$$V = \frac{1}{2}R^2(\theta - \sin(\theta))l + \frac{\pi d^2}{3}(3R - d) \tag{2.1}$$

Here, in Equation 2.1, R is the radius of the indenter tip (6.3 mm), l is the length of the wear track (2 mm), and θ is the angle between the sides of the wear path and centroid of the indenter tip (Figure 2.3d). The angle θ is itself a function of wear depth d as described by:

$$\theta = 2\cos^{-1}(1 - d/R) \tag{2.2}$$

First, the wear depth plots (Figures 2.3a,b) demonstrate significant material removal at 1000 °C, with the indenter tip penetrated to depths of over 210 μm, almost as deep as the top coat layer. In contrast, the wear at 23 °C never penetrated beyond 10 μm into the top coat, confirming that delamination did not occur at room temperature. Second, the wear rates (Figure 2.3c) at 23 °C were very low and stable, regardless of increasing normal load. In contrast, the wear rates at 1000 °C were two orders of magnitude greater and increased with normal load. These results further indicated the importance of temperature on the wear response of the coating.

Importantly, the wear depth plot at 1000 °C (Figure 2.3b) also reveals that the indenter quickly penetrated over 100 μm into the coating within the first 1000 cycles. Through about 10,000 cycles, the indenter continued to wear deeper into the coating but at a decreasing rate, finally stabilizing in the latter half of the test. This observation has two important implications: (i) the top coat did delaminate almost

immediately, which would explain the high initial coefficient of friction, and (ii) there was some mechanism introduced later in the test, which slowed the wear rate.

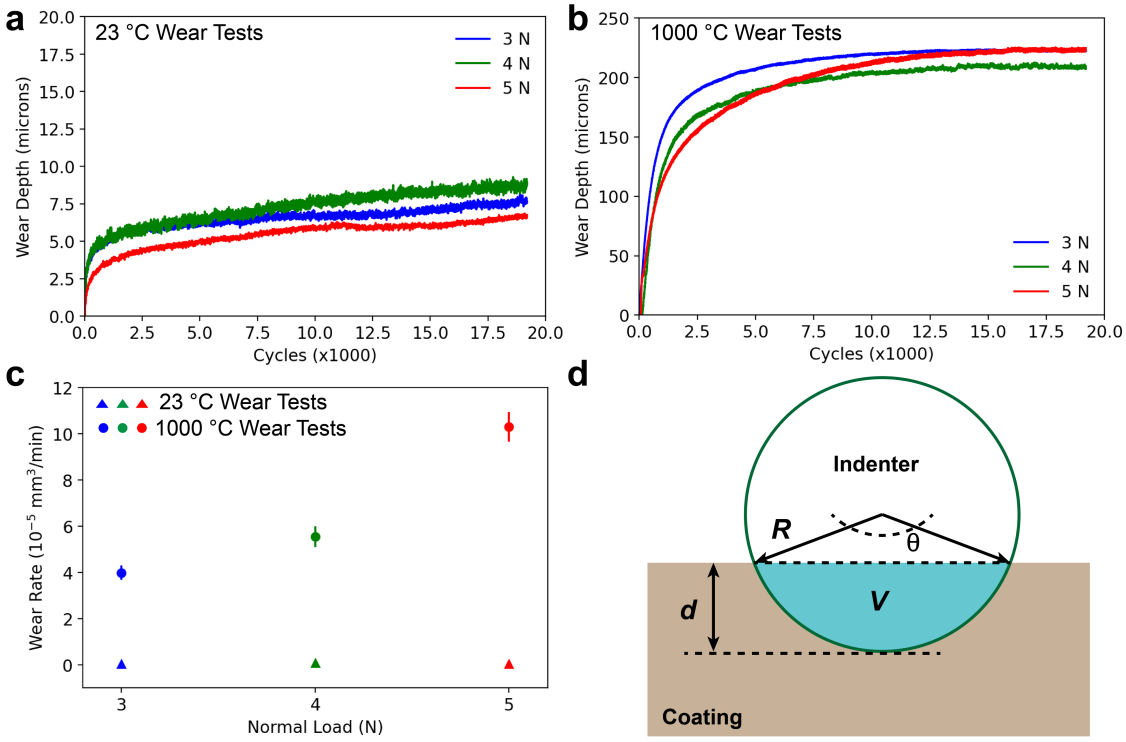

Figure 2.3. The *in-situ* wear depth plots from testing at (a) 23 and (b) 1000 °C. (c) The corresponding wear rates demonstrate significantly higher wear at 1000 °C and higher loads. (d) Graphical representation of the material volume removed during wear.

3.2. Scanning Electron Microscopy of Wear Damage

To qualitatively characterize the wear damage of the TBCs, scanning electron microscopy (SEM) images were obtained of cross-sectional cuts across the wear paths on the specimens. Each cross-section was mounted in epoxy and mechanically polished. Figure 2.4 presents images of the wear damage when the indenter oscillated in a direction corresponding to perpendicular to the page. It must be noted that air plasma sprayed TBCs are frequently characterized by pores and inter-splat cracks [9], and such features were observed in the specimens tested here. Attention was paid to cracks or microstructural features in close proximity to the wear zone. As expected, there were no signs of additional cracking or delamination in unworn areas nor in areas worn at room temperature (Figures 2.4a,c,e).

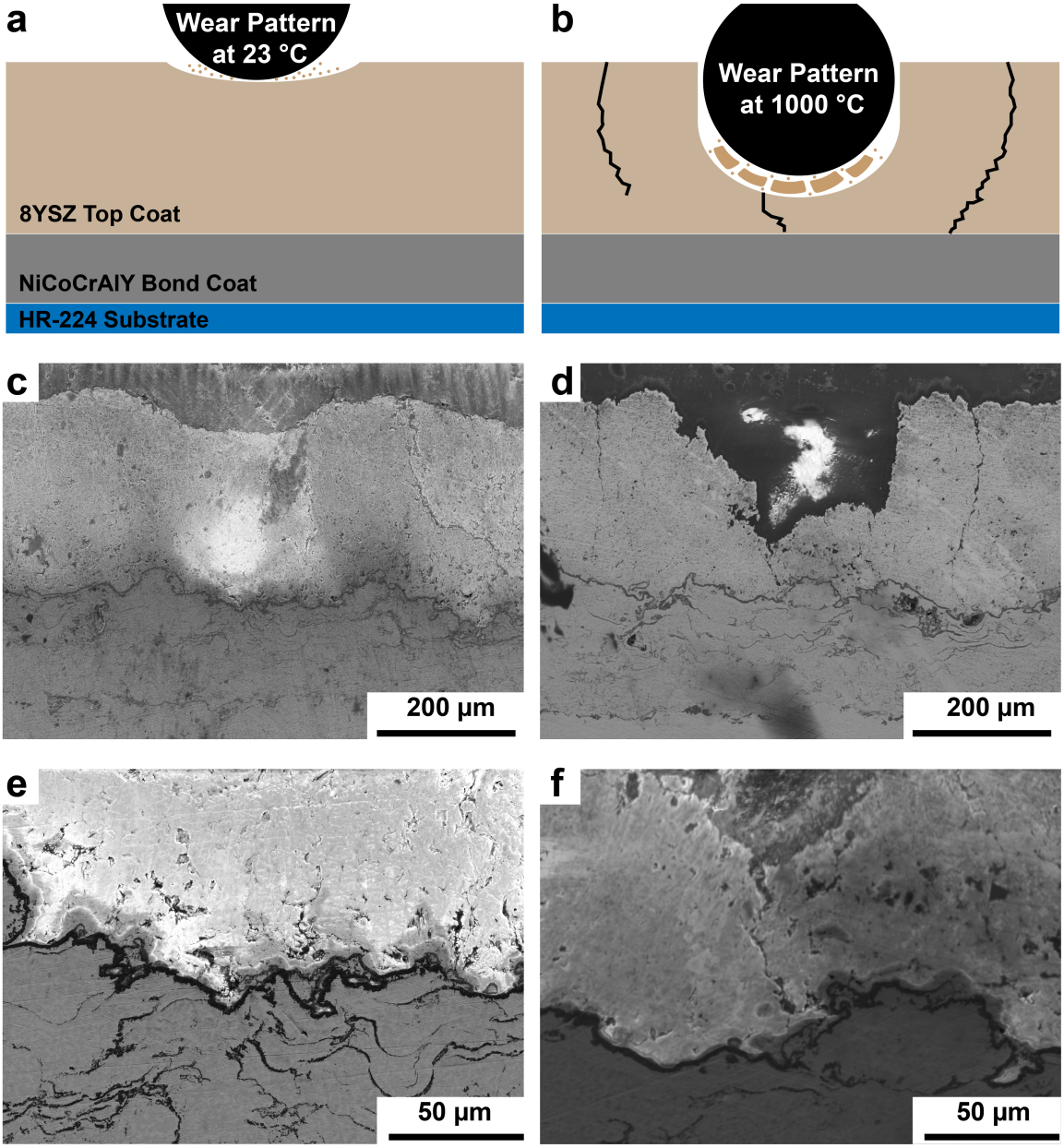

Figure 2.4. Graphical representations of the cross-sectional wear patterns after testing at (a) 23 and (b) 1000 °C. Cross-section micrographs show (c,e) little damage after testing at 23 °C but (d,f) significant wear after testing at 1000 °C. (e,f) Higher magnification images of the 8YSZ top coat / NiCoCrAlY bond coat interface.

In contrast, there was significant cracking and damage during the wear testing at high temperature (Figures 2.4b,d,f). Figure 2.4d clearly shows the deep wear depression left by the indenter as well as two lateral cracks running through the top coat layer. Figure 2.4f also shows cracking extending from the bottom

of the wear track to the bond coat. All cracking appears to arrest at the interface, indicating degradation of the top coat only.

Figure 2.5 depicts another cross-section cut in a specimen tested at 1000 °C made such that the direction of the indenter was from side to side. Large cracks and buckling were observed at the ends of the wear track and were attributed to the indenter, pushing and pulling on the top coat as it moved back and forth, causing it to tear apart and buckle. As previously noted, these buckling cracks were observed to traverse the top coat to the bond coat interface. The micrographs provided further support of a thermal effect on the wear pattern of the TBC, clearly showing different levels of degradation between tests at 23 and 1000 °C. The fracture patterns indicated substantial shear stresses within the top coat, which generated cracks directly under and within the vicinity of the contact wear.

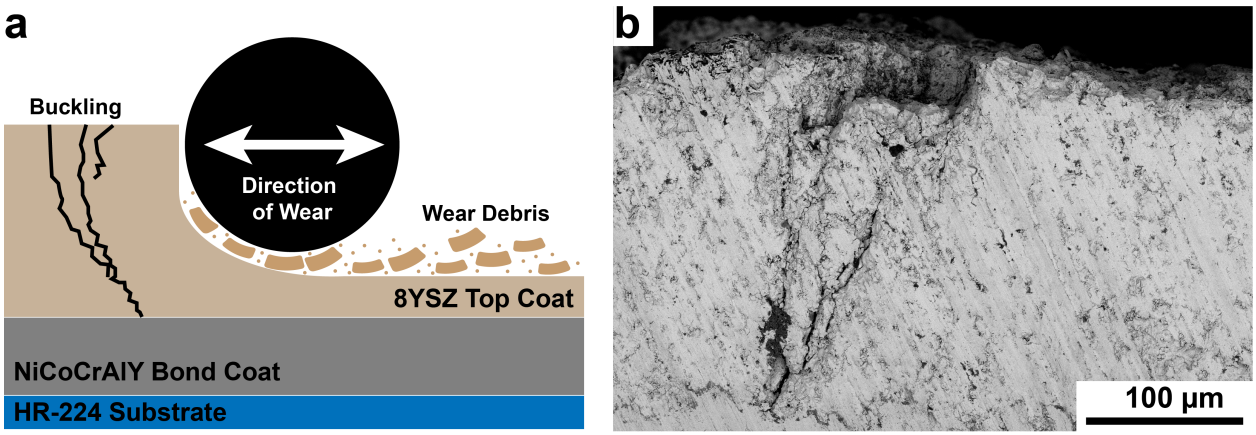

Figure 2.5. (a) Graphical representations of the cross-sectional wear pattern in the direction of wear at 1000 °C. (b) Micrograph in that same orientation captured buckling of the TBC at the ends of the wear track.

3.3. Characterizing the Extent of Wear with Digital Image Correlation

Using optical images of the coating before and after wear, digital image correlation (DIC) was performed to identify the extent of wear damage on the surface of the coating and complement the cross-sectional micrographs, using methods as described by Xu, *et al*. [19]. With the commercially available Correlated Solutions VIC-2D software, reference, undeformed features on the initial surface and deformed

features on the final worn surface were correlated to quantify the deformation. Figure 2.6b displays a representative map overlay on the worn surface of strain in the direction of the oscillating indenter. Certain regions were so deformed as to fail to render a correlation, thus outlining the extent of wear. All other regions of the coating are shaded to indicate little to no strain, which would indicate the TBC does not deform due to the wear. Rather, as expected of a ceramic material, it fractures in the region of localized stress. The coating was pulverized during wear, and debris was ejected out onto the surrounding surface, which accounted for the small, scattered areas where the correlation failed. These tests demonstrated that DIC can be used to map regions of severe wear; indeed, in all cases, the DIC-identified extent of wear degradation was limited to the region of contact with the indenter tip. Adjacent through-thickness cracking, as indicated by electron microscopy, was not detected.

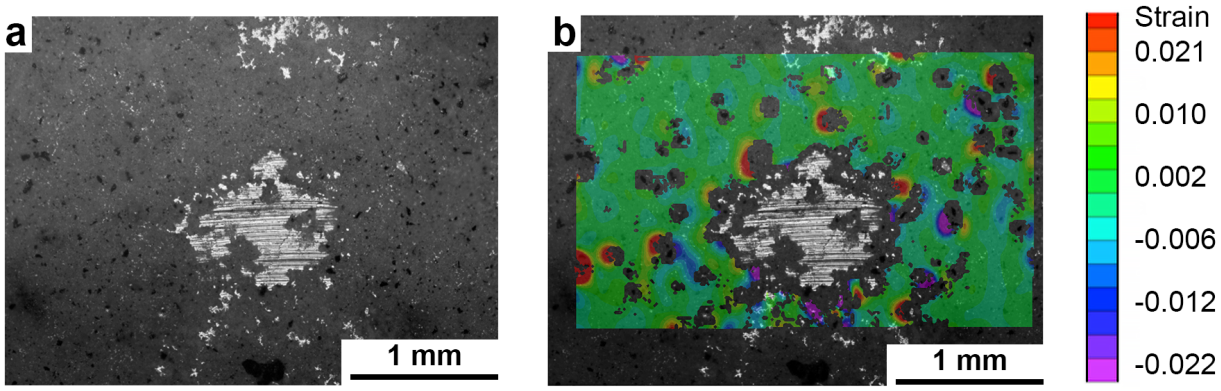

Figure 2.6. DIC between images of the (a) worn coating surface (5 N load at 23 °C) identified (b) the extent of coating wear degradation.

3.4. Energy Dispersive X-ray Mapping

In addition to the electron micrographs, energy dispersive X-Ray spectroscopy (EDS) mapping was conducted to determine the chemical makeup of the wear paths and to determine if any of the tests had managed to wear through the 8YSZ top coat to the NiCoCrAlY bond coat. Reference EDS maps were collected from a TBC cross-section prior to any testing to demonstrate the composition of the different layers of the unworn coating system (Figure 2.7). The top coat was clearly distinct, prominently shown by

the presence of zirconium in Figure 2.7f and the relatively low presence of oxygen, aluminum, iron, and nickel compared to the following layers. The bond coat could be distinguished by the greater density of aluminum (Figure 2.7c). The substrate (Ni-27.5Fe-20Cr-3.8Al [13]) is indicated by a high presence of aluminum, iron, and nickel, fitting with its element composition (Figures 2.7c,d,e).

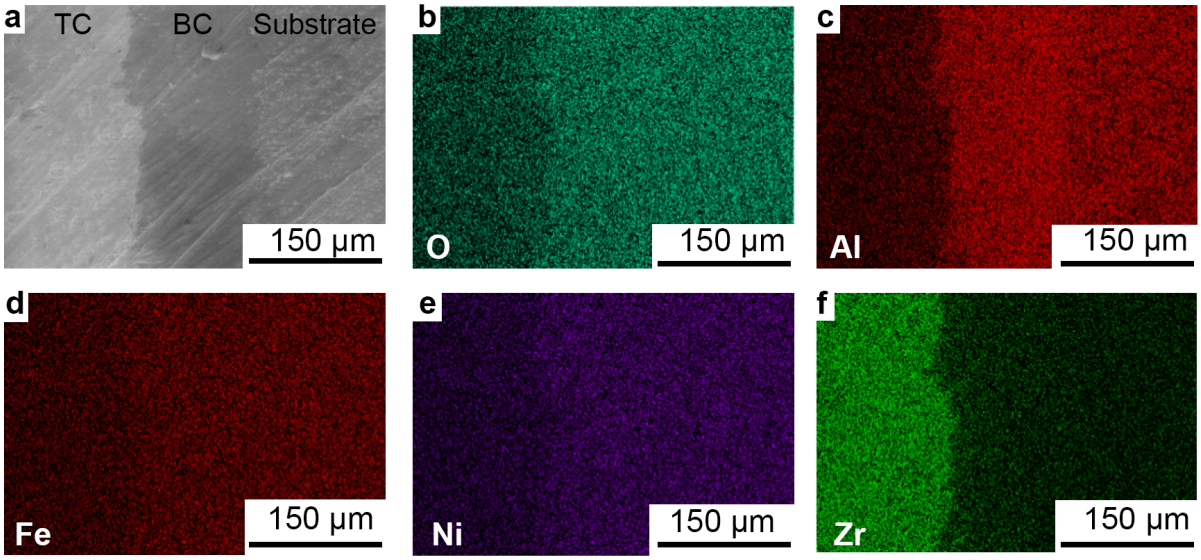

Figure 2.7. (a) A cross-sectional micrograph of the TBC system prior to any testing with the 8YSZ top coat (TC), NiCoCrAlY bond coat (BC), and HR-224 substrate noted. Corresponding EDS maps of (b) oxygen, (c) aluminum, (d) iron, (e) nickel, and (f) zirconium.

After the wear testing at both high and room temperatures, the TBC was again imaged by SEM, and new EDS maps were obtained of the most prominent materials detected (zirconium and oxygen) on the surface of the wear path. Representative element maps are presented in Figure 2.8 for wear at 23 and 1000 °C under an applied normal load of 3N. First, no changes were detectable between the regions of worn and unworn TBC surface at 23 °C. The map indicated a consistent level of zirconium to show no indenter penetration into the top coat, continuing to support the observation of very minor wear at room temperature. In contrast, EDS mapping of zirconium in Figure 2.8e showed the wear path clearly visible after testing at 1000 °C, indicating that the indenter had almost worn entirely through the top coat as supported by the wear

depth plots (Figure 2.3b). Similarly, Figure 2.8f shows the wear path characterized by a higher concentration of oxygen suggesting the growth of an additional oxide layer; it is commonly observed that 8YSZ/NiCoCrAlY coating systems will develop an alumina oxide layer, referred to as a thermally grown oxide layer, between the top coat and bond coat [20–22].

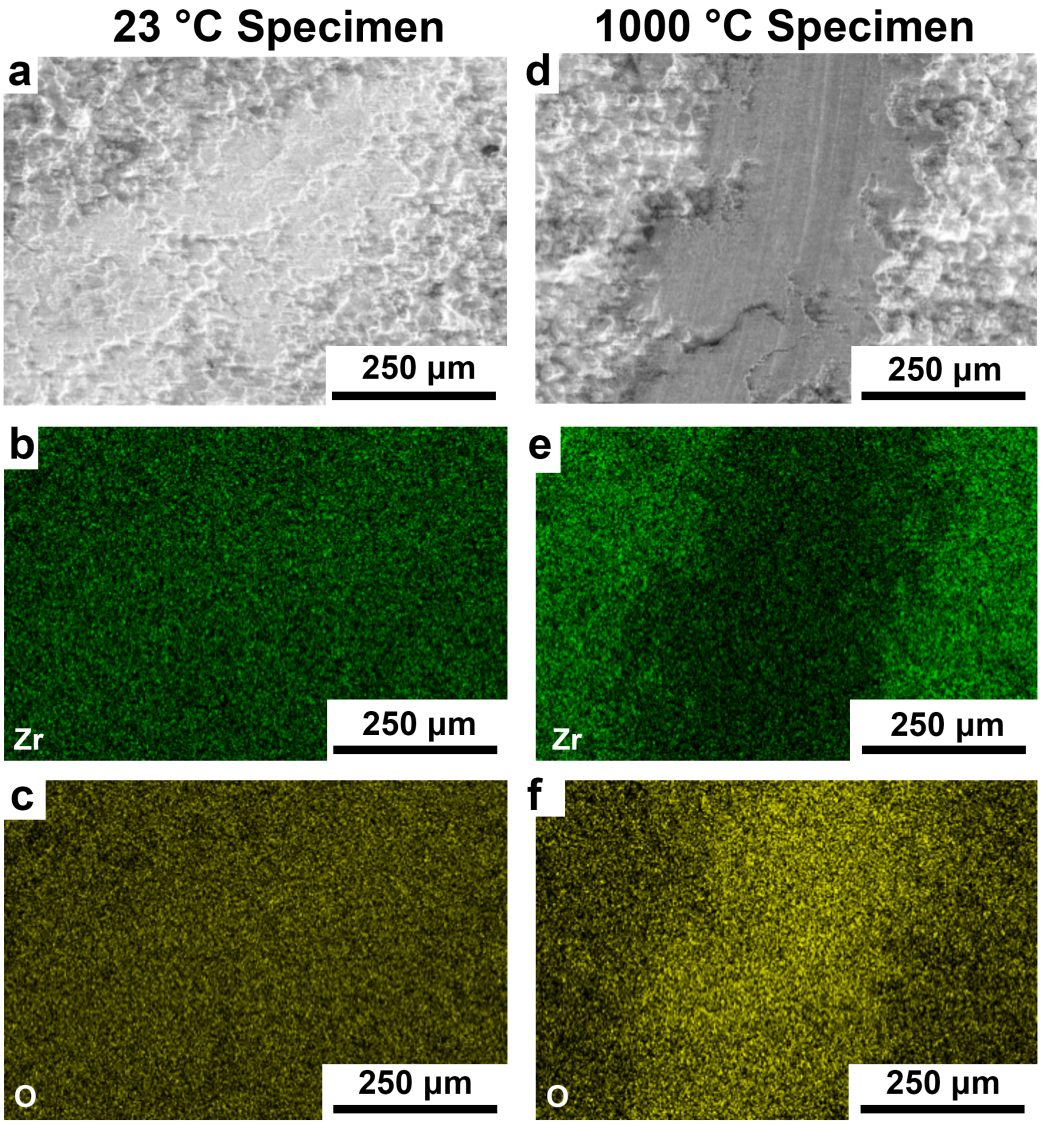

Figure 2.8. EDS mapping of the 3 N wear track after (left) 23 and (right) 1000 °C testing. (a) Wear at 23 °C did not reveal any distinguishing features in the coating as indicated by EDS maps of (b) zirconium and (c) oxygen. (d) The wear track at 1000 °C was characterized by (e) a lack of zirconium and (f) a concentration of oxygen.

3.5. Vickers Indentation Testing

Indentation tests were also conducted on the sample at both room temperature and 1000 ºC to compare the hardness of the coating layers. A sapphire Vickers indenter with an included angle of 136° was used for all hardness testing. Figures 2.9a,b,c show the indentations made at room temperature under an applied load of 30N. Figures 2.9d,e,f show the indentations made at 1000 ºC under an applied load of 15 N. At least five indentations were performed per region at each temperature. The diagonals of the indentions were measured and used to calculate the hardness. The Vickers hardness values, HV, is found using the equation:

$$HV = \frac{F}{A} = \frac{F}{(d_1 d_2)/(2\sin(\theta))} \tag{2.3}$$

where θ of 68 degrees is half the indentation angle, F is the applied load, and d_1 and d_2 are the diagonals of the indentation [17,23]. The measured Vickers hardness values are listed in Table 2.2.

Table 2.2. The hardness values of the coating layers from Vickers indentation testing at 23 and 1000 ºC.

Hardness Value (HV)	23 °C	1000 °C	Percent Diff.
Top Coat (8YSZ)	593 ± 14	352 ± 16	- 41%
Bond Coat (NiCoCrAlY)	397 ± 11	251 ± 13	-37%
Substrate (HR-224)	249 ± 8	220 ± 9	-12%

From Table 2.2, it is clear that the top coat was the hardest layer followed by the bond coat at both temperature conditions. However, temperature had a significant impact on the coating hardness; the top coat hardness value decreased by 41%, even though it remained the hardest layer at 1000 ºC. The softening of the TBC at elevated temperatures may be a contributing factor to the delamination that occurs. In support of these measurements, the hardness values obtained at room temperature agree with data in literature. The hardness of 8YSZ is difficult to narrow down and may vary with air plasma spray parameters, but the value of 593 HV, which is equivalent to a 5.6 GPa hardness value, fit neatly within the range of 3.5 to 5.8 GPa specifically reported by Jang, *et al*. and Kwon, *et al.* [23–25].

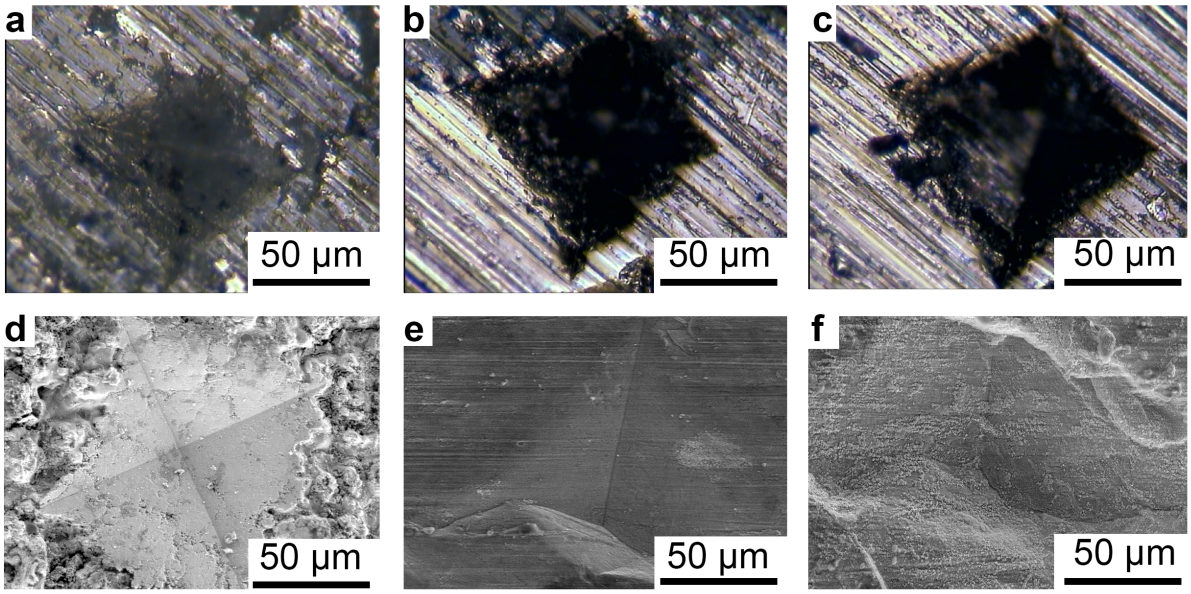

Figure 2.9. Optical images of Vickers indentations performed at 23 °C under a load of 30 N within the (a) 8YSZ top coat, (b) NiCoCrAlY bond coat, and (c) HR-224 substrate. SEM micrographs of Vickers indentations performed at 1000 °C under a load of 15 N within the (d) top coat, (e) bond coat, and (f) substrate.

3.6. Unveiling Coating Stress State with Hertz Contact Modeling

The friction, wear rate, and Vickers hardness data indicated a significant role of temperature on the wear degradation of the TBC. Furthermore, the wear damage observed under the electron microscope indicated significant stresses within and around the area of contact between the indenter and the TBC. To elucidate this stress field, a Hertz contact model was applied to describe the experimental wear test. A Hertzian contact model provides a fundamental understanding of the contact between two elastic bodies. The theory assumes the interaction is frictionless; hence, the only applied force is the applied normal load. In this case, one body was a sphere, the alumina indenter with a radius of 3.15 mm as shown in Figure 2.10. The other body was the thermal barrier coating, which when modeled as a flat plane, had a radius of curvature going to infinity [16].

Table 2.3. The Young's modulus and Poisson's Ratio data as reported in literature [13,26–30].

Temperature	Property	Alumina Indenter	8YSZ Top Coat	NiCoCrAlY Bond Coat	HR-224 Substrate
23 °C	Young's Modulus (GPa)	375	53	225	137
	Poisson's Ratio	0.24	0.31	0.3	0.3
1000 °C	Young's Modulus (GPa)	331	46	199	121
	Poisson's Ratio	0.21	0.27	0.25	0.25

Table 2.4. The calculated maximum shear stress and its depth beyond the contact point with the indenter.

Room Temperature Contact Model Analysis					
Normal Load (N)	**Indenter Depth (μm)**	**Max Shear (MPa)**	**Relative Depth to Max Shear (μm)**	**Depth of Max Shear (μm)**	**Region of Max Shear**
3	8.10 ± 0.41	165.7	24.84	32.9 ± 0.4	
4	9.30 ± 0.66	182.4	27.34	36.6 ± 0.7	Top Coat
5	6.87 ± 0.40	196.4	29.45	36.3 ± 0.4	
High Temperature Contact Model Analysis					
Normal Load (N)	**Indenter Depth (μm)**	**Max Shear (MPa)**	**Relative Depth to Max Shear (μm)**	**Total Depth of Max Shear (μm)**	**Region of Max Shear**
3	224 ± 4	148.8	26.21	250 ± 4	Top Coat/Bond Coat Interface
4	213 ± 6	163.8	28.85	242 ± 6	
5	226 ± 10	176.4	31.08	257 ± 10	

Using a Hertz contact model for elastic material deformation, the maximum shear and its depth *z* below the contact area were calculated. Characterizing the elastic response would provide a reasonable estimate of the stress state of this ceramic coating. The primary contribution to plastic deformation of this ceramic coating would be fracture itself; creep deformation was assumed to be negligible. First, the maximum pressure, P_{max}, was determined using the equation:

$$P_{max} = \frac{3F}{2\pi a^2} \tag{2.4}$$

where a is the contact radius and F is the applied force. The contact radius is found as follows:

$$a = \sqrt[3]{\frac{3F}{8}\frac{(1-v_1^2)/E_1+(1-v_2^2)/E_2}{\frac{1}{R_1}+\frac{1}{R_2}}} \tag{2.5}$$

where v is the Poisson's ratio, E is the Young's modulus, and R is the surface radius of each body in contact. The maximum shear stress, τ_{max}, is determined with the simple equation:

$$\tau_{max} = \frac{\sigma_x - \sigma_z}{2} \tag{2.6}$$

where σ_x and σ_z represent the principal stresses. The x direction was prescribed to run parallel with the oscillating indenter. The principal stresses were determined as follows [16]:

$$\sigma_x = -P_{max}\left[(1 - \left|\frac{z}{a}\right| tan^{-1}\left(\frac{1}{\left|\frac{z}{a}\right|}\right)(1+v) - \frac{1}{2\left(1+\frac{z^2}{a^2}\right)}\right] \tag{2.7}$$

$$\sigma_z = \frac{-P_{max}}{1+\frac{z^2}{a^2}} \tag{2.8}$$

The layer properties of the indenter and thermal barrier coating are presented in Table 2.3. The calculated shear and depth are listed in Table 2.4. The depth to max shear column was tabulated by combining the indenter depth from Table 2.1 with the relative depth of max shear from the point of contact. Using this total depth to the maximum shear, it was possible to identify the corresponding region or layer. As shown in Table 2.4, the maximum shear stress during wear occurred deeper in the coating as the applied normal load increased for both temperature conditions. However, at room temperature, the maximum shear occurred only within the top coat. In contrast, at 1000 °C, the shear stress occurred deeper within the coating than it did at room temperature, moving into the interface region between the top coat and bond coat. The magnitude of the shear stress at 1000 °C was also slightly lower than that at 23 °C, which can be attributed to material softening at temperature. These calculations revealed how significant the temperature effects on material properties impacted the stress distribution within the coating, pushing the depth of max shear much deeper into the coating, which would create a driving force for deeper wear.

However, the Hertz contact model had its limitations in this specific application; friction was not negligible as demonstrated by the wear tests themselves. Thus, a finite element (FE) model of the experimental wear test was assembled in LS-DYNA. FE models are frequently used to better understand the stresses present under different loading conditions, coating materials, and temperatures. Previously, Diao, *et al*. developed a FE model to evaluate sliding contact on a hard coating in order to evaluate the

maximum shearing stresses and the effect of coating thickness and friction, determining that a hard interlayer reduced the internal stresses during contact [6]. Similarly, Ahmadian, *et al*. used FE analysis to determine that parallel cracking within the top coat prompted coating failure [31]. Building from the success of prior FE analysis and the friction conditions specified in Table 2.1, a similar FE approach was applied using the material properties of the specific coating at both room and high temperatures. Using LS-DYNA, the TBC layers (Figure 2.10a) were modeled and subjected to a vertical indentation and lateral oscillations matching the behavior in the physical system during the 1000 °C wear tests. This simulation was conducted over five cycles, in which each cycle accounted for one full oscillation of the indenter back and forth. Each layer of the coating was modeled with 8-noded hexahedral elements in a 20x20 mesh, such that there were 8000, 4000, and 4000 elements in the top coat, bond coat, and substrate, respectively. Interfacial layers were connected with a tiebreak surface-to-surface method. A normal load was applied through the spherical indenter of 5 N, representing the largest test load from the wear experiments.

Figures 2.10b,c show the shear stress distribution of the TBC and the isolated top coat layer and clearly reveal that the maximum shear stress at 1000 °C occurred close to the interface with the bond coat. The model identified a max shear stress of the same magnitude, 176 MPa, as calculated via the Hertz contact model. Furthermore, the finite element model revealed a concentric ring of higher stress in the z (normal) direction outside the contact area as shown in Figure 2.10d, which aligned well with the adjacent cracks seen under SEM (Figure 2.4d). Thus, the model confirmed that the distribution of stresses extended beyond the immediate contact between the coating and indenter.

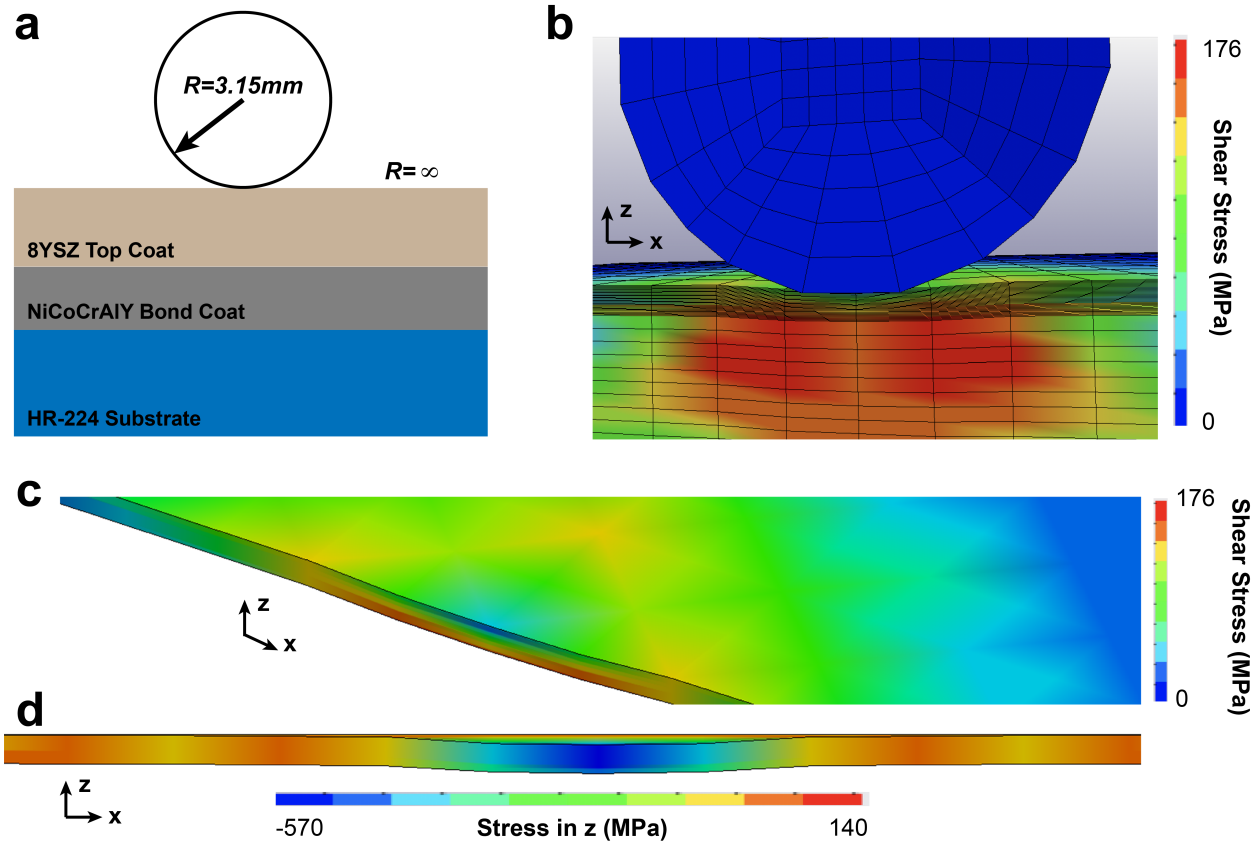

Figure 2.10. (a) Graphical representation of the TBC layers modeled in LS-DYNA. A perspective view of the shear stress of (b) the full TBC and (c) the isolated top coat layer under 5 N load. (d) The stress in the z-direction within the isolated top coat layer.

This max shear stress of 176 MPa was lower than the typical range (230 to 500 MPa) of fracture strength published in literature for as-deposited TBC systems [24,32]. However, the fracture strength of free-standing 8YSZ coatings has been demonstrated to be as low as 25 to 77 MPa [33]. It was important to recognized that the max shear stress from the model occurred after only five cycles and did not reflect the stress state after the over 19,000 cycles actually conducted in the experiments. However, this large shear stress early in the test could contribute to fracture and delamination of the coating over the first 1000 cycles as observed. The SEM images of the wear degradation and the Hertz contact model analysis all indicated that fracture, damage, and delamination occurred within the 8YSZ top coating. With this knowledge, the fracture energy (G_{II}) was calculated from the maximum shear stress (τ_{max}) using the equation:

$$G_{II} = \frac{\tau_{max}\, x}{2} \tag{2.10}$$

where the value x is the crack opening displacement. The stress intensity factor (K_{II}) was also calculated [34,35]:

$$K_{II} = \left(\frac{E\, G_{II}}{1-\nu^2}\right)^{1/2} \tag{2.11}$$

The crack opening displacement was measured from SEM images (Figure 2.4) to be an average of 3.48 μm. The fracture energy and stress intensity factors of the loading scenarios during the testing at 23 and at 1000 °C are listed in Table 2.5.

Table 2.5. Fracture energy and stress intensity factor calculated with the corresponding maximum shear stress during the room temperature and high temperature (1000 °C) testing.

Temperature (°C)	Applied Load (N)	τ_{max} (MPa)	G_{II} (J/m^2)	K_{II} (MPa/m^2)
23	3	165.7	288.6	4.03
23	4	182.4	317.7	4.23
23	5	196.4	342.1	4.39
1000	3	148.8	259.2	3.53
1000	4	163.8	285.3	3.71
1000	5	176.4	307.2	3.85

In a previous study, Xu, *et al*. were able to correlate the nominal shear stress to interfacial properties, fracture energy, and critical stress intensity factor during finite element simulated island shear testing. Xu, *et al.* noted the fracture energy and critical stress intensity factor ranged from 260 to 290 J/m^2 and from 5.2 to 5.5 MPa/m^2, respectively, for a similar, flame-sprayed 8YSZ TBC. In this work, Xu, *et al.* also thoroughly characterized other flexural, tensile, and pushout studies in literature, which importantly demonstrated variation in these values based on the specific bond coat and substrate materials used and on various annealing treatments [35]. The fracture energy and the estimated stress intensity factors after a few cycles (Table 2.5) were almost equivalent to the critical values identified by Xu, *et al.* In fact, the estimated stress intensity factors from both room temperature and high temperature fit with the range of the reported variation of critical stress intensity factors with different TBCs documented in literature (0.67 to 7.21 MPa/m^2) [36,37]. These stress intensity factors would suggest the rapid, almost immediate delamination of

the 8YSZ top coat in the wear testing, but the occurrence of such severe degradation at 1000 °C only strongly implied another active temperature-dependent stress mechanism; *i.e.*, the coating residual stress state.

Residual stress can be accumulated due to thermal expansion and thermal stress mismatch between the coating layers and can encourage early fracture. Other studies have documented both compressive residual stresses up to 250 MPa in magnitude and tensile residual stresses up to 100 MPa within TBCs [32,38,39]. Thus, it is necessary to revisit these TBC specimens to quantify the specific residual stress state in future work to fully understand the potential impact on the wear response; however, calculations of coating layer thermal stress hinted at a significant mismatch between the 8YSZ top coat and NiCoCrAlY bond coat, which would contribute to the residual stress state. Recent studies of the thermal properties of thermal barrier coatings identified the thermal expansion coefficient (α) of the each of the different coating layers used this particular specimen, as listed in Table 2.6 [40,41]. From these coefficient values, the thermal stress experienced by each layer was calculated as well using the equation:

$$\sigma_T = \frac{\alpha\, E\, \Delta T}{1-\nu} \tag{2.9}$$

where σ_T is the thermal stress and ΔT is the thermal gradient [41]. The difference between the expansion coefficient and thermal stress of the top coat and the remaining two coatings was readily apparent. The bond coat and the substrate had coefficient values that were nearly the same, meaning that as the specimen heated up, they would expand similarly. However, the top coat had a lower coefficient and a lower thermal stress and could not expand to match the bond coat beneath it. This top coat / bond coat interface must rectify a nearly 4 GPa thermal stress mismatch between the layers, setting up a significant residual stress state. It was commonly discussed in literature how the stress condition along this interface contributes to delamination [12,22,42], such as work by Zhao, *et al*., which demonstrated how varying rates of thermal expansion among coating layers led to spallation [43].

Table 2.6. The thermal expansion coefficients of each layer within the specimen as identified in previous studies [40,41] and the corresponding free material thermal stress state at 1000 °C.

Material	TEC (10^{-6} / °C)	Thermal Stress (GPa)
8YSZ Top Coat	12	0.74
NiCoCrAlY Bond Coat	17.9	4.64
HR-224 Substrate	18	2.84

This collection of experimentation, finite element simulation, and supporting literature thus unveiled the coupled thermomechanical mechanisms underpinning the wear of 8YSZ TBCs. The critical components of the wear degradation are temperature, which established a thermal stress disparity between coating layers, and applied load, which correlated with greater wear rates and larger localized shear stresses. Further enabled by moderate softening of the materials at ultra-high temperatures and a larger depth of max shear, the local shear stresses grew in magnitude to meet the critical stress intensity factor. At which point, fracture within the TBC initiated and grew. In contrast, at room temperature, the localized shear stresses remained low, without a contribution of thermal mismatch stresses and were insufficient to meet the critical crack initiation conditions.

4. Conclusions

Here, the coupled thermomechanical mechanisms of wear of 8YSZ thermal barrier coatings were investigated through wear testing of coatings under load at 23 and 1000 °C. Severe wear was observed at 1000 °C, indicating the degradation was primarily governed by a temperature-dependent mechanism. Optical and SEM imaging and EDS mapping were able to identify the extent and characterize the severity of wear damage. To elucidate the localized stresses induced by the mechanical wear, Hertz contact and finite element models were used to readily analyze the data gathered in tribological testing to locate the depth of maximum shear stress within the coating layers. However, the crucial factors in TBC wear and delamination were the presence of a significant thermal stress mismatch between the coating layers and large mechanical loads. The estimated stress intensity factors for wear experiments and simulations with a

load range from 3 to 5 N varied from 3.53 to 3.85 MPa/m^2 after only a few cycles, which were found to be only just below commonly reported critical stress intensity factors for crack initiation. Thus, the experiments and simulations indicate severe wear and delamination of YSZ TBCs under a sustained, oscillating mechanical load will occur rapidly.

5. References

[1] M. Belmonte, Advanced ceramic materials for high temperature applications, Adv. Eng. Mater. 8 (2006) 693–703. doi:10.1002/adem.200500269.

[2] M. Panţuru, D. Chicet, C. Paulin, A. Alexandru, C. Munteanu, Wear aspects of internal combustion engine valves, IOP Conf. Ser. Mater. Sci. Eng. 147 (2016) 012036. doi:10.1088/1757-899X/147/1/012036.

[3] X. Chen, M.Y.Y. He, I. Spitsberg, N.A. Fleck, J.W. Hutchinson, A.G. Evans, Mechanisms governing the high temperature erosion of thermal barrier coatings, Wear. 256 (2004) 735–746. doi:10.1016/S0043-1648(03)00446-0.

[4] R.K. Mishra, C. Beura, Life consumption assessment of a large jet engine, J. Fail. Anal. Prev. 14 (2014) 519–529. doi:10.1007/s11668-014-9842-2.

[5] C.B. Meher-Homji, G. Gabriles, Gas turbine blade failures - causes, avoidance, and troubleshooting, in: Proc. 27th Turbomach. Symp., 1998: pp. 129–179. http://citeseerx.ist.psu.edu/viewdoc/download?doi=10.1.1.462.4970&rep=rep1&type=pdf (accessed May 18, 2016).

[6] D.F. Diao, Y. Sawaki, H. Suzuki, Effect of interlayer on maximum contact stresses of hard coating under sliding contact, Surf. Coatings Technol. 86–87 (1996) 480–485. doi:10.1016/S0257-8972(96)02944-1.

[7] A. Moridi, M. Azadi, G.H. Farrahi, Thermo-mechanical stress analysis of thermal barrier coating system considering thickness and roughness effects, Surf. Coatings Technol. 243 (2014) 91–99. doi:10.1016/j.surfcoat.2012.02.019.

[8] L. Yang, F. Yang, Y. Long, Y. Zhao, X. Xiong, X. Zhao, P. Xiao, Evolution of residual stress in air plasma sprayed yttria stabilised zirconia thermal barrier coatings after isothermal treatment, Surf. Coatings Technol. 251 (2014) 98–105. doi:10.1016/j.surfcoat.2014.04.009.

[9] C. Lamuta, G. Di Girolamo, L. Pagnotta, Microstructural, mechanical and tribological properties of nanostructured YSZ coatings produced with different APS process parameters, Ceram. Int. 41 (2015) 8904–8914. doi:10.1016/j.ceramint.2015.03.148.

[10] L. Su, W. Zhang, X. Chen, T.J. Wang, Experimental investigation of the biaxial strength of thermal barrier coating system, Ceram. Int. 41 (2015) 8945–8955. doi:10.1016/j.ceramint.2015.03.168.

[11] Y.J. Han, F.X. Ye, K.Y. Ding, Z.P. Wang, G.X. Lu, Effects of supersonic fine particles bombarding on thermal barrier coatings after isothermal oxidation, Trans. Nonferrous Met. Soc. China (English Ed. 22 (2012) 1629–1637. doi:10.1016/S1003-6326(11)61366-6.

[12] R.T. Wu, X. Wang, A. Atkinson, On the interfacial degradation mechanisms of thermal barrier coating systems: Effects of bond coat composition, Acta Mater. 58 (2010) 5578–5585. doi:10.1016/j.actamat.2010.06.027.

[13] V.P. Deodeshmukh, S.J. Matthews, D.L. Klarstrom, High-temperature oxidation performance of a new alumina-forming Ni-Fe-Cr-Al alloy in flowing air, in: Int. J. Hydrogen Energy, Pergamon, 2011: pp. 4580–4587. doi:10.1016/j.ijhydene.2010.04.099.

[14] J.Y. Tong, X.F. Ding, M.L. Wang, Y.R. Zheng, K. Yagi, Q. Feng, Evaluation of a serviced turbine blade made of GH4033 wrought superalloy, Mater. Sci. Eng. A. 618 (2014) 605–613. doi:10.1016/j.msea.2014.09.025.

[15] F. Sun, J. Tong, Q. Feng, J. Zhang, Microstructural evolution and deformation features in gas turbine blades operated in-service, J. Alloys Compd. 618 (2015) 728–733. doi:10.1016/j.jallcom.2014.08.246.

[16] K.L. Johnson, Contact Mechanics, Cambridge University Press, 1985.

[17] W.C. Oliver, G.M. Pharr, An improved technique for determining hardness and elastic modulus using load and displacement sensing indentation experiments, J. Mater. Res. 7 (1992) 1564–1583. doi:10.1557/JMR.1992.1564.

[18] J.Y. Kim, S.K. Kang, J.J. Lee, J. il Jang, Y.H. Lee, D. Kwon, Influence of surface-roughness on indentation size effect, Acta Mater. 55 (2007) 3555–3562. doi:10.1016/j.actamat.2007.02.006.

[19] Z.H. Xu, M.A. Sutton, X. Li, Mapping nanoscale wear field by combined atomic force microscopy and digital image correlation techniques, Acta Mater. 56 (2008) 6304–6309. doi:10.1016/j.actamat.2008.08.044.

[20] Z. Lu, S.W. Myoung, Y.G. Jung, G. Balakrishnan, J. Lee, U. Paik, Thermal fatigue behavior of air-plasma sprayed thermal barrier coating with bond coat species in cyclic thermal exposure, Mater. 6 (2013) 3387–3403. doi:10.3390/ma6083387.

[21] P. Seiler, M. Bäker, J. Rösler, Multi-scale failure mechanisms of thermal barrier coating systems, Comput. Mater. Sci. 80 (2013) 27–34. doi:10.1016/j.commatsci.2013.04.028.

[22] S.R. Choi, J.W. Hutchinson, A.G. Evans, Delamination of multilayer thermal barrier coatings, Mech. Mater. 31 (1999) 431–447. doi:10.1016/S0167-6636(99)00016-2.

[23] S. Nath, I. Manna, J.D. Majumdar, Nanomechanical behavior of yttria stabilized zirconia (YSZ) based thermal barrier coating, Ceram. Int. 41 (2015) 5247–5256. doi:10.1016/j.ceramint.2014.11.039.

[24] H.J. Jang, D.H. Park, Y.G. Jung, J.C. Jang, S.C. Choi, U. Paik, Mechanical characterization and thermal behavior of HVOF-sprayed bond coat in thermal barrier coatings (TBCs), Surf. Coatings Technol. 200 (2006) 4355–4362. doi:10.1016/j.surfcoat.2005.02.170.

[25] J.Y. Kwon, J.H. Lee, H.C. Kim, Y.G. Jung, U. Paik, K.S. Lee, Effect of thermal fatigue on mechanical characteristics and contact damage of zirconia-based thermal barrier coatings with HVOF-sprayed bond coat, Mater. Sci. Eng. A. 429 (2006) 173–180. doi:10.1016/j.msea.2006.05.082.

[26] P. Auerkari, Mechanical and physical properties of engineering alumina ceramics, 1996. http://www.vtt.fi/inf/pdf/tiedotteet/1996/T1792.pdf (accessed April 16, 2018).

[27] W. Pabst, E. Gregorová, D. Malangré, J. Hostaša, Elastic properties and damping behavior of alumina–zirconia composites at room temperature, Ceram. Int. 38 (2012) 5931–5939. doi:10.1016/j.ceramint.2012.04.045.

[28] A. Keyvani, M. Saremi, M. Heydarzadeh Sohi, Z. Valefi, A comparison on thermomechanical properties of plasma-sprayed conventional and nanostructured YSZ TBC coatings in thermal cycling, J. Alloys Compd. 541 (2012) 488–494. doi:10.1016/j.jallcom.2012.06.062.

[29] C. Eberl, D.S. Gianola, K.J. Hemker, Mechanical characterization of coatings using microbeam bending and digital image correlation techniques, Exp. Mech. 50 (2010) 85–97. doi:10.1007/s11340-008-9187-4.

[30] J.M. Antunes, J. V. Fernandes, N.A. Sakharova, M.C. Oliveira, L.F. Menezes, On the determination of the Young's modulus of thin films using indentation tests, Int. J. Solids Struct. 44 (2007) 8313–8334. doi:10.1016/j.ijsolstr.2007.06.015.

[31] S. Ahmadian, C. Thistle, E.H. Jordan, Experimental and finite element study of an air plasma sprayed thermal barrier coating under fixed cycle duration at various temperatures, J. Am. Ceram. Soc. 96 (2013) 3210–3217. doi:10.1111/jace.12552.

[32] H. Waki, A. Kobayashi, Influence of the mechanical properties of CoNiCrAlY under-coating on the high temperature fatigue life of YSZ thermal-barrier-coating system, Vacuum. 83 (2008) 171–174. doi:10.1016/j.vacuum.2008.03.063.

[33] J. Wan, M. Zhou, X.S. Yang, C.Y. Dai, Y. Zhang, W.G. Mao, C. Lu, Fracture characteristics of freestanding 8 wt% Y2O3–ZrO2 coatings by single edge notched beam and Vickers indentation tests, Mater. Sci. Eng. A. 581 (2013) 140–144. doi:10.1016/j.msea.2013.05.086.

[34] T. Diehl, On using a penalty-based cohesive-zone finite element approach, Part I: Elastic solution benchmarks, Int. J. Adhes. Adhes. 28 (2008) 237–255. doi:10.1016/j.ijadhadh.2007.06.003.

[35] Z.H. Xu, Y. Yang, P. Huang, X. Li, Determination of interfacial properties of thermal barrier coatings by shear test and inverse finite element method, Acta Mater. 58 (2010) 5972–5979. doi:10.1016/j.actamat.2010.07.013.

[36] A. Vasinonta, J.L. Beuth, Measurement of interfacial toughness in thermal barrier coating systems by indentation, Eng. Fract. Mech. 68 (2001) 843–860. doi:10.1016/S0013-7944(00)00130-2.

[37] Y.C. Zhou, T. Tonomori, A. Yoshida, L. Liu, G. Bignall, T. Hashida, Fracture characteristics of thermal barrier coatings after tensile and bending tests, Surf. Coatings Technol. 157 (2002) 118–127. doi:10.1016/S0257-8972(02)00154-8.

[38] J. Matejicek, S. Sampath, P.C. Brand, H.J. Prask, Quenching, thermal and residual stress in plasma sprayed deposits: NiCrAlY and YSZ coatings, Acta Mater. 47 (1999) 607–617. http://www.sciencedirect.com/science/article/pii/S1359645498003607 (accessed May 18, 2016).

[39] J. Zhu, H. Xie, Z. Hu, P. Chen, Q. Zhang, Residual stress in thermal spray coatings measured by curvature based on 3D digital image correlation technique, Surf. Coatings Technol. 206 (2011) 1396–1402. doi:10.1016/j.surfcoat.2011.08.062.

[40] R. Tu, T. Goto, Thermal cycle resistance of yttria stabilized zirconia coatings prepared by MO-CVD, Mater. Trans. 46 (2005) 1318–1323. http://jlc.jst.go.jp/DN/JALC/00256823330?from=Google (accessed April 18, 2016).

[41] Y. Song, Z. Lv, Y. Liu, X. Zhuan, T.J. Wang, Effects of coating spray speed and convective heat transfer on transient thermal stress in thermal barrier coating system during the cooling process of fabrication, Appl. Surf. Sci. 324 (2015) 627–633. doi:10.1016/j.apsusc.2014.10.157.

[42] E. Obelode, J. Gibmeier, Residual Stress Analysis on Thick Film Systems by the Incremental Hole-Drilling Method - Simulation and Experimental Results, Exp. Mech. 53 (2013) 965–976. doi:10.1007/s11340-013-9720-y.

[43] S. Zhao, Y. Zhao, B. Zou, X. Fan, J. Xu, Y. Hui, X. Zhou, S. Liu, X. Cao, Characterization and thermal cycling behavior of La2(Zr0.7Ce0.3)2O7/8YSZ functionally graded thermal barrier coating prepared by atmospheric plasma spraying, J. Alloys Compd. 592 (2014) 109–114. doi:10.1016/j.jallcom.2014.01.001.

CHAPTER 3: PREDICTING RESIDUAL STRESSES IN THERMAL SPRAY COATINGS BY DIGITAL IMAGE CORRELATION

1. Introduction

Thermal spray coatings are used in a wide variety of applications to improve surface thermal, mechanical, and chemical properties [1,2]. While the function and durability of coatings depend on many parameters including coating thickness, roughness, and residual stress [3,4], these properties, and stress in particular, are difficult to ascertain in real time during coating preparation and application. Indeed, the most widely accepted residual stress evaluation techniques are *ex-situ* and frequently destructive, such as Raman spectroscopy [5] or X-ray diffraction (XRD) [6] of cross sectioned samples. A robust monitoring technique that could evaluate some these properties in real time would have positive implications for coating durability and consistency and eliminate the need of destructive testing. In this work, we demonstrate digital image correlation (DIC) enabled methods for in-process monitoring of thermal spray systems that are able to probe coating surface profile and residual stresses.

Residual stress, caused by nonuniform heating and thermal expansion and lattice mismatch between substrate and coating, is often measured in laboratory settings by Raman spectroscopy [5] or XRD [7,8] techniques, although neither technique is suitable for in-process applications in harsh manufacturing environments. An alternative method of measuring residual stresses by specimen curvature during processing was first introduced by Matejicek [9] and used by many others [10,11], although this required prior knowledge of mechanical properties for the substrate and coating. In this method, a beam is supported on one or both ends, and curvature is measured with displacement sensors affixed to the back of the specimen as the front is coated [9] or with various non-contact optical or laser techniques [12,13]. In particular, the non-contact methods have demonstrated surface-profile measurements to accuracies on the order of 10-100 μm, although they may struggle to provide full-field surface measurements [12,13]. The tediousness and difficulty of mounting wired sensors to coating samples limit widespread use. Measured curvature may be coupled with deformation models to provide residual stress contours throughout the sample thickness. In this work, this model is extended from bi-layer coating systems to

arbitrarily multilayered coating systems as described in Section 2.1. Implementation of the curvature method with non-contact, full-field surface profile measurements would enable simultaneous, real-time measurement of coating curvature and thus residual stress and also eliminate the requirement for wired sensors, improving upon existing methods or destructive techniques.

Curvature methods have proven effective in holistically measuring residual stress gradients but fail to capture microscopic mechanisms that alter residual stresses. For instance, the tetragonal to monoclinic ($t \rightarrow m$) phase transformation within yttria-stabilized zirconia (YSZ) thermal barrier coatings (TBC) results in volume expansions and may significantly alter residual stress [14]; this transformation has been observed after aging at temperatures above 1300 °C for several hundred hours [6,15]. Low temperature $t \rightarrow m$ transformation below 425 °C has been observed in 5 mol %YSZ (5YSZ) [16], although not for the higher concentration 8 mol% YSZ (8YSZ) commonly used in TBC systems and tested in this study. However, after annealing at high temperatures, the metastable 8YSZ t' phase segregates into yttria-lean and yttria-rich t phases [17], of which the lean phase may undergo the $t \rightarrow m$ transformation at lower temperature. Complementary XRD [6] or Raman spectroscopy [15,16] studies are therefore essential to identify the $t \rightarrow m$ transformation within the TBC systems.

Initially developed in the field of experimental mechanics, the three-dimensional DIC (3D-DIC) technique is an optical non-contact measurement procedure that processes stereoscopic images of specimens to extract surface profile and deformation information [18]; full-field measurements are obtained by dividing a larger area of interest in the images into small subsets and matching surface features of each subset in images acquired throughout the experiment through numerical optimization algorithms [19]. For any given pair of images in which the surface coating is perturbed (such as during coating deposition), surface contour, curvature and position can be extracted. On the other hand, if the surface pattern remains unperturbed, deformation measurements may also be obtained. Under ideal conditions with appropriate lighting and high contrast surface patterns, 3D-DIC methods measure surface profiles to an accuracy of 1/20,000th of camera-object distance [20,21], which for a reasonable camera-

object distance of about 500 mm, corresponds to an accuracy of approximately 25 μm. Thus, 3D-DIC presents a novel route for residual stress measurement; the DIC-obtained curvature may be converted to residual stresses. Due to the versatility of the 3D-DIC method, residual stress measurements are demonstrated at temperatures up to 800 °C.

2. Research Methods

2.1. Curvature-Based Residual Stress Measurements for Multi-Layered Coatings

The theoretical and experimental basis for studying residual stresses of bilayered plasma-sprayed coatings is well established (*e.g.*, [9,22,23]); however, these models are deficient for complex multi-layered coating systems that are widely employed in industry, such as thermal barrier coating systems with top coat, bond coat, and substrate layers, or other functionally graded coating systems. Here, a curvature-based residual stress model for arbitrarily multi-layered coating systems is derived from Euler-Bernoulli beam theory. For this work, the multi-layered model is reduced to $n = 3$ layers to extract residual stress data for a thermal barrier coating system with top coat, bond coat, and substrate layers. Although elementary, this derivation is presented in brief due to the importance of residual stresses in the performance of multi-layer coating systems and the absence of such models in the literature.

First, the geometry of an arbitrarily-layered beam (Figure 3.1) is assumed. Using the Euler-Bernoulli beam theory conventions, a linear and continuous strain distribution is assumed in the form [9,10]:

$$\varepsilon_{xx}(z) = c_1 z + c_2. \tag{3.1}$$

Given this deformation gradient, force and moment equilibria conditions are satisfied with the following

$$\sum_{i=1}^{n} E_i \left(\begin{bmatrix} \frac{z_{i+1}^2}{2} & z_{i+1} \\ \frac{z_{i+1}^3}{3} & \frac{z_{i+1}^2}{2} \end{bmatrix} - \begin{bmatrix} \frac{z_i^2}{2} & z_i \\ \frac{z_i^3}{3} & \frac{z_i^2}{2} \end{bmatrix} \right) \begin{bmatrix} c_1 \\ c_2 \end{bmatrix} = \sum_{i=1}^{n} E_i \alpha_i \Delta T \left(\begin{bmatrix} z_{i+1} \\ \frac{z_{i+1}^2}{2} \end{bmatrix} - \begin{bmatrix} z_i \\ \frac{z_i^2}{2} \end{bmatrix} \right), \tag{3.2}$$

where E_i and α_i are the elastic modulus and coefficient of thermal expansion for the i^{th} layer, and ΔT is the deviation from equilibrium temperature. The strain gradient parameters c_1 and c_2 are easily

determined with this relationship given the mechanical properties of each layer. Using linear-elastic and isotropic relationships within each layer, the residual stress at a given point in the i^{th} layer is found in terms of mechanical properties:

$$\sigma_{xx}^{Residual}(z) = E_i \times (\varepsilon_{xx}(z) - \alpha_i \Delta T). \tag{3.3}$$

By geometric inspection, it can be shown that the unknown parameter c_1 is equivalent to the specimen curvature

$$c_1 = \frac{1}{\rho} = C_{xx}, \tag{3.4}$$

where ρ is the surface's radius of curvature.

This set of equations may be used to extract residual stresses by three different means. First, the stresses may be solved theoretically only in terms of mechanical properties and specimen dimensions. Second, experimental curvature measurements may provide c_1, enabling the solution of c_2 using one of the equilibrium conditions in Eq. 3.2. Finally, if DIC strain measurements are obtained at the equilibrium temperature, surface strain measurements may be converted directly to residual stresses after subtracting thermal expansion strains.

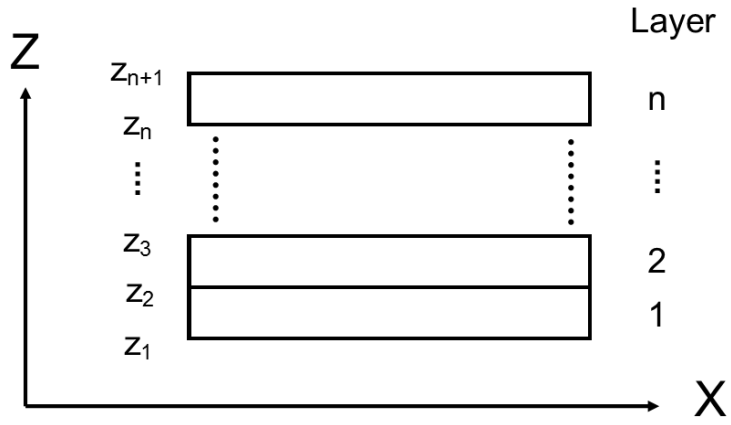

Figure 3.1. n-layered composite beam model for residual stress calculations.

2.2. Accuracy of 3D-DIC Curvature Measurements for APS Coatings

The accuracy of 3D-DIC techniques for curvature measurements on a sample of APS coating was first verified. Experiments involved a thermal barrier coating (TBC) specimen of 8YSZ with a bond coat of NiCoCrAlY on a HR 224 nickel alloy substrate. For validation, sample curvature was measured using a tribometer as a surface profiler by scanning a sharp indenter tip over the surface profile (UMT 3, Bruker Nano). The profiler applied a constant contact force of 1 N, sufficient force to maintain probe contact without deforming the sample. Height and spatial accuracy on the profiler were found to be better than 1 μm.

As intrinsic DIC surface patterns generally possess inferior contrast to artificially generated patterns (*e.g.*, spray paint application), the influence of various experimental imaging parameters was assessed to optimize the use of 3D-DIC for surface profile measurement. First, optimal camera-object distance was determined experimentally by adjusting camera-sample distance and comparing extracted surface profiles to reference profile measurements. The TBC sample was imaged at distances between 300 and 900 mm and analyzed with 3D-DIC to compute the apparent surface profile. Multiple images were captured at each camera distance without moving the sample, and artificial displacements between images at each distance were used to quantify the in-plane and out-of-plane accuracies of each measurement. Comparison in measured sample height between the DIC and reference profiles was used to holistically prove convergence of the 3D-DIC measurements. Average curvatures were computed and compared from the 3D-DIC and reference data by fitting circular profiles to the data using a least-squares method.

As summarized in Table 3.1, all DIC experiments used dual 5 megapixel CCD cameras (PointGrey Research) with 50 mm compact lenses (Schneider Kreuznach). The 3D-DIC setup was configured to increase depth of field as well as minimize noise and distortion from convective currents by using small apertures, relatively long exposure times and low-heat LED lighting. It was determined qualitatively that oblique flood lighting at angles of approximately 30° improved correlation results by exaggerating shadows caused by coating surface roughness.

Table 3.1. 3D-DIC parameters.

Imaging Parameters	
Cameras	5 megapixel CCD (PointGrey)
Lenses	50 mm compact lens (Schneider)
Exposure	5 ms
Aperture	f/8
Stereo angle	~25°
3D-DIC Analysis	
Subset Size	41 px
Step Size	7 px
Software	VIC-3D

2.3. Influence of Phase Transformation and Temperature on Residual Stress

Residual stress of the TBC sample was obtained by the non-contact 3D-DIC curvature method at temperatures between 22 °C and 900 °C after repeated annealing cycles to induce a phase transformation within the YSZ top coat. Curvature was first obtained after two three-hour annealing treatments at 1200 °C (totaling 6 hours) in ambient conditions, which established an equilibrium temperature for thermal expansion and relieved quenching-based residual stresses in the NiCoCrAlY bond coat [8]; the sample was exposed to 900 °C for approximately 20 minutes in subsequent annealing treatments. *In-situ* curvature measurements were obtained during subsequent heatings up to 800 °C and 900 °C as outlined in Table 3.2. Notation in Table 3.2 concisely describes the annealing state. A description of "2x 1200 °C" indicates two, 3-hour annealings at 1200°C while a description of "2x 1200 °C (6 hrs) + 1x 900 °C (20 min)" indicates an additional 20-minute annealing to 900 °C. The 3D-DIC curvature measurement method is depicted in Figure 3.2. The TBC specimen was mounted at one end to an alumina plate with high temperature cement (Omega Engineering) to minimize artificial curvature constraints. After heating to a designated temperature in a box furnace (MTI Corporation), the sample was allowed to equilibrate for 15 minutes, and the furnace door was gently opened to acquire images. Approximately 30 images were captured at each temperature over a period of 10 seconds, and the furnace was subsequently closed and heated to the next temperature. Heating and cooling rates were less than $5\ °C/min$.

Image distortion due to mixing of air at the furnace threshold was controlled in two ways. First, the specimen was positioned at the front and bottom of the furnace to minimize the amount of air mixing between the samples and camera, and a fan forced air upwards across the furnace opening to promote even and faster mixing [24]. Second, all images at each temperature were averaged on a pixel basis to eliminate distortion caused by random convective currents. Y-direction curvature was extracted by fitting circular profiles to the surface profiles obtained at each temperature using a least-squares scheme. X-direction curvature was ignored due to relatively small dimension and complex boundary conditions imposed by the cement base (Figure 3.2).

Table 3.2. Curvature test matrix. DIC measurements acquired throughout entire temperature range unless otherwise noted.

Starting Anneal state	Temperature Range	Curvature measurements during: Heating?	Cooling?
2x 1200 °C (6 hrs)	22-800 °C	✓	
2x 1200 °C (6 hrs)	22-900 °C	✓	
2x 1200 °C (6 hrs), 1x 900 °C (20 min)	22-800 °C	✓	✓
2x 1200 °C (6 hrs), 1x 900 °C (20 min)	22-900 °C	✓ (at 25 °C)	✓ (at 25 °C)
2x 1200 °C (6 hrs), 2x 900 °C (40 min)	22-900 °C	✓ (22-800 °C)	✓ (22-800 °C)

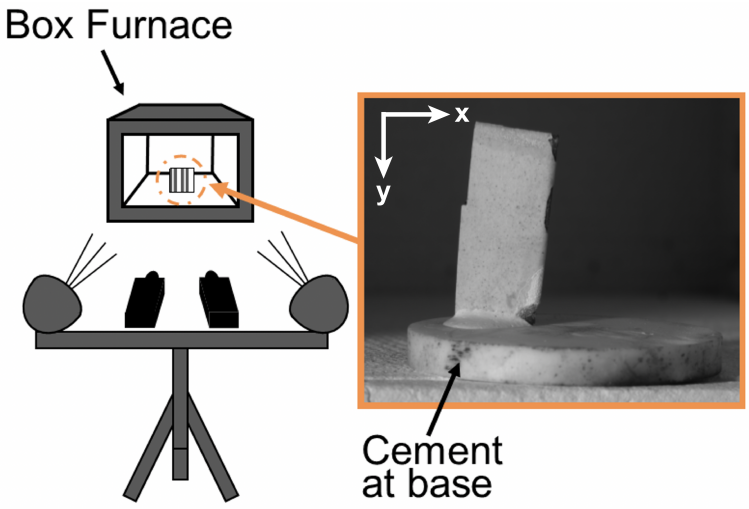

Figure 3.2. Experimental setup to measure curvature of the 8YSZ / NiCoCrAlY / HR-224 sample. Sample is 12 x 25 mm in size and positioned with the as-deposited top coat facing the cameras.

XRD patterns of the top coat were obtained at various stages of annealing using a powder diffractometer (X'Pert Panalytical Pro MPD, Philips) with monochromatic copper radiation at 45 kV and 40 mA. Diffraction measurements were obtained at $2\theta = 5 - 80°$ in $0.05°$ steps, which enabled identification of phase content within both the $28° < 2\theta < 32°$ and $72 < 2\theta < 76°$ regions. Results from 3 scans at each annealing state were averaged to reduce noise. A Reitveld refinement scheme was performed with monoclinic, tetragonal, and cubic phases using the Profex-BGMN software package to determine composition and lattice parameters.

Residual stress was computed from the curvature measurements using Equations 3.1-3.3. The TBC sample had nominal 8YSZ top coat thickness of 250 μm, NiCoCrAlY bond coat thickness of 200 μm, and HR-224 substrate thickness of 1000 μm. While thin (<5 μm) oxide layers were observed on the exposed back surface of the superalloy substrate as well as at the interface between the top coat and bond coat, the contribution of these layers to bending stiffness was considered negligible compared to the much thicker primary constituent layers.

Computations used experimental values for elastic moduli and literature values for thermal expansion coefficients. High-temperature nanoindentation (NanoTest Vantage, Micro Materials) with a cubic boron nitride (cBN) Berkovich indenter and microindentation (UMT 3 tribometer, Bruker Nano) with a Sapphire Vickers indenter were used to probe the temperature dependence of elastic moduli of the top coat, bond coat, and substrate in the TBC sample at temperatures between 22 °C and 900 °C. Stiffness information of each layer was extracted from the nanoindentation force-displacement curves with the Oliver-Pharr method [25]. Calculations assumed temperature-insensitive elastic modulus and Poisson's ratio of 800 GPa and 0.12 for the cBN indenter and 375 GPa and 0.24 for the sapphire indenter [26] and Poisson's ratios of 0.31, 0.31, and 0.3 for the top coat, bond coat, and substrate of the TBC sample [8,27]. Nanoindentation load was 50 mN to produce deep indents that sampled material across many grains, and microindentation load was 3 N. Coefficients of the thermal expansion of 12.0, 17.9 and 18.0 $\times 10^{-6}/°C$

were obtained from the literature for the top coat, bond coat, and HR-224 substrate [28,29].

2.4. Accuracy of 3D-DIC for APS Coatings

The surface profile of the TBC sample was obtained by 3D-DIC at different camera distances, as plotted in Figure 3.3a. It was found that for camera-sample distances below 600 mm, the observed surface profiles converged toward an identical, approximately parabolic profile. For unknown reasons, the profiles obtained at higher camera-sample distances possessed exaggerated curvature. Profiles obtained from larger camera-sample distances displayed pronounced local and systematic deviations from this profile. These profiles were compared to tribometer measurements (solid line in Figure 3.3a) and showed that the 3D-DIC measurements at camera distances less than 600 mm indeed converged toward the actual surface profile.

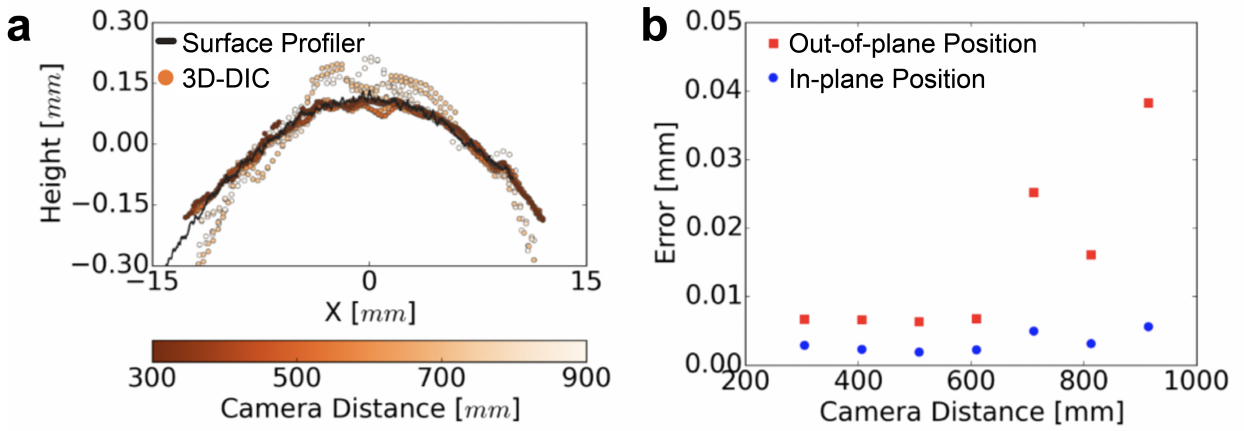

Figure 3.3. Assessment of 3D-DIC surface profile measurement accuracy as a function of camera distance. (a) Comparison of measured surface profiles as a function of camera distance (colored circles). The surface profile obtained by profilometer is displayed as a solid black line. (b) Standard deviation in in-plane position (blue circles) and out-of-plane position (red squares) measurements.

The accuracy of 3D-DIC profile measurements was further quantified by computing phantom displacements between images captured without moving the sample or camera. Errors associated with in-plane and out-of-plane position were separately computed and are plotted in Figure 3.3b. Positional error demonstrated similar trends as a function of camera-sample distance with best performance at distances less than 600 mm; although, error associated with out-of-plane measurements was consistently higher. The standard deviation associated with in-plane position was less than 2.4 μm for all camera-sample distances less than 600 mm and thereafter increased to 5.6 μm at a distance of 910 mm. Standard deviation of the out-of-plane position was less than 6.8 μm for distances less than 600 mm and increased to 39 μm at distance of 910 mm.

Of particular relevance to the computation of residual stress, average curvatures were extracted from the profilometer and 3D-DIC (distance = 600 mm) surface profiles. These two methods produced radii of curvature equal to 347.3 ± 8.6 and 361.9 ± 1.4 mm, respectively; the difference between these measurements was 4.2 %. Since residual stress in plasma sprayed coatings was a linear function of curvature, this measurement suggested that 3D-DIC measurements may be used to compute residual stresses to similar accuracy.

Several important trends emerged from these results. Most obviously, there existed a limit to the accuracy of 3D-DIC profile measurements such that further improvements could not be achieved with reductions in camera-sample distance. Accuracy plateaued at values of 8.8 μm (based on vector addition of in-plane and out-of-plane accuracies) for camera distances below 600 mm. Since the DIC method computed surface profiles by averaging the location of micro-scale textural features (*i.e.*, surface roughness) within a subset, it was concluded that surface roughness physically governed the accuracy of 3D-DIC measurements on the plasma sprayed coatings. This finding contrasted with conventional DIC experiments that use artificially generated surface patterns, in which both camera-sample distance and feature size may be reduced to improve accuracy.

Second, the accuracy of the 3D-DIC APS measurements compared favorably with other

measurements in the literature. Using a 99 % confidence level on total positional error, these results suggested a maximum error of 22.6 μm, or 1/26,500th of camera-sample distance. This value was slightly better than found in the literature [20] and emphasized that the surface profile of APS coatings may be accurately measured with 3D-DIC without artificial surface patterns. Based on the limitations imposed by surface roughness, it was anticipated that rougher coatings would demonstrate slightly worse performance.

3. Residual Stress Measurements of TBC sample

Non-contact residual stress values on the TBC sample were obtained via 3D-DIC and compared to the Euler-Bernoulli model for residual stress. The TBC sample was heat treated at 1200 °C for 6 hours to establish an equilibrium temperature, at which temperature creep eliminated residual stresses and curvature [8]. Upon cooling the specimen demonstrated pronounced convex curvature on the top coat surface due to thermal expansion misfit.

3.1. Curvature Measurement by 3D-DIC

TBC curvatures at elevated temperatures after different annealing treatments are reported in Figure 3.4, which showcases a complex relationship between temperature and curvature. Most obviously, the curvatures exhibited primarily linear decreases with temperature from 22-800 °C regardless of heat treatment; slope of this relationship remained unchanged for all heat treatments at $-2.43 \pm .141 \times 10^{-6} mm^{-1^{\circ}} C^{-1}$. Extrapolation of the linear curvature trends suggested an equilibrium temperature of above 1500 °C that was well above the initial annealing temperatures, which hinted at either nonlinearity in material properties above 900 °C or permanent deformation.

However, treatment above 800 °C enhanced room-temperature curvature. This repeatable effect was demonstrated by three annealings at 900 °C, which resulted in increases in room temperature curvature of $4.2, 1.1$ and $1.0 \times 10^{-4}\ mm^{-1}$, and measurable increases in curvature did not occur when heated to only

800 °C. We note that although the last two increases were less than the 4.2 % measurement error determined in Section 2.4, the increases in curvature were persistent at all temperatures and verified by profilometer at room temperature. More precise identification of the critical temperature associated with this increase in curvature was somewhat hindered by measurement error; although, examination of the green 2x 1200 °C trial in Figure 3.4 suggested this increase occurred above 850 °C as curvature jumped to be in line with the 2x 1200 °C + 1x 900 °C treatment curve. In contrast, after heating to only 800 °C (Table 3.2), no measurable increase in curvature at any temperature between heating and cooling curves was observed for the blue 2x 1200 °C + 1x 900 °C trial.

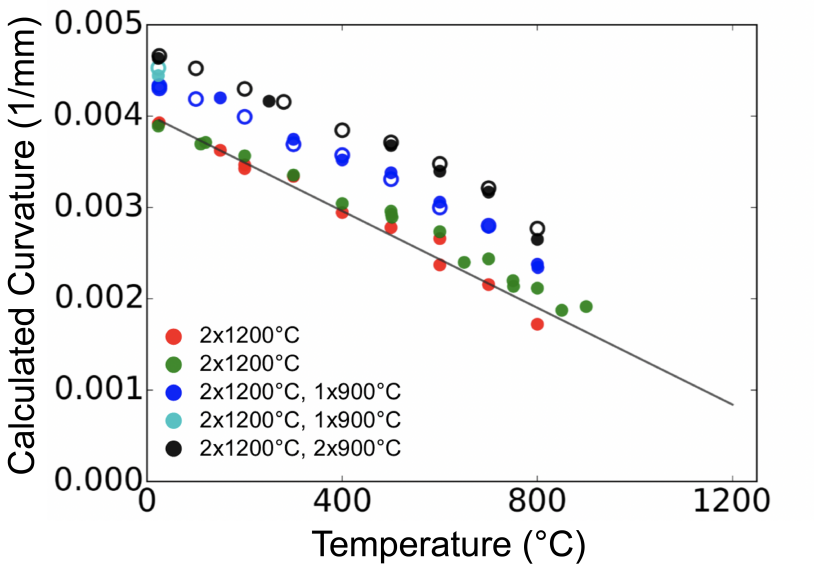

Figure 3.4. 3D-DIC enabled curvature measurements of the TBC sample at various stages of annealing. Solid circles indicate measurements obtained during heating, and open circles indicate measurements obtained during cooling.

3.2. High Temperature Mechanical Characterization of TBC Sample

The calculated elastic moduli were determined based on the unloading curves obtained from indentation according to the Oliver-Pharr method [25], as shown in Figure 3.5 and are presented in Figure 3.5c as a function of temperature up to 900 °C. The three constituent materials demonstrated approximately linear softening trends up to 900 °C, which was consistent with findings for 8YSZ in the

literature [27]; the average moduli decreased from 54.9 to 43.5 GPa in the 8YSZ top coat, from 222.1 to 181.3 GPa in the NiCoCrAlY bond coat, and from 111.2 to 86.2 GPa in the HR-224 substrate. Error in these measurements was about 9 % for each measurement as indicated by error bars in the figure. The jump of the substrate average modulus at 400 °C remained within the deviation of the observed trend. The impact on the moduli due to phase transformation and yielding was considered. Although the γ to β phase transformation has been observed in NiCoCrAlY bond coats between 600 and 800 °C [8], no effect on material stiffness was observed. This softening trend has important implications in explaining residual stress relaxation at elevated temperatures, which is discussed further in Section 3.4.

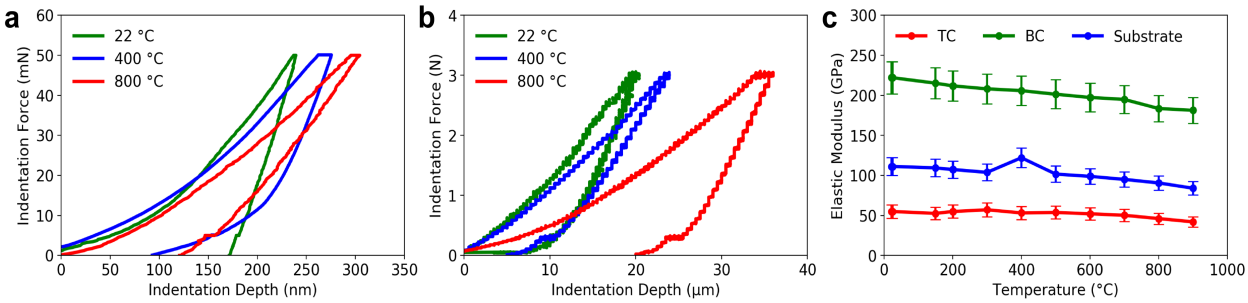

Figure 3.5. Determination of high-temperature TBC mechanical properties via indentation. Selected indentation loading curves from (a) the 8YSZ top coat (TC) and (b) the NiCoCrAlY bond coat (BC) at temperatures that demonstrate reductions in stiffness and yield stress with temperature. (c) Elastic moduli of the three constituent layers up to 900 °C.

3.3. Phase Composition Evolution of TBC

Phase content within the top coat was determined using XRD over diffraction angles $2\theta = 5°$ to $80°$, and a narrow region of these patterns is shown in Figure 3.6a to highlight the growth of monoclinic phases during heat treatment. Phase composition for corresponding heat treatments determined using Reitveld refinement methods are presented in Table 3.3. The deposited coating was somewhat impure, containing measureable amounts of both cubic c and monoclinic m phases in addition to tetragonal

phases. Monoclinic content within the top coat increased from 1.6 % in an untreated state up to 2.8 % after 2x 1200 °C and 2x 900 °C annealing treatments, indicating a $t \rightarrow m$ transformation; at the same time, c content diminished with increasing heating to trivial amounts. Trends in t were unclear, possibly due to strong overlap between these peaks. Monoclinic content decreased after mechanical removal and pulverization of the top coat.

Table 3.3. XRD computed phase composition.

Annealing State	t	c	m
Untreated	93.2 ± 0.6 %	5.2 ± 0.5 %	1.6 ± 0.2 %
1x 1200 °C	97.9 ± 0.3 %	0.3 ± 0.2 %	1.7 ± 0.2 %
2x 1200 °C, 2x 900 °C	94.6 ± 0.4 %	2.6 ± 0.4 %	2.8 ± 0.2 %
1x 1200 °C, Pulverized	84.6 ± 0.6 %	14.6 ± 0.6 %	0.8 ± 0.5 %

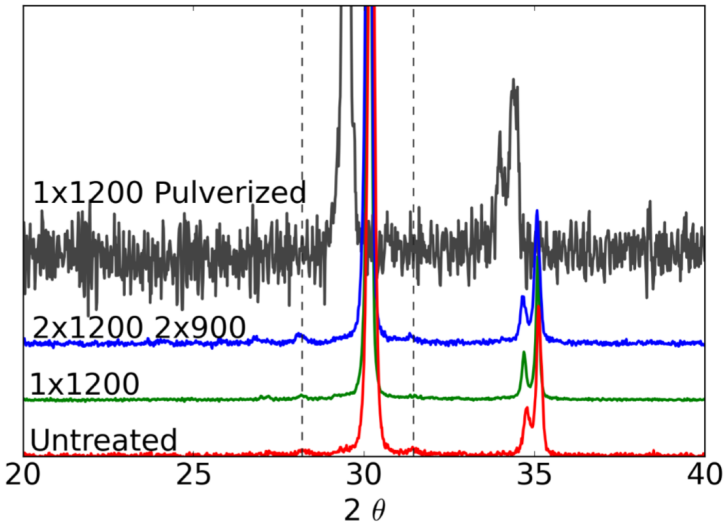

Figure 3.6. Phase composition analysis by XRD. XRD patterns between 20° and 40° at various stages of heat treatment, with m $(1\ 1\ \bar{1})$ and m $(1\ 1\ 1)$ peaks marked at $2\theta = 28.2°$ and 31.5° by vertical lines.

The peak locations shifted subtly to smaller 2θ with increasing heat treatment. Since XRD measurements were obtained on the planar top surface of the TBC sample, the decrease in 2θ indicated

tensile lattice strains in the coating thickness direction; these effects could be construed as Poisson's ratio effects due to in-plane compression with increasing heat treatment. By tracking the combined $t(1\,0\,1)$, and $c(1\,1\,1)$ peaks at $\approx 30.2°$, out-of-plane strains of $\epsilon_{zz} = 0.16\%$ and 0.25% were obtained for the 1x 1200 °C and 2x 1200 °C + 2x 900 °C treatments. Assuming a Poisson's ratio of 0.31 for the top coat (Section 0 [8,27]) and linear elasticity, these peaks would correspond to in-plane surface compressive strains of $\epsilon_{xx} = 0.51\%$ and 0.80%. Using the beam curvature model outlined in Section 2.1 and room temperature mechanical properties outlined in Section 3.2, these surface strains would correspond to changes in curvature of 0.0074 and 0.012; these curvatures were larger than those measured in Section 3.1 by a factor of 2.6. Moreover, the XRD-measured surface compression strains were larger than could simply be explained by the small volume fraction of m phase. Thus, it was concluded that in addition to the $t \rightarrow m$ transformation, other mechanisms contributed to changes in curvature.

3.4. Residual Stress Calculations

Residual stress was determined by two different methods. First, the Euler-Bernoulli model derived in Section 2.1 was solved using a system of linear equations to identify the unknown coefficients C_1 and C_2 in Equations 3.1-3.3. Second, 3D-DIC-derived curvature data were used to directly calculate the unknown coefficient C_1 within the model and then the residual stress. "Theoretical" residual stresses from the beam model were compared to the curvature-based experimental results (Figure 3.7). The compressive residual stress determined by the Euler-Bernoulli model was linear with temperature and indicated that all residual stress would be relieved by 1200 °C. Residual stresses computed by 3D-DIC curvature followed a similar linear trend and showed slight increases in residual stress with increasing heat treatment that closely matched changes in curvature (Figure 3.4). By this calculation, the residual stresses within the coating would be fully relieved at 1200°C, which was caused by the assumption of equilibrium temperature; in contrast, curvature measurements demonstrated no such trend.

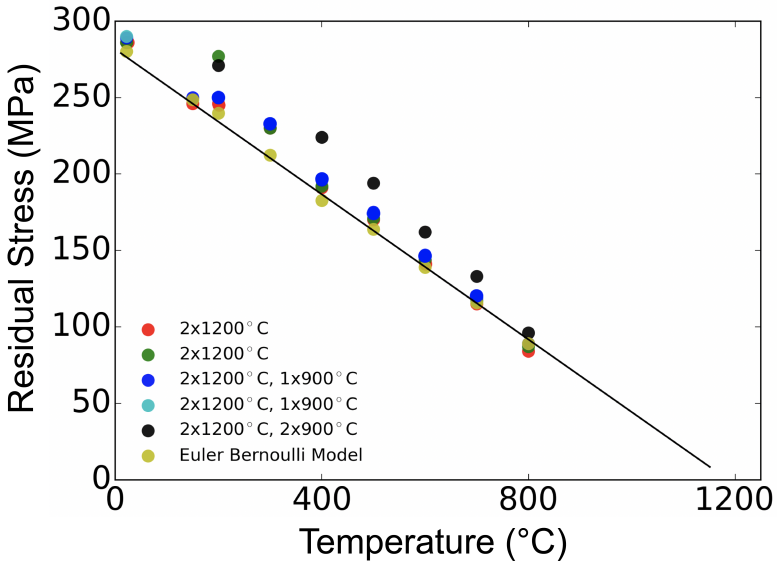

Figure 3.7. The compressive residual stress determined based on a Euler-Bernoulli model and with 3D-DIC curvature data of a TBC specimen over repeated heating and cooling treatments. The solid black line is the trendline associated with the Euler Bernoulli theoretical data.

4. Discussion

We have demonstrated the unique capability of 3D-DIC as a system for obtaining curvature measurements and conducting residual stress calculations in harsh plasma spray coating environments. These achievements have many implications for spraying applications and understanding of TBC mechanical behavior at high temperatures.

4.1. Accuracy of Measurements

The 3D-DIC system demonstrated repeatable and facile surface profile measurements with curvature measured within 4 % of tribometer profile measurement. While the profile measurements obtained by 3D-DIC were comparable to those of the profilometer methods, the 3D-DIC method demonstrated a key advantage in speed of acquisition. After camera setup, only a single pair of images was required for profile extraction. In contrast, measurement with alternative profilometer or confocal microscope

techniques would demand multiple line scans to inspect similarly sized regions of interest. For specific applications that demand only ~10 μm precision, such as determination of macroscopic surface contours of thermally sprayed systems, 3D-DIC inspection would serve as a high-throughput, high-accuracy alternative. On the other hand, 3D-DIC measurements were limited by camera resolution and intrinsic spatial averaging of surface profiles over subset domains and would therefore be infeasible for measurements of microscopic roughness. These encouraging results complement studies by McNeill, *et al*. [20] and others [18,19,20] who have demonstrated the potential of DIC for reliable surface profile measurements. Based on these promising findings, 3D-DIC techniques could be reliably applied to a wide variety of APS coatings.

4.2. Temperature- and Phase-Transformation Induced Curvature

As discussed in Section 3.1, anomalous increases in TBC curvature occurred upon heating above 800 °C. XRD measurements provide evidence of the expansive $t \rightarrow m$ transformation within the top coat that partially explained curvature evolution. However, complementary mechanisms are required to fully explain these changes.

One possible but unlikely cause for increases in curvature was growth of oxide layers at elevated temperatures; if these oxide layers formed on a curved sample, they could contribute to progressive increases in curvature. However, the constituent materials, being designed for operation at 1200 °C, were mostly stable at the experimental temperatures. Weight measurement before and after heating to 900 °C (after the initial 2x 1200 °C annealing) revealed weight loss of 0.05 %, indicating that the initial annealing treatments had formed stable and fully-developed oxide scales and that only insignificant loss of material was observed. Moreover, the oxide layers would be too small to contribute significantly to curvature; thickness of the TGO layer on the bond coat / top coat interface as well as the oxide scale on the uncoated face of the substrate were less than 5 μm.

As observed by Chen, *et al*., there exists a well-defined γ to β transformation in NiCoCrAlY between

600-800°C that results in expansion of the bond coat upon cooling, and therefore, may increase curvature. However, these strains were found to result only after quenching from high temperatures [8]; slow cooling throughout the experiment mitigated this effect by allowing stress release through creep. It is unlikely that this phase transformation had any significant effect on curvature during heating to 900 °C.

The key limitation of the theoretical model calculations was the assumption of linear elasticity and absence of stress relaxation at all temperatures. According to more complex material models, regions of the coating under tensile stress could elongate and enhance curvature. Residual stresses using the linear elastic model with experimental mechanical properties at 900 °C and actual sample geometry are calculated and shown in Figure 3.8, which revealed average compressive stress of 58 MPa in the top coat and average tensile stress of 57 MPa in the bond coat. In light of the experimental results, stresses in the tension-loaded bond coat are of particular relevance.

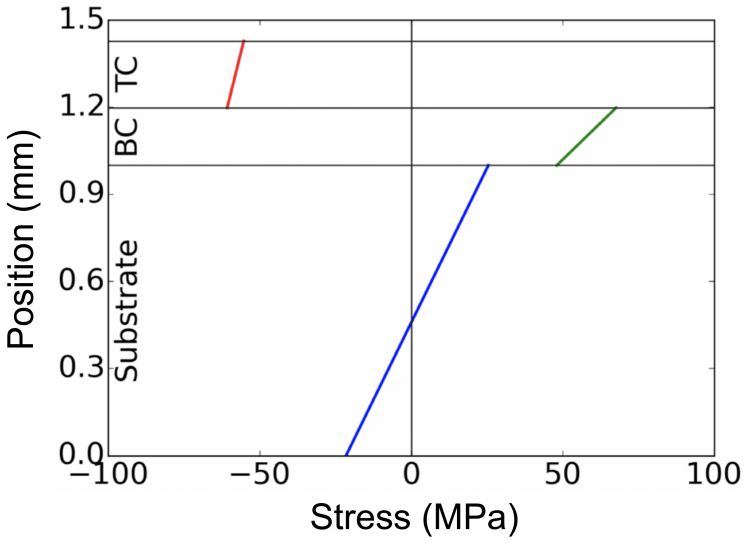

Figure 3.8. Estimated residual stress at 900 °C using trilayer beam model in Equations 3.1-3.3.

Prior work in the literature has shown creep initiation in NiCoCrAlY bond coats at 850 °C at stresses below 15 MPa [30]; presumably, the critical creep stress would continue to decrease at higher temperatures. Within the context of this work, tensile residual stresses in the bond coat must exceed the

temperature-dependent critical creep stress to initiate this curvature-enhancing mechanism. Presumably this criterion was not satisfied at temperatures below 800 °C but was satisfied at higher temperatures. Importantly, this mechanism would also explain the diminishing increases in curvature in successive heating to 900 °C; creep in the bond coat would reduce residual stresses in the coatings below the critical value, at which point the curvature would no longer increase.

4.3. Coupled Stress- and Temperature-Induced Phase Changes

Experimental results in this work demonstrated that the $t \rightarrow m$ transformation within the 8YSZ coating occurred with increasing heat treatment above 800 °C and that this transformation was somewhat reversible upon the release of residual stresses. The monoclinic phase content increased to 2.6 ± 0.4 % after 2x 1200 °C (6 hrs) + 2x 900 °C (20 min) heat treatment, which was much higher than the $0.50 - 1\ mol\%$ equilibrium m content reported in other works [31,32]; although, this current study involved annealing at higher temperatures for shorter duration than in [31] (up to 1200 °C for ~6 hours compared to 155 °C for 48 hours). A key difference, however, was the much higher residual stresses in the YSZ coating in this current study of $\approx -300\ MPa$. What was the source of $t \rightarrow m$ transformation?

Since deposition and annealing temperatures remained well below 1300 °C with short annealing times, the mechanism of the observed $t \rightarrow m$ transformation was certainly different than equilibration during long (upwards of 1000 hours) annealing times at higher temperatures [6]. In fact, even if the YSZ coating were briefly heated above 1300 °C, the $t \rightarrow m$ transformation would occur much more slowly than observed in this work [15].

In other works, the $t \rightarrow m$ transformation has occurred in yttria-lean t phases (4-6 mol% YSZ). Using empirical relationships developed by Ilavsky and Stalik [32], the yttria content within the tetragonal phase may be determined using the lattice parameters:

$$mol\%\ YO_{1.5} = (1.0225 - c/a)/0.001311. \tag{3.5}$$

The composition of the YSZ coating was determined to be $7.44\ mol\%$ and $7.06\ mol\%$ in the

untreated and 2x 1200 °C + 2x 900 °C annealed states, respectively; no $t \rightarrow m$ transformation has been previously reported for this yttria concentration. Additionally, the tetragonal composition in yttria-lean YSZ would be regenerated upon heating above T_0 temperature, and m generation depends on cooling rate. Since identical cooling rates were achieved and yttria concentration remained high, this mechanism inadequately explains the growth of monoclinic phase.

In summary, these findings suggest an alternative transformation mechanism that may be related to the high residual stresses within the YSZ coating. The complexities of this experiment due to multiple coating layers made it difficult to fully isolate mechanisms of the phase transformation; future studies are required to fully explain this mechanism.

4.4. Residual Stress

High fidelity, facile curvature measurements enabled accurate measurement of residual strains as a function of temperature. Coupled with independent property measurement at high temperatures, the residual stresses within a TBC sample were determined to 5 % accuracy ($\pm$9.3 MPa, based on curvature accuracy at room temperature). In agreement with other studies [31,33], it was observed that the TBC was under a compressive stress in as-deposited condition due to thermal misfit with the HR-224 substrate. Yang, *et al*. observed a compressive stress of the TBC layer of about 130 MPa, less than the approximately 300 MPa compressive stress observed in this study [33]; however, this difference may be attributed to different sample thicknesses and to the reverse phase transformation, $m \rightarrow t$, which was accompanied by a volume shrinkage and reduction of curvature. In contrast, Scardi, *et al*. observed a $t \rightarrow m$ transformation and progressive increase of compressive stress with temperature, but the magnitude of the stress was much lower, about 30 MPa [31]. As previously discussed, this difference in residual stress may be explained by the different monoclinic phase content; however, further scrutiny of the cause of the transformation is needed to identify the source and understand the impact of annealing temperature and duration.

In this study, the linear trend displayed in Figure 3.7 suggests that the compressive residual stress was relieved by 1200 °C as predicted by the Euler-Bernoulli model. While the theoretical model did agree with the initial experimental test using 3D-DIC (within 5 % difference), progressive heating, which was observed to lead to coupled phase-temperature induced phase changes, increased the residual stress gradually to values approximately 16 % different from the theoretical data. With future studies to enhance understanding of the mechanisms of the observed $t \rightarrow m$ transformation, these mechanisms can be addressed within the model to introduce a corresponding corrective term. Although certain assumptions in the model such as linear elasticity were insufficient, the residual stress computations proved instructive and could readily be corrected for more complex material models.

4.5. Implications

Several key implications of this study deserve further investigation. The source of the observed $t \rightarrow m$ transformation, which initiated the increased curvature with heating, may be investigated in order to derive an appropriate residual stress model, building off the Euler-Bernoulli model presented in this study. Furthermore, this understanding of the phase transformation would enable greater understanding of the residual stress evolution above 800 °C.

It must be stated that any inherent limitations with the Euler-Bernoulli beam theory must be accounted for in examination of the applicability of this residual stress model. Unlike the Timoshenko beam theory, the Euler-Bernoulli beam theory does not account for shear deformation, limiting its application to long, thin beam structures [34–36]; for reference, the thickness to length ratio of the TBC specimens examined in this study was 3:50. However, a Timoshenko beam theory may be considered in future characterization, particularly of a multilayered beam. Thermal expansion mismatch between coating layers, such as that noted here between 8YSZ top coat and NiCoCrAlY bond coat, may contribute to local shear between coating layers, thus highlighting a need for the Timoshenko beam theory.

Curvature and residual stress within the top coat were measured to 800 °C, and linear extrapolation of

these trends predicted full curvature release above 1500 °C, which was well above the maximum annealing temperature. The DIC-curvature method could be extended to much higher temperatures with appropriate UV illumination and narrow-bandpass filters, as per [37], enabling direct measurement of nonlinear curvature behavior. Indeed, time-dependent curvature and strain related phenomena such as creep and diffusion-based kinetics could be observed in real time.

Importantly, the capability of 3D-DIC to provide a holistic understanding of APS residual stresses in real time has important implications for coatings manufacturing and operation. Real time stress measurements may empower customized manufacturing and operation adjustments to minimize stress within the coating layers. Such capability may provide more reliable APS coatings while reducing manufacturing costs and waste. The impact of 3D-DIC residual stress monitoring on manufacturing and the spraying process will be explored in future studies.

5. Conclusions

3D-DIC was studied in detail as a method for *in-situ*, real-time evaluation of APS coating curvature and residual stress. The inherent texture of APS coatings enabled the direct measurement surface profile during exposure to high-temperature environments. It was found that accuracy of the 3D-DIC measurements was limited by surface roughness, which governed the minimum feature size available for surface profile measurement. With appropriate lighting and camera-sample distances, the 3D-DIC measurements demonstrated positional accuracy of 22.6 μm, or 1/26,500th of camera-sample distance, which compared favorably to available values in the literature. A residual stress model for multilayered coatings was derived using Euler-Bernoulli beam theory and linear-elastic material models to predict residual stress within HR-224 substrate, NiCoCrAlY bond coat, and YSZ top coat TBC system up to 800 °C, and results were compared to experimental curvature measurements obtained by 3D-DIC. The model compressive stresses matched within 5 % of experimental results after initial heat treatment at 1200 °C but could not capture increases in curvature after subsequent annealing treatments above 800 °C. The

increases in curvature were attributed to both creep in the bond coat as well as $t \rightarrow m$ phase transformation within the top coat. The $t \rightarrow m$ transformation were unexpected and were suspected to be induced by both stress and temperature.

6. References

[1] P. Fauchais, Understanding plasma spraying, J. Phys. D. Appl. Phys. 37 (2004) R86–R108. doi:10.1088/0022-3727/37/9/R02.

[2] J. Matejicek, S. Sampath, Intrinsic residual stresses in single splats produced by thermal spray processes, Acta Mater. 49 (2001) 1993–1999. http://www.sciencedirect.com/science/article/pii/S1359645401000994 (accessed May 18, 2016).

[3] P. Fauchais, M. Vardelle, A. Vardelle, Reliability of plasma-sprayed coatings: monitoring the plasma spray process and improving the quality of coatings, J. Phys. D. Appl. Phys. 46 (2013) 224016. doi:10.1088/0022-3727/46/22/224016.

[4] J.R. Fincke, W.D. Swank, R.L. Bewley, D.C. Haggard, M. Gevelber, D. Wroblewski, Diagnostics and control in the thermal spray process, Surf. Coatings Technol. 146–147 (2001) 537–543. doi:10.1016/S0257-8972(01)01432-3.

[5] M. Tanaka, M. Hasegawa, A.F. Dericioglu, Y. Kagawa, Measurement of residual stress in air plasma-sprayed Y2O3–ZrO2 thermal barrier coating system using micro-Raman spectroscopy, Mater. Sci. Eng. A. 419 (2006) 262–268. doi:10.1016/j.msea.2005.12.034.

[6] G. Witz, V. Shklover, W. Steurer, S. Bachegowda, H.P. Bossmann, Phase evolution in yttria-stabilized zirconia thermal barrier coatings studied by Rietveld Refinement of X-ray powder diffraction patterns, J. Am. Ceram. Soc. 90 (2007) 2935–2940. doi:10.1111/j.1551-2916.2007.01785.x.

[7] Y.C. Yang, E. Chang, Measurements of residual stresses in plasma-sprayed hydroxyapatite coatings on titanium alloy, Surf. Coatings Technol. 190 (2005) 122–131. doi:10.1016/j.surfcoat.2004.02.038.

[8] Y. Chen, X. Zhao, Y. Dang, P. Xiao, N. Curry, N. Markocsan, P. Nylen, Characterization and understanding of residual stresses in a NiCoCrAlY bond coat for thermal barrier coating application, Acta Mater. 94 (2015) 1–14. doi:10.1016/j.actamat.2015.04.053.

[9] J. Matejicek, S. Sampath, In situ measurement of residual stresses and elastic moduli in thermal sprayed coatings part 1: Apparatus and analysis, Acta Mater. 51 (2003) 863–872. doi:10.1016/S1359-6454(02)00478-0.

[10] A.M. Kamara, K. Davey, A numerical and experimental investigation into residual stress in thermally sprayed coatings, Int. J. Solids Struct. 44 (2007) 8532–8555. doi:10.1016/j.ijsolstr.2007.06.031.

[11] F. Hugot, J. Patru, P. Fauchais, L. Bianchi, Modeling of a substrate thermomechanical behavior during plasma spraying, J. Mater. Process. Technol. 190 (2007) 317–323. doi:10.1016/j.jmatprotec.2007.02.023.

[12] A. Nadeau, L. Pouliot, F. Nadeau, J. Blain, S.A. Berube, C. Moreau, M. Lamontagne, A new approach to online thickness measurement of thermal spray coatings, J. Therm. Spray Technol. 15 (2006) 744–749. doi:10.1361/105996306X147054.

[13] D. V Semenov, I.S. Sidorov, E. Nippolainen, A.A. Kamshilin, Speckle-based sensor system for real-time distance and thickness monitoring of fast moving objects, Meas. Sci. Technol. 21 (2010) 045304. doi:10.1088/0957-0233/21/4/045304.

[14] J. Chevalier, L. Gremillard, A. V. Virkar, D.R. Clarke, The tetragonal-monoclinic transformation in zirconia: Lessons learned and future trends, J. Am. Ceram. Soc. 92 (2009) 1901–1920. doi:10.1111/j.1551-2916.2009.03278.x.

[15] V. Lughi, D.R. Clarke, High temperature aging of YSZ coatings and subsequent transformation at low temperature, Surf. Coatings Technol. 200 (2005) 1287–1291. doi:10.1016/j.surfcoat.2005.07.089.

[16] V. Lughi, D.R. Clarke, Low-temperature transformation kinetics of electron-beam deposited 5 wt.% yttria-stabilized zirconia, Acta Mater. 55 (2007) 2049–2055. doi:10.1016/j.actamat.2006.11.007.

[17] V. Lughi, D.R. Clarke, Transformation of electron-beam physical vapor-deposited 8 wt% yttria-stabilized zirconia thermal barrier coatings, J. Am. Ceram. Soc. 88 (2005) 2552–2558. doi:10.1111/j.1551-2916.2005.00452.x.

[18] J. Helm, S.R. Mcneill, M.A. Sutton, Improved three-dimensional image correlation for surface displacement measurement, Opt. Eng. 35 (1996) 1911–1920.

[19] M.A. Sutton, J.J. Orteu, H.W. Schreier, Image Correlation for Shape, Motion and Deformation Measurements, 1st ed., New York, 2009.

[20] S.R. McNeill, M.A. Sutton, Z. Miao, J. Ma, Measurement of surface profile using digital image correlation, Exp. Mech. 37 (1997) 13–20. doi:10.1007/BF02328744.

[21] M.N. Rossol, J.H. Shaw, H. Bale, R.O. Ritchie, D.B. Marshall, F.W. Zok, Characterizing weave geometry in textile ceramic composites using digital image correlation, J. Am. Ceram. Soc. 96 (2013) 2362–2365. doi:10.1111/jace.12468.

[22] G.G. Stoney, The Tension of Metallic Films Deposited by Electrolysis, Proc. R. Soc. A Math. Phys. Eng. Sci. 82 (1909) 172–175. doi:10.1098/rspa.1909.0021.

[23] Y.C. Tsui, T.W. Clyne, An analytical model for predicting residual stresses in progressively deposited coatings Part 1: Planar geometry, Thin Solid Films. 306 (1997) 23–33. doi:10.1016/S0040-6090(97)00199-5.

[24] J.S. Lyons, J. Liu, M.A. Sutton, High-temperature deformation measurements using digital-image correlation, Exp. Mech. 36 (1996) 64–70.

[25] W.C. Oliver, G.M. Pharr, An improved technique for determining hardness and elastic modulus using load and displacement sensing indentation experiments, J. Mater. Res. 7 (1992) 1564–1583. doi:10.1557/JMR.1992.1564.

[26] F. Richter, M. Herrmann, F. Molnar, T. Chudoba, N. Schwarzer, M. Keunecke, K. Bewilogua, X.W. Zhang, H.G. Boyen, P. Ziemann, Substrate influence in Young's modulus determination of thin films by indentation methods: Cubic boron nitride as an example, Surf. Coatings Technol. 201 (2006) 3577–3587. doi:10.1016/j.surfcoat.2006.08.124.

[27] W. Pabst, E. Gregorová, M. Černý, Isothermal and adiabatic Young's moduli of alumina and zirconia ceramics at elevated temperatures, J. Eur. Ceram. Soc. 33 (2013) 3085–3093. doi:10.1016/j.jeurceramsoc.2013.06.012.

[28] Y. Song, Z. Lv, Y. Liu, X. Zhuan, T.J. Wang, Effects of coating spray speed and convective heat transfer on transient thermal stress in thermal barrier coating system during the cooling process of fabrication, Appl. Surf. Sci. 324 (2015) 627–633. doi:10.1016/j.apsusc.2014.10.157.

[29] R. Tu, T. Goto, Thermal cycle resistance of yttria stabilized zirconia coatings prepared by MO-CVD, Mater. Trans. 46 (2005) 1318–1323. http://jlc.jst.go.jp/DN/JALC/00256823330?from=Google (accessed April 18, 2016).

[30] K.A. Khor, C.T. Chia, Y.W. Gu, F.Y.C. Boey, High temperature damping behavior of plasma sprayed NiCoCrAlY coatings, J. Therm. Spray Technol. 11 (2002) 359–364. doi:10.1361/105996302770348745.

[31] P. Scardi, M. Leoni, L. Bertamini, Influence of phase stability on the residual stress in partially stabilized zirconia TBC produced by plasma spray, Surf. Coatings Technol. 76–77 (1995) 106–112. doi:10.1016/0257-8972(95)02496-4.

[32] J. Ilavsky, J.K. Stalick, Phase composition and its changes during annealing of plasma sprayed YSZ, Surf. Coatings Technol. 127 (2000) 120–129. doi:10.1016/S0257-8972(00)00562-4.

[33] L. Yang, F. Yang, Y. Long, Y. Zhao, X. Xiong, X. Zhao, P. Xiao, Evolution of residual stress in air plasma sprayed yttria stabilised zirconia thermal barrier coatings after isothermal treatment, Surf. Coatings Technol. 251 (2014) 98–105. doi:10.1016/j.surfcoat.2014.04.009.

[34] A. Labuschagne, N.F.J. van Rensburg, A.J. van der Merwe, Comparison of linear beam theories, Math. Comput. Model. 49 (2009) 20–30.

[35] X. Zhang, D. Thompson, X. Sheng, Differences between Euler-Bernoulli and Timoshenko beam formulations for calculating the effects of moving loads on a periodically supported beam, J. Sound Vib. 481 (2020) 115432. doi:10.1016/j.jsv.2020.115432.

[36] O.A.A. Bauchau, J.I.I. Craig, Euler-Bernoulli Beam Theory, in: Struct. Anal., 2009: pp. 173–221. doi:10.1007/978-90-481-2516-6_5.

[37] B. Pan, D. Wu, L. Yu, Optimization of a three-dimensional digital image correlation system for deformation measurements in extreme environments., Appl. Opt. 51 (2012) 4409–4419.

CHAPTER 4: IN-SITU CHARACTERIZATION OF HIGH-TEMPERATURE DELAMINATION MECHANISMS OF THERMAL BARRIER COATINGS

1. Introduction

Thermal barrier coatings (TBCs) are commonly used to increase the durability and operating temperatures of gas turbines, with the goal of improving engine efficiency and reducing operating cost [1,2]. Typically, these coatings are multilayered, such as the commonly used yttria-stabilized zirconia (YSZ) top coat (TC) / NiCoCrAlY intermetallic bond coat (BC) / superalloy substrate TBC system. Each of the constituent layers has different thermal and mechanical properties, resulting in a complex strain/stress state during thermal cycling. Moreover, the coating interfaces are generally rough, and the coatings themselves contain defects and are highly porous [3]. This nonlinearity makes robust numerical simulation difficult and fully-detailed analytical solutions all but impossible. To date, there has been no *in-situ* study to quantitatively relate crack initiation or propagation with respect to the microstructure, which is essential to validating the boundary conditions and results of finite-element (FE) TBC failure simulations. Recent synchrotron X-ray approaches have only partially solved this problem; they simply capture lattice strains without regard to microstructure using high-temperature synchrotron X-ray diffraction (XRD) [4,5] or alternately capture deformation as a function of microstructure with room-temperature *ex-situ* synchrotron X-ray computed tomography (XCT) [6]. These measurements reveal a nonlinear stress pattern through the coating thickness, but it is not clear how strain relates to microstructure during thermal cycling.

The failure mechanisms of TBC systems have been widely studied with both FE and post-failure microscopy techniques. Remarkable scientific progress has been achieved by these methods with regards to interfacial delamination of TBCs, which generally occurs between the top coat and bond coat or bond coat and substrate [7–10]. However, these models and experiments assume a homogeneous ceramic top coat without surface cracks. It has recently been established through FE simulations that small vertical or horizontal cracks near the TC / BC layer interface can reduce tensile stresses in the thermally grown oxide

(TGO) layer and inhibit delamination [11]. Periodically spaced surface cracks, which penetrate the top coat from the free surface to the TGO interface, increase coating compliance, and enhance interfacial durability [12,13], which is the motivating factor for so-called "Dense Vertically Cracked" (DVC) TBCs. It can be expected that surface cracks may significantly alter the failure mechanisms of TBCs in ways that have not been studied.

Second, the role of microstructural variation on TBC failure is not well understood. Coatings deposited by air plasma spray (APS) contain a microstructure with many pores, cracks, and inter-splat voids [3], which are potential failure initiation sites. Some of these features, in particular the inter-splat voids, are oriented parallel to the TC/BC interface, and large defects may redistribute stress away from the TGO and inhibit delamination near the TC/BC interface [11]. This stress redistribution may contribute to an alternative delamination mechanism.

In the current work, a DVC TBC system is shown to exhibit vertical cracks from the TC surface to the TGO interface, and horizontal cracks that branch off of the vertical crack (Figure 4.1). The two types of cracks are shown to interact and prevent delamination along the TC / BC interface. Instead, the horizontal crack is shown to grow with repeated thermal cycling at temperatures up to 1200°C and eventually lead to coating failure. Through this comprehensive study, a new TBC failure mechanism of delamination is established in the middle of the TC thickness. First, polished cross-sections of as-deposited TBC samples were thermally cycled from 25 °C to a maximum temperature between 1000 °C and 1200 °C under an optical microscope and analyzed with high-temperature digital image correlation (DIC) techniques [14]. Full-field thermomechanical deformation results are then related to (a) crack growth measurements and (b) salient microstructural features. Experimental results are reported in Section 3. Second, a high-throughput FE-based fracture analysis scheme elucidates the cracking mechanisms observed in the DIC experiments. This approach incorporates the effects of TC / BC interfacial roughness, uses experimentally measured high-temperature mechanical properties and systematically varies the horizontal crack position and crack length to understand the crack driving forces.

This modeling approach is somewhat similar to recent work by Richards [15], with the important distinction of incorporating experimentally measured interface geometries and nonlinear material models, which are shown to strongly influence the failure behavior of TBCs [8,16,17]. Fracture analysis results are reported in Section 4.

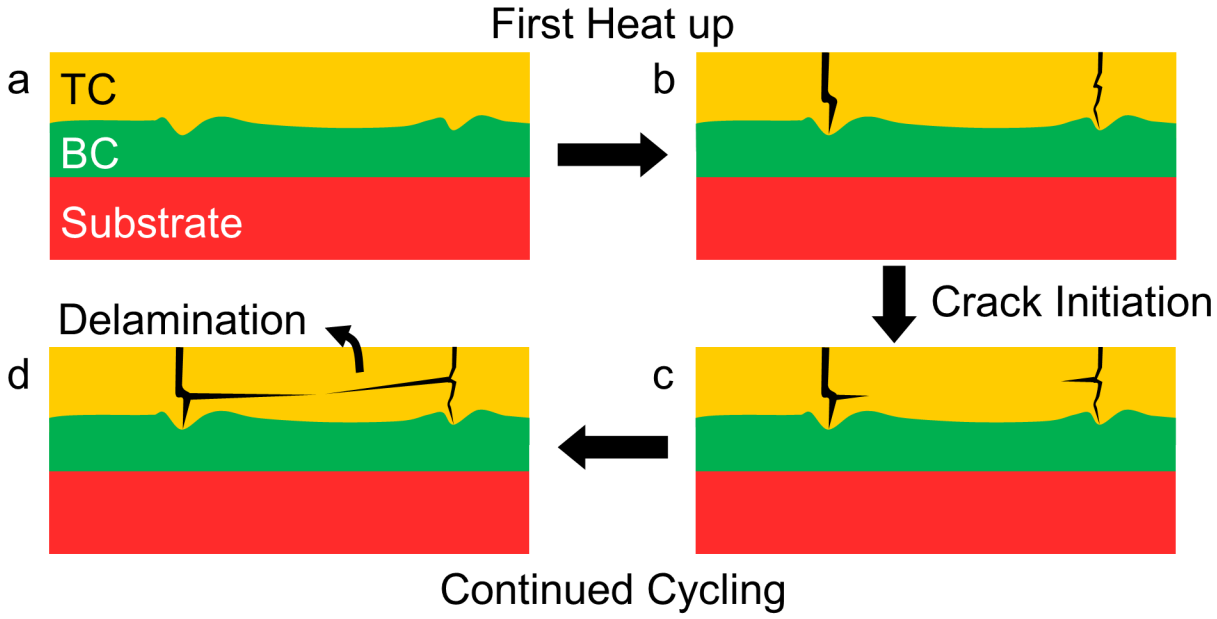

Figure 4.1. Schematic of new coating failure mechanism. (a) After coating deposition, the coating is crack-free. (b) During the first heating cycle, vertical cracks form near "valleys" in the TC / BC interface geometry, and (c) horizontal cracks are found to branch off of the vertical crack. (d) During subsequent heating, the horizontal cracks propagate and lead to coating delamination.

2. Experimental Methods

Thermal cycling experiments were performed on TBC samples with representative coating materials and thicknesses (Table 4.1). The coating system consisted of an 8 wt% YSZ (8YSZ) top coat, a NiCoCrAlY bond coat and a Haynes HR-224 substrate. The as-deposited coatings were sectioned into ~2 mm x 10 mm sections and then polished with standard metallographic techniques. During thermal cycling, a thin TGO layer grew on the BC layer.

2.1. Thermal Cycling Experimental Methodology

To study the crack initiation and propagation mechanisms, polished TBC cross-sections were thermally cycled in an optical microscope heating stage (Linkham Scientific, TS1500) and simultaneously imaged at 20x magnification. Five samples were heated (30 °C / minute), one each to a maximum temperature of 1000, 1050, 1100, 1150, and 1200 °C, held at this temperature for 60 minutes, and then cooled to a minimum temperature of 100 °C (also at 30 °C / minute); this heating cycle was repeated for a total of 4 cycles per sample. An additional sample was thermally cycled to a maximum temperature of 1200 °C for 80 cycles to study crack propagation and failure.

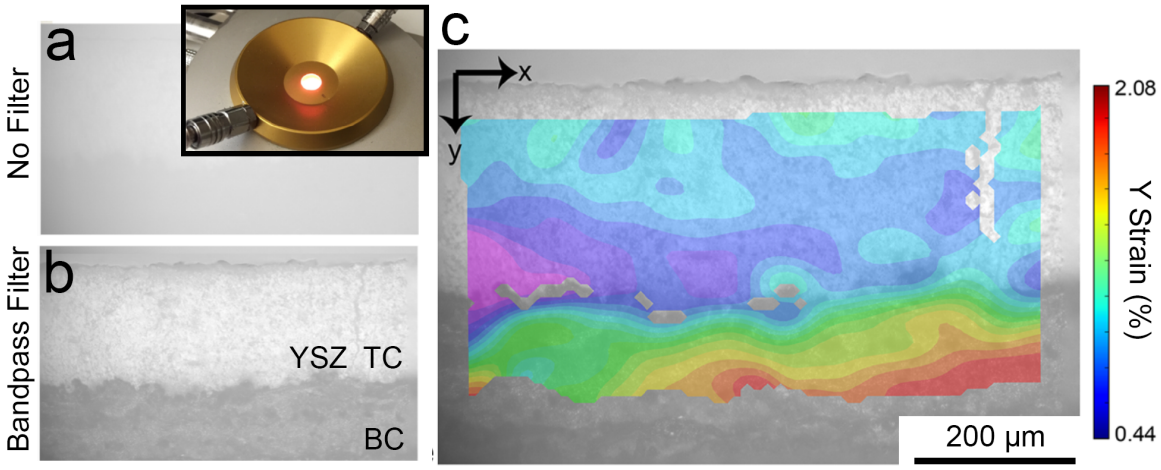

Figure 4.2. Optical micrographs of the TC (a) without and (b) with a UV bandpass filter. (c) Unprocessed DIC measured strains, showing thermal expansion of the coating layers at 1200 °C.

Digital images (5 Megapixel, PointGrey Research) of each sample were acquired before cycling, as well as at 100 °C, 600 °C, and at the maximum temperature during both the heating and cooling portions of the loading cycle. Ultraviolet lighting and narrow UV bandpass filters (450 ± 20 nm wavelength) enabled high-contrast imaging of the TBC sample at elevated temperatures (Figure 4.2), which was necessary for successful image correlation [14]. After using commercial focus-stacking software to create

a fully-focused image, the stitched images were correlated with commercial DIC software (VIC-2D, Correlated Solutions) to extract full-field local strain measurements throughout the TC cross-section.

The TC's intrinsic porosity provided a suitable high-contrast surface pattern for accurate correlation [18]. The porosity of the 8YSZ TC varied across the five samples from 5.2 % to 10.1 % as determined via quantitative image analysis of the collected optical micrographs as described by Du, *et al*. [19] and Laksmana, *et al*. [20]. The area of interest was carefully defined to exclude the TGO and BC layers, which would otherwise introduce bias to the strain measurements. The resulting DIC dataset was used to identify cracking and other failure events, as the crack opening displacements produced large pseudo-strains. To isolate mechanical deformation and crack-opening strains, thermal expansion relative to the reference state was subtracted from the measured DIC strain fields using literature thermal expansion coefficients (12.0×10^6 °C^{-1} for TC) [21,22]. Finally, it is emphasized that DIC's subpixel resolution enables highly-sensitive detection of deformation and cracking, even if microscopic crack opening is not visible in the image.

DIC error associated with thermal convective currents and focus stacking was evaluated by correlating several images acquired at 1200 °C. As a measure of error, the standard deviation of the computed artificial strains was found to be $\Delta\varepsilon_{xx} = 0.021$ % and $\Delta\varepsilon_{yy} = 0.041$ %. Error in ε_{yy} was random, while error in ε_{xx} show undulatory behavior with the largest error associated with image stitching boundaries; this error was attributed to overlapping regions with poor focus [23]. In all cases, this error was found to be an order of magnitude below crack-opening pseudo-strains and did not have a significant effect on strain calculations.

2.2. High-Temperature Mechanical Properties Through Nanoindentation

To assist with FE analysis, the high-temperature mechanical properties of the coating system were obtained by nanoindentation. The elastic modulus from 25-1000 °C was obtained from indentation loading/unloading curves using the Oliver-Pharr method [24]. Indentations were performed on a

nanoindenter (MicroMaterials Vantage) and a tribometer (Bruker Nano UMT 3) using a cubic boron nitride (cBN) Berkovich indenter and a sapphire Vickers indenter respectively. Individual grains in the TC and BC were targeted for nanoindentation with loads of 50 and 100 mN, which was found to reduce measurement variation. Calculations assumed $\nu_{cBN} = 0.12$, $E_{cBN} = 800\ GPa$, $\nu_{sapphire} = 0.24$, $E_{sapphire} = 375\ GPa$ at room temperature [25] and indenter mechanical properties were corrected for elevated temperature dependence to conform with reported temperature dependence in literature [26,27]. To compute TC fracture toughness, an array of 15 indentations at a peak indentation load of 500 mN was performed at 25 °C on both untreated and 1200 °C-treated (40 cycles) specimens. SEM measurement of the resulting radial cracks was used to compute fracture toughness (K_{IC}) using the relationship,

$$K_{IC} = B\sqrt{\frac{E_Y}{H}}\frac{F}{c^{3/2}} \tag{5.1}$$

where B is an indenter geometry constant, E_Y is the Young's modulus, H is the hardness, F is the applied load, and c is the crack length [28,29].

Indentation results are briefly summarized in Figure 4.3, which maps the Young's modulus as a function of temperature and position in each TBC material. The stiffness of each layer decayed linearly up to 1000 °C (Figure 4.3a); for example, the modulus of the TC was 58.6 GPa at 25 °C and 41.9 GPa at 1000°C, which agreed closely with literature values [30]. The elastic moduli obtained by nanoindentation varied significantly from layer to layer (Figure 4.3b), resulting in severe gradients at layer interfaces. The material adjacent to the TGO/BC and BC/Substrate interfaces exhibited low stiffness for unexplored reasons, possibly due to compositional gradients or interfacial defects. Moderate modulus variation was also observed within individual layers due to stochastic microstructural effects (voids, cracks and other defects) [31,32]. Elastic moduli for each layer were linearly extrapolated to 1200 °C to provide mechanical properties for FE simulations. The average calculated TC fracture toughness of the untreated TBC was $K_{IC} = 1.77\ MPa\ m^{1/2}$ while the average toughness of the 1200°C-treated TBC specimen was $K_{IC} = 1.46\ MPa\ m^{1/2}$; converted to the energy release rate (ERR), the two fracture toughnesses were

$G_{IC} = 53.5$ and $36.4\ J\ m^{-2}$, respectively. These values were on the lower end of ranges presented in other literature [33–35]. The 17.4% decrease in K_{IC} after thermal cycling suggested that continued exposure to ultra-high temperatures and material oxidation significantly reduces the fracture resistance and facilitates crack propagation. We emphasize that the indentations targeted dense material in the TC, meaning that these experiments provided upper bounds for G_C and that crack growth along weak interfaces could be substantially easier.

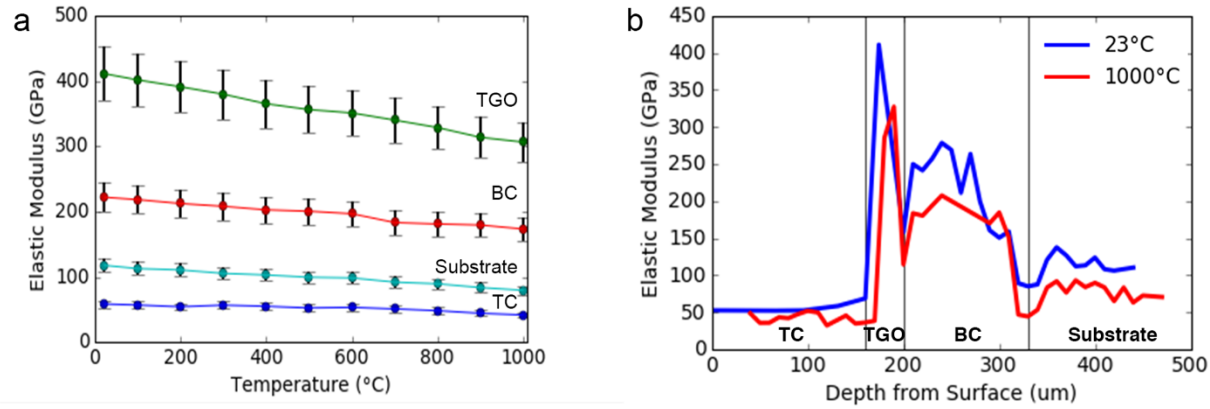

Figure 4.3. Nanoindentation results. (a) Stiffness of TBC materials was probed at temperatures up to 1000 °C (based partially on [18]). (b) The modulus distribution across the TBC cross-section at 25 °C and 1000 °C.

2.3. FE Model Development

Several FE simulations were performed to understand the fracture mechanisms of the TBC sample. Separate models with flat and experimentally-measured interface geometries were developed, with the coating thickness and interface geometry (Figure 4.4) established from optical micrographs and X-ray computed tomography (Xradia microXCT 200). The rough interface was irregular with roughness $R_a = 16.2\ \mu m$, a maximum peak-to-valley distance of $69.7\ \mu m$, and a characteristic wavelength of $\approx 200\ \mu m$. The interfaces between coating layers were modeled with shared nodes, since interfacial delamination was not of interest to these simulations.

The central objective of the simulations was to characterize the initiation and propagation of

horizontal cracks from the vertical crack. To achieve this, a vertical crack was positioned at an experimentally accurate location near a "valley" in the TC/TGO interface, and a horizontal crack of length L branched off of the vertical crack at a depth d from the top surface. Both d and L were manipulated over the range $d \in (25, \dots, 230\ \mu m)$ and $L \in (10, \dots, 250\ \mu m)$ to fully map the crack growth characteristics as a function of microstructure. Material models were developed for each of the coating layers with both experimental (Section 2.2) and literature values for material properties, as summarized in Table 4.2. The bond coat material used a linear elastic / perfectly plastic material model based on prior literature values [36]. The nominal element size away from the crack tip was 3.75 μm, and the mesh was refined to a size of 0.08 μm near the crack tip (Figure 4.4b). Each model consisted of approximately 13500 nodes and 13250 elements, of which 1700 nodes and 1700 elements were located in the refined crack tip mesh. Mesh generation was automated with a Python script, facilitating high-throughput fracture analysis of the TBC failure mechanism.

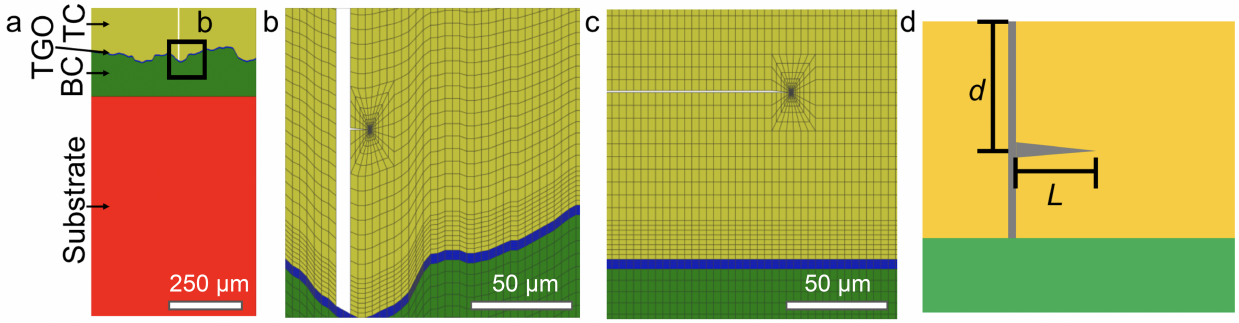

Figure 4.4. Overview of FE mesh geometry of the 8YSZ top coat (TC), NiCoCrAlY bond coat (BC), and HR-224 substrate. (a) Overview of FE mesh with detail of interface geometry. (b) Detail of FE mesh with vertical and horizontal cracks. Note the local mesh refinement around the crack tip. (c) Detail of FE mesh with a longer crack, and flat interface geometry. (d) Summary of fracture analysis parameters in this analysis.

The FE models were subjected to ramped temperature profile between 25 °C and 1200 °C with a reference temperature of 25 °C, as well as from 1200 °C to 25 °C with a reference temperature of 1200 °C. These two conditions approximated the sample's first annealing after coating deposition in which the

sample is approximated as initially free of residual stress and cool down after stress relaxation at maximum operating temperature. Since the material models were independent of time, these simulations neglected creep and stress relaxation effects; the temperature profiles should be interpreted to have rapid heating and cooling rates to prevent viscoplastic effects. The crack driving force in each model was evaluated with the virtual crack closure technique, which enabled the computation of energy release rate at the crack tip [37]. Energy release rate was computed at every 25 °C temperature increment in the loading profile, providing a deep understanding of the crack growth mechanism during thermal cycling.

3. Thermal Cycling Results

3.1. Crack Initiation

Temperature-corrected DIC strain maps acquired during the initial heating of the TBC samples revealed a heterogeneous strain distribution, indicative of localized cracking and microstructure-dependent deformation. Maps of ε_{xx} and ε_{yy} for the 1100 °C sample are presented in Figures 4.5 and 4.6 respectively, which are representative of strain fields for all 5 samples. The ε_{xx} strain field was periodic with an apparent wavelength of ~200 μm, and the strain peaks spanned most of the TC thickness. Inspection of the underlying micrograph revealed the presence of dense vertical cracks at each local maximum, implying that these strain fields were caused by crack opening pseudo-strains; growth of these cracks was driven by bulk tensile stresses in the TC when heating from a stress-free state (Figure 4.5c) [18]. At 600 °C, the magnitude of each local maximum was $\varepsilon_{xx} \approx 0.025$; at 1100 °C, the pseudostrain at the primary crack increased to $\varepsilon_{xx} = 0.05$, while the magnitude of strain at the minor crack remained constant. Therefore, the growth of the primary vertical crack relieved the stress on adjacent vertical cracks and prevented further crack opening.

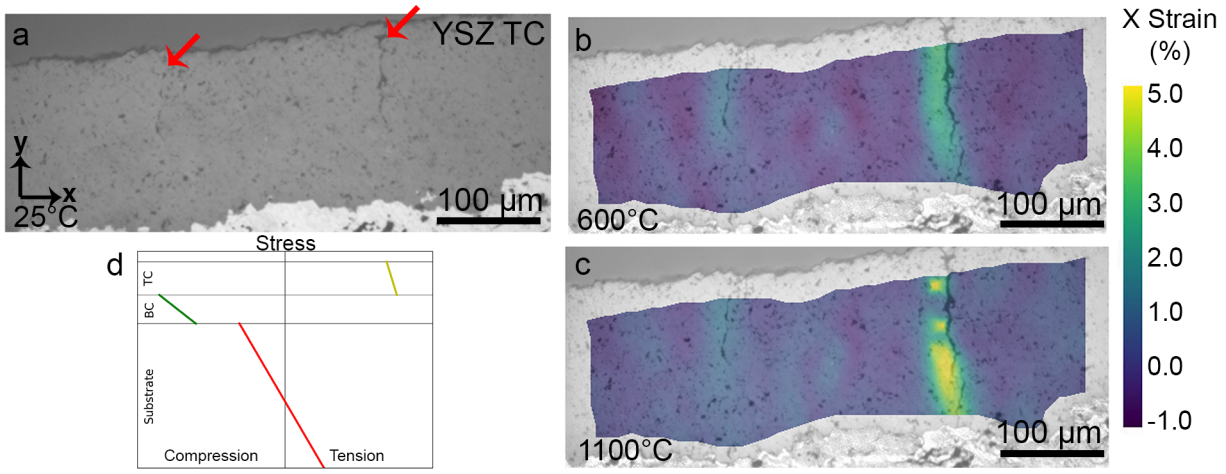

Figure 4.5. Vertical crack formation in the 8YSZ TBC 1100 °C sample. (a) Micrograph of TBC sample before heating, showing two vertical proto-cracks (marked by arrows). (b) Plot of temperature-corrected ε_{xx} at 600 °C, showing early formation of DVCs. (c) Plot of temperature-corrected ε_{xx} at 1100 °C. (d) Nominal σ_{xx} distribution in TBC due to thermal expansion mismatch during heating [18]. All strains are "temperature corrected" by subtracting thermal expansion.

During the initial heating, horizontal cracks formed off of the vertical crack (Figure 4.6) as marked by a pattern of ε_{yy} pseudostrains. Their initiation appeared as regions of elevated ε_{yy} strain below 600 °C, and crack opening displacement (COD) grew upon heating at 1100 °C (Figures 4.6b-c). This indicated crack formation at lower temperature and continued growth at elevated temperatures. High-magnification SEM analysis (Figure 4.6d) confirmed the presence of lateral cracks and also showed that lateral cracks initiated at corners in the vertical crack, revealing that their formation was closely coupled with vertical crack deflection; these mechanisms are analyzed in more detail in Section 3.3. The initiation of cracks at lower temperatures was unexpected, given that thermomechanical stresses due to mismatched thermal expansion were low for small ΔT. This early crack initiation highlighted the importance of residual stress, pre-existing flaws, and the elevated stresses around the crack tip during vertical crack formation in initiating the horizontal cracks.

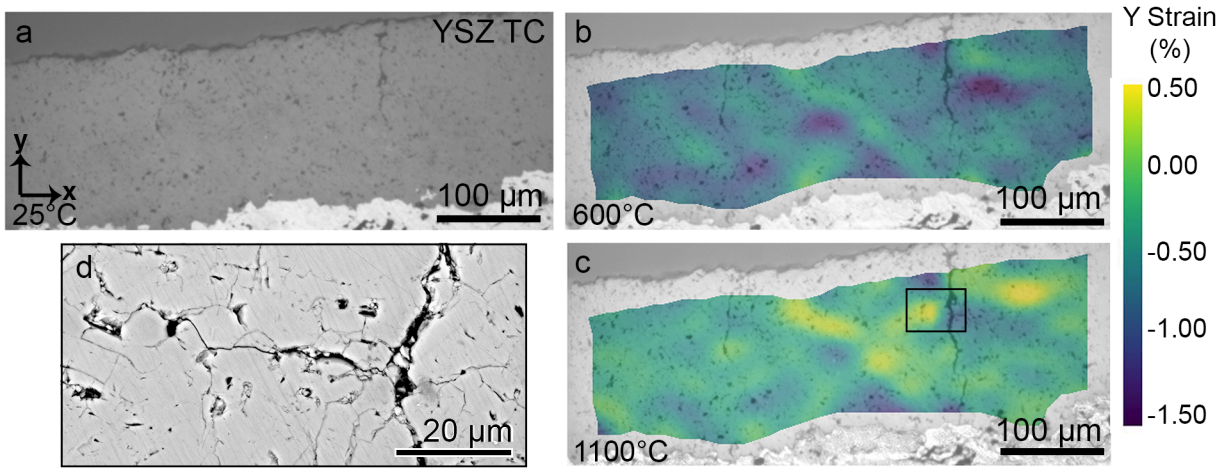

Figure 4.6. Horizontal crack formation in 8YSZ TBC 1100 °C sample. (a) Optical micrograph of TC before heating. (b) Plot of temperature-corrected ε_{yy} at 600 °C, showing early formation of horizontal cracks. (c) Plot of temperature-corrected ε_{yy} at 1100 °C (d) SEM image of highlighted region in (c), showing horizontal crack.

3.2. Crack Propagation

While the samples were assumed to be stress-free before thermal cycling (reference temperature of 25 °C), stress relaxation occurred at elevated temperatures to modify the reference temperature for residual stress models based on mismatched thermal expansion. This transition changed the thermomechanical stress field which drives crack growth and marked a change between "crack initiation" and "crack propagation" phases. This creep-driven transition was studied by tracking the median DIC strain (which is insensitive to crack opening) during 4 thermal cycles at temperatures between 1000 °C and 1200 °C, with results summarized in Figure 4.7. Using the image acquired immediately upon reaching the maximum cycling temperature as the reference image, these plots indicated that a steady-state stress distribution in each sample was not achieved until after the fourth cycle (Figure 4.7). Evidence of a strain-ratcheting effect was present in all five samples, with median ε_{xx} decreasing linearly to values between $\varepsilon_{xx} = -.015$ and $-.025$ after four cycles, but thereafter achieved a steady-state strain distribution (Figure 4.7b). The median ε_{xx} in the 1200 °C sample quickly reached a steady-state values of $\varepsilon_{xx} = -0.02$ after the second cycle, while the median strain in the remaining samples continued to decrease for 4 cycles. Minimal

deformation occurred during the first hour-long exposure at the maximum temperature ($i.e., t = 1\ hour$) in Figure 4.6a, indicating most strain accumulation occurred during the cooling portion of each cycle. While the median strain was larger for the 1100, 1150, and 1200 °C samples compared to the 1000 and 1050 °C samples, indicating that the ratcheting effect generally scaled with temperature, variation in sample roughness prevented robust conclusions about this trend. Indeed, the median strain of the 80-cycle 1200 °C sample achieved a peak median $\varepsilon_{xx} = -0.032$ after two hours but returned to an equilibrium strain of $\varepsilon_{xx} = -0.02$; the difference in behavior compared to the other samples was attributed to higher interface roughness (compare Figure 4.6 vs. Figure 4.8).

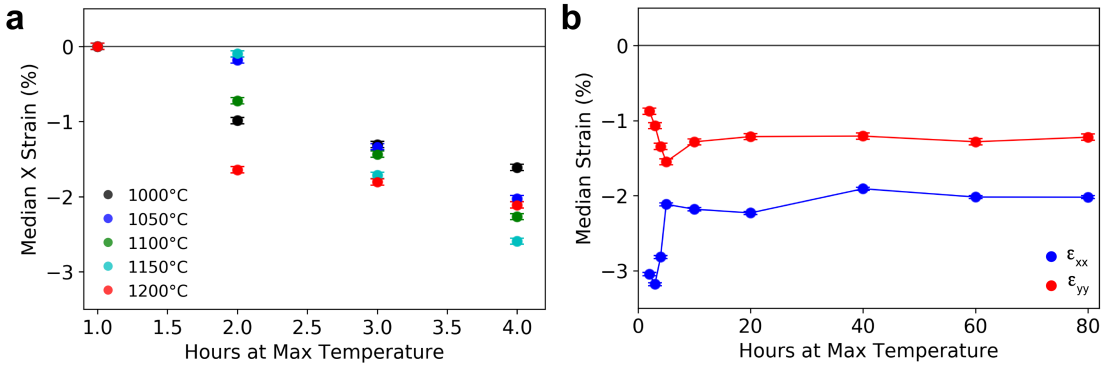

Figure 4.7. Evidence for temperature-dependent transition between crack initiation and propagation phases wihtin the 8YSZ top coat. (a) Median ε_{xx} strain as function of annealing time. (b) Median ε_{xx} and ε_{yy} measured over 80 cycles to temperature of 1200 °C.

Temperature-corrected ε_{yy} maps are presented in Figure 4.7 for the 80-cycle test, which reveal the basic crack propagation mechanisms associated with DVC TBCs. Prior to 10 cycles (Figure 4.8a-b), the ε_{yy} pseudostrains associated with crack propagation were concentrated about 50 μm below the surface (crack marked by * in Figure 4.8b). In subsequent cycling, another region of crack growth (marked by † in Figure 4.8d) about 50 μm above the TGO interface developed significant COD and became the most prominent region of crack growth by the 20th cycle (Figure 4.8c-d). This location continued to experience the most growth through 80 cycles. These results suggested that the near-surface crack initially possessed

critical ERR for crack growth, but both the natural stress field for long near-surface cracks as well as crack shielding effects from the near-interface cracks reduced ERR to subcritical values. The mechanism of this transition from one prominent crack formation to a second is analyzed further with FE simulations (Section 4.2). In both positions, the cracks angled gently toward the BC interface at an angle of ~15°, suggesting that growth toward the interface resulted in most favorable ERR for long cracks. Close inspection of the crack path (Figure 4.8e) revealed that crack growth occurred through preferential linkage of pores and voids along this critical angle. Growth did not occur in other directions, even along paths with seemingly favorable microstructures for fracture, such as the chain of large pores along the top of Figure 4.8e. The highlighted path exhibited widespread bridging, indicating that the complex APS microstructure possessed irregular fracture toughness and that voids adjacent to the crack path altered crack-tip stresses. Depending on these local stress states, the crack may propagate around or through the defect.

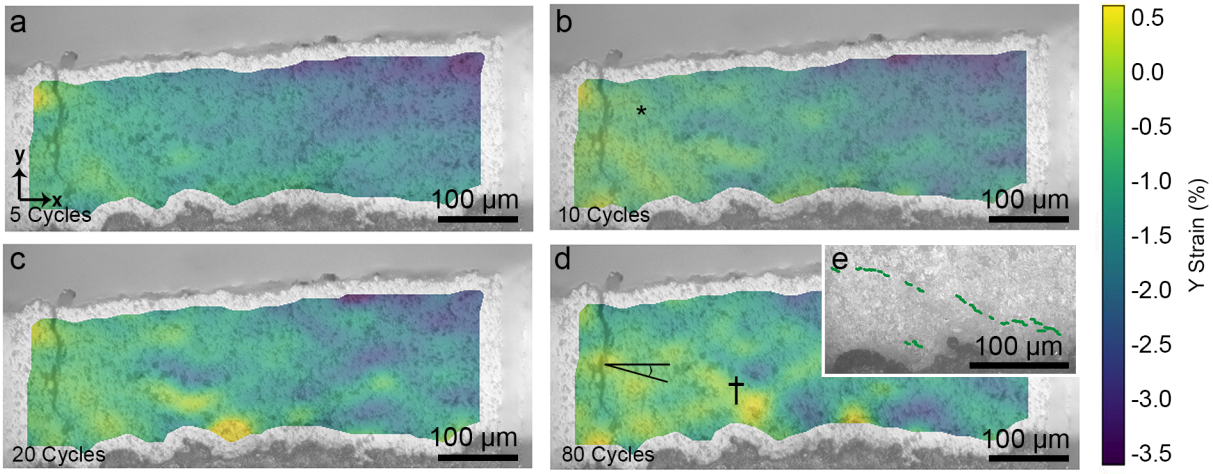

Figure 4.8. Thermal cycling to an annealing temperature of 1200 °C prompted the growth of lateral cracking within the 8YSZ top coat, indicated by tensile strain ($\varepsilon_{yy} > 0.0$, in yellow) within the top coat. (a) Early crack growth was located just below the surface of the top coat (indicated by ⋆); however, (b) by 10 cycles, prominent crack growth was observed in the middle of the top coat, progressing through (c) 20 and (d) 60 cycles (indicated by †). (e) Horizontal cracks highlighted in green after 80 cycles.

3.3. Cracking Mechanisms

SEM imaging of the TBC samples after 4 thermal cycles (Figure 4.9) was used to analyze the crack initiation and propagation mechanisms. Regardless of cycling temperature, all lateral cracks branched off of vertical cracks (marked by red arrows in Figure 4.9a-g) and appeared to originate at deflections in the vertical crack path, confirming that the initiation of vertical and horizontal cracks was strongly coupled. The location of horizontal cracks suggested that as vertical cracks were arrested at microstructural barriers, lateral microcracks branched off of the obstacle; this branching is depicted schematically in Figure 4.9h. The insensitivity of crack formation mechanism to temperature indicated that the lateral cracks formed at temperatures below the smallest cycling temperature (<1000 °C), which was consistent with the formation of vertical cracks and DIC results.

The longest horizontal cracks and most sample damage occurred in the 1000 °C sample compared to samples cycled at higher temperatures. After 4 cycles, the 1000 °C specimen exhibited surface and near surface damage (Figure 4.9a) that was not observed in specimens cycled to higher temperatures. In conjunction with median-strain results presented in Figure 4.7, this damage pattern suggested that stress relaxation occurred slowly at 1000 °C compared to higher temperatures, and that rapid stress relaxation inhibited the critical growth of lateral cracks. The severity of damage in the 1000 °C sample during the early stages of thermal cycling indicated that per-cycle damage in the "crack initiation" regime was more severe than in "crack propagation".

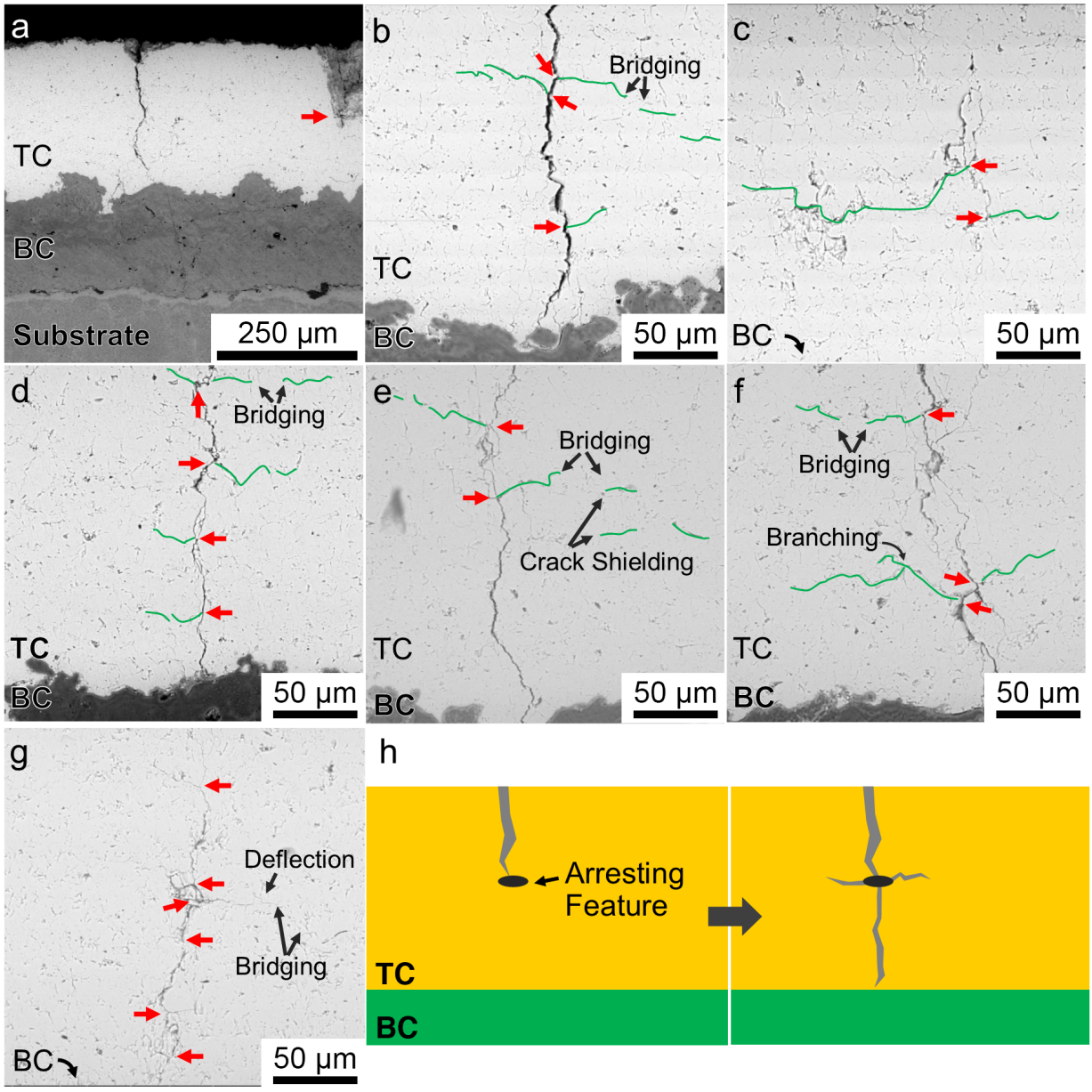

Figure 4.9. SEM backscatter images showing the formation of vertical and horizontal 8YSZ TC cracks after four thermal cycles. Horizontal cracks are highlighted in green, and their initiation sites on a vertical crack are marked by red arrows. Selected crack-propagation features are labeled. (a) 1000 °C specimen, showing distribution of vertical cracks and large spallation associated with horizontal crack formation (red arrow). (b-g) Detail of horizontal cracking in various specimens: (b-c) 1000 °C, (d) 1050 °C, (e) 1100 °C, (f) 1150 °C, (g) 1200 °C. (h) Proposed TC cracking mechanism.

Finally, the SEM images revealed specific mechanisms of crack propagation, showing that crack growth was highly irregular and regulated by microstructure. These images provided several examples of bridging, shielding, branching, and deflection of cracks, which suggested that microstructural features both arrested primary crack growth and promoted secondary cracking adjacent or ahead of the crack tip at weak interfaces. These cracking mechanisms were essential to the formation a network of cracks as the arrest of a particular lateral crack enabled the growth of adjacent cracks. At the same time, the interrupted cracking pattern also meant that the 8YSZ TC material retained strength and toughness; however, the increased coating compliance could substantially alter interfacial stresses and vulnerability to other damage mechanisms.

4. Finite Element Analysis

4.1. Crack Initiation and the Role of Interface Geometry

Results of simulations to probe the crack driving force during the sample's first heating are summarized in Figure 4.10. Simulation results are presented for both experimental and flat interface geometries, which emphasize that ERR was a nonlinear function of crack position and temperature. At moderate temperatures below 850 °C, cracks positioned near the TC / BC interface ($d > 170$ μm) as well as near the TC surface ($d < 100$ μm) experienced an elevated ERR compared to cracks at intermediate depths, and ERR increased monotonically with temperature. At temperatures above 900 °C, the ERR became insensitive to increasing temperature; this transition was attributed to the reduced yield strength of the BC layer, suggesting that plastic flow strongly limited the crack driving force at elevated temperatures.

Second, TC / BC interface roughness strongly influenced ERR and created very different crack growth behaviors near the interface. This was evident both quantitatively in the maximum calculated ERR as well as qualitatively in the ERR contour shape as a function of temperature and crack position. With the experimental geometry, the maximum ERR occurred at 1200 °C at a position 50 μm above the TC /

BC interface with $G_{max} = 43.0\, J/m^2$. With the flat geometry simulation, the maximum energy release rate occurred at 825 °C on the TC / BC interface with $G_{max} = 54.5\, J/m^2$. Thus, it could be expected that the interface geometry governs the maximum energy release rate as well as the location and temperature at which it occurs. Compared to the experimental (rough) interface geometry, the flat interface at moderate temperatures (T between 500 and 900 °C) increased the amount of material with enhanced ERR in interior of the TC and reduced the amount of material with elevated ERR near the interface. In addition, above 900 °C and with the flat interface geometry, the ERR was nearly uniformly distributed for all crack positions; crack growth on the interior of the TC therefore became competitive with crack growth along the TC / BC interface.

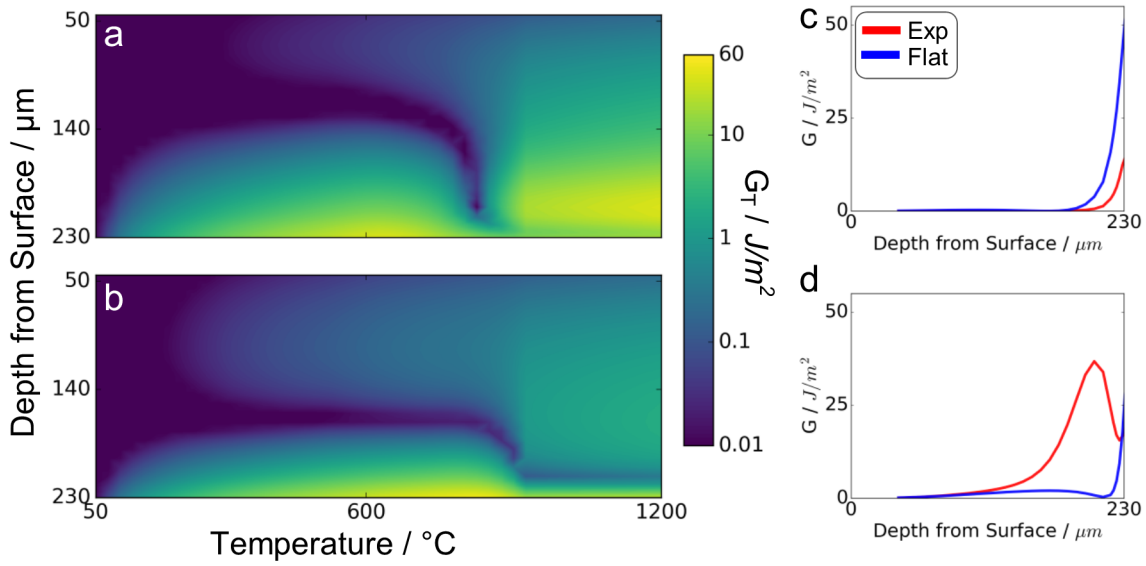

Figure 4.10. (a-b) Contour plots of total Energy Release Rate (G_T,J/m^2) as function of interface geometry. (a) Experimental interface geometry. (b) Flat interface geometry. (c) G_T at 800 °C as function of crack position, and (d) G_T at 1200 °C as function of crack position. All analyses performed with a 10 μm crack.

With respect to the experimentally-observed crack growth mechanisms, the flat interface geometry facilitated the initiation of cracks on the interior of the top coat layer. Since the distribution of large flaws

was statistical, and ERR was shown to increase with crack length, the larger interior region of material with elevated ERR increased the likelihood that a critical ERR was achieved. Although the ERRs for $L = 10\ \mu m$ were below G_C, equivalent analyses with $L = 20\ \mu m$ showed larger ERR at all temperatures in the sample interior. SEM analysis of unheated TBC samples revealed crack-like flaws longer than 50 μm, which could increase ERR in the sample interior to levels approaching G_C.

4.2. Crack Propagation

As the majority of experimental crack propagation occurred after annealing at high temperatures, the crack driving force was also simulated during cool down from a hot reference temperature of 1200 °C. In Figure 4.11, ERR is presented at $T = 25\ °C$ as a function of crack position d and crack length L. Results are shown only for the flat interface, as it was impossible to simulate a purely horizontal crack near a rough TC / BC interface; the horizontal crack would have penetrated into the BC and would have simulated interfacial delamination. In general, ERR increased with crack length and as the crack depth approaches the TC / BC interface. A maximum ERR of $G_{max} = 185\ J/m^2$ was achieved for a crack length of 160 μm at the TC / BC interface. The ERR along the TC / BC interface decayed slightly for longer lengths yet remained large. In agreement with DIC results, this large ERR suggested that sustained crack growth was energetically favorable and that long cracks would drive gradually toward the TC / BC interface. The notable exception to this trend occurred for short cracks near the TC surface ($d < 150\ \mu m$, $L < 50\ \mu m$); in this region, the ERR decayed until a critical crack length before ERR monotonically increased. This phenomenon was explained by shear lag as material immediately adjacent to the vertical crack flanks would experience low stress. The primary implication of this "ERR valley" was that growth of short, near-surface delamination cracks would be arrested, even if they initially possessed the most favorable ERR. Beyond this point, growth of cracks closer to the TC / BC interface would dominate (Figure 4.11b).

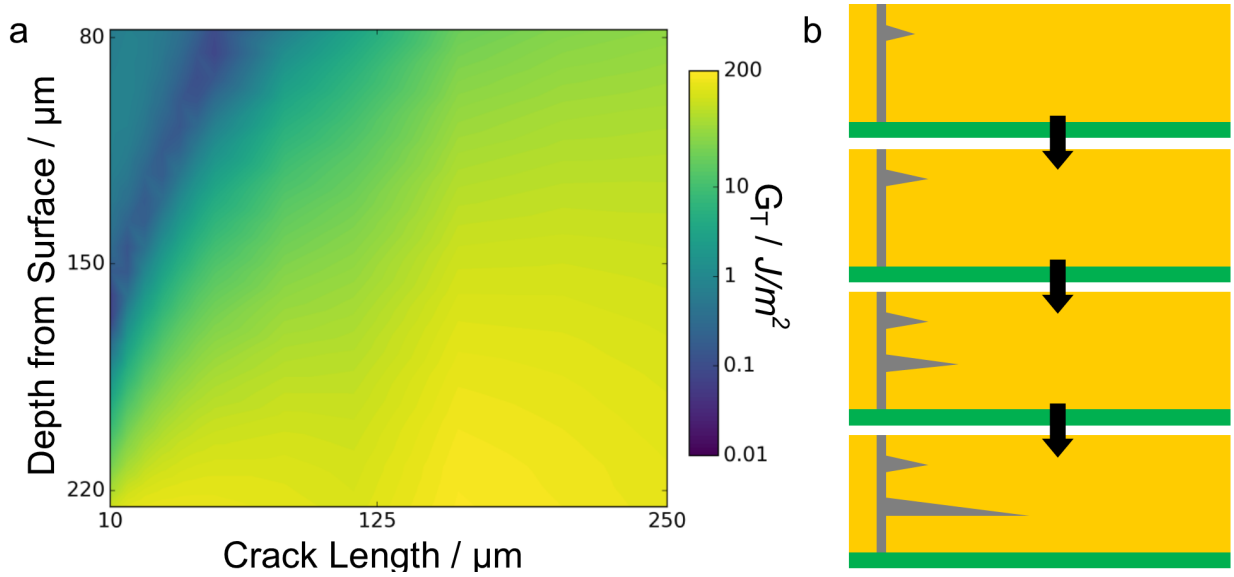

Figure 4.11. ERR at 25 °C during crack propagation regime with T_{ref} = 1200 °C. (a) ERR is presented as a function of crack length and crack position. (b) Schematic illustration of crack arresting mechanism for short near-surface cracks (TC in yellow, BC in green).

5. Discussion

5.1. Crack Formation Mechanisms

In-situ observation of the crack formation with DIC revealed the vertical cracks in the TC formed near the top surface and grew toward the BC interface, driven by tensile stress during the initial heating. Vertical crack initiation and growth in subsequent thermal cycles was minimal due to stress relaxation effects. Some vertical cracks did not reach either the top surface or BC interface, suggesting that the vertical cracks initiated on the interior of the surface. This observation was critical to understanding the formation mechanism of vertical cracks, which has not previously been reported. For instance, vertical cracks were previously modeled as initiating on the surface [38]; with these results in mind, the term "surface cracks" may misrepresent the actual formation mechanism.

The vertical crack path was jagged, indicating that the crack deflected around many obstacles within the TC. Crack branching at these locations gave rise to horizontal cracks, as most of the horizontal cracks initiated at sharp deflections in the vertical crack. It should be noted that many microstructural features,

such as inter-splat boundaries, had a distinct horizontal orientation, which would facilitate both vertical crack deflection and branching along the horizontal interface, and FE simulations revealed that small flaws adjacent to the vertical crack could produce favorable ERR for crack growth through almost the entire TC thickness. This mechanism explained the simultaneous formation of vertical and horizontal crack in DIC images during the first heating cycle as well as in SEM images after only four cycles. This formation mechanism is especially relevant for DVC TBCs, which are typically deposited with large APS passage thicknesses to increase vertical crack density [39], resulting in a microstructure that contains several prominent horizontal interfaces. These interfaces still exist in conventional APS coatings, but the sparsity of vertical cracks may inhibit lateral crack formation at these locations.

5.2. Crack Propagation Mechanisms

SEM inspection of the lateral cracks showed a complex crack growth pattern characterized by extensive deflection, crack bridging, and crack shielding, which can be explained by the TC microstructure and abundance of pre-existing flaws. When the lateral crack encountered an obstacle, elevated crack-tip stresses enabled crack deflection, as well as growth along weak interfaces adjacent to or in front of the crack tip. This mechanism resulted in a network of many horizontal cracks along weak interfaces, as well as the segmented crack growth observed in Figures 4.8e and 4.9. This mechanism is also key to interpreting the FE crack growth results. While the FE-computed ERR for short cracks was generally below G_C obtained by nanoindentation, the pervasive lateral crack propagation indicated that the fracture toughness along weak interfaces was substantially lower. We note that the nanoindentation experiments targeted dense TC grains, such that fracture toughness along porous interfaces could be substantially lower.

Importantly, the FE simulations predicted a region associated with short lateral cracks near the top surface (small d and L) where crack growth would become arrested. The primary implication of this result was that propagation was not favorable for all lateral cracks. This observation was supported by

DIC strain maps in Figure 4.8, which revealed that crack growth was most prominent near the TC / BC interface, even though several short cracks near the top surface were apparent in earlier DIC strain maps and SEM images. Second, the simulation results supported the direction of crack growth, which was observed to angle in the direction of highest ERR toward the TC / BC interface. Upon reaching the interface, failure by conventional delamination mechanisms may be expected.

A key uncertainty in this study is the role of a free-surface effect on the crack propagation mechanisms. The experimental and FE simulations examined the in-plane degradation of the 8YSZ top coat, but the free-surface effect would relax local stresses. I hypothesize that this free-surface effect on the in-plane DVC and lateral cracks observed in these experiments would be minor; however, this effect would have a significant impact on the out-of-plane crack growth mechanisms through the coating due to free-surface relaxation of the stress mismatch between top coat and bond coat. To validate this hypothesis, X-ray tomography may be performed in future work to characterize volumetric crack growth within the 8YSZ top coat, using the inherent porosity as a correlation pattern as performed here with two-dimensional optical imaging. Such volumetric analysis would clearly distinguish any free-surface effect on the fracture mechanisms.

6. Conclusions

New fundamental failure mechanisms of DVC TBCs at temperatures up to 1200 °C were captured *in-situ* using high-temperature DIC and FE fracture mechanics analyses, which revealed the coupled formation of vertical and horizontal cracks based on microstructural crack-deflecting features. Crack initiation was observed at low temperatures during heating from a stress-free state, while crack propagation occurred after cooling from a stress-free state achieved via stress relaxation. Horizontal cracks originated at locations of vertical crack deflection throughout the TC layer, indicating that crack branching at these features contributed to horizontal crack formation. In contrast, lateral crack propagation strongly favored the lower TC region near the BC interface and was found to occur through

crack deflection, crack bridging and crack shielding mechanisms. High-throughput FE fracture simulations revealed favorable energy release rates for lateral crack initiation near the TC surface as well as near the BC interface, and stable crack propagation toward the BC interface, which agreed with experimental results. Upon reaching the BC, crack propagation along the interface ultimately leads to coating delamination. This mechanism is unique from conventional delamination failures, in which damage occurs primarily along the interface.

7. References

[1] R.K. Mishra, C. Beura, Life consumption assessment of a large jet engine, J. Fail. Anal. Prev. 14 (2014) 519–529. doi:10.1007/s11668-014-9842-2.

[2] C.B. Meher-Homji, G. Gabriles, Gas turbine blade failures - causes, avoidance, and troubleshooting, in: Proc. 27th Turbomach. Symp., 1998: pp. 129–179. http://citeseerx.ist.psu.edu/viewdoc/download?doi=10.1.1.462.4970&rep=rep1&type=pdf (accessed May 18, 2016).

[3] C. Lamuta, G. Di Girolamo, L. Pagnotta, Microstructural, mechanical and tribological properties of nanostructured YSZ coatings produced with different APS process parameters, Ceram. Int. 41 (2015) 8904–8914. doi:10.1016/j.ceramint.2015.03.148.

[4] K. Knipe, A. Manero Ii, S.F. Siddiqui, C. Meid, J. Wischek, J. Okasinski, J. Almer, A.M. Karlsson, M. Bartsch, S. Raghavan, Strain response of thermal barrier coatings captured under extreme engine environments through synchrotron X-ray diffraction, Nat. Commun. 5 (2014) 4559. doi:10.1038/ncomms5559.

[5] C. Li, S.D.M. Jacques, Y. Chen, P. Xiao, A.M. Beale, M. di Michiel, N. Markossan, P. Nylen, R.J. Cernik, Precise strain profile measurement as a function of depth in thermal barrier coatings using high energy synchrotron X-rays, Scr. Mater. 113 (2016) 122–126. doi:10.1016/j.scriptamat.2015.10.032.

[6] D. Khoshkhou, M. Mostafavi, C. Reinhard, M.P. Taylor, D.S. Rickerby, I.M. Edmonds, H.E. Evans, T.J. Marrow, B.J. Connolly, Three-dimensional displacement mapping of diffused Pt thermal barrier coatings via synchrotron X-ray computed tomography and digital volume correlation, Scr. Mater. 115 (2016) 100–103. doi:10.1016/j.scriptamat.2015.10.033.

[7] S.R. Choi, J.W. Hutchinson, A.G. Evans, Delamination of multilayer thermal barrier coatings, Mech. Mater. 31 (1999) 431–447. doi:10.1016/S0167-6636(99)00016-2.

[8] R.W. Jackson, M.R. Begley, Critical cooling rates to avoid transient-driven cracking in thermal barrier coating (TBC) systems, Int. J. Solids Struct. 51 (2014) 1364–1374. doi:10.1016/j.ijsolstr.2013.12.029.

[9] A.G. Evans, J.W. Hutchinson, The mechanics of coating delamination in thermal gradients, Surf. Coatings Technol. 201 (2007) 7905–7916. doi:10.1016/j.surfcoat.2007.03.029.

[10] J.W. Hutchinson, A.G. Evans, On the delamination of thermal barrier coatings in a thermal gradient, Surf. Coatings Technol. 149 (2002) 179–184. doi:10.1016/S0257-8972(01)01451-7.

[11] L. Wang, J.S. Yang, J.X. Ni, C.G. Liu, X.H. Zhong, F. Shao, H.Y. Zhao, S.Y. Tao, Y. Wang, Influence of cracks in APS-TBCs on stress around TGO during thermal cycling: A numerical simulation study, Surf. Coatings Technol. 285 (2016) 98–112. doi:10.1016/j.surfcoat.2015.11.036.

[12] X.L. Fan, R. Xu, W.X. Zhang, T.J. Wang, Effect of periodic surface cracks on the interfacial fracture of thermal barrier coating system, Appl. Surf. Sci. 258 (2012) 9816–9823. doi:10.1016/j.apsusc.2012.06.036.

[13] H. Guo, H. Murakami, S. Kuroda, Thermal cycling behavior of plasma sprayed segmented thermal barrier coatings, Mater. Trans. 47 (2006) 306–309. doi:10.2320/matertrans.47.306.

[14] B. Pan, D. Wu, Z. Wang, Y. Xia, High-temperature digital image correlation method for full-field deformation measurement at 1200 °C, Meas. Sci. Technol. 22 (2011) 015701. doi:10.1088/0957-0233/22/1/015701.

[15] B.T. Richards, S. Sehr, F. De Franqueville, M.R. Begley, H.N.G. Wadley, Fracture mechanisms of ytterbium monosilicate environmental barrier coatings during cyclic thermal exposure, Acta Mater. 103 (2016) 448–460. doi:10.1016/j.actamat.2015.10.019.

[16] P. Seiler, M. Bäker, J. Rösler, Multi-scale failure mechanisms of thermal barrier coating systems, Comput. Mater. Sci. 80 (2013) 27–34. doi:10.1016/j.commatsci.2013.04.028.

[17] R. Xu, X. Fan, T.J. Wang, Mechanisms governing the interfacial delamination of thermal barrier coating system with double ceramic layers, Appl. Surf. Sci. 370 (2016) 394–402. doi:10.1016/j.apsusc.2016.02.180.

[18] B.P. Croom, C.H. Bumgardner, X. Li, Unveiling residual stresses in air plasma spray coatings by digital image correlation, Extrem. Mech. Lett. 7 (2016) 126–135. doi:10.1016/j.eml.2016.02.013.

[19] H. Du, J.H. Shin, S.W. Lee, Study on porosity of plasma-sprayed coatings by digital image analysis method, J. Therm. Spray Technol. 14 (2005) 453–461. doi:10.1361/105996305X76450.

[20] F.L. Laksmana, L.J. Van Vliet, P.J.A. Hartman Kok, H. Vromans, H.W. Frijlink, K. Van Der Voort Maarschalk, Quantitative image analysis for evaluating the coating thickness and pore distribution in coated small particles, Pharm. Res. 26 (2009) 965–976. doi:10.1007/s11095-008-9805-y.

[21] R. Tu, T. Goto, Thermal cycle resistance of yttria stabilized zirconia coatings prepared by MO-CVD, Mater. Trans. 46 (2005) 1318–1323. http://jlc.jst.go.jp/DN/JALC/00256823330?from=Google (accessed April 18, 2016).

[22] Y. Song, Z. Lv, Y. Liu, X. Zhuan, T.J. Wang, Effects of coating spray speed and convective heat transfer on transient thermal stress in thermal barrier coating system during the cooling process of fabrication, Appl. Surf. Sci. 324 (2015) 627–633. doi:10.1016/j.apsusc.2014.10.157.

[23] M.A. Sutton, J.H.H. Yan, V. Tiwari, H.W. Schreier, J.J. Orteu, The effect of out-of-plane motion on 2D and 3D digital image correlation measurements, Opt. Lasers Eng. 46 (2008) 746–757. doi:10.1016/j.optlaseng.2008.05.005.

[24] W.C. Oliver, G.M. Pharr, An improved technique for determining hardness and elastic modulus using load and displacement sensing indentation experiments, J. Mater. Res. 7 (1992) 1564–1583. doi:10.1557/JMR.1992.1564.

[25] F. Richter, M. Herrmann, F. Molnar, T. Chudoba, N. Schwarzer, M. Keunecke, K. Bewilogua, X.W. Zhang, H.G. Boyen, P. Ziemann, Substrate influence in Young's modulus determination of thin films by indentation methods: Cubic boron nitride as an example, Surf. Coatings Technol. 201 (2006) 3577–3587. doi:10.1016/j.surfcoat.2006.08.124.

[26] J.M. Wheeler, J. Michler, Invited Article: Indenter materials for high temperature nanoindentation, Rev. Sci. Instrum. 84 (2013) 101301. doi:10.1063/1.4824710.

[27] J.M. Wheeler, D.E.J. Armstrong, W. Heinz, R. Schwaiger, High temperature nanoindentation: The state of the art and future challenges, Curr. Opin. Solid State Mater. Sci. 19 (2015) 354–366. doi:10.1016/j.cossms.2015.02.002.

[28] D.B. Marshall, B.R. Lawn, An Indentation Technique for Measuring Stresses in Tempered Glass Surfaces, J. Am. Ceram. Soc. 60 (1977) 86–87. doi:10.1111/j.1151-2916.1977.tb16106.x.

[29] B. Bhushan, X. Li, Nanomechanical characterisation of solid surfaces and thin films, Int. Mater. Rev. 48 (2003) 125–164. doi:10.1179/095066003225010227.

[30] W. Pabst, E. Gregorová, M. Černý, Isothermal and adiabatic Young's moduli of alumina and zirconia ceramics at elevated temperatures, J. Eur. Ceram. Soc. 33 (2013) 3085–3093. doi:10.1016/j.jeurceramsoc.2013.06.012.

[31] N. Zotov, M. Bartsch, G. Eggeler, Thermal barrier coating systems — analysis of nanoindentation curves, Surf. Coatings Technol. 203 (2009) 2064–2072. doi:10.1016/j.surfcoat.2009.02.008.

[32] A.A. Kulkarni, A. Goland, H. Herman, A.J. Allen, J. Ilavsky, G.G. Long, F. De Carlo, Advanced microstructural characterization of plasma-sprayed zirconia coatings over extended length scales, J. Therm. Spray Technol. 14 (2005) 239–250. doi:10.1361/10599630523818.

[33] P. Dahl, I. Kaus, Z. Zhao, M. Johnsson, M. Nygren, K. Wiik, T. Grande, M.A. Einarsrud, Densification and properties of zirconia prepared by three different sintering techniques, Ceram. Int. 33 (2007) 1603–1610. doi:10.1016/j.ceramint.2006.07.005.

[34] S.R. Choi, N.P. Bansal, Flexure Strength, Fracture Toughness, and Slow Crack Growth of YSZ/Alumina Composites at High Temperatures, J. Am. Ceram. Soc. 88 (2005) 1474–1480. doi:10.1111/j.1551-2916.2005.00252.x.

[35] J. Wan, M. Zhou, X.S. Yang, C.Y. Dai, Y. Zhang, W.G. Mao, C. Lu, Fracture characteristics of freestanding 8 wt% Y2O3–ZrO2 coatings by single edge notched beam and Vickers indentation tests, Mater. Sci. Eng. A. 581 (2013) 140–144. doi:10.1016/j.msea.2013.05.086.

[36] A.M. Karlsson, A.G. Evans, A numerical model for the cyclic instability of thermally grown oxides in thermal barrier systems, Acta Mater. 49 (2001) 1793–1804. doi:10.1016/S1359-6454(01)00073-8.

[37] R. Krueger, Virtual crack closure technique: History, approach, and applications, Appl. Mech. Rev. 57 (2004) 109. doi:10.1115/1.1595677.

[38] W.X. Zhang, X.L. Fan, T.J. Wang, The surface cracking behavior in air plasma sprayed thermal barrier coating system incorporating interface roughness effect, Appl. Surf. Sci. 258 (2011) 811–817. doi:10.1016/j.apsusc.2011.08.103.

[39] H.B. Guo, R. Vaßen, D. Stöver, Atmospheric plasma sprayed thick thermal barrier coatings with high segmentation crack density, Surf. Coatings Technol. 186 (2004) 353–363. doi:10.1016/j.surfcoat.2004.01.002.

CHAPTER 5: CHARACTERIZING HERMETIC FAILURE OF CERAMIC TUBES BY DIGITAL IMAGE CORRELATION AND ACOUSTIC EMISSION

1. Introduction

In recent years, significant effort has been placed on developing next-generation accident tolerant nuclear fuel systems and robust materials to extend reactor design safety to include non-ideal, extreme reactor conditions, addressing the critical safety concerns following the Fukushima incident [1–4]. While there are several leading, material-based solutions addressing concerns with current fuel claddings, one of the more auspicious and heavily investigated is silicon carbide (SiC) continuous fiber-reinforced SiC matrix (SiC/SiC) composites. SiC ceramic matrix composites (CMC) are favored due to their high temperature strength, chemical inertness, irradiation tolerance, and improved damage tolerance, all of which indicate a general compatibility with the harsh environment within a nuclear reactor [2–5]. Furthermore, SiC CMCs have been rigorously tested within the aerospace community, where high temperature properties and corrosion resistance are critical requirements of many materials [6–8]. In a reactor environment, the onset of matrix microcracking coupled with the loss of cladding hermeticity can allow the escape of radiative fuel and gases with potentially disastrous consequences, even though the cladding may still possess full load bearing capabilities [9,10]. In order for these CMCs to be accepted by the stringent nuclear community, they must be exhaustively evaluated and examined through a suite of investigations to elucidate their full failure behavior.

Mechanical testing of SiC nuclear fuel cladding CMCs is greatly complicated by several factors: (i) anisotropy of both mechanical and thermomechanical properties; (ii) complex, multiscale failure mechanisms induced from the fiber-matrix structure; (iii) a laminated, thin-walled cylindrical geometry; and (iv) the relatively small failure strains of monolithic SiC [11,12]. Furthermore, these factors contribute to a convoluted definition of failure, where matrix cracking, fiber cracking, loss of hermeticity, and loss of load-bearing function may occur at distinctly different strains. Currently, this relationship between microcracking and gas tightness remains unresolved as available *ex-situ* hermetic evaluations are unable to account for likely microcrack closing upon mechanical unloading [13]. Therefore, the *in-situ* hermetic

failure behavior under loading must be thoroughly addressed to progress the implementation of advanced CMC materials for use in extreme applications [5,13,14]; this unknown hermeticity behavior is the subject addressed in this work.

Here, a novel, *in-situ* hermeticity monitoring setup is developed and validated, utilizing three-dimensional digital image correlation (3D-DIC) and acoustic emission (AE) detection to investigate the relationship between microcracking and spatial damage with the hermetic seal of SiC CMC fuel claddings. This experimental setup was evaluated on brittle ceramics and glasses, and a preliminary characterization of *in-situ* SiC/SiC CMC hermeticity was conducted. This methodology represents the world's first conglomeration of comprehensive sensors (helium leak detection, AE detection, and 3D-DIC) designed for sequentially determining the onset of cracking, loss of hermeticity, and ultimate failure while accommodating SiC/SiC fuel claddings without the need for special modification or specimen dependent gripping section.

There are few suitable test designs already documented in the literature; one possible design was the U-frame cladding bend rig [15–17]. Four-point bending, however, is the most logical choice for investigating hermetic failure as it concentrates compressive and tensile strains at known orientations, providing simple He sensor positioning and a route to internal pressurization through non-obstructed specimen ends [18,19], unlike conventional tension or compression testing. Extending the design template described in ASTM C1684 – 18 for bending of brittle rods, custom-designed, load-distributing cradles were fabricated and utilized to reduce contact point stresses [20]. Composites have historically presented a challenge for experimentalists due to the highly non-uniform stress state, which produces spatial strain gradients that cannot be accurately determined using conventional strain gauges [12,18,19,21,22]. Addressing this challenge, 3D-DIC was leveraged to measure spatial strain fields over a targeted area of interest with sufficient resolution to track local strain concentrations associated with composite architectural features [23–26]. AE monitoring was used to identify the strains at the onset and progression of cracking, leading up to loss of He gas tightness [27–29]. This work is intended to advance the scientific evaluation of brittle constituent tubes and progress the optimization of SiC/SiC CMCs for extreme conditions.

2. Experimental Methods

2.1. Materials

Table 5.1 lists the specifications of the four different materials tested, including outer diameter (OD) and inner diameter (ID). Alumina (96-99.8 % purity), borosilicate glass, and 4130 steel tubes were purchased from McMaster-Carr. Diameter sizes were limited to commercial availability and were selected to be similar to the diameter of the CMCs. Single layer, chemical vapor infiltrated (CVI) SiC/SiC tubular CMCs (consisting of Hi-Nicalon Type S fibers and pyrolytic carbon (pyrocarbon) fiber/matrix interphase) with a nominal, tri-axial braid orientation of ± 55° from the tube axis were purchased from General Atomics; notably, the CMC tubes were coated with a CVD SiC layer with the outer diameter ground smooth. These SiC/SiC samples are prototypes of SiC-based nuclear fuel cladding currently under development and are not necessarily representative of a fully optimized SiC cladding. Specimens were cut to a 152 mm (6 in) length using a water-cooled, circular-bladed diamond saw. To establish an internal helium pressure with potential to exceed 2 atm, both specimen ends were sealed with a urethane adhesive (3M Scotch-Weld 620 epoxy adhesive) with one end containing a high-pressure plastic tube in which helium could be infused. Prior to testing, all specimens were coated with a thin, speckle pattern layer of matte white and black paint (Rustoleum) to provide a trackable surface pattern for DIC.

Table 5.1. Tubular specimen properties.

Material	Specimen Identifier	OD (mm/in)	ID (mm/in)	Vendor
Alumina	A	9.53 / 0.375	6.35 / 0.250	McMaster-Carr
Borosilicate Glass	B	9.53 / 0.375	5.59 / 0.220	McMaster-Carr
4130 Steel	S	9.53 / 0.375	8.00 / 0.315	McMaster-Carr
SiC/SiC CMC	CMC	9.53 / 0.375	7.15 / 0.281	General Atomics

2.2. Experimental Setup

All tests were conducted at room temperature using an Admet eXpert 2611 table-top, universal testing machine with an Admet 1210AJ-2K-B, 8.9 kN load cell using a loading rate of 0.5 mm/min. Inspiration for the design of the loading fixtures originated from a design used by the Idaho National Laboratory [18].

Specimens were supported using four cylindrical cradles as shown in Figure 5.1, which were sized such that the cradle width matched the roller diameter as specified in ASTM C1684-18. Support span distances of l_U/l_L = 42/84, 50/100, and 33/100 mm/mm were used; selection of these spans was guided by the recommendation of l_U/l_L = 40/80 in ASTM C1684-18 for ceramic rods with a diameter in the range of 4 to 12 mm. The cradles were machined to a diameter of 10.4 mm to accommodate the diameter of the tubes and were allowed to rotate at the support to maintain contact throughout specimen bending (Figure 5.1). It should be noted that a nominally smooth tube surface with less than 0.2 mm deviations is ideal to prevent point concentrations at the cradles. It was discovered in early testing that free cradles would move and alter the load distribution; the pivot points were secured with pins to prevent the cradles from sliding during loading. Support pivot points were lubricated to minimize any frictional effects.

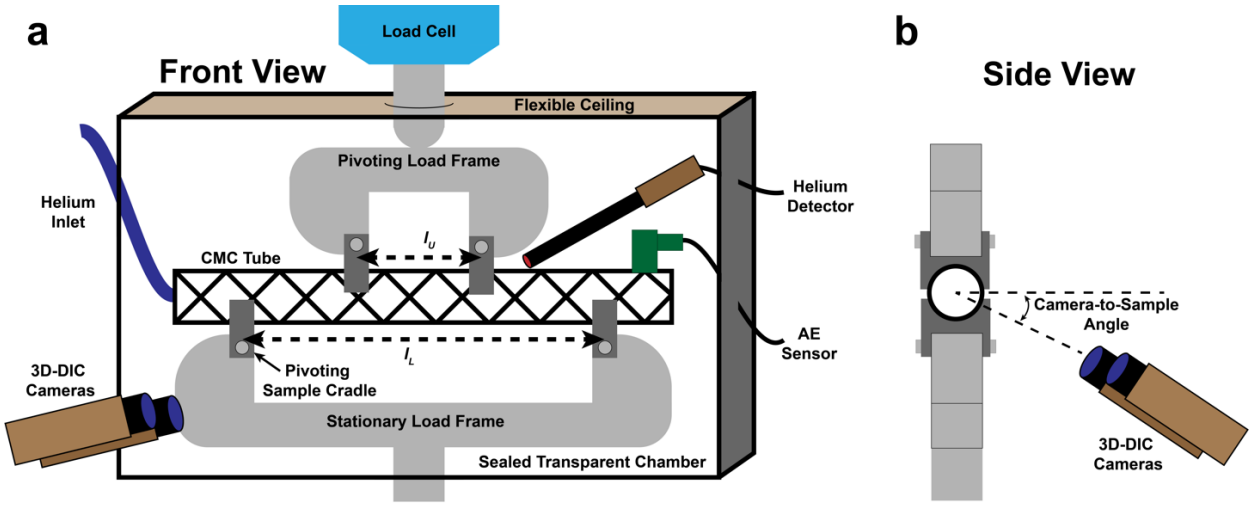

Figure 5.1. (a) Schematic of the novel, four-point bend setup for investigating *in-situ* hermetic failure of tubular composites and (b) camera-to-sample definition, representing how the cameras were positioned to view the underside of specimens, where maximum tensile strain occurs.

The loading fixtures and each test specimen, pressurized with 2 atm (30 psi) of internal pressure, were contained in a sealed, plastic chamber with a transparent, polycarbonate front window through which optical images for DIC analysis could be acquired. A flexible chamber ceiling was constructed from a thin,

plastic veil that sealed at the base of the load cell and on the chamber walls, enabling the upper loading fixture to move within the sealed environment. Air inlet and outlet ports were included to vent and purge helium from the chamber after specimen failure. A combination of clay and masking tape were utilized to provide a temporary seal at the chamber window edges, which could be quickly removed to provide access to the specimen and loading fixtures. This sealed chamber presented two key advantages: (i) it isolated the test environment from ambient helium, and (ii) it could be purged to enable quick successive testing.

Acoustic emissions were acquired by a Mistras 1283 USB AE Node at a rate of 1MHz with a threshold of 10 dB throughout the duration of testing. The AE sensor was secured directly to the specimen by an adjustable hose clamp. Helium leak rate was recorded by an Inficon Protec P3000 Helium Sniffer Leak Detector at a rate of 10 Hz with a minimum leak rate of 1 $*10^{-7}$ mbar l/s and a reaction time of ~400 ms with the probe directly above the bending center. In order to account for the sensor reaction time and to ensure that the leak rate and acoustic activity could be directly correlated with mechanical strain with minimal error, a stepped displacement profile was used, which would displace the crosshead at a rate of 0.5 mm/min in 0.01 mm increments with a 2 second hold period. This intermittent displacement profile is considered equivalent to a typical quasi-static rate.

Digital images were acquired through the chamber window with two FLIR Grasshopper 3 GS3-U3-50S5M-C digital CMOS cameras equipped with Schneider 21-100197 50 mm compact lenses at a capture rate of 5 Hz. 3D-DIC analysis was performed using a commercial correlation software, Correlated Solutions VIC-3D 8. For each analysis, an ideal subset size and step size were chosen based on the applied speckle pattern size. Typical subset sizes ranged from 19 to 35 pixels, and step sizes ranged from 6 to 9 pixels. All VIC-3D datasets were processed with a calibration of at least 30 images and rigid body motion removal via built-in functions. DIC strain error was quantified by imaging each specimen prior to loading and averaging the measured strain variation; the max DIC strain error was found to be 0.006 % strain, which is an order of magnitude below the strains associated with fracture of the CMCs. Data graphing and calculations were done in Python 3.6. Scanning electron microscope (SEM) images were taken by a FEI Quanta 650 Scanning Electron Microscope equipped with a Circular Backscatter Detector (CBS).

2.3. Data Processing

As previously described, multiple data streams were acquired from the universal test frame, the DIC cameras, the AE sensor, and the leak detector within a single test. All sensor data was temporally aligned via an average of several comparison points, enabling alignment and correlation of events detected with individual data streams.

The normalized cumulative acoustic energy (NC-AE) is a metric frequently used to evaluate the initiation, progression, and frequency of cracking events in ceramic composites [30,31]. Acoustic data was normalized by the total cumulative acoustic energy within each individual test; normalizing the acoustic energy minimizes variation in sensor sensitivity between consecutive tests, which stems from varying sensor contact pressure [32].

Strain data was exported from VIC-3D for every pair of images acquired. The DIC out-of-plane measurements were found to have an accuracy of ~0.002 mm as determined from variation between DIC strain profiles acquired at zero load. Each strain profile provided full-field measurements within a global coordinate system in millimeters, including x, y, and z position; u, v, and w displacements; and strains ε_{xx}, ε_{yy}, and ε_{xy} at every pixel location. These profiles were cropped to only include data within the inner load points associated with pure bending and subsequently analyzed to extract the camera-to-sample angle; to view the location of maximum bending tensile strains, the camera was located below horizontal (Figure 5.1b). Relative to the camera, vertical test frame displacements have y and z dimensions. The angle of the cameras was derived by the following equation:

$$\theta_i = \tan^{-1}\left(\frac{w_i}{v_i}\right) \tag{5.1}$$

where θ_i is the camera angle at every time step, and v_i and w_i are the specimen displacements in y and z, respectively. The camera angle converged to a value over time, which is the true camera-to-sample angle. Each cropped profile was rotated about the camera-to-sample angle such that all v displacements of the specimen occurred in the loading direction, thus reducing w displacements to zero.

The strain data was analyzed to determine surface bending strain. Extracting such parameters was necessary to convert from the spatial strains collected from DIC to singular points to use for conventional stress-strain curves and modulus calculations. For every *y* position down the cross-section of the specimen, all the strains were averaged down the length of the bending zone [33,34]. For the purpose of generating the stress-strain curve, averaging minimizes variation in local DIC strain profiles caused by variation of the underlying microstructure. For CMC results only, the effect of a pseudo-strain measurement, which was caused by crack opening displacement, was determined via a histogram analysis of the bending section strains. Typically, strain data fell along a normal distribution until onset of cracking, at which point outlying pseudo-strains would skew this distribution. Pseudo-strains were removed by filtering out the individual measurements above a 90-percentile threshold to ensure the measured strains reflected bending alone. Through averaging the filtered strains, we can identify the strain gradient across the specimen cross section (Figure 5.2). The standard deviation of the strains averaged down the length of this inner section was nominally 0.04 % strain. Strain at the lowest cross-sectional position, referred to as the peak strain, was extracted and used for stress-strain curves and modulus calculations as the maximum tensile strain due to bending.

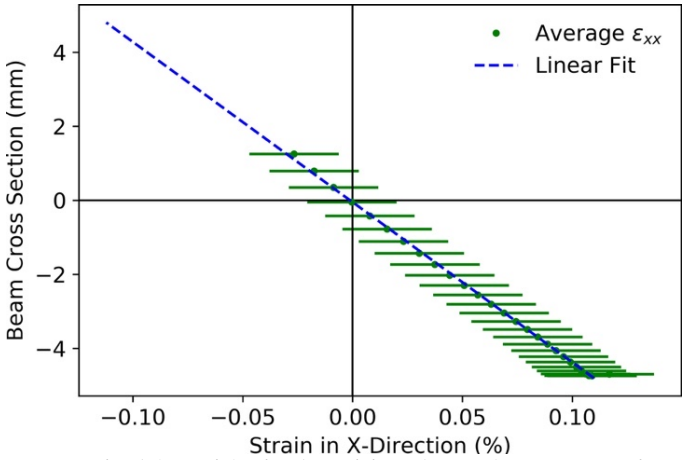

Figure 5.2. At every vertical (y-axis) pixel position down the cross section of the specimen, strains were averaged in the horizontal (x-axis) to reveal a Euler-Bernoulli beam-in-bending strain profile.

3. Theory

3.1. Stress Calculations

The maximum bending stress experienced by each specimen was calculated as follows:

$$\sigma = \frac{M(OD)}{2I} \tag{5.2}$$

where M is the bending moment and I is the moment of inertia. M and I are given by:

$$M = \frac{1}{4}F(l_L - l_U) \tag{5.3}$$

$$I = \frac{\pi(OD^4 - ID^4)}{64} \tag{5.4}$$

In Equations 5.2 to 5.4, l_L and l_U are the spans between the outer load points and inner load points, respectively; F is the applied load, and OD and ID represent the outer and inner diameters, respectively. The Young's modulus was calculated as the slope of a linear fit to the initial region of the stress-strain curves prior to the point of deviation from linearity. Where applicable, the proportional limit or the deviation from linearity strain (DFLS) values were calculated by shifting the linear fit over by 0.005% strain and finding the intersection point with the stress-strain curves.

3.2. Numerical Model

The four-point bending fixture presented here represents a slight modification to the accepted standard (ASTM C1684-18 / Figure 5.3a) and to the design presented by van Rooyen, *et al*. [18] (Figure 5.3b) concerning four-point bending of brittle rods at ambient temperatures. This alteration allows the fixture to consist only of rigid, metal components (316 stainless steel), which potentially qualifies the fixture for future higher temperature conditions. The alteration entails a different yet functionally equivalent method of cradle attachment (see standard for more details). Past designs have relied on rubber bands or springs to secure the cradles, which are balanced against / upon pins and are guided by slots in the fixture such that they are free to rotate only about an axis perpendicular to the specimen length with minimal opportunity to translate (Figure 5.3c). Using pins to secure the cradle pivot points, this new design enables the cradle to constrain itself to allow only the same rotation as the specimen while also providing a loose means of

attachment to the main fixture (Figure 5.3d), which was necessary to prevent cradle translation during bending. Additionally, the new custom cradles have an internal radius customized for nuclear fuel cladding sized diameters; this radius provides a more uniform specimen contact area and is an accepted option in ASTM C1684-18 for contact sensitive specimens. Given the changes to the four-point bending fixture, it must be demonstrated that these modifications do not promote significant strain concentrations or constraint under the expected bending conditions for SiC CMCs and other high stiffness materials. Therefore, a three-dimensional numerical model was developed by Heim [35] to replicate the experimental four-point bending fixture. This numerical model is presented here for continuity in Figure 5.3e, which indicated there was not a significant strain or stress concentration due to the grip. This fixture model was implemented for alumina, borosilicate, and 4130 steel tubes with correct geometry, including results for three different span measurements (l_U/l_L = 42/84, 50/100, and 33/100 mm/mm).

An extensive study to verify minimal strain concentration formation in regions underneath the grips and outside of the view of the 3D-DIC analysis was done for the three materials at strains seen via DIC. The steel tube is more ductile than the CMCs seen in this study and presents a case of extreme deflection or rotation of the cradles to ensure that no strain concentrations associated with wedging stresses form before 0.5% strain, which is greater than the anticipated strains incurred by the CMCs. Thus, it can be demonstrated that the modified fixture and attachment pins will not induce any undesirable constraint on the free rotation of the cradles during this range of bending deformation. There may still exist the possibility of a bending constraint past what deformation is experienced by CMCs, but the deformation when this would occur is dependent on the diameter of the pins that loosely attach the cradle to the support fixture and therefore, is capable of being changed if needed. Hence, this fixture should be used carefully when testing ductile materials to extended strains, as is the same case of the ASTM standard fixture, which is noted only for ceramics and glasses.

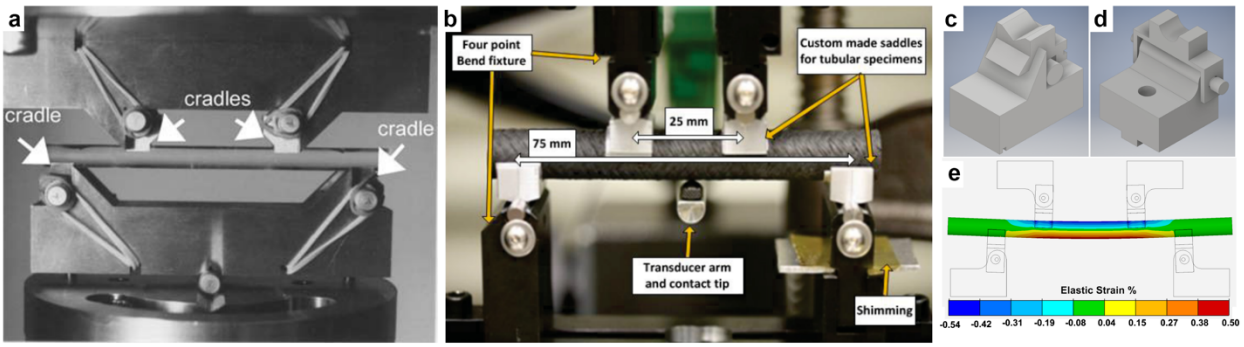

Figure 5.3. Iterations of four-point bend test rigs as presented by (a) ASTM C1684 and by (b) van Rooyen, *et al*. [18]. Computer-aided design model of (c) the ASTM standard and (d) custom bend cradles. (e) Numerical model, courtesy of Heim, *et al*. [35], of the custom bend setup with a steel tube confirms lack of strain concentrations with an even bending profile. Here l_U = 42 mm and l_L = 84 mm.

4. Results

4.1. Steel

SiC CMCs are expected to exhibit pseudo-plasticity and survive to several percent strain. Therefore, steel tubes were tested on the custom four-point bend fixture to investigate the effects of high bending deformation on the reliability of the cradles to evenly distribute the loading force and prevent localized damage, which can be compared to the above numerical model. Individual properties derived from 3D-DIC and the universal testing machine is presented in Table 5.2, while individual stress-strain curves and a representative DIC strain profile at 0.5 % bending strain is presented in Figure 5.4.

Measured Young's modulus and yield strength data all agreed well with the expected properties. Most encouragingly, the DIC profile maintained a uniform, Euler-Bernoulli strain profile across the bending zone for each specimen for a range of strains through 0.5 % (slightly greater than the largest strain achieved by a CMC specimen). There were no indicators of strain concentrations, which might hint to any imposed constraint by the setup. These physical observations combined with the numerical model validate the test methodology for the range of motion necessary for accurate testing of CMC tubes.

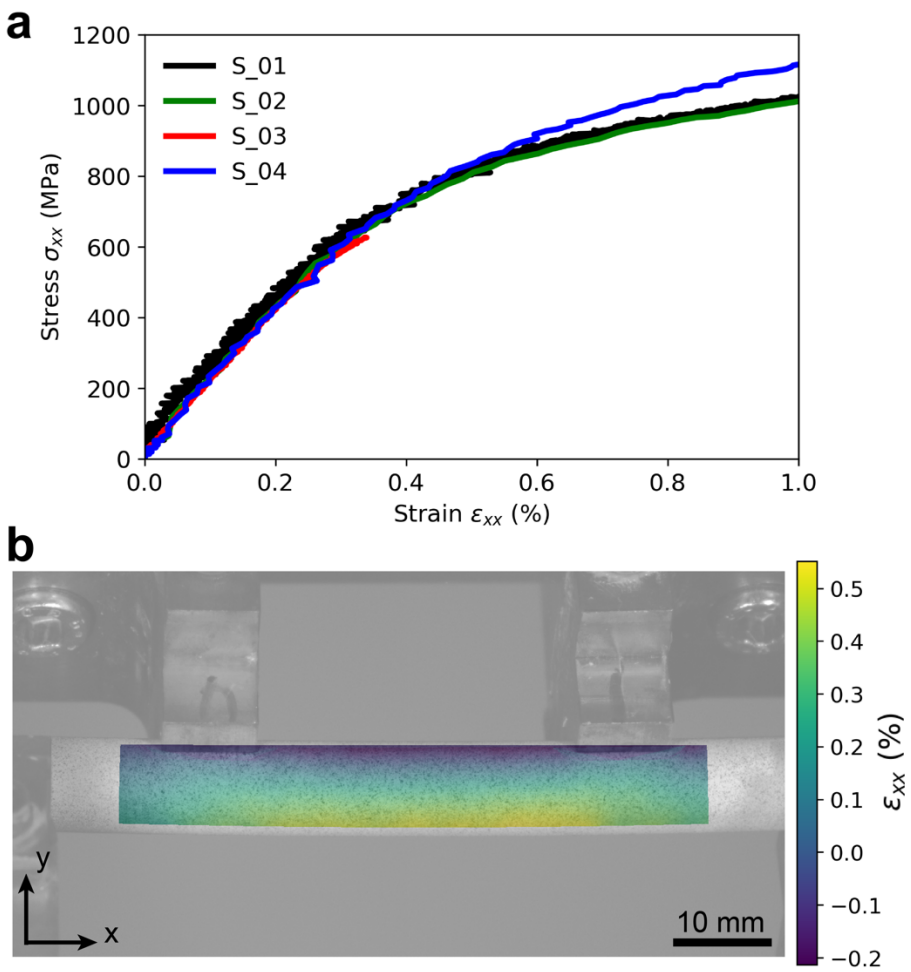

Figure 5.4. Plot of (a) stress-strain responses and a typical DIC profile (b) for steel tube, S_04.

Table 5.2. Summary of 4130 steel experimental properties. Expected values were provided from the retailer McMaster-Carr.

Specimen ID	Material	l_U (mm)	l_L (mm)	Expected Young's Modulus (GPa)	Young's Modulus (GPa)	Expected Yield Strength (MPa)	Yield Strength (MPa)
S_01	Steel	42	84	190-205	195	435-485	525
S_02	Steel	42	84	190-205	202	435-485	444
S_03	Steel	42	84	190-205	195	435-485	473
S_04	Steel	42	84	190-205	204	435-485	445

4.2. Alumina and Borosilicate Glass

Six alumina and six borosilicate glass specimens were tested as previously described using two different support span ratios (l_U/l_L= 34/100 and 50/100 mm/mm). Representative DIC strain profiles immediately prior to fracture are presented in Figure 5.5, and a summary of measured moduli, fracture strength, and strain is provided in Table 5.3. Despite the brittle fracture exhibited by both alumina and borosilicate specimens, DIC processing could distinguish a conventional Euler-Bernoulli bending profile with compressive strains along the upper region of the specimen and tension underneath. Borosilicate glass specimens failed at a higher bending strain than alumina, 0.19 % compared to 0.09 % strain on average. The borosilicate specimens exhibited a profile more clearly reflective of the expected Euler-Bernoulli trend, yet the strain profiles of alumina specimens showed relatively substantial variation. However, the individual properties derived from the DIC and mechanical tester fell within expected ranges, demonstrating the fundamental accuracy of this methodology.

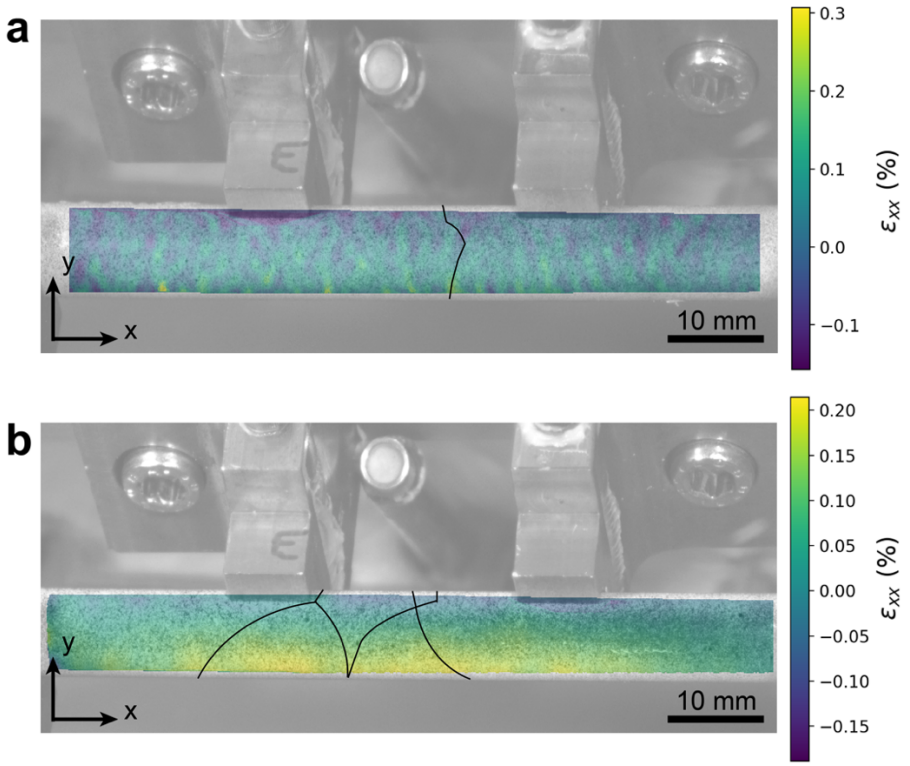

Figure 5.5. Spatial bending ε_{xx} strain (%) profile of (a) a representative alumina and (b) borosilicate tube immediately prior to fracture with the overlaid corresponding fracture patterns in black.

Table 5.3. Summary of alumina and borosilicate glass experimental properties. Expected values derive from the retailer McMaster-Carr and literature [36–38].

Specimen ID	Material	l_U (mm)	l_L (mm)	Expected Young's Modulus (GPa)	Young's Modulus (GPa)	Expected Fracture Strength (MPa)	Fracture Strength (MPa)	Failure Strain (%)
A_01	Alumina	34	100	340-370	358	210-350	252	0.062
A_02	Alumina	34	100	340-370	382	210-350	279	0.065
A_03	Alumina	34	100	340-370	389	210-350	281	0.067
A_04	Alumina	50	100	340-370	366	210-350	351	0.095
A_05	Alumina	50	100	340-370	372	210-350	353	0.086
A_06	Alumina	50	100	340-370	363	210-350	353	0.093
B_01	Borosilicate	34	100	60-65	62	69-340	116	0.155
B_02	Borosilicate	34	100	60-65	61	69-340	145	0.198
B_03	Borosilicate	34	100	60-65	56	69-340	121	0.187
B_04	Borosilicate	50	100	60-65	61	69-340	129	0.181
B_05	Borosilicate	50	100	60-65	62	69-340	117	0.165
B_06	Borosilicate	50	100	60-65	61	69-340	136	0.188

The brittle fracture nature of both alumina and borosilicate specimens is best illustrated in the stress-strain, normalized cumulative acoustic energy (NC-AE), and helium leak rate plots (Figure 5.6). The stress-strain plots indicate only a linear, elastic regime before an abrupt fracture, supported by the occurrence of a single acoustic event at fracture. Despite some noise, generally $<10^{-6}$ mbar l/s, leak rate data also indicated a single event. It comes as no surprise that the alumina and borosilicate specimens failed by fast fracture where onset of cracking immediately propagated to relieve all stress and release all pressurized gas at once. While the sharp acoustic profile would seemingly indicate a concentrated crack network as observed on alumina (Figure 5.5a), borosilicate specimens tended to shatter (Figure 5.5b) with a network of cracks spanning out along the length of the specimens. We note the fracture patterns of the borosilicate specimens closely resembled those depicted in ASTM C1684-18, where initial fracture occurs at the bottom of the "V-like" intersection of the fracture line with the region of maximum tensile strain seen in Figure 5.5b.

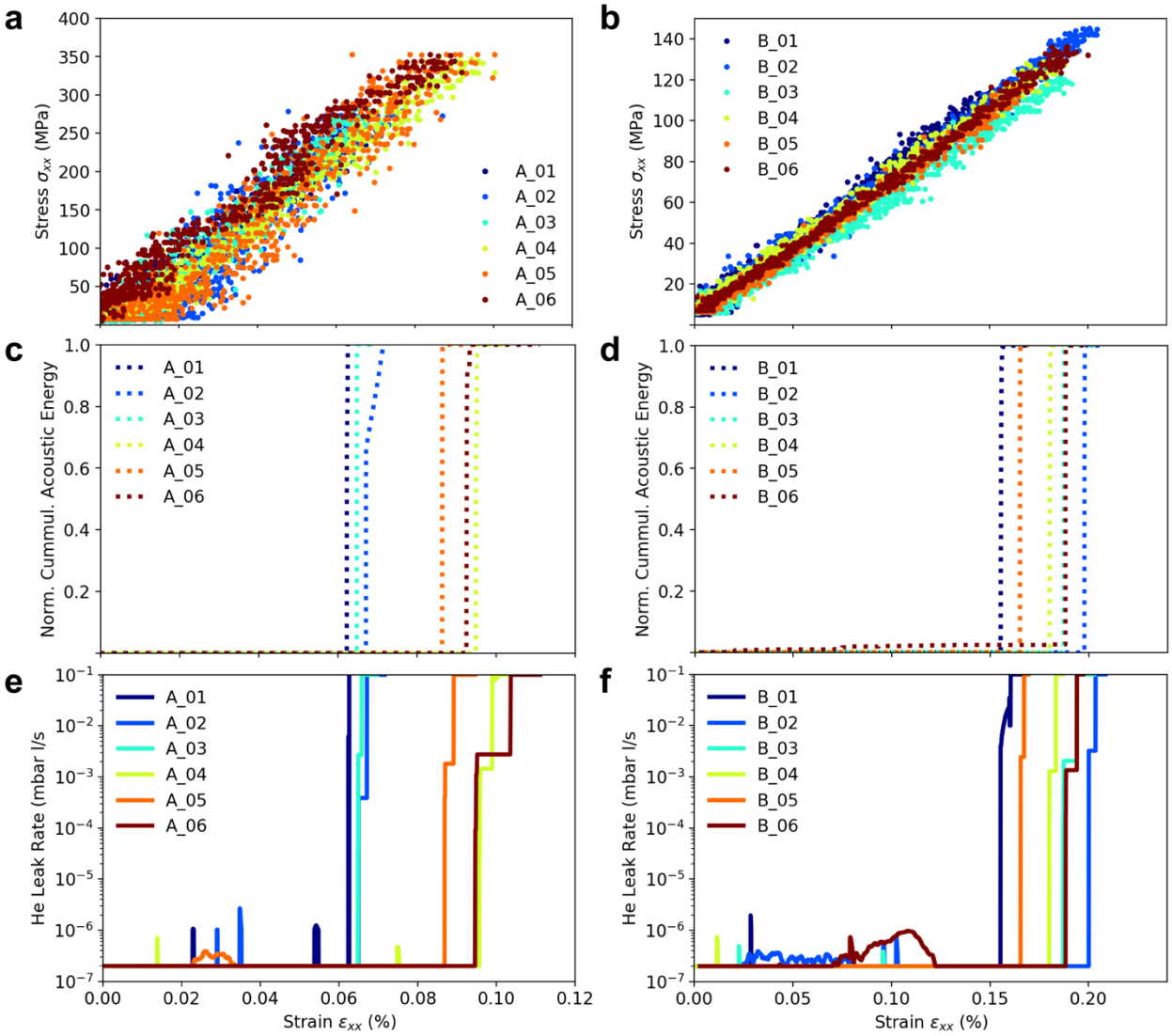

Figure 5.6. (a,b) Stress-strain curves, (c,d) NC-AE, and (e,f) leak rate over increasing strain of all alumina (left) and borosilicate glass tubes (right), covering two span distances/ratios.

The critical finding of the testing on alumina and borosilicate specimens is that the sensors and the analysis procedures developed were capable of capturing the fast fracture event of brittle ceramics. Furthermore, the initial fracture locations of all 12 brittle specimens occurred well within the inner bending zone, indicating a high repeatability of successful tests. Therefore, this methodology is more than adequate to reliably capture the prolonged fracture events of CMC failure.

4.3. SiC/SiC CMC

Three CMC specimens were tested; CMC_01 and CMC_03 were tested until complete loss of load bearing capability, and CMC_02 was tested until significant leaking was detected. Future testing is being conducted to characterize the damage mechanisms of these specimens, but here, we can assess the capability of the test methodology to capture certain mechanisms and stages in the progression of CMC failure. As previously described, stress-strain curves were generated for each specimen to derive the modulus, fracture strength, and DFLS values reported in Table 5.4. All specimens were found to have a modulus and fracture strength within establish literature trends, but a direct comparison is impossible without an identical architecture. DFLS values occurred for all three specimens around the same point, 0.04 to 0.05 % strain.

Table 5.4. Summary of CMC experimental properties and literature properties [5,14,39,40].

Specimen ID	Material	l_U (mm)	l_L (mm)	Expected Young's Modulus (GPa)	Young's Modulus (GPa)	Expected Fracture Strength (MPa)	Fracture Strength (MPa)	DFL Stress (MPa)	DFL Strain (%)
CMC_01	SiC/SiC	42	84	230-250	238	220-300	178	139	0.043
CMC_02	SiC/SiC	42	84	230-250	265	220-300	N/A	162	0.055
CMC_03	SiC/SiC	42	84	230-250	260	220-300	265	132	0.043

Figure 5.7 presents the DIC strain profiles immediately prior to the test end; these show the full range of recorded strains without the 90th percentile filter. Within these profiles, multiple, large strain concentrations immediately stand out, reaching upwards from the underside of the specimens. These large strain concentrations along the tube surface correspond to crack opening and are not respective of the true bending of the tube; such strain due to crack opening will be referred to as pseudo-strains. Since they are more a measure of crack opening and not material strain, the pseudo-strains were removed from the stress-strain data analysis via a threshold filter as described in Section 2.3.

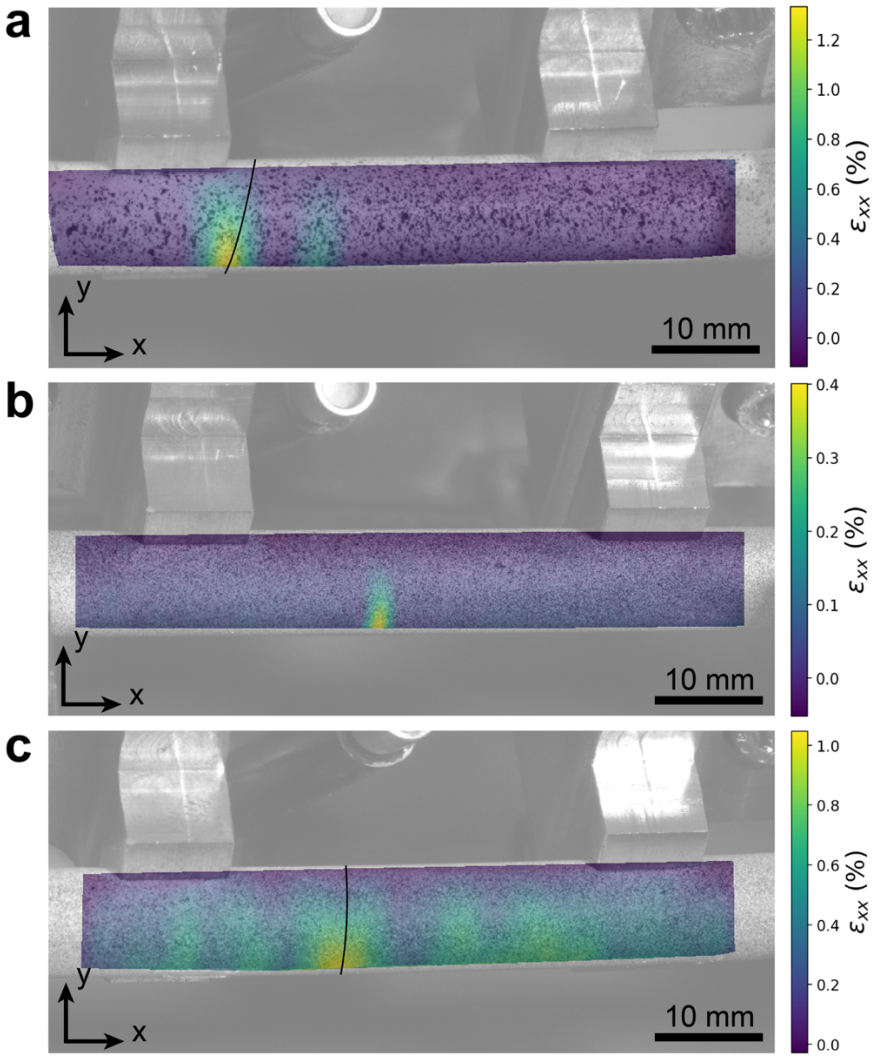

Figure 5.7. Strain bending profiles for all three CMC specimens, showing immediately prior to (a) loss of load-bearing capability for CMC_01, (b) initial helium leakage of CMC_02, and (c) loss of load-bearing capability for CMC_03. Location of final fracture marked in black. Note varied color scales.

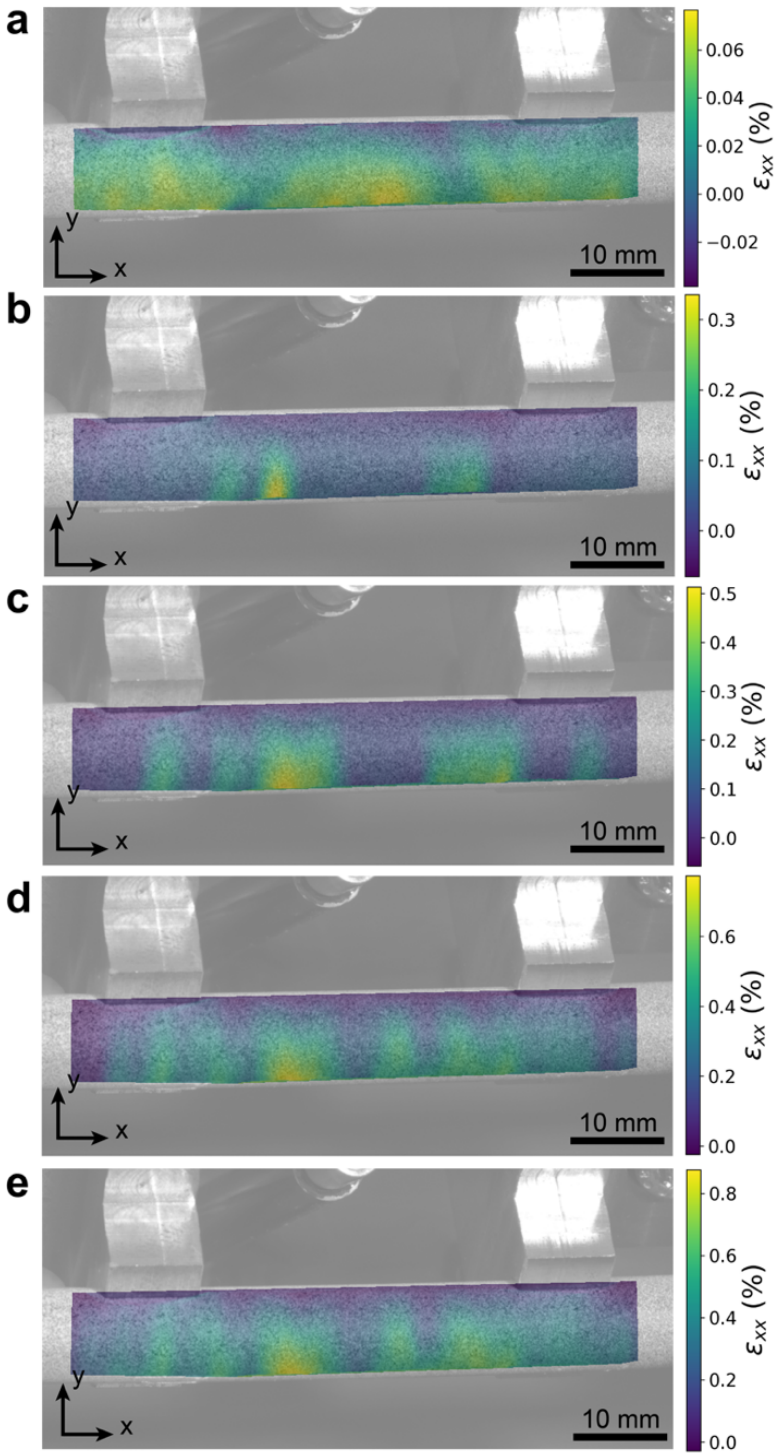

Figure 5.8. Strain bending profile of CMC_03 (a) at the onset of increased NC-AE, (b) at the onset of increased helium leak rate, (c) at the first large increase of helium leak rate, (d) at the second large increase of helium leak rate, (e) at the third large increase of helium leak rate up to sensor saturation. Note varied color scales and strain ranges are without the 90th percentile filter.

All specimens cracked within the bending zone, but specimens CMC_01 and CMC_02 exhibited one or two prominent cracks while CMC_03 showcased a distribution of cracks down the bending zone. Looking closely at the buildup of strain within CMC_03 (Figure 5.8), it is possible to see the Euler-Bernoulli profile early in the test before acoustic activity; corresponding stress-strain locations of the images seen in Figure 5.8 are labeled in Figure 5.9a. As acoustic events were detected, pseudo-strain concentrations grew along the bending zone, indicating that cracking had initiated (Figure 5.8a). Eventually, the cracks penetrated the matrix, forming a narrow channel for gas to begin to slowly escape (Figure 5.8b). The progressive increase in deformation opened up more cracks and widened any penetrating cracks, initiating the first, large jump in helium leak rate around 0.09% bending strain (Figure 5.8c). Two more sequential jumps in helium leak rate (Figure 5.8d,e) were caused by additional crack opening before final loss of load-bearing capacity of CMC_03.

The elastic response of each CMC specimen aligned well (Figure 5.9a), but the continued response beyond the DFLS highlighted the differences between the specimens. CMC_02, which was removed at the onset of leaking, only achieved a strain just past the DFLS. CMC_01 obtained a slightly higher strain, but CMC_03 achieved the highest strength and strain before fracture. From AE (Figure 5.9b), it is clear that the DFLS point occurs nearly concurrent with the onset of acoustic activity (0.042 %), signaling that these acoustic events correspond to matrix microcracking and the transfer of load to the fiber tows. Leaking from CMC_01 began shortly after the DFLS point as well, corresponding to 0.043 % strain but was delayed for CMC_02 and CMC_03 at 0.069 % and 0.090 % strains, respectively. The delayed leaking of CMC_03 is an interesting behavior that likely stems from the more distributed cracking behavior seen for this CMC and warrants more investigation.

Of the two specimens taken to load bearing capability, the acoustic and leak data trends are quite distinct. For CMC_01, the buildup of acoustic and leak rate data followed the same trend, occurring in stages and associated with onset of matrix microcracking and initial leaking, the onset of fiber cracking and opening of matrix channels, and the final fracture of the tows. In contrast, the leak rate of CMC_03 followed a similar three-stage trend, but the buildup of acoustic activity was much more linear without any distinct

stages. This linear increase of acoustic activity reflects the greater occurrence of cracks down the length of the bending. From the higher fracture strain of CMC_03, it is apparent that the uniform distribution of cracks effectively distributes stresses. Furthermore, the early leaking of CMC_01 indicates the possibility of a flaw, which may have propagated fracture near the inside of an upper loading support; the mechanistic cause of the difference between specimens is being investigated as part of an ongoing study.

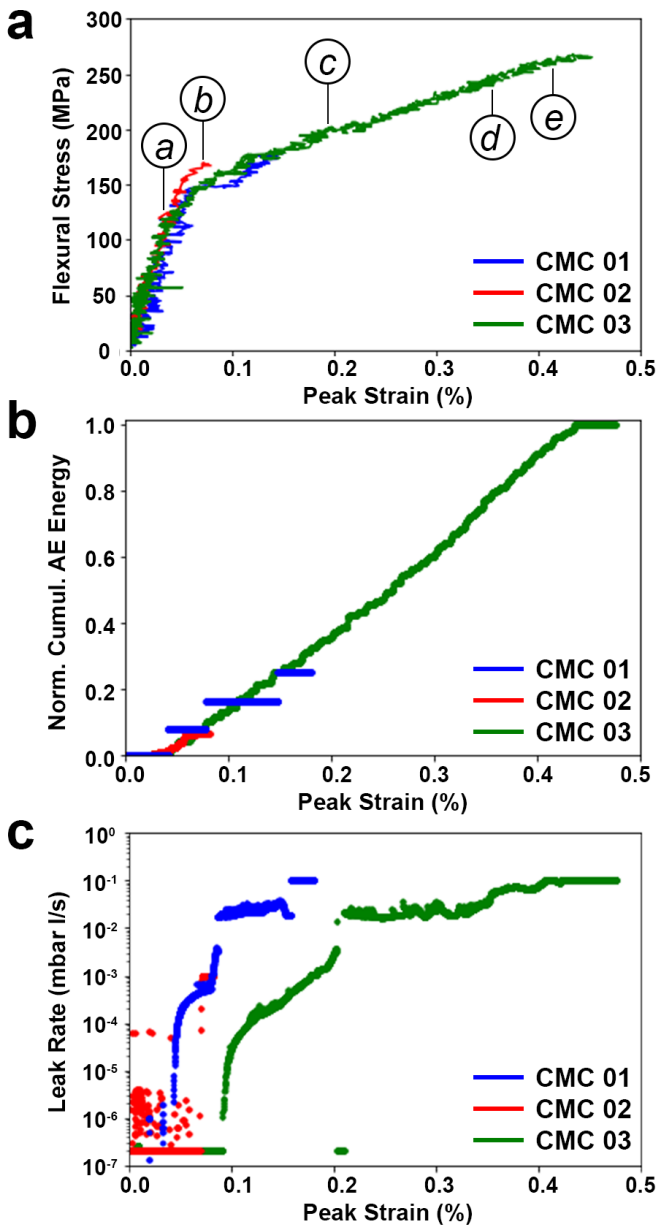

Figure 5.9. (a) Four-point bending stress-strain curves, (b) AE, and (c) helium leak rate response over bending strain of CMC tubes. The circled lettering corresponds directly to the labeled strain profiles seen in Figure 5.8.

5. *Discussion*

The CMC results highlight the strength of this methodology to correlate load, strain, acoustic emissions, and leak rate together. Thus, it is possible to readily determine how key sequential events occur. It must be noted that this study neglects the effects of fuel pellets on the failure mechanisms of the cladding; pellet expansion and mechanical contact with the cladding will certainly affect local stress states within the cladding and thus impact the failure mechanisms [41,42]. This effect should be addressed in future testing, but in this study, the focus remained the failure mechanisms of the CMC cladding alone. Here, this test methodology tracked the onset of matrix microcracking, the initiation of through-matrix cracks causing leaking, the transfer of stress from the matrix to the fibers as matrix cracking progresses, and finally, fracture of the fiber tows themselves leading to loss of all load bearing capability. Importantly, the test setup minimized any contact induced damage to the tubes, which might have an effect on the recorded mechanical performance. The CMCs were visually inspected before and after testing. SEM inspection (Figure 5.10) of the fracture regions and cradle contact points confirmed that the custom-fitted cradles performed as designed and did not crush or damage the specimen at the contact points during loading.

These experiments and simple finite element simulations demonstrate that this DIC/AE four-point bend, hermeticity test methodology is effective for both ductile and brittle materials. All nonmetal materials failed with a strain of less than 0.5 % (Figure 5.11a). Of these materials, the CMC achieved the largest bending strain at failure, demonstrating the role of CMC architecture on improved toughness compared to conventional ceramics and glasses. Together, alumina and borosilicate glass specimens demonstrated the rapid response and accuracy of DIC, AE, and leak rate measurements. Steel specimens revealed the capability of the custom bending fixture to reliably handle larger strains without inducing unwanted constrains or contact damage. Properties from McMaster-Carr and literature [43] were used to compare the failure strain of the steel specimens to the ceramic specimens, but we note again that accommodations to the setup and possibly specimen dimensions would be necessary to extend the range of pure bending. Furthermore, ductile materials like steel are unlikely to fracture under bending.

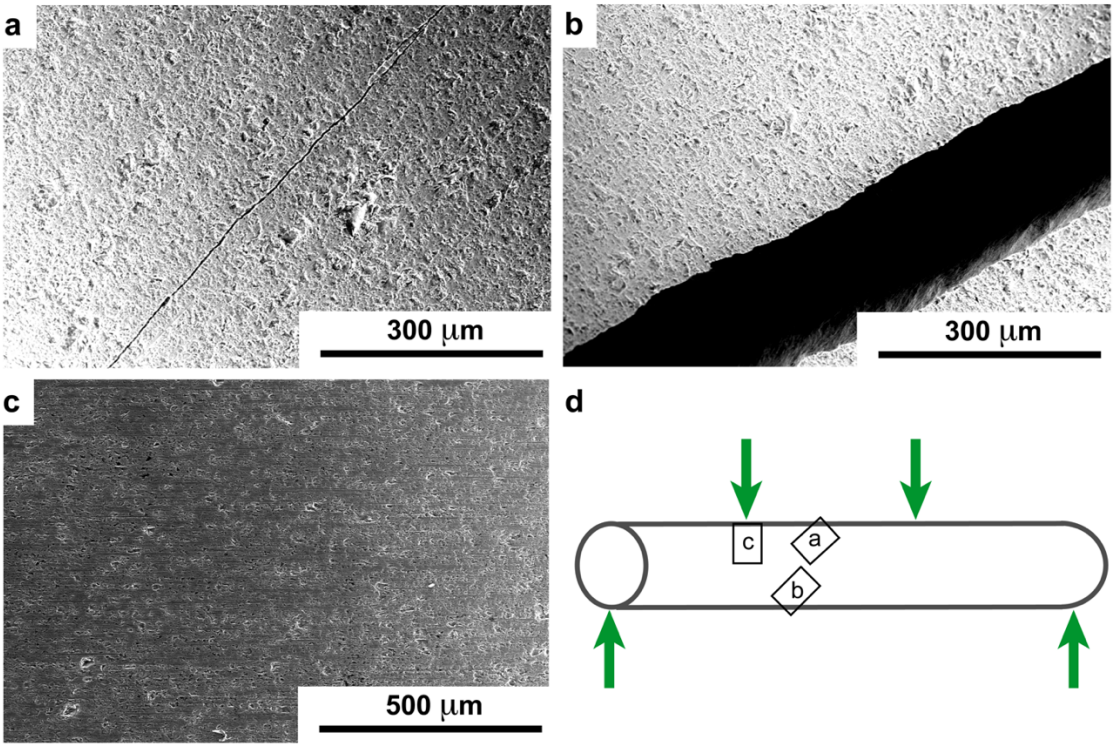

Figure 5.10. SEM micrographs of CMC_01, showing the specimen outer surface at (a) the crack running through the compressive region and (b) the crack widening through the tensile region. (c) No damage was observed under the cradles. (d) Schematic of the locations of each image on the specimen relative to loading points.

While the CMCs exhibited a larger fracture strain than the other ceramics, the CMCs experienced loss of hermeticity earlier than either alumina or borosilicate glass (Figure 5.11b). This disparity between strain at loss of hermeticity and final fracture represents a key advantage of CMCs over monolithic ceramics and highlights the complicated failure mechanisms governing CMC degradation. Alumina and borosilicate specimens lost hermeticity and load-bearing capability in a sudden fracture event; the CMCs retained some load-bearing capability after loss of hermeticity until larger strains. In fact, it was observed in the case of CMC_02 that the leak rate dropped upon unloading, suggesting that the cracks and channels created at the point of loss of hermeticity may close, allowing the tube to re-seal when load is relieved. Thus, it was postulated that the cracks and channels within the CMC allowing gas to escape were contained within the matrix as the fibers bore the load. As the load increased and the fibers began to break, the CMC passed a

point where cracks did not fully close to re-obtain a hermetic seal even when load was removed; this response was noted with CMC_01 and CMC_03.

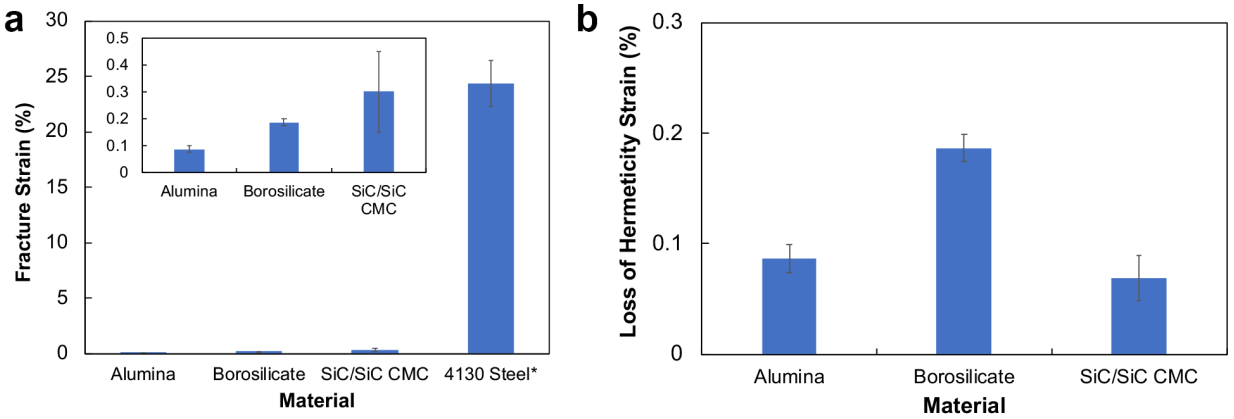

Figure 5.11. (a) The fracture strain and (b) loss of hermeticity strain of alumina, borosilicate, and SiC/SiC CMC as measured in this study compared with that of commonly observed in 4130 steel [43], showing the significant disparity in mechanical response between ceramic and ductile materials.

Together, the hermeticity and fracture response of the CMCs illuminated in these bending experiments (Figure 5.12) fits well within previously described failure behavior as governed by CMC architecture [5,30,39]. This behavior appears to fit into four stages. Initially, the CMC cladding bears the strain without damage until a point between 0.04 to 0.06 % strain when the matrix begins to crack and transfer load to the fiber tows; this point marks the first stage of failure. It also corresponds to the DFLS location, indicating the onset of matrix cracking (Figure 5.12b). By a maximum of 0.09% strain, cracking is extensive enough to penetrate through the cladding, leading into the second stage, loss of gas tightness under load (Figure 5.12c). The range of strain values at key events between different specimens may be attributed to geometric differences and merits future scrutiny. It may be possible to retain hermeticity after this point if fiber tows have not yet begun to fracture, and load is relieved. If the load is not relieved and continues to increase, the fiber tows will begin to break, marking the third stage at which point it becomes impossible to fully close cracks even when load is reduced (Figure 5.12d). The fourth and final stage of failure is the point when the last fibers fail and lose all load bearing capability (Figure 5.12e). This behavior, however, suggests that

there may be two key metrics for future nuclear cladding application: (i) the strain at initial loss of gas tightness and (ii) the strain at which point the cladding can no longer recover hermeticity even when load is reduced.

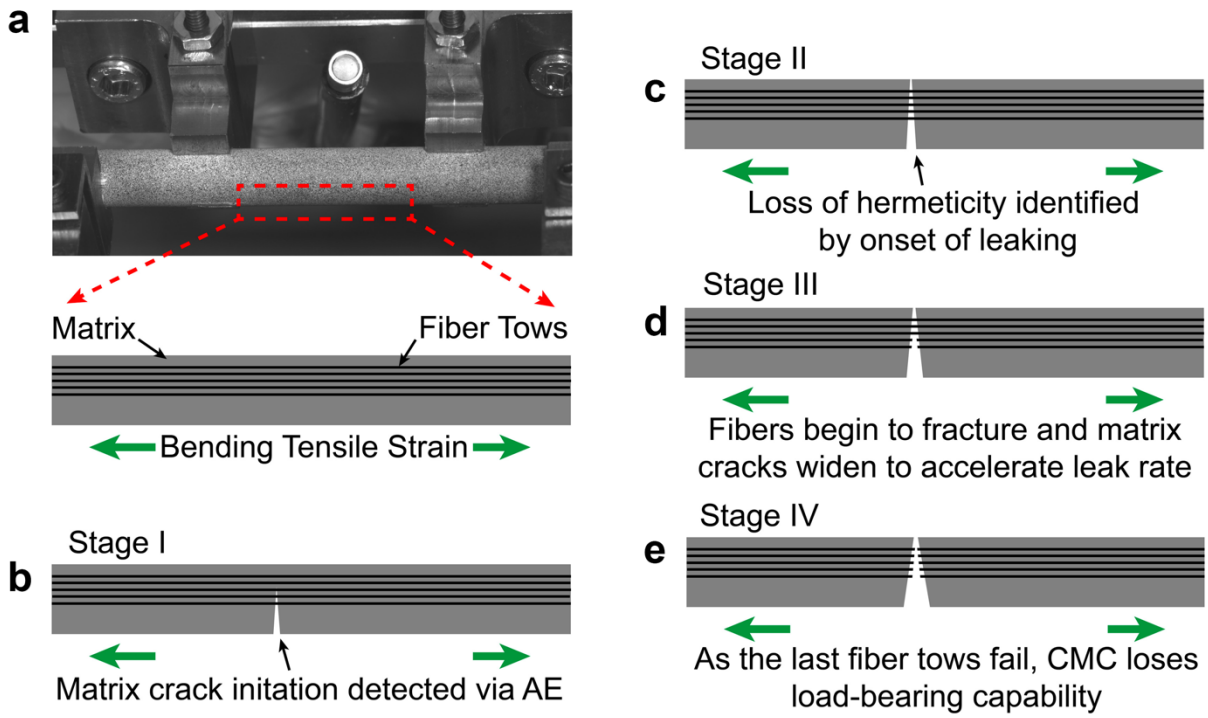

Figure 5.12. A schematic of the observable failure mechanisms of the CMC cladding. (a) The CMC structure undergoes stages of failure: (b) onset of matrix cracking, (c) loss of hermeticity, (d) fiber fracture, and (e) final fracture.

6. Conclusions

A DIC/AE enabled, *in-situ* hermeticity, four-point bend setup and methodology was presented to unveil critical fracture events for a variety of ceramic tubes, including prototypic nuclear-grade SiC/SiC fuel cladding CMC tubes currently under development. These samples were used for initial verification of this test setup, which integrated a triad of complementary sensors, including 3D-DIC, AE, and helium leak rate. The reliability and accuracy of this sensor suite, in combination with our unique four-point bend setup, was demonstrated on both ductile and brittle tubes with established mechanical properties. Conventional stress-strain curves and properties were calculated from an Euler-Bernoulli beam-in-bending formulation and

presented for alumina, borosilicate glass, 4130 steel, and SiC-SiC CMCs tubes, including results for multiple four-point support spans (l_U/l_L= 42/84, 50/100 and 34/100 mm/mm), which all agreed well with expected values. The fast, singular fracture events of alumina and borosilicate glass demonstrated the accuracy and quick response time of our setup and correlation technique. The ductility of 4130 steel tubes and a replicating numerical finite element model were used to confirm the validity and minimization of contact strain concentrations of our setup past strains typically exhibited by CMCs. Of urgent concern to the nuclear industry, the spatial strains at critical fracture events could be investigated for CMC fuel cladding tubes, including the onset of matrix cracking, loss of hermitic seal, and loss of load-bearing capability. Matrix cracking was well defined by the DFLS at strains ranging from 0.04 - 0.06 % and was shortly followed by initial loss of hermetic seal by 0.09 % bending strain. Leaking increased in distinct steps over a span of 0.1- 0.2 % bending strain and intermediate results indicate that prior to fiber fracture, it might be possible to regain hermeticity upon unloading. The slower, stepped progression of NC-AE events and He leak rate demonstrate the gentler, delayed failure behavior characteristic of CMCs over four distinct steps. This technique was developed to progress the standardization of a test methodology for such critical nuclear reactor components and to resolve the mechanisms that control these distinct steps of CMC failure.

7. References

[1] M. Hirano, T. Yonomoto, M. Ishigaki, N. Watanabe, Y. Maruyama, Y. Sibamoto, T. Watanabe, K. Moriyama, Insights from review and analysis of the Fukushima Dai-ichi accident, J. Nucl. Sci. Technol. 49 (2012) 1–17. doi:10.1080/18811248.2011.636538.

[2] Z. Karoutas, J. Brown, A. Atwood, L. Hallstadius, E. Lahoda, S. Ray, J. Bradfute, The maturing of nuclear fuel: Past to Accident Tolerant Fuel, Prog. Nucl. Energy. 102 (2018) 68–78. doi:10.1016/j.pnucene.2017.07.016.

[3] M. Kurata, Research and development methodology for practical use of accident tolerant fuel in light water reactors, Nucl. Eng. Technol. 48 (2016) 26–32. doi:10.1016/j.net.2015.12.004.

[4] P. Yvon, F. Carré, Structural materials challenges for advanced reactor systems, J. Nucl. Mater. 385 (2009) 217–222. doi:10.1016/j.jnucmat.2008.11.026.

[5] C.P. Deck, G.M. Jacobsen, J. Sheeder, O. Gutierrez, J. Zhang, J. Stone, H.E. Khalifa, C.A. Back, Characterization of SiC-SiC composites for accident tolerant fuel cladding, J. Nucl. Mater. 466 (2015) 1–15. doi:10.1016/j.jnucmat.2015.08.020.

[6] G.N. Morscher, V. V. Pujar, Design guidelines for in-plane mechanical properties of SiC fiber-reinforced melt-infiltrated SiC composites, Int. J. Appl. Ceram. Technol. 6 (2009) 151–163. doi:10.1111/j.1744-7402.2008.02331.x.

[7] J.Z. Gyekenyesi, N.P. Bansal, High Temperature Tensile Properties of Unidirectional Hi-Nicalon/Celsian Composites In Air, 2000. https://ntrs.nasa.gov/archive/nasa/casi.ntrs.nasa.gov/20000085860.pdf (accessed May 25, 2017).

[8] M.N. Rossol, V.P. Rajan, F.W. Zok, Effects of weave architecture on mechanical response of 2D ceramic composites, Compos. Part A Appl. Sci. Manuf. 74 (2015) 141–152. doi:10.1016/j.compositesa.2015.04.003.

[9] B.P. Croom, P. Xu, E.J. Lahoda, C.P. Deck, X. Li, Quantifying the three-dimensional damage and stress redistribution mechanisms of braided SiC/SiC composites by in situ volumetric digital image correlation, Scr. Mater. 130 (2017) 238–241. doi:10.1016/j.scriptamat.2016.12.021.

[10] V. V. Vasiliev, E. V. Morozov, Composite pressure vessels, in: Adv. Mech. Compos. Mater. Struct., 4th ed., Elsevier, 2018: pp. 787–821. doi:10.1016/B978-0-08-102209-2.00012-8.

[11] D. Ding, Processing, properties and applications of ceramic matrix composites, SiCf/SiC: an overview, in: I.M. Low (Ed.), Adv. Ceram. Matrix Compos., 2nd ed., Woodhead Publishing, 2014: pp. 9–26. doi:10.1016/C2016-0-03477-0.

[12] O.I. Isaac M. Daniel, Engineering mechanics of composite materials, 2nd ed., Oxford University Press, New York, 2006.

[13] Y. Katoh, X. Hu, T. Koyanagi, G.P. Singh, Determination of He and D permeability of neutron-irradiated SiC tubes to examine the potential for release due to micro-cracking, 2017. doi:10.2172/1394374.

[14] G. Singh, S.T. Gonczy, C.P. Deck, E. Lara-Curzio, Y. Katoh, Interlaboratory round robin study on axial tensile properties of SiC-SiC CMC tubular test specimens, Int. J. Appl. Ceram. Technol. (2018) 1–16. doi:10.1111/ijac.13010.

[15] H. Wang, J.A.J. Wang, T. Tan, H. Jiang, T.S. Cox, R.L. Howard, B.B. Bevard, M. Flanagan, Development of U-frame bending system for studying the vibration integrity of spent nuclear fuel, J. Nucl. Mater. 440 (2013) 201–213. doi:10.1016/j.jnucmat.2013.05.009.

[16] J.J.A. Wang, H. Wang, T. Tan, Reversal bending fatigue testing, US8863585, 2014.

[17] J.J.A. Wang, H. Wang, T. Tan, H. Jiang, T. Cox, Y. Yan, Progress letter report on U-frame test setup and bending fatigue test for vibration integrity study, Oak Ridge, TN, 2011.

[18] I.J. van Rooyen, W.R. Lloyd, T.L. Trowbridge, S.R. Novascone, K.J. Wendt, I.J. Van Rooyen, T.L. Trowbridge, S.R. Novascone, K.J. Wendt, S.M. Bragg-Sitton, SiC-CMC-Zircaloy-4 nuclear fuel cladding performance during 4- point tubular bend testing, LWR Fuel Perform. Meet. Fuel 2013. (2013).

[19] M.L. Vinogradov, V.T. Barchenko, Measurement of the gas permeation through the composite materials, (2015) 40–44. doi:10.1109/eiconrusnw.2015.7102228.

[20] G.D. Quinn, B.T. Sparenberg, P. Koshy, L.K. Ives, S. Jahanmir, D.D. Arola, Flexural strength of ceramic and glass rods, J. Test. Eval. 37 (2009) 222–244. doi:10.1520/JTE101649.

[21] N.J. Pagano, J.M. Whitney, Geometric design of composite cylindrical characterization specimens, J. Compos. Mater. 4 (1970) 360–378. doi:10.1177/002199837000400307.

[22] J.M. Whitney, G.C. Grimes, P.H. Francis, Effect of end attachment on the strength of fiber-reinforced composite cylinders, Exp. Mech. 13 (2006) 185–192. doi:10.1007/bf02322651.

[23] M.A. Sutton, J. Yan, X. Deng, C.-S. Cheng, P. Zavattieri, Three-dimensional digital image correlation to quantify deformation and crack-opening displacement in ductile aluminum under mixed-mode I/III loading, Opt. Eng. 46 (2007) 051003. doi:10.1117/1.2741279.

[24] H. Schreier, J.J. Orteu, M.A. Sutton, Image correlation for shape, motion and deformation measurements: Basic concepts, theory and applications, Springer US, 2009. doi:10.1007/978-0-387-78747-3.

[25] V.P. Rajan, M.N. Rossol, F.W. Zok, Optimization of digital image correlation for high-resolution strain mapping of ceramic composites, Exp. Mech. 52 (2012) 1407–1421. doi:10.1007/s11340-012-9617-1.

[26] R. Ghorbani, F. Matta, M.A. Sutton, Full-field deformation measurement and crack mapping on confined masonry walls using digital image correlation, Exp. Mech. 55 (2014) 227–243. doi:10.1007/s11340-014-9906-y.

[27] G. Ojard, D. Goberman, J. Holowczak, Acoustic emission as a screening tool for ceramic matrix composites, AIP Conf. Proc. 1806 (2017). doi:10.1063/1.4974568.

[28] E. Munch, L. Duisabeau, M. Fregonese, L. Fournier, Acoustic emission detection of environmentally assisted cracking in Zircaloy-4 alloy, EUROCORR 2004. 36 (2004). http://www.iaea.org/inis/collection/NCLCollectionStore/_Public/36/105/36105030.pdf.

[29] Z. Kral, W. Horn, J. Steck, Crack propagation analysis using acoustic emission sensors for structural health monitoring systems, Sci. World J. 2013 (2013). doi:10.1155/2013/823603.

[30] G.N. Morscher, H.M. Yun, J.A. Dicarlo, In-plane cracking behavior and ultimate strength for 2D woven and braided melt-infiltrated SiC/SiC composites tensile loaded in off-axis fiber directions, J. Am. Ceram. Soc. 90 (2007) 3185–3193. doi:10.1111/j.1551-2916.2007.01887.x.

[31] G. Morscher, J. Gyekenyesi, Room temperature tensile behavior and damage accumulation of Hi-Nicalon reinforced SiC matrix composites, 22nd Annu. Conf. Compos. Adv. Ceram. Mater. Struct. (2009). https://ntrs.nasa.gov/archive/nasa/casi.ntrs.nasa.gov/19980237335.pdf (accessed November 9, 2017).

[32] G.N. Morscher, Modal acoustic emission source determination in silicon carbide matrix composites, AIP Conf. Proc. 509 (2000). doi:10.1063/1.1306075.

[33] D.P. Holmes, Mechanics of Materials: Bending - Normal Stress, Bost. Univ. Mech. Eng. Mech. Slender Struct. (2018). https://www.bu.edu/moss/mechanics-of-materials-bending-normal-stress/ (accessed October 28, 2018).

[34] S. Timoshenko, History of Strength of Materials, McGraw-Hill, New York, 1953.

[35] C.H. Bumgardner, F.M. Heim, D.C. Roache, A.I. Jarama, P. Xu, R. Lu, E.J. Lahoda, B.P. Croom, C.P. Deck, X. Li, Unveiling hermetic failure of ceramic tubes by digital image correlation and acoustic emission, J. Am. Ceram. Soc. 103 (2020) 2146–2159. doi:10.1111/jace.16854.

[36] P. Auerkari, Mechanical and physical properties of engineering alumina ceramics, 1996. http://www.vtt.fi/inf/pdf/tiedotteet/1996/T1792.pdf (accessed April 16, 2018).

[37] M. Asmani, C. Kermel, A. Leriche, M. Ourak, Influence of porosity on Youngs modulus and poisson's ratio in alumina ceramics, J. Eur. Ceram. Soc. 21 (2001) 1081–1086. doi:10.1016/S0955-2219(00)00314-9.

[38] X. Nie, W.W. Chen, A.A. Wereszczak, D.W. Templeton, Effect of loading rate and surface conditions on the flexural strength of borosilicate glass, J. Am. Ceram. Soc. 92 (2009) 1287–1295. doi:10.1111/j.1551-2916.2009.03019.x.

[39] F. Bernachy-Barbe, L. Gélébart, M. Bornert, J. Crépin, C. Sauder, Anisotropic damage behavior of SiC/SiC composite tubes: multiaxial testing and damage characterization, Compos. Part A Appl. Sci. Manuf. 76 (2015) 281–288. doi:10.1016/J.COMPOSITESA.2015.04.022.

[40] E. Rohmer, E. Martin, C. Lorrette, Mechanical properties of SiC/SiC braided tubes for fuel cladding, J. Nucl. Mater. 453 (2014) 16–21. doi:10.1016/J.JNUCMAT.2014.06.035.

[41] J.T.A. Roberts, E. Smith, N. Fuhrman, D. Cubicciotti, On the pellet-cladding interaction phenomenon, Nucl. Technol. 35 (1977) 131–144. doi:10.13182/NT77-A31856.

[42] J.H. Gittus, D.A. Howl, H. Hughes, Theoretical analysis of cladding stresses and strains produced by expansion of cracked fuel pellets, Nucl. Appl. Technol. 9 (1970) 40–46. doi:10.13182/NT70-A28726.

[43] H. Carpenter, Alloy steels their manufacture, properties, and uses, J. R. Soc. Arts. 76 (1928) 278–297.

CHAPTER 6: CHARACTERIZING ENVIRONMENT-DEPENDENT FRACTURE MECHANISMS OF CERAMIC MATRIX COMPOSITES VIA DIGITAL IMAGE CORRELATION

1. Introduction

For multiple energy applications, most prominently high temperature aerospace and harsh environment nuclear fuel applications, silicon carbon fiber / silicon carbide ceramic matrix composites (SiC/SiC CMCs) are highly attractive materials due to their thermal stability, corrosion resistance, and irradiation stability [1–6]. Monolith SiC is very brittle, which would seemingly restrict its engineering applications [7]. However, SiC/SiC CMCs possess an engineered architecture of woven or braided ceramic fiber tows infiltrated with a ceramic matrix to achieve a "pseudo-plastic" deformation response, enabling greater mechanical resilience than a monolith ceramic. As the ceramic matrix begins to fail, it cracks to relieve stress, but rather than fail rapidly like a monolith ceramic, the load is instead redistributed to the fiber tows. Thus, the CMC can sustain continued loading and deformation. This behavior is enabled by the tailoring of the fiber/matrix interface, either with a pyrolytic carbon or boron nitride coating, which helps to deflect or arrest crack growth within the matrix from directly propagating to the fibers [8–11].

With these properties, CMCs would serve in mission-critical roles, such as gas turbine shroud and combustor components [12] and as nuclear fuel claddings [13]. As a result, CMCs have been rigorously tested and evaluated to elucidate pertinent degradation and failure mechanisms for these applications. Numerous studies have examined the mechanical performance of CMCs via tensile [11,14–16] and flexural testing [17,18]. Conventional mechanical test methodologies, such as those described by ASTM C1275 and C1684, rely on displacement-based measurements to calculate specimen strain, such as extensometers and strain gauges [10,11,19,20]; however, these techniques do not distinguish non-uniform or local strain concentrations. Thus, these techniques fail to address the effect of strains concentrated within the matrix or fiber tows [21] and overrepresent material deformation by incorporating pseudo-strains due to crack opening displacement (COD).

Fracture within a CMC is associated with critical stages of material failure, and thus, it is important to derive precise measurements and distinctions between actual deformation and strain of the material against

pseudo-strains. For example, it has been noted that the onset of matrix microcracking and load transfer to the fiber tows is associated with the proportional limit point (PLS) or deviation from linearity (DFL) [14,16]. Fracture within the matrix can also jeopardize the hermeticity or gas-tightness of the CMC; in nuclear fuel applications, loss of hermeticity would represent a dangerous threshold at which point radioactive gases could escape the fuel cladding [17,22,23]. Furthermore, microcracks through the matrix create channels for oxygen or other environmental gas ingression, which can lead to oxidation of CMC constituents, particularly the fiber interfacial coating. Environmentally-assisted crack growth can lead to composite embrittlement and microcracking at low stress levels as has been demonstrated in standard air and even inert environments [19,20,24]. Thus, it is critical to capture microcracking events during mechanical testing to detect anomalies like subcritical crack growth or loss of hermeticity.

Unlike conventional extensometers and strain gauges, digital image correlation (DIC) provides full-field, spatial displacement and strain fields during mechanical testing by tracking optical images of the specimen and quantifying deformation relative to a reference image [25,26]. Full field DIC techniques are thus well suited to resolve local discontinuities, such as local pseudostrain concentrations due to COD [27,28]. In preparation for DIC, the specimen is treated with a high contrast speckle pattern. However, the capability of DIC to detect microcracks is dependent on several factors: camera resolution, field-of-view, subset size, and speckle size. Ideally, the camera should be positioned as close to the sample as possible to enhance the resolution of the test gage section. Speckles should then be sized to be approximately two to four pixels in diameter. The subset then must be sized to contain a distinct field of speckles, three to five, for accurate tracking and correlation [25,26,29,30]. These parameters impose practical limitations on the accuracy of DIC measurements and the detectable crack size.

In-situ DIC techniques have been used to study the deformation and fracture of CMCs. Work by Bernachy-Barbe, *et al*. demonstrated local deformation and cracks across individual fiber tows in an investigation of the role of tow interfaces, spacing, and configuration effects on that deformation fracture [28]. Whitlow, *et al*. examined a larger strain field across the full test gage section of CMC specimens under a tensile load, showing concentrations due to local porosity and eventually due to fracture [31].

Furthermore, high resolution DIC has been extended to CMCs via scanning electron microscopy (SEM) [14] and X-ray tomography (XCT) [32,33], which has unveiled microcracks within the tows and around individual fibers.

Here, we apply *in-situ* three-dimensional (3D-DIC) to characterize the degradation of SiC/SiC CMC tubes during bending and demonstrate a method to quantify fracture properties, such as COD and crack spacing, during deformation. We will also examine the environmental impact on CMC fracture via characterization of CMC specimens after exposure in various high temperature (1200°C) environments.

2. Experimental Methods

2.1. Materials

SiC/SiC CMC tubular specimens (Figure 6.1) were purchased from General Atomics, reproducing the dimensions of prototype nuclear fuel claddings, with an inner and outer diameter of 8.4 mm and 10.1 mm, respectively. The CMCs contained three plies of Hi-Nicalon type-S fibers in a diamond pattern biaxial braid (± 50° orientation); individual fibers were coated with a pyrolytic carbon interphase (approximately 100 to 150 nm thick). The fiber tows were completed with a chemical vapor infiltrated SiC matrix. An outer SiC layer was applied via chemical vapor deposition (CVD) [34].

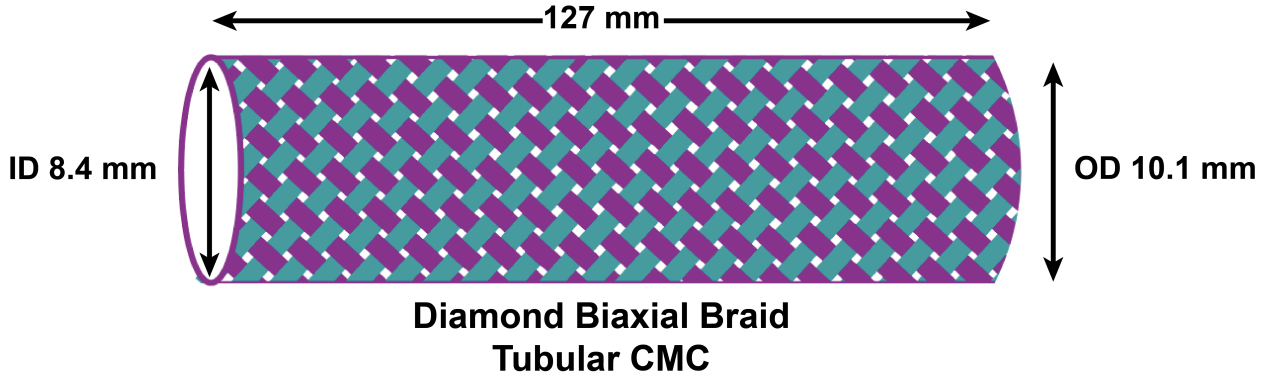

Figure 6.1. A schematic of the CMC tubular specimens used in this study. Not shown is the outer CVD SiC layer, which covers the braided architecture.

Specimens were subjected to one of four environments prior to mechanical testing: (A) no treatment, (B) 48 hours at 1200 °C in open air, (C) 48 hours at 1200 °C in vacuum, and (D) 48 hours at 1200 °C in helium. These environments are briefly summarized in Table 6.1. Specimen ends were left as cut and were not coated with CVD SiC. The mechanical performance of the specimens (A01 and A02) tested without a heat treatment were previewed in [35] along with tension testing of SiC/SiC CMC specimens. All temperature treatments were performed in a tube furnace (MTI Corporation GSL-1800X). Oxygen content within the tube furnace during conditions B and D was measured with an MTI Corporation Oxygen Analyzer. For condition D, the tube was first evacuated then a flow of helium (99.995% pure He) was introduced for the duration of the treatment; a low purity helium with relatively high oxygen content (~ 5 ppm) was selected to evaluate any oxidation effect. Two specimens were prepared per treatment and were designated, for condition A for example, as A01 and A02.

Table 6.1. The CMC specimen pre-experiment treatment environments.

Condition	A	B	C	D
Temperature	-	1200 °C	1200 °C	1200 °C
Duration	-	48 hours	48 hours	48 hours
Atmosphere	Open air	Open air	Vacuum	Helium
Oxygen Content	18.1 ± 2.2 % O_2	18.2 ± 2.2 % O_2	-	0.13 ± 0.02 % O_2

2.2. Mechanical Testing Methods

The flexural tests were all conducted at room temperature using the four-point bend apparatus developed by Bumgardner, Heim, *et al*. for investigating the hermetic failure of CMC tubes [17] and modeled after ASTM C1684-17. The test frame (Figure 6.2a) was configured using an Admet eXpert 2611 table top universal testing machine and Admet 1210AJ-2K-B, 8.9 kN load cell. Each CMC specimen was painted (Rustoleum matte spray paint) with a fine black-and-white speckle pattern for image correlation (Figure 6.2b). A gas inlet tube was inserted into one end of each specimen, and both ends of the tubular specimen were sealed with 3M Scotch-Weld 620 epoxy adhesive, creating a hermetic seal.

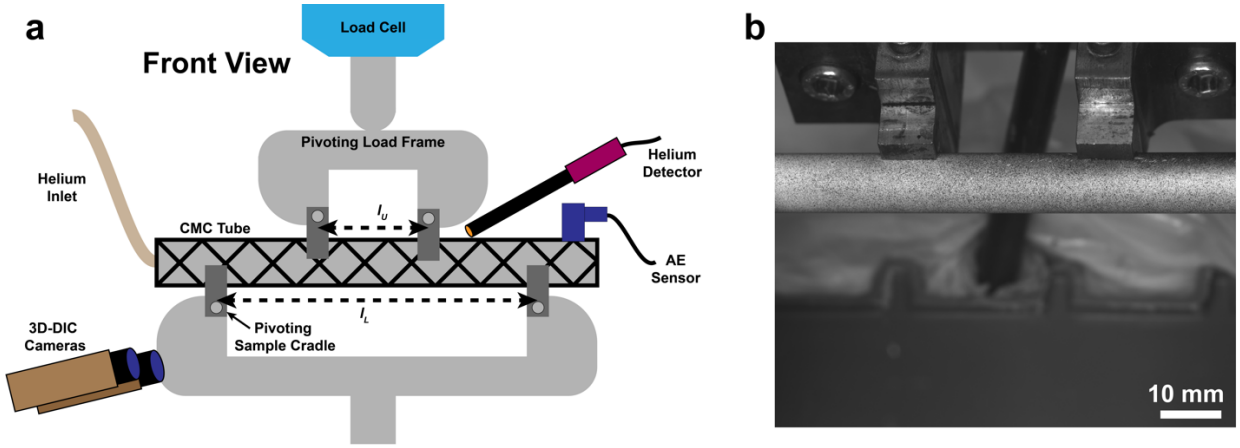

Figure 6.2. (a) A schematic of the four-point bend test frame as adapted from [17]. (b) An optical image of the sample loaded in the test frame, showing a representative field of view between the two lower pivoting cradles and of the applied speckle pattern.

Each specimen was loaded in the test frame. Load points were spaced such that $l_U/l_L = 34/100$ mm/mm (Figure 6.2a). Custom, pivoting cradles were machined to fit the outer diameter of the CMC tubes to prevent a local concentration of stress [17], which could otherwise promote subcritical cracking. Each specimen was loaded at a rate of 0.5 mm/min until complete failure of the tube, where failure was categorized as the point at which the specimen lost all load-bearing capability. Optical images were acquired during each test at a rate of 5 Hz using two FLIR Grasshopper 3 GS3-U3-50S5M-C digital CMOS cameras and Schneider 21-100197 35 mm compact lenses (Table 6.2). Acoustic emissions were recorded by a Mistras 1283 USB AE Node at a rate of 1 MHz with a threshold of 10 dB. This sensor was affixed to one end of the CMC specimen by an adjustable hose clamp.

In-situ leak detection was provided by an Inficon Protec P3000 Helium Sniffer Leak Detector, measuring leak rate at a rate of 10 Hz. A minimum leak rate of 10^{-7} mbar l/s, the lowest detector reading, was confirmed before each test to ensure ambient levels of helium would not adversely affect the test results. The leak detector had a response time of about 400 ms, so to ensure leak rate could be correlated with the mechanical strain due to loading, a stepped displacement profile was programmed in the universal testing machine. This displacement profile specified the crosshead would displace at a rate of 0.5 mm/min in 0.01

mm increments with a 2 second hold period, more than enough time for the leak detector to respond.

Select specimens were also imaged under SEM (FEI Quanta 650) with a circular backscatter detector (CBS) after testing with energy dispersive X-ray spectroscopy (EDS), probed with indentation (Micro Materials Ltd. Nanotest Vantage) to measure fracture toughness, and scanned with atomic force microscopy (Bruker Nano Inc. Dimension Icon).

2.3. DIC Data Processing and Crack Detection Methods

Table 6.2. Typical parameters for DIC analysis of strain data and crack detection used in this study.

DIC Configuration	Strain Computation	Crack Detection
Technique Used	2x Stereoscopic 3D Image Correlation	
Camera	2x FLIR Grasshopper 3 CMOS	
Lens	2x Schneider Kreuznach 35 mm	
Pixel Resolution	2448 x 2048 px	
Image Acquisition Rate	5 Hz	
DIC Software	Correlated Solutions VIC-3D 8	
Subset Size	21 to 29 px	15 to 19 px
Step Size	7 px	
Image Pre-smoothing	15 px	
Displacement Noise Floor	$<1\times 10^{-4}$ mm	
Strain Calculation	Engineering	
Strain Noise Floor	$\sim 2 \times 10^{-5}$ mm/mm (or ~0.002 %)	

3D-DIC analysis was performed using the commercially available software, Correlated Solutions VIC-3D 8 (Table 6.2). Specific subset size and step size depended on the field-of-view of the camera and relative speckle size in each test; individual tests occurred days to weeks apart, so the cameras were continuously set up and broken down. A representative study of the effect of subset size is presented in Section 4.3. For strain computation, all images were processed with a DIC subset size of 21 to 29 px, depending on the field of view across all specimens. The subset size to l_U was about 0.025 px/px. All datasets were processed with calibration images to calculate the orientation of the two cameras to derive out-of-plane measurements; at least 30 calibration images were acquired prior to each test of calibration grids with known speckle geometries. The data was also run through VIC-3D's built-in rigid body removal function. The measured strain floor in the x-direction for all DIC analysis was observed to be less than 2×10^{-5} mm/mm. Subsequent post-processing and analysis was performed in Python 3.6.

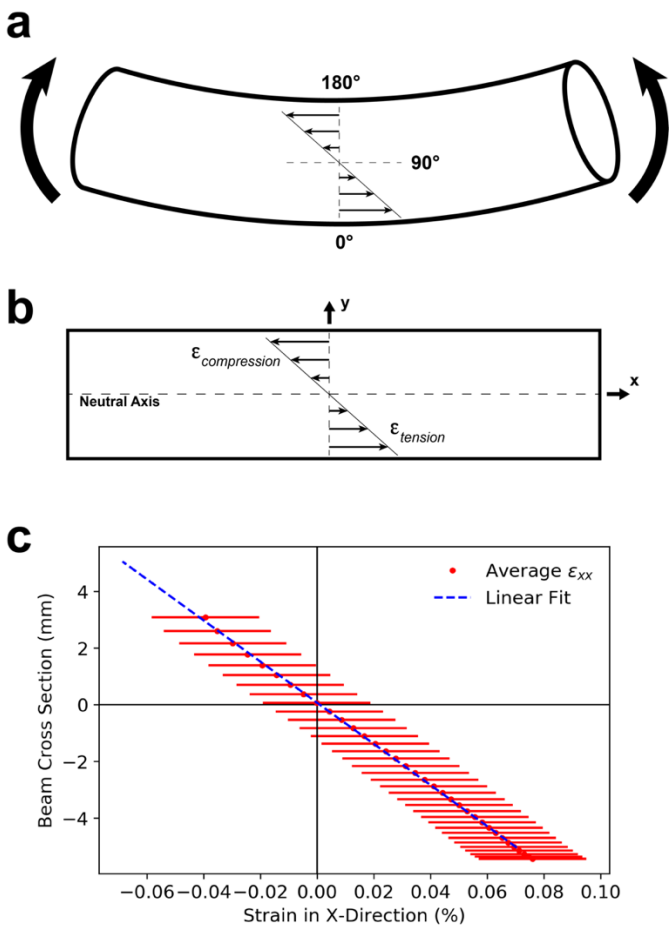

Figure 6.3. (a) A schematic of the strain profile across a beam-in-bending, where (b) the strain varies from compression at the top of the specimen to tension at the bottom. (c) DIC strain fit this expected profile.

Stress calculations and correlation of DIC data with acoustic and leak rate data was summarized in prior work [17]. However, the derivation of strain from DIC was re-examined here. Output data files from DIC included position (x, y, z), displacement (u, v, w) and strain (ε_{xx}, ε_{yy}, ε_{xy}) data at pixel locations per pair of digital images acquired during mechanical testing. Converting a two-dimensional data set to a one-dimension strain data set for plotting a stress-strain curve was complicated and dependent on the loading mode. For example, in a tension test, the entire specimen would be pulled in tension; of course, local strain distribution within a CMC can be highly variable [11,14–16]. In a flexural test, like these four-point bend experiments, the CMC is subjected to both compression and tension, which varies in magnitude through

the cross section (Figure 6.3).

To convert the full-field DIC strain data into a one-dimensional measurement for stress-strain analysis, the full-field dataset was first cropped to only include the region within the two inner loading points, l_U, corresponding to the region of pure bending. At every *y*-pixel position down the cross-section of the specimen, the strains in the x-direction (tube axial direction) ε_{xx} were isolated. Pseudo-strains due to COD were removed by filtering out strains above a 90 % threshold, and the remaining strains were averaged (Figure 6.3c). The standard deviation of the strains at every *y*-pixel was about 0.04 % across all tests. The resulting cross-section strain profile confirmed the expected beam-in-bending profile and re-enforced that the maximum strains occurred at the upper and lower surfaces of the specimen. Prior work has demonstrated that fracture and failure initiate in the tensile underside of the specimen, so the maximum tensile strain from this cross-section profile was extracted at each time step, providing a one-dimensional strain dataset to plot in the stress-strain and subsequent analyses.

To isolate individual cracks, all images were re-processed in VIC-3D with a finer subset size of 15 to 19 px, depending on the field of view across all specimens. The subset size to l_U was < 0.02 px/px in order to provide finer resolution. Crack detection was performed using the two-dimensional dataset based on the discontinuities within the displacement field *u*. A spatial derivative approach has been documented in the literature to isolate individual cracks [36–39]. The spatial derivative $\frac{\partial u}{\partial x}$ was calculated from the displacement field *u* in the direction of loading *x.* To bring out and isolate the discontinuities, a scalar, intensity threshold *I* was calculated as follows:

$$I = 3s_i - \frac{\widetilde{\partial u}}{\partial x_i} + \frac{\widetilde{\partial u}}{\partial x_f} \tag{6.1}$$

where s_i is the standard deviation on the initial spatial derivatives dataset and subscripts *i* and *f* denote the initial (reference dataset prior to loading) and final (dataset of interest) median spatial derivative $\frac{\widetilde{\partial u}}{\partial x}$ [35].

Filtering the two-dimensional DIC data by this intensity threshold isolates the spatial derivative peaks, corresponding to cracks and provides *x* and *y* position data for those cracks. Here, we assumed all COD

occurred in the x-direction along the axis of the tubular specimens. COD values were computed by subtracting the displacement on the left (u_l) and right (u_r) side of each discontinuity at the half maximum positions associated with every spatial derivative peak:

$$COD = u_r - u_l. \tag{6.2}$$

3. Results

SiC/SiC CMC tubular specimens were loaded under four-point bending until failure, and optical images were processed initially with a DIC subset size of 21 to 29 px to quantify flexural strains. The subset size to l_U was about 0.025 px/px. The resulting DIC strain profiles (Figure 6.4) followed expected trends: (i) there was a clear beam-in-bending strain profile from compressive strains above the neutral axis to tensile along the underside of the sample, (ii) matrix microcracking, as indicated by strain concentrations, originated along the tensile underside of the specimens and grew up toward the neutral axis, and (iii) eventually, fracture (traced in black) occurred across the tows, resulting in failure of each specimen.

Table 6.3. Measured properties of the CMC specimens.

Specimen	Young's Modulus (GPa)	DFL Stress (MPa)	DFL Strain (%)	Strain at Onset of AE Activity (%)	Strain at Onset of Leaking (%)	Failure Stress (MPa)	Failure Strain (%)
A01	268	120	0.044	0.038	0.045	233	0.473
A02	292	109	0.042	0.047	0.061	199	0.358
B01	232	-	-	0.032	0.032	92	0.037
B02	184	-	-	0.035	0.042	101	0.045
C01	293	81	0.032	0.034	0.051	153	0.236
C02	224	116	0.036	0.041	0.051	116	0.054
D01	268	107	0.038	0.037	0.041	221	0.513
D02	285	86	0.029	0.038	0.044	228	0.901

A summary of the mechanical properties of each specimen is presented in Table 6.3. DFL stress and strain were determined from a 0.005 % strain offset applied to the measured flexural stress and strain (Figure 6.5a). The DFL strain correlated with the onset of acoustic activity and leaking, which confirmed the conventional understanding of the DFL point; this point marks the onset of matrix microcracking and transfer of loading from the matrix to the fiber tows. Leaking occurred very soon after, if not concurrently

with, onset of acoustic activity, indicating these microcracks instantly penetrated the full thickness of the SiC cladding. The modulus values were fairly consistent, which reflected the properties of the SiC matrix. The onset of microcracking also began consistently within a range of about 0.032 to 0.051 % strain as

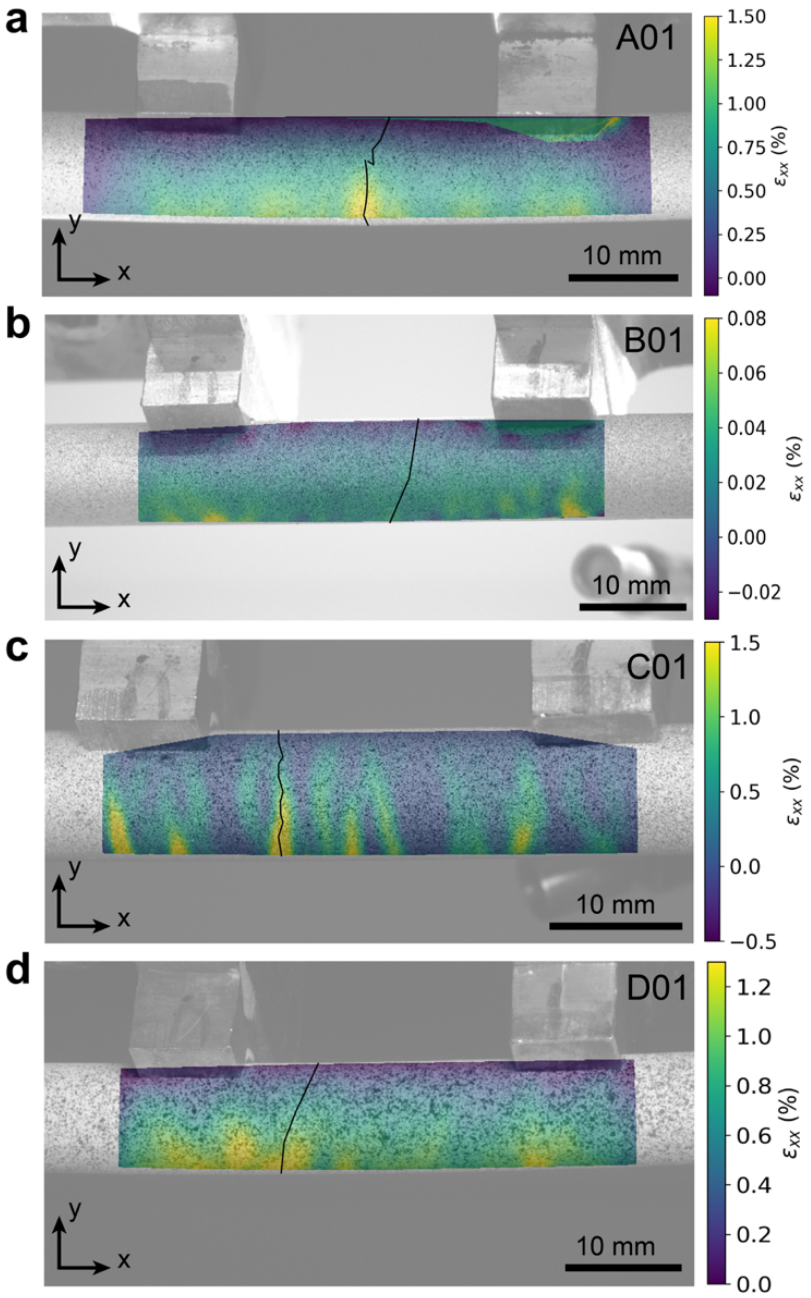

Figure 6.4. Representative DIC strain profiles of select specimens at the point right before final fracture corresponding to each type of treatment: (a) no heat treatment, (b) treatment at 1200 °C in open air, (c) at 1200 °C in vacuum, and (d) at 1200 °C in helium. The location of final fracture is marked in black.

indicated by the DFL point, acoustic activity, and leak rate. Specimens A01, A02, D01, and D02 performed the best, achieving high fracture strains >0.4 %. Specimens B01 and B02, both of which were treated in open air at 1200 °C, performed the worst with early fracture < 0.045 % strain and no clear DFL point, indicating that matrix microcracking progressed rapidly and continued through the fiber tows, resulting in fast brittle fracture.

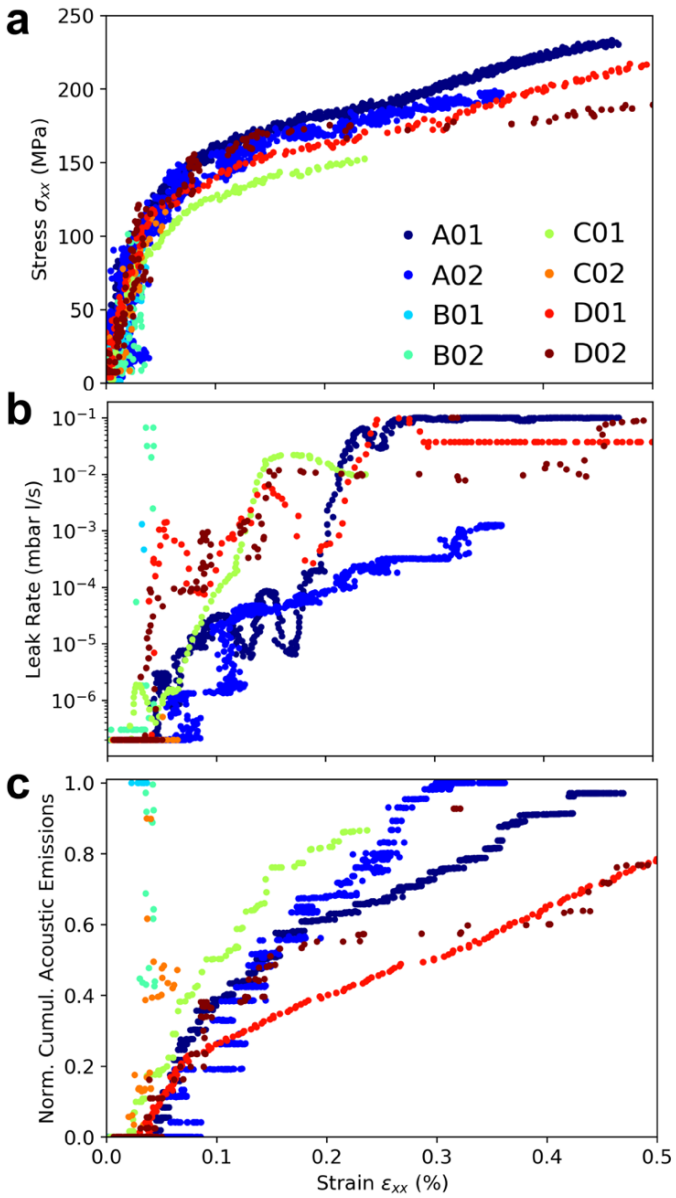

Figure 6.5. Four-point bending data for all CMC specimens. (a) Stress-strain curves through 0.5 % flexural strain. (b) Leak rate response over bending strain. (c) Normalized cumulative acoustic energy activity over the measured bending strains.

4. Discussion

4.1. Environmental Impact and Characterization

The properties of A01, A02, D01, and D02 (Table 6.3) fell within expected ranges for SiC/SiC CMCs documented in literature [17,35,40–42]. Specimens B01 and B02 performed the worst and exhibited instant brittle failure, and specimens C01 and C02 fell in the middle in terms of their failure strain. Of course, these specimens were subjected to different heat treatments, which could explain the variation in performance. However, CMC performance is highly variable, and microstructural variation, porosity, and pre-existing cracking can also account for this variation.

SiC/SiC CMCs are generally thermally stable [6,43], but studies in literature do document some degradation due to heat treatments and environmental exposure, which may explain the mechanical performance observed here. Wing and Halloran [44] performed Raman spectroscopy of reaction-bonded silicon carbide after thermal annealing and found significant reduction in the residual stress state of the Si and SiC phases of the material, 78 % and 35 % stress relaxation, respectively. This stress relaxation occurred only after 30 minutes of annealing at 1200 °C; annealing for extended durations only resulted in minimal further stress relaxation. Even greater stress relaxation of silicon phases, up to 90 %, have been documented [45,46]. Knauf, *et al*. conducted Raman spectroscopy stress measurements of the SiC matrix within SiC/SiC CMCs (with boron nitride fiber coating) and reported no significant change in the stress state after heat treatments up to 1300 °C [47]. Potential changes in the residual stress state are significant; these changes could either raise or lower the energy barrier to fracture initiation and propagation.

Chai, *et al*. reported a reduction of as much as 49.6 % in the fracture toughness of the SiC fibers after heat treatments of 1 hour at 1100 °C [48]. This finding was further supported by earlier work by Araki, *et al*., who reported a reduction of fracture strength of Hi-Nicalon Type-S SiC fibers subjected to heat treatments of 1000 °C in vacuum for 1 hour. Notably, the Hi-Nicalon Type-S SiC fibers still outperformed Nicalon and Hi-Nicalon fibers and displayed comparably minimal microstructural degradation or weight loss [49]. These observations in literature suggest that the specimens treated in open air at 1200 °C

(Specimens B01 and B02) may be subject to structural degradation, leading to a reduced fracture toughness.

Indentations were performed to probe the fracture toughness of the CMC after each treatment. Young's modulus (E) and hardness (H) were extracted from nanoindentations (depths < 1 μm) as described by the Oliver-Pharr methodology [50,51]. Microindentations (depths > 1 μm) were performed to induce fracture at some prescribed load (P); these indentations cracks (c) were subsequently measured under SEM (Figure 6.6) to quantify the fracture toughness as described by:

$$K_{IC} = \alpha \left(\frac{E}{H}\right)^{1/2} \left(\frac{P}{c^{3/2}}\right). \tag{6.3}$$

The value α is a geometric factor dependent on the geometry of the indenter tip; here, 0.016 was used as the value of α for a Berkovich tip [52–54]. At least eight indentations were performed per load per specimen.

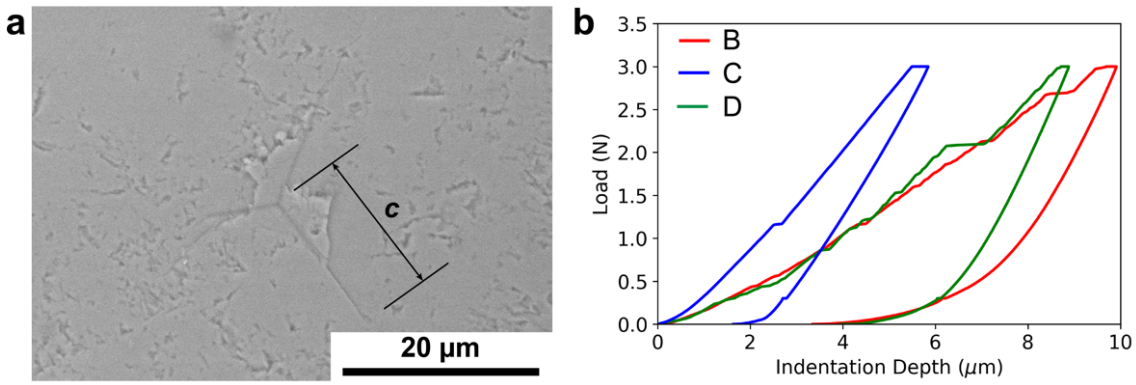

Figure 6.6. (a) A representative micrograph of an indentation on the CVD matrix with crack length c. (b) Select indentation curves showing steps associated with cracking.

Table 6.4. Modulus, hardness, and fracture toughness measurements on the CVD SiC via nanoindentation.

Treatment	Young's Modulus (GPa)	Hardness (GPa)	Fracture Toughness (MPa $m^{1/2}$)
A	414 ± 24	30.5 ± 5.5	4.14 ± 0.55
B	408 ± 18	32.7 ± 4.9	2.77 ± 0.25
C	410 ± 15	33.1 ± 3.9	3.68 ± 0.16
D	415 ± 22	32.8 ± 4.3	3.70 ± 1.16

These modulus and hardness values (Table 6.4) were notable larger than the bulk properties (Table 6.3) and reflected the properties of the individual CMC constituents. Specifically, these properties were those of the CVD SiC; the microindentations necessary to generate cracks were too large (20 to 30 μm in diameter) to isolate the properties and fracture toughness of individual fibers or the CVI matrix. Nonetheless, the measured fracture toughness of the CVD SiC agreed with the findings reported in literature [55]. There was significant degradation of the fracture toughness of the CVD SiC after the heat treatment in open air; the fracture toughness decreased by 33 % compared to the specimens without heat treatment and by 25 % compared to the other specimens treated in vacuum or in helium. In contrast, the specimens treated in vacuum and in helium experienced degradation of fracture toughness of about 10 %. This outcome would heavily imply that even if there was some contribution from typical CMC microstructural variation to the reduced mechanical performance of the treatment B samples, the environmental effects of the open air treatment on fracture toughness were significant and detrimental.

To further investigate the impact of the heat treatments, SEM with EDS mapping was performed on the outer surface of select specimens (Figure 6.7). Treatment A, no heat treatment, was associated with no oxidation of the outer surface. Treatments C and D, where treatments at 1200 °C were performed in vacuum and helium respectively, exhibited equivalent degrees of surface oxidation, about 39 % oxygen content on the surface. Treatment B, in contrast, exhibited the largest degree of oxidation with a surface oxygen content of 48 %.

SEM and EDS maps of the cross-section of these specimens (Figure 6.8) showed most of the oxidation was located along the exposed surfaces of the CMCs, and they continued to show greater oxidation of the specimens treated in open air. Oxidation of SiC CMCs has been, and continues to be, researched within the context of semiconductor, aerospace, and nuclear energy applications, where specific environments [56] and fiber and matrix materials composition [57,58] can dictate the rates of silica formation and SiC recession. An investigation of oxidation of Hi-Nicalon Type S SiC fibers has demonstrated rapid growth of silica over a span of minutes after exposure to high temperatures (>800 °C), and significant oxide crystallization was reported at temperatures greater than 1000 °C [59]. Oxidation of these tubular CMC

specimens was expected, and the fracture toughness measurements would suggest the level of oxidation due to the open air treatment induced sufficient degradation to result in brittle CMC failure.

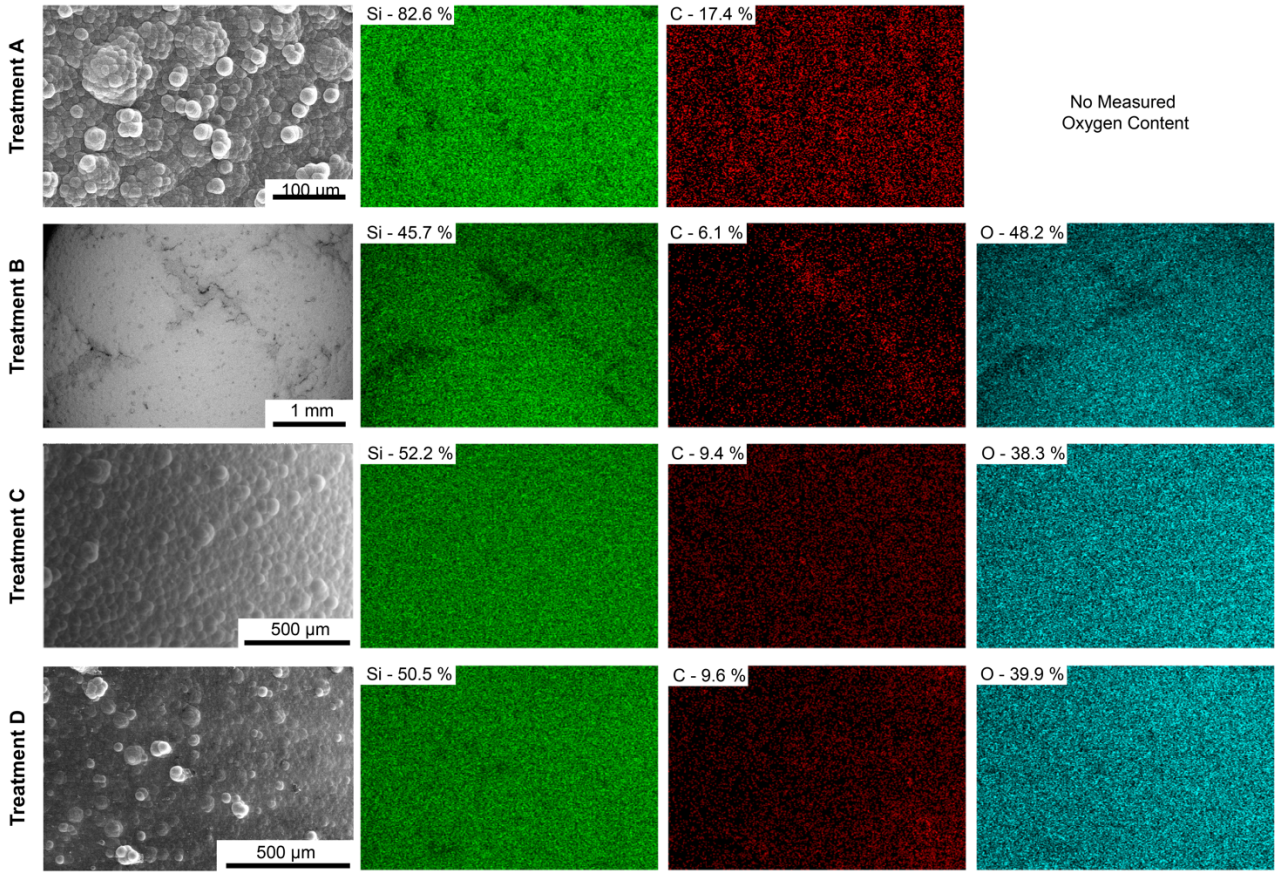

Figure 6.7. SEM and EDS maps of the outer CVD SiC surface of select specimens from each pre-experiment heat treatment: A, B, C, and D. The relative percentage of silicon (green), carbon (red), and oxygen (blue) is presented for each map.

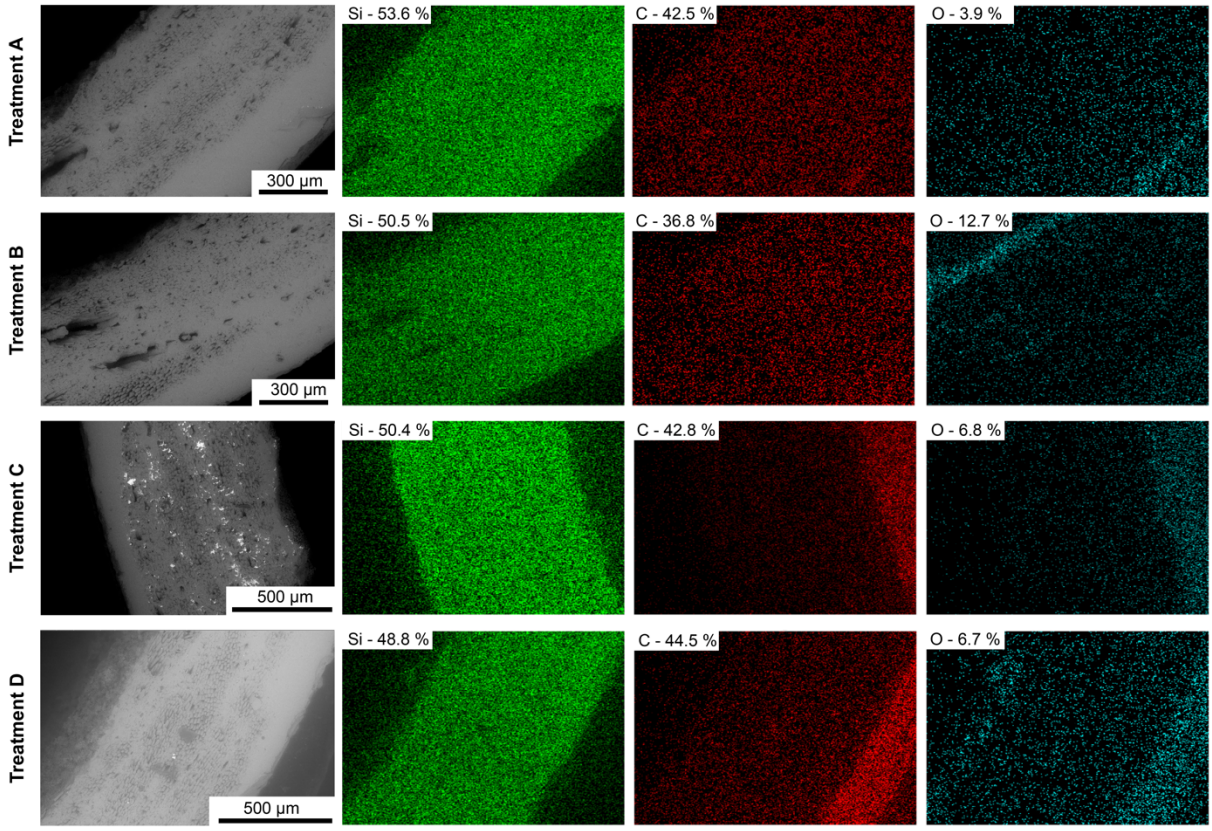

Figure 6.8. SEM and EDS maps of cross-sections of select SiC/SiC CMC specimens from each pre-experiment heat treatment: A, B, C, and D. The relative percentage of silicon (green), carbon (red), and oxygen (blue) is presented for each map.

4.2. Crack Opening and Fracture Energy

Characterization of the fracture pattern of each specimen may be important to unveil further insight into the failure mechanisms of SiC/SiC CMCs. SEM of the specimens after fracture revealed a consistent crack pattern (Figure 6.9). Multiple cracks were present along the flexural region of the specimens (within the l_U distance). These cracks were typically only a few microns (< 5 µm) wide and uniformly spaced (Figure 6.9a). Cracks were found to cross across the individual CVD deposits as previously noted [35] (Figure 6.9b). The location of final fracture marked the widest instance of cracking, exceeding a few hundred microns wide and wide enough to see locations of fiber pullout from the matrix (Figure 6.9c). The B01 and B02 specimens were outliers in that the only located instance of cracking was the location of the

final fracture. The edges of fracture were also imaged (Figure 6.9d) and probed with AFM (Figure 6.9e), which indicated these cracks, while trans-deposit (*i.e.,* through the chemical vapor deposits), were intergranular; the fracture surface has a pebbled texture as the crack passed around SiC grains.

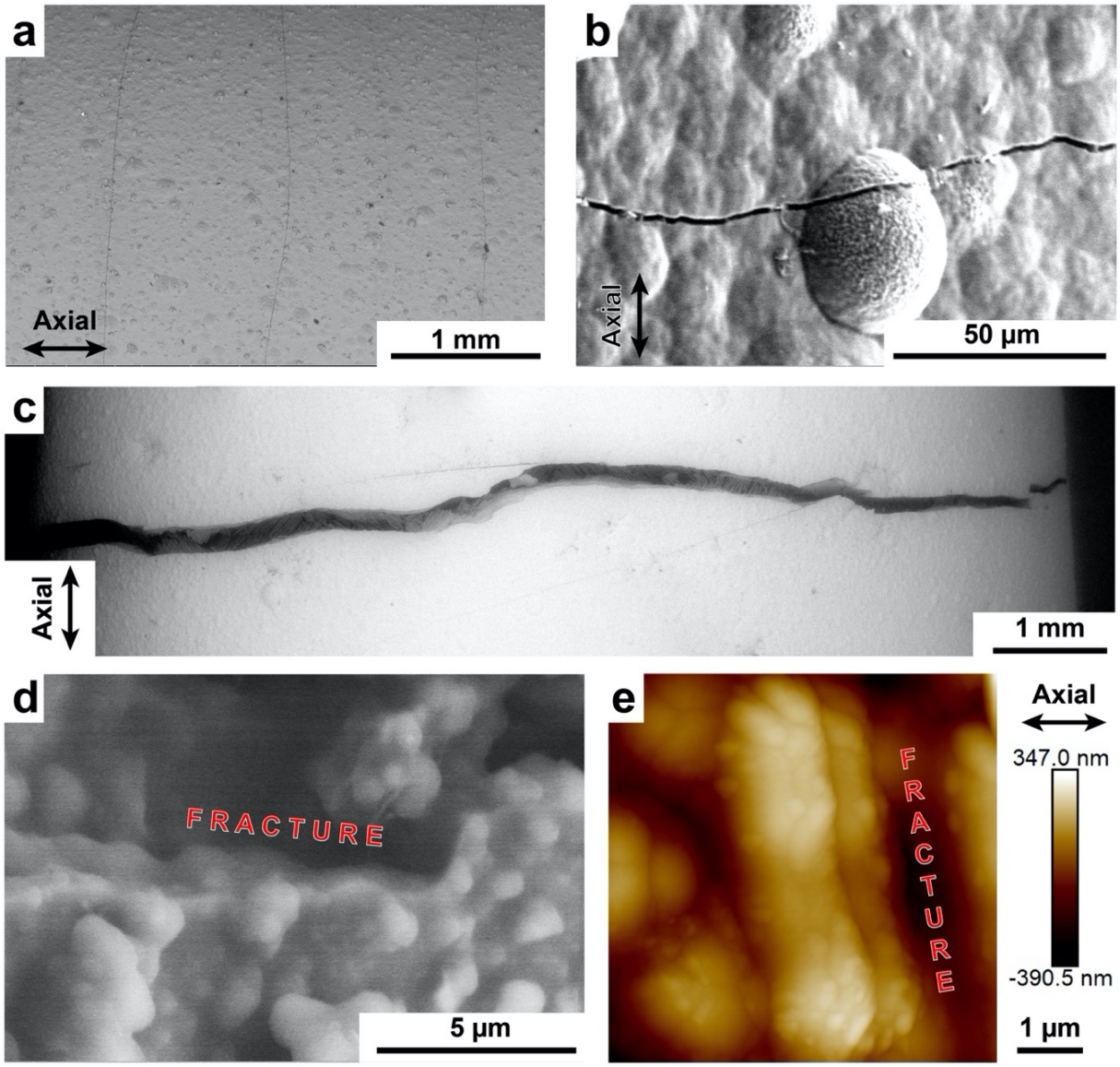

Figure 6.9. (a) A micrograph of the outer surface of the CMC specimens after testing, showing uniformly spaced cracks. (b) These cracks traversed the CVD deposits. (c) The site of final failure featured a wide crack, revealing fiber pull-out from the matrix. (d) SEM and (e) AFM scans of the fracture suggest the cracks are intergranular. These micrographs and scans show (a,b,c,e) A01 and (d) A02 but are representative of fracture observed in the other specimens.

However, post-experiment SEM did not elucidate the in-process fracture growth characteristics. To do so, DIC-enabled crack detection was applied to the *in-situ* optical images (Section 2.3). These images were all re-processed in VIC-3D with a finer subset size of 15 to 19 px, depending on the field of view across all specimens. The subset size to l_U was < 0.02 px/px in order to provide finer resolution to bring out individual cracks. The effect of subset size on the DIC-based mechanical properties is discussed in Section 4.3. With

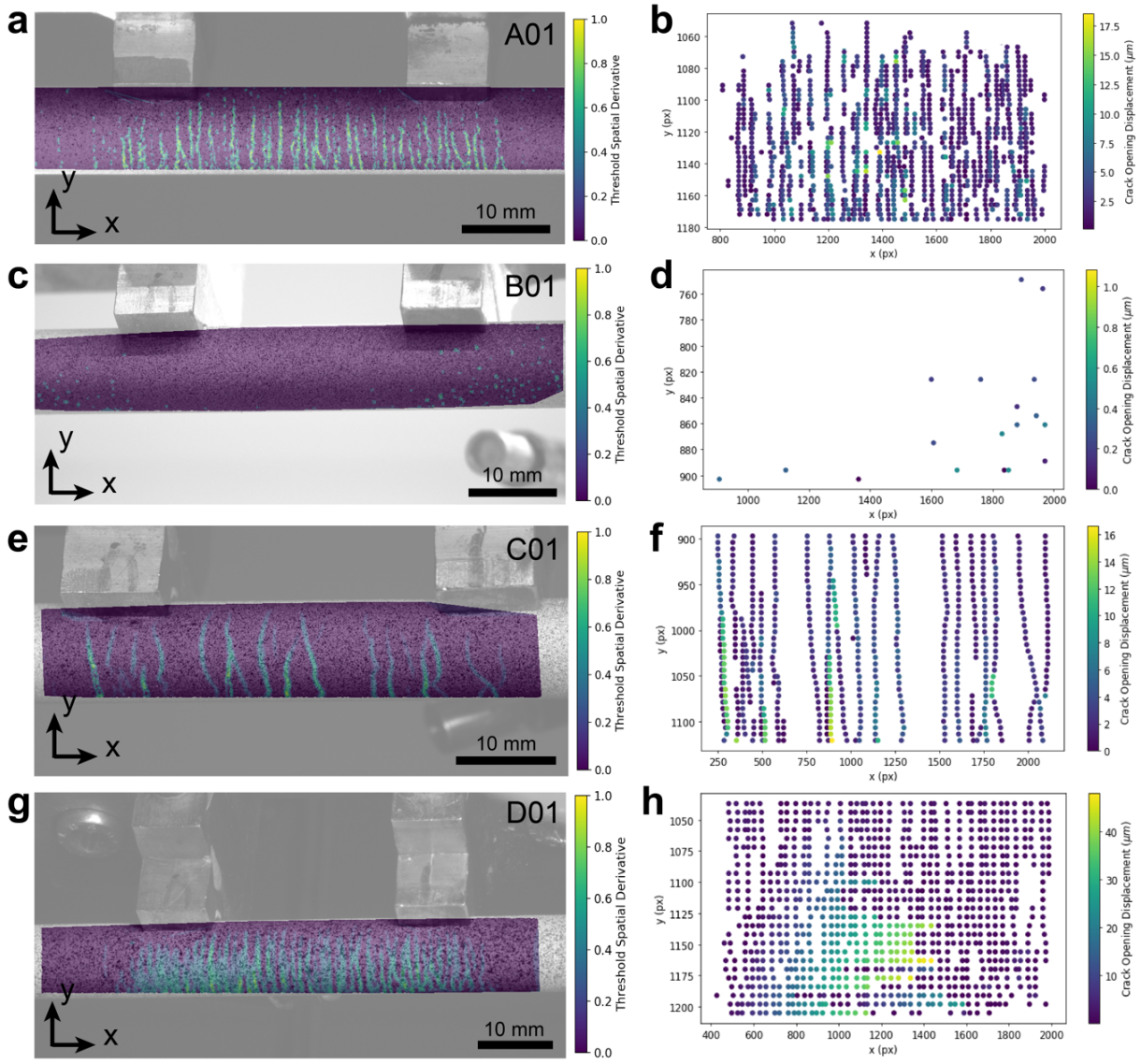

Figure 6.10. Spatial derivatives maps (left) and calculated COD (right) based on *in-situ* DIC displacement data corresponding to the last image right before final failure. Maps are presented for a specimen from each heat treatment: (a,b) A01, (c,d) B01, (e,f) C01, and (g,h) D01.

this crack detection analysis, the crack location was isolated, and the COD was calculated. COD calculations were compared to SEM images, which confirmed the calculations correctly indicated the approximate range of crack opening. COD measurement resolution was ~100 nm.

Selected fracture maps, indicated by the spatial derivative data, and COD calculations are presented in Figure 6.10 for each heat treatment; these maps correspond to the image collected of each specimen at the maximum strain before fracture. With the exception of B01 and B02, the maps confirmed observations from SEM; transverse cracking travelled from the tensile underside of the specimens up nearly around the full circumference of the specimen. COD values were small, less than 5 μm in most locations, indicating most cracks were hairline fracture within the matrix. Isolated instances of large COD values corresponded to locations where final fracture initiated.

Importantly, this COD data was available throughout the duration of each test via analysis of all DIC optical images. For example, Figure 6.11a-d presents the spatial derivative maps for specimen A01 at different stages of flexural strain, showing the rapid initiation of numerous cracks at the onset of acoustic activity and leaking. Thus, key fracture characteristics, like average COD and crack spacing, can be quantified and tracked throughout each experiment. COD was found to increase linearly during bending for all tests (Figure 6.11e). Crack spacing; *i.e.*, the separation between individual cracks, was measured and averaged for every image (Figure 6.11f). Initially, cracks were widely spaced; however, this spacing rapidly decreased as many cracks initiated. Importantly, these maps reveal that multiple crack initiation sites were present along the bending zone. By about 0.2 % strain, the number of cracks and the crack spacing stabilized. Specimen C01 was a bit of an outlier with larger crack spacing while specimen D02 had the smallest crack spacing (*i.e.*, greatest crack density), as also visualized in Figure 6.10e. Cracking is commonly observed down the bending zone of CMCs during flexural testing, where they relieve stresses [17,35]. As the samples with more cracks achieved greater ultimate failure strains, it may be interpreted that more cracking helps relieve stress to enable greater mechanical performance at the cost of hermeticity.

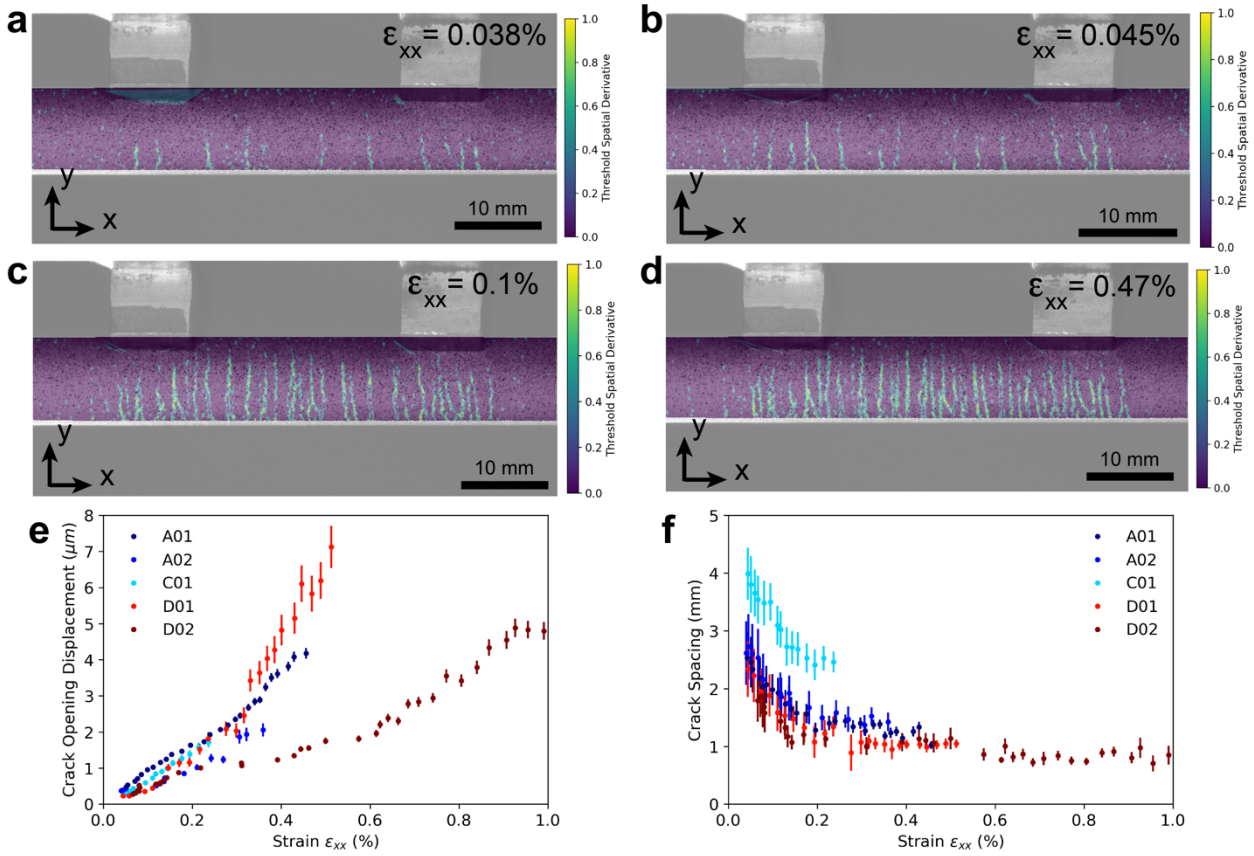

Figure 6.11. Spatial derivatives maps of specimen A01 at (a) the onset of AE activity, (b) onset of leaking, (c) at 0.1 % flexural strain, and (d) right before final failure. (e) COD and (f) crack spacing could be tracked with flexural strain for the duration of each test; shown, here representative trends for each heat treatment.

Consistent with prior observations of CMC fracture, the uniform crack spacing indicated a strong correlation with the CMC architecture. It was hypothesized that crack spacing aligned with tow cross-over positions, which were found to be 0.81 ± 0.03 mm [35]. The indicated crack spacing is generally larger than the cross-over spacing, but we further hypothesize that local stress relaxation due to cracking may reduce the local stress for crack initiation at the next nearest tow cross-over. Work by Croom, *et al*. and Van Rooyen, *et al*. provided further support of this hypothesis. Croom performed *in-situ* X-ray tomography while loading a SiC/SiC CMC tubular specimen in an expanding plug test configuration. X-ray tomographs and volumetric-DIC identified the origins of fracture as tow cross-over locations and further identified that

variations in tow cross-over spacing to be an important criterial in the onset location of fracture [33]. Similar flexural testing of CMC tubes by Van Rooyen, *et al*. unveiled fracture originating from tow cross-over locations, where Van Rooyen observed greater porosity [18]. Their work and the work by others in the literature [60–62] suggested that stresses between contacting, non-parallel tows can promote debonding of the tows and matrix, thereby initiating cracks (Figure 6.12a,b).

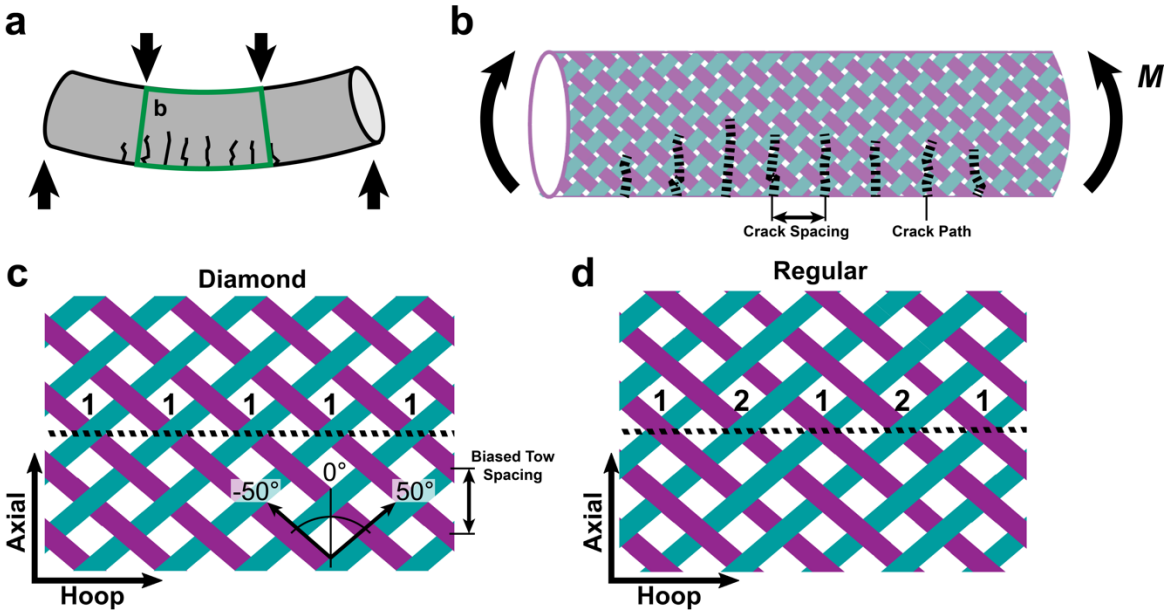

Figure 6.12. A schematic of the crack growth profile due to (a) bending of the CMC tubular specimens. (b) Crack spacing indicates fracture originated at tow cross-over points. Schematics of (c) diamond and (d) regular biaxial braids (adapted from [35]). Notations of "1" and "2" indicate uniform or non-uniform tow cross-over orientation.

A possible remedy to this fracture mechanism may be to manufacture the CMC claddings with a regular braid rather than the diamond braid tested here. While it is possible the diamond biaxial braid (Figure 6.12c) works to widely distribute cracks and consume energy, the many discontinuous crossover regions would seem to provide a more concentrated fracture zone than for a regular biaxial braid (Figure 6.12d). A circumferential crack path would transcend a multitude of uniform tow crossings within a diamond braid, like those tested in this dissertation, but these crossover points are not uniform in a regular braid. It is

expected that this non-uniform tow pattern would convolute the crack path, possibly delaying the onset or slowing the propagation of fracture. Alternately, it may be preferential to avoid tow contact altogether with the use of filament winding techniques and multiple plies with variable orientations, where delamination is not a critical concern, such as in bending or internal expansion.

It was also previously mentioned that onset of fracture was closely associated with onset of leaking as demonstrated by the acoustic and leak rate data (Figure 6.5). To help understand the driving force for the through-thickness matrix cracking, the normalized fracture energy release was quantified based on the flexural stress and strain of specimen B01. From the experiment, there are two basic modes of fracture growth: (i) along either side of the circumference of the CMC tube or (ii) through the 0.85 mm thick CMC wall. Quantifying the fracture energy in either mode is not easy. The CMC microstructure is highly complex with fiber, pores, and other constituents imposing local redistribution of stresses, which would impose a mixed fracture mode. Axial cross-sections (Figure 6.13a) of the cladding showed that through-thickness cracks did not penetrate straight across the cladding; instead, they appeared to branch through the fiber tows and shift at pores (Figure 6.13b).

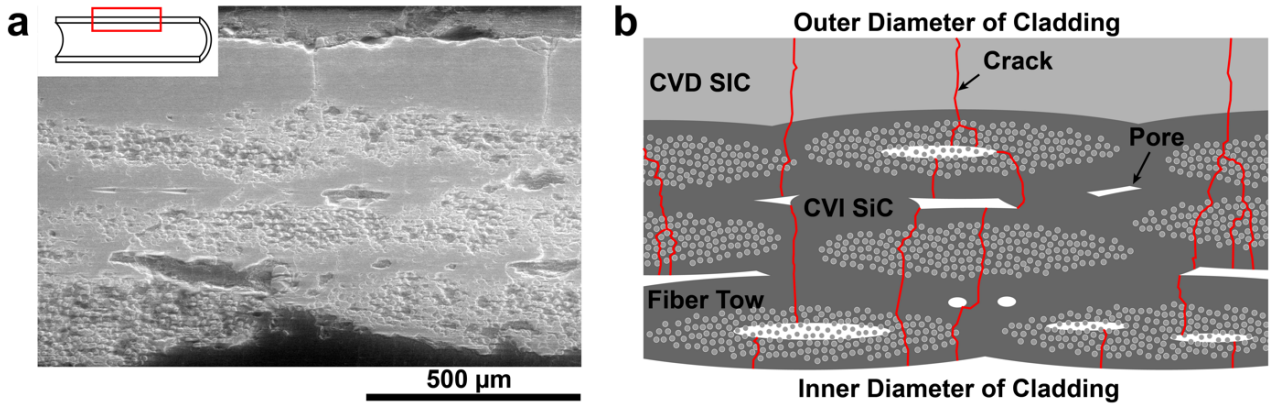

Figure 6.13. (a) A micrograph of an axial cross-section of specimen A01, showing through-thickness cracking. (b) A schematic of the through-thickness fracture pattern, presenting the branching and shifts in the cracks (red lines) due to interactions with the fiber tows and CMC porosity.

For a rudimentary understanding of the fracture energy, the material was assumed to be uniform matrix, uninterrupted by pores and fibers; thus, both fracture modes were assumed to be mode I. This assumption was based on the observation that matrix microcracking occurred early, before fiber fracture (excluding B01 and B02). This matrix microcracking also penetrated the full thickness of the specimens, leading to loss of hermeticity and travel, in some instances, around the full circumference of the tube. Thus, matrix microcracking exhibited both modes of fracture growth.

The stresses across the sample were also not constant and extended from the max tensile stress from one orientation to the max compressive stress at the other (Figure 6.14a). Here again, another a simplification is made. In the case of circumferential cracking, the material was assumed to be a flat plate subjected to a bending moment (Figure 6.14b,c). Here, the fracture energy release can be described by:

$$G = \frac{K_I^2(1-\nu^2)}{E} = \frac{\pi a P^2 M^2 y^2 (1-\nu^2)}{I^2 E}, \tag{6.4}$$

where a is the crack length, P is the applied load, M is the bending moment, and I is the moment of inertia [63,64].

In the other case of through-thickness cracking, the strain/stress field was assumed to be relatively uniform through the thickness (Figure 6.14d). Here, the fracture energy release can be described by:

$$G = \frac{K_I^2(1-\nu^2)}{E} = \frac{\pi a^3 \sigma^2 P^2 (1-\nu^2)}{E}, \tag{6.5}$$

where σ is the local tensile stress [64].

In both cases, the model examined one crack contained with a unit of the tubular specimen (Figure 14c,d). These simplifications, of course, fail to account for the local redistribution of stresses and strain due to the CMC architecture and for the impact of CMC constituents and porosity on crack growth (Figure 6.13). Thus, a quantitative value of fracture energy release would be subject to high error; instead, the fracture energy was normalized to emphasize the trend with crack length. In both cases, representing circumferential crack growth (Figure 6.14e) and through-thickness crack growth (Figure 6.14f), the fracture energy release followed an exponential trend, indicative of runaway fracture. This trend is consistent with the experimental behavior, where the correlation of acoustic and leak rate data indicated cracks penetrated

the full thickness of the tubular specimens almost instantly. In the circumferential direction, DIC strain and crack maps also revealed rapid crack growth, but crack growth in this orientation would be affected by the fiber tows.

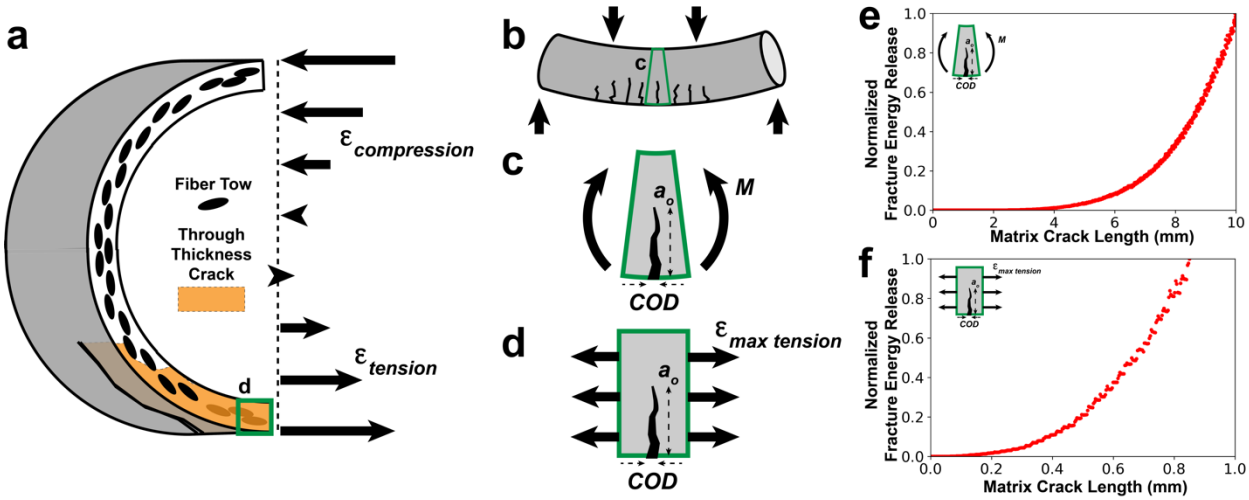

Figure 6.14. (a) A graphical cross-section of the CMC tubular specimens, representing the microstructural complexity and strain field. Fracture energy was modeled via two simplifications of the (b) bending profile: (c) as a flat plate subjected to a bending moment to represent circumferential crack growth and (d) as a flat plate subjected to uniform tension to represent through-thickness crack growth. The normalized fracture energy release for a single crack within (e) the full circumferential unit in bending and (f) the through-thickness region at the point of max tension are presented.

In sum, this analysis builds a greater understanding of the fracture mechanisms of SiC/SiC CMCs and unveils key insights for the future manufacture of CMC fuel claddings. Crack propagation through the thin CMC wall is nearly instantaneous, leading to rapid loss of hermeticity. However, crack growth in the circumferential orientation is somewhat delayed by the obstruction of many more fiber tows. The initiation of multiple fracture sites and uniform spacing of cracks further indicates that CMC fracture is dependent on the braid structure. A possible remedy to this fracture mechanism may be to manufacture the CMC claddings with a regular braid rather than the diamond braid to introduce non-uniform tow cross-over orientation as a means of achieving greater fracture resistance. Furthermore, short periods of high

temperature exposure can have significant detrimental effects on the fracture toughness, particularly if exposed to an oxidizing atmosphere. The impact of the environmental heat treatment or other exposure on the CMCs may be addressed with the use of an environmental barrier coating, which are in use in aerospace applications [65,66] and under consideration for nuclear cladding applications.

4.3. DIC Subset Fitting

DIC crack detection was enabled by minimizing the subset size to isolate individual cracks. Reducing the subset size increased the computational time for the image correlation, but it also becomes important to consider the impact of reducing the subset size on the flexural strain measurements. To quantify this effect, specimen A01 was re-analyzed for a range of subset sizes (9 to 75 px), which corresponded to a range of subset-to-l_U ratios of 0.011 to 0.090 px/px. To simulate the strain quantification via conventional extensometer measurements, a virtual extensometer analysis was applied to the DIC data over the range l_U using the built-in extensometer tool within VIC-3D. The resulting stress-strain behavior is presented in Figure 6.15a, which shows the strain measurements increase in magnitude with increasing subset size, and modulus values are reported in Table 6.5.

Table 6.5. Young's modulus variation of A01 with DIC subset size and strain measurement via a virtual extensometer.

Subset-to-l_U Ratio	Young's Modulus (GPa)
0.011	273
0.018	270
0.037	265
0.054	263
0.073	252
0.090	239
Virtual Extensometer	239

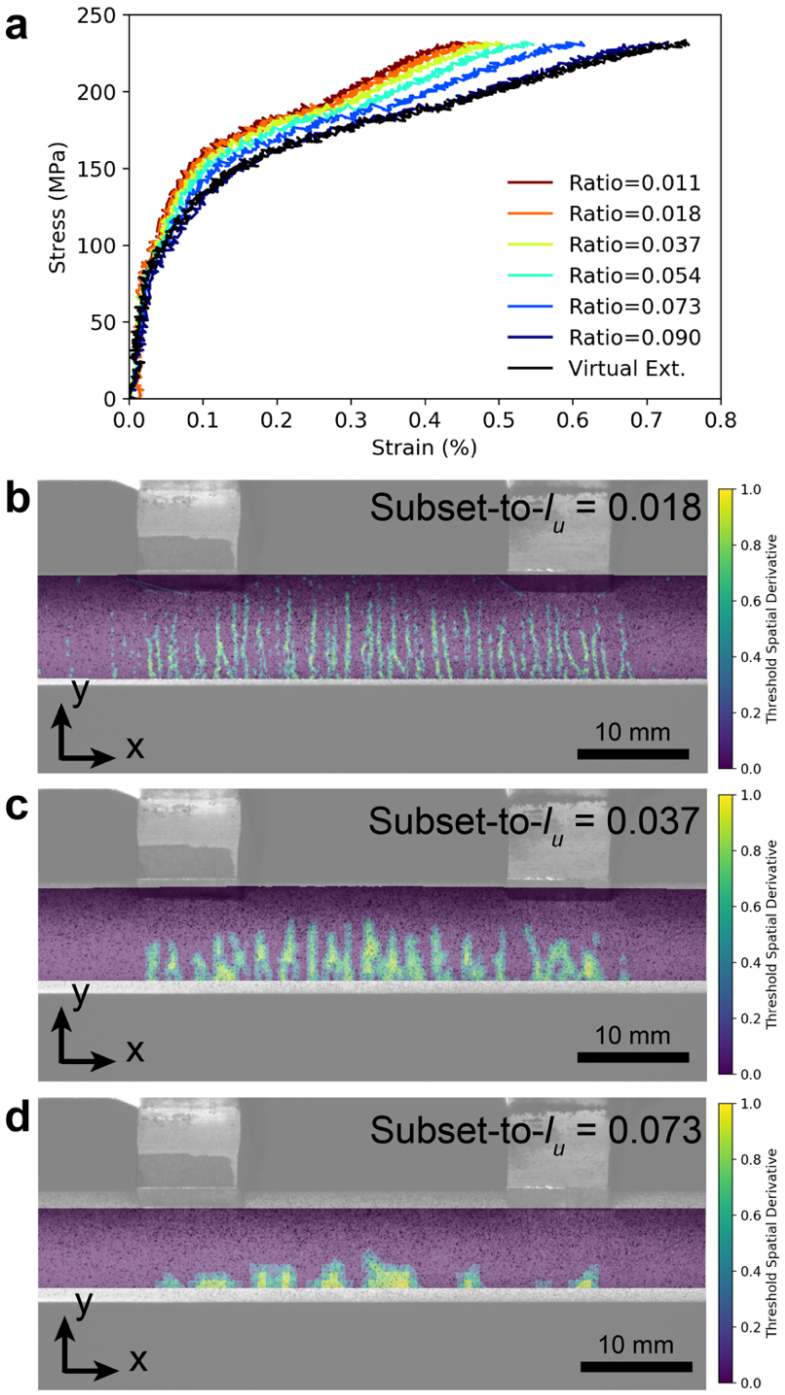

Figure 6.15. (a) The stress-strain curve of A01 was re-analyzed with increasing subset-to-l_U ratios to evaluate the effect of DIC subset size. Select spatial derivative maps show the loss of resolution and missed detection of cracks with increasing subset-to-l_U ratios of (b) 0.018, (c) 0.037, and (d) 0.073. The maps correspond to the image right before final failure.

Other researchers have investigated how to select the optimal subset size. Various experiments and computational simulations have unveiled the need to strike a balance between uncorrelated subsets, resolution, and noise reduction, typically quantified by the root mean square error [29,67,68]. Such investigations have identified the basic rules: a subset should be large enough to contain three to five speckles, where each speckles should be two to four pixels in diameter [25,26,29,30]. Larger subsets, in essence, average out fine displacement gradients, such as those due to cracking. In the case of these CMC specimens, the deformation and strain will include a significant contribution due to COD, exaggerating the actual strain of the material itself. The loss of resolution inherent with larger subsets obscures these pseudo-strain peaks, gradually averaging them into bulk flexural deformation of the tubular specimens while increasing the magnitude of that bulk deformation.

Strain measurements with an extensometer, or virtual extensometer, reflect the total displacement of the sample; thus, local variation in the displacement fields remains unresolved. We note that the data for the largest tested subset size (subset-to-l_U = 0.090 px/px) was roughly equivalent to that of the extensometer, reflecting the degree to which the local deformation data associated with cracking was obscured. This effect is visualized in the corresponding spatial derivative maps (right before final failure) across a range of subset sizes (Figure 6.15b-d). Fine detail of the fracture pattern was quickly obscured at larger subsets, hindering accurate measurement of COD and crack spacing. This subset size analysis emphasized the importance of balancing the DIC parameters based on the test objectives. Strain measurement, especially if performed for comparison with conventional strain gauge or extensometer measurements, may lean towards larger subsets while crack detection necessitates smaller subsets.

5. Conclusions

Coupled four-point bend / hermeticity testing unveiled the fracture mechanisms of SiC/SiC CMC tubular specimens and indicated near instantaneous loss of hermeticity with the onset of matrix

microcracking. *In-situ* DIC strain measurements provided high fidelity visualization of displacement and strain concentrations due to cracking and COD. Spatial derivatives of the DIC displacement fields were analyzed to isolate discontinuities due to cracking, providing in-process maps of crack growth. Subsequent analysis of COD and crack spacing revealed the initiation and growth of tightly spaced circumferential cracks long the length of the bending zone of the specimen.

Furthermore, CMC specimens were tested after four different heat treatments: no treatment, 48 hours at 1200 °C in open air, 48 hours at 1200 °C in vacuum, and 48 hours at 1200 °C in helium. Specimens treated in open air at 1200 °C were observed to fail via a brittle fracture mode while the other specimens exhibited typical CMC failure in stages of matrix microcracking, load transfer to fibers, and final fiber fracture. Fracture toughness of the specimens measured via indentation revealed a 30 % decrease in the fracture toughness of the specimens treated in open air, indicative of significant material degradation due to the environmental exposure. Protective coatings may be necessary in applications where CMCs, whether by design or accident, may be exposed to high temperatures in open air.

6. References

[1] Z. Karoutas, J. Brown, A. Atwood, L. Hallstadius, E. Lahoda, S. Ray, J. Bradfute, The maturing of nuclear fuel: Past to Accident Tolerant Fuel, Prog. Nucl. Energy. 102 (2018) 68–78. doi:10.1016/j.pnucene.2017.07.016.

[2] M. Kurata, Research and development methodology for practical use of accident tolerant fuel in light water reactors, Nucl. Eng. Technol. 48 (2016) 26–32. doi:10.1016/j.net.2015.12.004.

[3] P. Yvon, F. Carré, Structural materials challenges for advanced reactor systems, J. Nucl. Mater. 385 (2009) 217–222. doi:10.1016/j.jnucmat.2008.11.026.

[4] C.F. Bacalski, G.M. Jacobsen, C.P. Deck, Characterization of SiC-SiC accident tolerant fuel cladding after stress application, American Nuclear Society - ANS, United States, 2016.

[5] G.N. Morscher, V. V. Pujar, Design guidelines for in-plane mechanical properties of SiC fiber-reinforced melt-infiltrated SiC composites, Int. J. Appl. Ceram. Technol. 6 (2009) 151–163. doi:10.1111/j.1744-7402.2008.02331.x.

[6] J.Z. Gyekenyesi, N.P. Bansal, High Temperature Tensile Properties of Unidirectional Hi-Nicalon/Celsian Composites In Air, 2000. https://ntrs.nasa.gov/archive/nasa/casi.ntrs.nasa.gov/20000085860.pdf (accessed May 25, 2017).

[7] L.L. Snead, T. Nozawa, Y. Katoh, T.S. Byun, S. Kondo, D.A. Petti, Handbook of SiC properties for fuel performance modeling, J. Nucl. Mater. 371 (2007) 329–377. doi:10.1016/j.jnucmat.2007.05.016.

[8] R. Naslain, Design, preparation and properties of non-oxide CMCs for application in engines and nuclear reactors: an overview, Compos. Sci. Technol. 64 (2004) 155–170. doi:10.1016/S0266-3538(03)00230-6.

[9] C. Cady, A.G. Evans, K.E. Perry, Stress redistribution around mechanical attachments in ceramic matrix composites, Composites. 26 (1995) 683–690. https://ac.els-cdn.com/001043619591134Q/1-s2.0-001043619591134Q-main.pdf?_tid=4a24cf2c-cafa-11e7-800f-00000aacb35e&acdnat=1510856379_d3635520f9c97814588bb24dfbfb732b (accessed November 16, 2017).

[10] G. Morscher, J. Gyekenyesi, Room temperature tensile behavior and damage accumulation of Hi-Nicalon reinforced SiC matrix composites, 22nd Annu. Conf. Compos. Adv. Ceram. Mater. Struct. (2009). https://ntrs.nasa.gov/archive/nasa/casi.ntrs.nasa.gov/19980237335.pdf (accessed November 9, 2017).

[11] G.N. Morscher, H.M. Yun, J.A. DiCarlo, Matrix cracking in 3D orthogonal melt-infiltrated SiC/SiC composites with various z-fiber types, J. Am. Ceram. Soc. 88 (2004) 146–153. doi:10.1111/j.1551-2916.2004.00029.x.

[12] G.S. Corman, A.J. Dean, S. Brabetz, M.K. Brun, K.L. Luthra, L. Tognarelli, M. Pecchioli, Rig and engine testing of melt infiltrated ceramic composites for combustor and shroud applications, J. Eng. Gas Turbines Power. 124 (2002) 459–464. doi:10.1115/1.1455637.

[13] C.P. Deck, G.M. Jacobsen, J. Sheeder, O. Gutierrez, J. Zhang, J. Stone, H.E. Khalifa, C.A. Back, Characterization of SiC-SiC composites for accident tolerant fuel cladding, J. Nucl. Mater. 466 (2015) 1–15. doi:10.1016/j.jnucmat.2015.08.020.

[14] K.M. Sevener, J.M. Tracy, Z. Chen, J.D. Kiser, S. Daly, Crack opening behavior in ceramic matrix composites, J. Am. Ceram. Soc. 100 (2017) 4734–4747. doi:10.1111/jace.14976.

[15] G.N. Morscher, Stress-dependent matrix cracking in 2D woven SiC-fiber reinforced melt-infiltrated SiC matrix composites, Compos. Sci. Technol. 64 (2004) 1311–1319. doi:10.1016/j.compscitech.2003.10.022.

[16] H.M. Yun, J.Z. Gyekenyesi, Y.L. Chen, D.R. Wheeler, J.A. Dicarlo, Tensile behavior of SiC/SiC composites reinforced by treated Sylramic SiC fibers, Ceram. Eng. Sci. Proc. (2001) 521–531. http://onlinelibrary.wiley.com/store/10.1002/9780470294680.ch60/asset/ch60.pdf?v=1&t=ja1et44c&s=ce79b0421089ac5ed8ee192361d317a2f1bcc654 (accessed November 6, 2017).

[17] C.H. Bumgardner, F.M. Heim, D.C. Roache, A.I. Jarama, P. Xu, R. Lu, E.J. Lahoda, B.P. Croom, C.P. Deck, X. Li, Unveiling hermetic failure of ceramic tubes by digital image correlation and acoustic emission, J. Am. Ceram. Soc. 103 (2020) 2146–2159. doi:10.1111/jace.16854.

[18] I.J. Van Rooyen, W.R. Lloyd, T.L. Trowbridge, S.R. Novascone, K.J. Wendt, S.M. Bragg-Sitton, I. Van Rooyen, K.M. Wendt, SiC-CMC-Zircaloy-4 nuclear fuel cladding performance during 4- point tubular bend testing, in: LWR Fuel Perform. Meet. Fuel 2013, 2013.

[19] S.R. Choi, J.P. Gyekenyesi, Load-rate dependency of ultimate tensile strength in ceramic matrix composites at elevated temperatures, Int. J. Fatigue. 27 (2005) 503–510. doi:10.1016/j.ijfatigue.2004.10.001.

[20] S.R. Choi, N.P. Bansal, M.J. Verrilli, Delayed failure of ceramic matrix composites in tension at elevated temperatures, J. Eur. Ceram. Soc. 25 (2005) 1629–1636. doi:10.1016/j.jeurceramsoc.2004.05.024.

[21] F.M. Heim, B.P. Croom, C.H. Bumgardner, X. Li, Scalable measurements of tow architecture variability in braided ceramic composite tubes, J. Am. Ceram. Soc. 101 (2018) 4297–4307. doi:10.1111/jace.15564.

[22] F. Breede, S. Hofmann, N. Jain, R. Jemmali, Design, manufacture, and characterization of a carbon fiber-reinforced silicon Carbide Nozzle extension, Int. J. Appl. Ceram. Technol. 13 (2016) 3–16. doi:10.1111/ijac.12496.

[23] Y. Katoh, D.F. Wilson, C.W. Forsberg, Assessment of Silicon Carbide Composites for Advanced Salt- Cooled Reactors, Oak Ridge, TN, TN, 2007. http://info.ornl.gov/sites/publications/files/Pub8156.pdf (accessed August 18, 2016).

[24] D. Chen, C.J. Gilbert, X.F. Zhang, R.O. Ritchie, High-temperature cyclic fatigue-crack growth behavior in an in-situ toughened silicon carbide, Acta Mater. (2000) 659–674. www.elsevier.com/locate/actamat (accessed February 12, 2017).

[25] M.A. Sutton, J.-J. Orteu, H.W. Schreier, Image Correlation for Shape, Motion and Deformation Measurements, 1st ed., New York, 2009.

[26] J.D. Helm, S.R. McNeill, M.A. Sutton, Improved three-dimensional image correlation for surface displacement measurement, Opt. Eng. 35 (1996) 1911–1920. doi:10.1117/1.600624.

[27] R. Ghorbani, F. Matta, M.A. Sutton, Full-field deformation measurement and crack mapping on confined masonry walls using digital image correlation, Exp. Mech. 55 (2014) 227–243. doi:10.1007/s11340-014-9906-y.

[28] F. Bernachy-Barbe, L. Gélébart, M. Bornert, J. Crépin, C. Sauder, Characterization of SiC/SiC composites damage mechanisms using digital image correlation at the tow scale, Compos. Part A Appl. Sci. Manuf. 68 (2015) 101–109. doi:10.1016/j.compositesa.2014.09.021.

[29] Z. Chen, X. Shao, X. Xu, X. He, Optimized digital speckle patterns for digital image correlation by consideration of both accuracy and efficiency, Appl. Opt. 57 (2018) 884. doi:10.1364/ao.57.000884.

[30] B. Pan, D. Wu, L. Yu, Optimization of a three-dimensional digital image correlation system for deformation measurements in extreme environments., Appl. Opt. 51 (2012) 4409–4419.

[31] T. Whitlow, E. Jones, C. Przybyla, In-situ damage monitoring of a SiC / SiC ceramic matrix composite using acoustic emission and digital image correlation, Compos. Struct. 158 (2016) 245–251. doi:10.1016/j.compstruct.2016.09.040.

[32] B.P. Croom, W.M. Wang, J. Li, X. Li, Unveiling 3D deformations in polymer composites by coupled micro X-ray computed tomography and volumetric digital image correlation, Exp. Mech. 56 (2016) 999–1016. doi:10.1007/s11340-016-0140-7.

[33] B.P. Croom, P. Xu, E.J. Lahoda, C.P. Deck, X. Li, Quantifying the three-dimensional damage and stress redistribution mechanisms of braided SiC/SiC composites by in situ volumetric digital image correlation, Scr. Mater. 130 (2017) 238–241. doi:10.1016/j.scriptamat.2016.12.021.

[34] C.P. Deck, H.E. Khalifa, B. Sammuli, T. Hilsabeck, C.A. Back, Fabrication of SiC–SiC composites for fuel cladding in advanced reactor designs, Prog. Nucl. Energy. 57 (2012) 38–45. doi:10.1016/J.PNUCENE.2011.10.002.

[35] C.H. Bumgardner, F.M. Heim, D.C. Roache, A. Jarama, M.C. Price, C.P. Deck, X. Li, Analysis of SiC/SiC composites for energy applications at ambient conditions, J. Am. Ceram. Soc. 104 (2021) 481–491. doi:10.1111/jace.17462.

[36] V.P. Rajan, M.N. Rossol, F.W. Zok, Optimization of digital image correlation for high-resolution strain mapping of ceramic composites, Exp. Mech. 52 (2012) 1407–1421. doi:10.1007/s11340-012-9617-1.

[37] M.A. Sutton, J. Yan, X. Deng, C.-S. Cheng, P. Zavattieri, Three-dimensional digital image correlation to quantify deformation and crack-opening displacement in ductile aluminum under mixed-mode I/III loading, Opt. Eng. 46 (2007) 051003. doi:10.1117/1.2741279.

[38] L.C.S. Nunes, J.M.L. Reis, Estimation of crack-tip-opening displacement and crack extension of glass fiber reinforced polymer mortars using digital image correlation method, Mater. Des. 33 (2012) 248–253. doi:https://doi.org/10.1016/j.matdes.2011.07.051.

[39] S. Lai, L. Shi, A. Fok, H. Li, L. Sun, Z. Zhang, A new method to measure crack extension in nuclear graphite based on digital image correlation, Sci. Technol. Nucl. Install. (2017) 2416545. doi:10.1155/2017/2416545.

[40] G. Singh, S.T. Gonczy, C.P. Deck, E. Lara-Curzio, Y. Katoh, Interlaboratory round robin study on axial tensile properties of SiC-SiC CMC tubular test specimens, Int. J. Appl. Ceram. Technol. (2018) 1–16. doi:10.1111/ijac.13010.

[41] F. Bernachy-Barbe, L. Gélébart, M. Bornert, J. Crépin, C. Sauder, Anisotropic damage behavior of SiC/SiC composite tubes: multiaxial testing and damage characterization, Compos. Part A Appl. Sci. Manuf. 76 (2015) 281–288. doi:10.1016/J.COMPOSITESA.2015.04.022.

[42] E. Rohmer, E. Martin, C. Lorrette, Mechanical properties of SiC/SiC braided tubes for fuel cladding, J. Nucl. Mater. 453 (2014) 16–21. doi:10.1016/J.JNUCMAT.2014.06.035.

[43] S. Wu, L. Cheng, Q. Zhang, L. Zhang, Y. Xu, Thermophysical and mechanical properties of a three-dimensional Hi – Nicalon / SiC composite, Int. J. Appl. Ceram. Technol. 3 (2006) 75–79. doi:10.1111/j.1744-7402.2006.02056.x.

[44] B.L. Wing, J.W. Halloran, Relaxation of residual microstress in reaction bonded silicon carbide, Ceram. Int. 44 (2018) 11745–11750. doi:10.1016/j.ceramint.2018.03.253.

[45] D. Maier-Schneider, J. Maibach, E. Obermeier, D. Schneider, Variations in Young's modulus and intrinsic stress of LPCVD-polysilicon due to high-temperature annealing, J. Micromechanics Microengineering. 5 (1995) 121–124. doi:10.1088/0960-1317/5/2/016.

[46] X. Zhang, T. Zhang, M. Wong, Y. Zohar, Effects of high-tempearture rapid thermal annealing on the residual stress of LPCVD-polysilicon thin films, in: Tenth Annu. Work. Micro Electro Mech. Syst. IEEE 1997 Jan 26–30; Nagoya, Japan. IEEE; 1997535–40., Nagoya, Japan, 1997: pp. 535–540.

[47] M.W. Knauf, C.P. Przybyla, A.J. Ritchey, R.W. Trice, R.B. Pipes, Measuring the effects of heat treatment on SiC/SiC ceramic matrix composites using Raman spectroscopy, J. Am. Ceram. Soc. (2019) 1293–1303. doi:10.1111/jace.16724.

[48] Y. Chai, X. Zhou, H. Zhang, Y. Zhang, The effect of heat treatment on the properties of SiC/SiC composites prepared with different SiC fibers, Fusion Sci. Technol. 75 (2019) 112–119.

[49] H. Araki, H. Suzuki, W. Yang, S. Sato, T. Noda, Effect of high temperature heat treatment in vacuum on microstructure and bending properties of SiCf/SiC composites prepared by CVI, J. Nucl. Mater. 258–263 (1998) 1540–1545. doi:10.1016/S0022-3115(98)00293-1.

[50] W.C. Oliver, G.M. Pharr, An improved technique for determining hardness and elastic modulus using load and displacement sensing indentation experiments, J. Mater. Res. 7 (1992) 1564–1583. doi:10.1557/JMR.1992.1564.

[51] W.C. Oliver, G.M. Pharr, Measurement of hardness and elastic modulus by instrumented indentation: Advances in understanding and refinements to methodology, J. Mater. Res. 19 (2004) 3–20. doi:10.1557/jmr.2004.19.1.3.

[52] X. Li, B. Bhushan, Micro/nanomechanical characterization of ceramic films for microdevices, Thin Solid Films. 340 (1999) 210–217. doi:10.1016/S0040-6090(98)01153-5.

[53] T. Zhang, Y. Feng, R. Yang, P. Jiang, A method to determine fracture toughness using cube-corner indentation, Scr. Mater. 62 (2010) 199–201. doi:10.1016/j.scriptamat.2009.10.025.

[54] B.R. Lawn, A.G. Evans, D.B. Marshall, Elastic / plastic indentation damage in ceramics: I. the median / radial crack system, J. Am. Ceram. Soc. 63 (1980) 574.

[55] D. Frazer, C.P. Deck, P. Hosemann, High-temperature nanoindentation of SiC/SiC composites, Jom. 72 (2020) 139–144. doi:10.1007/s11837-019-03860-7.

[56] T. Koyanagi, Y. Katoh, G. Singh, M. Snead, SiC / SiC Cladding Materials Properties Handbook, Oak Ridge, TN, 2017. https://info.ornl.gov/sites/publications/Files/Pub100714.pdf.

[57] M. Wilson, E.J. Opila, A review of SiC fiber oxidation with a new study of Hi-Nicalon SiC fiber oxidation, Adv. Eng. Mater. 18 (2016) 1698–1709. doi:10.1002/adem.201600166.

[58] B. McFarland, E.J. Opila, Silicon carbide fiber oxidation behavior in the presence of boron nitride, J. Am. Ceram. Soc. 101 (2018) 5534–5551. doi:10.1111/jace.15807.

[59] R.S. Hay, G.E. Fair, R. Bouffioux, E. Urban, J. Morrow, A. Hart, M. Wilson, Hi-nicalon-S SiC fiber oxidation and scale crystallization kinetics, J. Am. Ceram. Soc. 94 (2011) 3983–3991. doi:10.1111/j.1551-2916.2011.04647.x.

[60] M.Z. Berbon, K.L. Rugg, M.S. Dadkhah, D.B. Marshall, Effect of weave architecture on tensile properties and local strain heterogeneity in thin-sheet C-SiC composites, J. Am. Ceram. Soc. 85 (2002) 2039–2048. doi:10.1111/j.1151-2916.2002.tb00401.x.

[61] G.N. Morscher, H.M. Yun, J.A. Dicarlo, In-plane cracking behavior and ultimate strength for 2D woven and braided melt-infiltrated SiC/SiC composites tensile loaded in off-axis fiber directions, J. Am. Ceram. Soc. 90 (2007) 3185–3193. doi:10.1111/j.1551-2916.2007.01887.x.

[62] C.P. Yang, G.Q. Jiao, B. Wang, T. Huang, Mechanical degradation mechanisms of 2D-C/SiC composites: Influences of preloading and oxidation, J. Eur. Ceram. Soc. 35 (2015) 2765–2773. doi:10.1016/j.jeurceramsoc.2015.04.011.

[63] I. Hofinger, M. Oechsner, H.A. Bahr, M. V. Swain, Modified four-point bending specimen for determining the interface fracture energy for thin, brittle layers, Int. J. Fract. 92 (1998) 213–220. doi:10.1023/A:1007530932726.

[64] Y. Yin, Y. Qiao, S. Hu, Four-point bending tests for the fracture properties of concrete, Eng. Fract. Mech. 211 (2019) 371–381. doi:10.1016/j.engfracmech.2019.03.004.

[65] J. Xu, V.K. Sarin, S. Dixit, S.N. Basu, Stability of interfaces in hybrid EBC/TBC coatings for Si-based ceramics in corrosive environments, Int. J. Refract. Met. Hard Mater. 49 (2015) 339–349. doi:10.1016/j.ijrmhm.2014.08.013.

[66] M.P. Appleby, D. Zhu, G.N. Morscher, Mechanical properties and real-time damage evaluations of environmental barrier coated SiC/SiC CMCs subjected to tensile loading under thermal gradients, Surf. Coatings Technol. 284 (2015) 318–326. doi:10.1016/j.surfcoat.2015.07.042.

[67] M.N. Rossol, J.H. Shaw, H. Bale, R.O. Ritchie, D.B. Marshall, F.W. Zok, Characterizing weave geometry in textile ceramic composites using digital image correlation, J. Am. Ceram. Soc. 96 (2013) 2362–2365. doi:10.1111/jace.12468.

[68] S. Yaofeng, J.H.L. Pang, Study of optimal subset size in digital image correlation of speckle pattern images, Opt. Lasers Eng. 45 (2007) 967–974.

CHAPTER 7: PROBING THE LOCAL CREEP MECHANISMS OF SiC/SiC CERAMIC MATRIX COMPOSITES WITH HIGH TEMPERATURE NANOINDENTATION

1. Introduction

Silicon carbide fiber, silicon carbide matrix composites (SiC/SiC CMCs) are extensively studied materials for aerospace and nuclear energy applications and highly valued for their excellent thermomechanical properties. Their mechanical performance is the subject of many past and ongoing studies, which aim to elucidate critical relationships between bulk composite mechanical properties and individual constituent properties [1–4], CMC weave architecture [5,6], load rate and orientation [7,8], porosity, and temperature [9,10]. It is also well documented that the tensile stress-strain behavior of CMCs varies with the composite architecture and microstructure. Work performed by Morscher *et al*. [6,8] closely examined the mechanical performance during tension testing of multiple CMCs, distinguished by architecture, fiber fraction, and off-axis loading angle. Such prior work has demonstrated the importance of the local microstructure to CMC mechanical performance. Thus, it is important to consider the properties of individual constituents during the manufacture of CMCs in order to optimize the bulk composite performance and properties.

In this study, the time-dependent mechanical performance and creep response of SiC/SiC CMCs were considered, which have not been as thoroughly investigated. Particularly for aerospace applications, where turbine operating temperatures can exceed 1300°C [11,12], it is critically important to probe the creep response of these materials. Creep is a recognized cause of failure of turbine blades at high temperature, but it is not limited to high temperatures. It is commonly misinterpreted that ceramics do not creep at low temperatures (less than a third of the melting temperature); however, this assumption is not always valid. Both metals and ceramics can undergo diffusion-controlled creep though the activation energies required for creep in metals are much lower than in ceramics. If the activation energy is reached in a ceramic, either due to high temperature, large stress (such as the large local stress due to indentation [13]), or a combination of both, the material will creep [14]. For this reason, creep rate was expected to increase with the test temperature. Furthermore, it was hypothesized that increasing microstructural complexity, such as that

experienced when testing single crystals through ceramic composites, would significantly impact the creep response. Single crystal creep is likely limited to vacancy diffusion through the lattice, but with greater material heterogeneity, vacancies may travel along grain and material constituent boundaries [14]. Under certain situations, it could be appropriate to model this creep response with Nabarro-Herring or Coble creep equations; however, in recognition of the large degree of structural variation in CMC components, a more rudimentary equation was proposed to describe the creep response presented in Sections 3.2 and 3.3.

Thus, the objective of this work was to begin to fill the gaps in literature and to elucidate the connection between the creep response of individual constituents and of the bulk SiC/SiC composite. Prior studies have examined the bulk tensile creep of CMCs [15,16] and creep of individual SiC fibers [17]. However, bulk tensile testing cannot isolate the contributions of individual constituents nor can testing of individual components alone fully illustrate how composites integrate mechanical properties. It is important the creep response of CMCs is well understood to correlate the effects of elevated temperature with the fast fracture mechanisms of CMCs and to ascertain the role of individual constituents toward the bulk composite creep response to inform CMC manufacturing.

A challenge in isolating the contributions of individual constituents was the limited availability of suitable experimental methodologies; most creep studies relied on tension or flexural experiments, which prohibit identifying the role of local features within the CMC structure. Here, instrumented nanoindentation was applied at temperatures up to 800 °C to probe the creep response of constituents within the CMC as well as the response of single and poly crystalline Si and SiC and reaction bonded SiC. This approach gradually introduced greater material heterogeneity to resolve the role of CMC heterogeneity on bulk composite creep. Finally, a rule of mixtures analytical model was proposed to describe the contribute of individual constituent creep response to the overall response of the CMC.

2. Experimental Procedure

2.1. Materials

Indentations were performed on specimens of single (sc) and poly crystalline (pc) silicon and silicon carbide (University Wafer) and reaction bonded (rb-SiC) silicon carbide (CoorsTek). Si and SiC materials were cut as wafers and mechanically polished to a mirror-like finish. The sc-Si wafer had a <100> orientation; the sc-SiC wafer was a 6-hexagonal polymorph. All wafers were at least 250 μm thick, ensuring adequate material for indentations as deep as 7.5 μm without experiencing edge effects (most indentations were performed to depths <1 μm).

Panels of multilayer SiC/SiC CMCs with a two-dimensional, woven tow architecture (0°/90° tow orientation) were provided by Rolls-Royce Corporation for testing. The CMC tows consisted of Hi-Nicalon Type S fibers, chemical vapor infiltrated (CVI) SiC matrix, and boron nitride fiber/matrix interphase. The tow preform was infiltrated via silicon melt infiltration (SMI), resulting in a SiC matrix with silicon alloy particulates. Specimens were cut with a thickness of about 1 mm using a circular-bladed diamond saw and mechanically polished using mineral oil and 0.5 μm grit diamond paste.

2.2. Experimental Setup

All tests were conducted on a Micro Materials Ltd. Nanotest Vantage [18,19] indenter with high temperature stage, which enabled fine displacement control with a resolution of <0.01 nm. All indentations were performed with an alumina spherical indenter. An integrated optical microscope stage was used to precisely position indentations on the specimen to target specific constituents. Importantly, it must be acknowledged early that the use of the alumina indenter tip raised a challenge. SiC and the alumina indenter tip have comparable material hardness, so the tip could not be assumed to be rigid relative to the substrate material. Thus, system compliance was measured before and after testing at each temperature and corrected for prior to analyzing indentation results. Compliance tests were conducted with a single crystal sapphire wafer of similar stiffness to the indenter to account for compliance of the indenter tip itself.

Nanoindentation was performed according to the Oliver-Pharr methodology [20,21], where the Young's modulus may be derived using the equation:

$$\frac{1}{E_R} = \frac{(1-\upsilon_i{}^2)}{E_{Y,i}} + \frac{(1-\upsilon_s{}^2)}{E_{Y,s}} \tag{7.1}$$

Here, *i* and *s* refered to the indenter and substrate properties of Young's Modulus, E_Y, and Poisson's ratio, ν. The reduced modulus E_R was calculated from properties extracted directly from the indentation curve as shown here:

$$E_R = \beta \frac{S}{2}\sqrt{\frac{\pi}{A}} \tag{7.2}$$

The term β is a geometric factor based on the indenter geometry. The initial slope of the unloading curve is equivalent to the material stiffness *S*. The indentation contact area *A* is calculated as follows:

$$A = \pi R_c^2 = \pi(2d_c R - d_c^2) \tag{7.3}$$

Here, *R* was the indenter radius (250 μm), R_c was the contact radius with the surface, and d_c was the contact depth (Figure 7.1a).

Material creep, or the indenter displacement at the max load, was recorded for each individual indentation. A max load hold time of 60 s was used to ensure sufficient time to obtain a clear primary and secondary (pseudo-steady-state) creep region.

Indentations were performed across each specimen at a load of 300 mN to minimize the variation in local indentation contact stress. The high temperature configuration (Figure 7.1b) featured two heating elements, within the indenter and sample stage, and three thermocouples, mounted to the indenter, the sample stage heater (located about 1 cm behind the actual sample), and on the surface of the sample stage just to the side of the specimen. The power to the indenter and stage heating elements was adjusted to minimize thermal drift and to achieve the desired test temperature as measured by the thermocouple mounted on the stage surface. A heating rate of 1.6 °C/min was used for all temperature testing with a stabilization period of at least 30 min to allow the system to reach a stable temperature. All tests at elevated temperature were performed in an inert Argon gas environment.

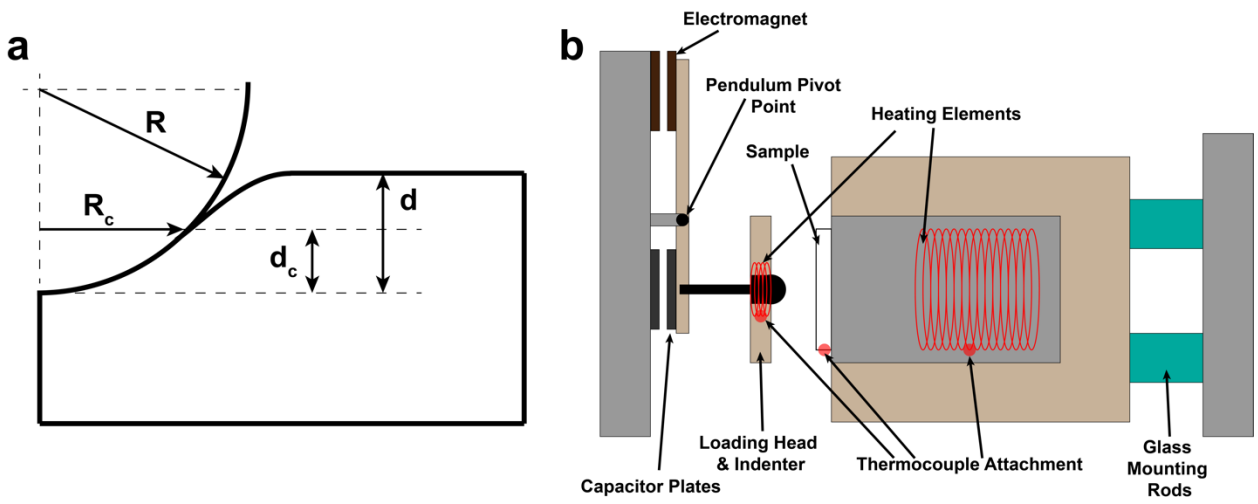

Figure 7.1. (a) Diagram of the indentation displacement d and contact depth d_c. (b) Schematic of the Micro Materials high temperature indentation setup, featuring heating elements within the loading head and sample stage and three thermocouples.

3. Theory

3.1. Spherical Indentation Material Deformation

Indentation is advantageous over tensile testing in its inherent capability to target local mechanical properties; thus, it is possible to isolate individual constituents within a composite. Furthermore, it is not feasible or meaningful to draw a direct comparison between tensile and indentation creep results despite the temptation. Much like tensile creep testing, indentation creep testing, conducted in a manner consistent as described in Section 2.2 will produce a creep strain curve reminiscent of one obtained from a tensile creep testing with distinguishable primary and secondary creep regions. However, it is a technical challenge to measure material plasticity via indentation; the plastic response will depend on the yield and work hardening response of the material, on indentation depth, and on the indenter shape. There is no uniformly loaded sample, and the load and distribution of stresses within the material will change with indentation depth and shape and by surrounding material constituents. It is technically improper to denote the observed secondary region of indentation creep as steady-state because as the material creeps, the stress is itself time dependent. However, the effective indentation stress was quantified in this study as a function of load F

and contact radius R_c (itself a function of time t), as shown by Herbert, *et al*. [22] and others [23]:

$$\sigma = \frac{F}{\pi(R_C(t))^2} \tag{7.4}$$

This effective stress established a point around which to compare the secondary creep rate of the various materials tested in this study.

Accounting for the deformation of the surrounding material constituents was even more challenging, and the task of describing this material deformation has been the subject of many studies over decades. These works have theorized there are zones of material deformation beneath the indenter contact point; these zones are summarized by Nix and Gao [24]. Beginning at the point of contact, there is a hydrostatic core, then moving outward, there are plastic and elastic deformation zones [24–26]. These material models have been studied and supported by experimental indentation on single and poly crystalline materials [27,28], but these works also acknowledge the size and shape of these zones will vary by indentation geometry and substrate material. For conical or spherical indenters, it was assumed the zones were hemispherical.

This zone of deformation may be characterized by elastic and plastic deformation. In the case of ceramics, the contributors to the plastic deformation would be the crushing of the material from the indenter contact and from diffusion-controlled creep within individual grain lattice structures and/or along grain/constituent boundaries [14]. Thus, it was also assumed that interactions with multiple constituents for heterogeneous materials like CMC would impact these zones, distorting their shape and impact on the material deformation, creating an indentation creep location dependence. It then became necessary to estimate a zone of deformation influence, *i.e*., a volume of material around the indentation which influences the deformation and creep, and to determine which constituents are contained within that zone.

3.2. Numerical Simulation

To quantify the limits of these deformation zones, an axisymmetric finite element model (Figure 7.2) was assembled in ANSYS Mechanical APDL (version 19.2). For initial modeling of the indentation of

single crystal materials, the simulation applied a linear-elastic, isotropic material model, which was modified to capture the inelastic creep response according to the equation [29]:

$$\varepsilon_{cr} = \frac{C_1 \sigma^{C_2} t^{C_3+1} e^{-C_4/T}}{C_3+1} + C_5 \sigma^{C_6} t e^{-C_7/T} \tag{7.5}$$

Here, the coefficients C_i were found by fitting Equation 7.5 to experimental data using a least squares methodology coded in Python. Coefficients C_1 and C_5 were scaling factors, coefficients C_4 and C_7 regulated the temperature dependence, and coefficients C_2 and C_6 controlled the stress dependence. Generally speaking, the $e^{-C_i/T}$ terms would decay with time, representing the transition from primary to secondary creep. From Equation 7.4, we had also shown that σ was itself a function of time t.

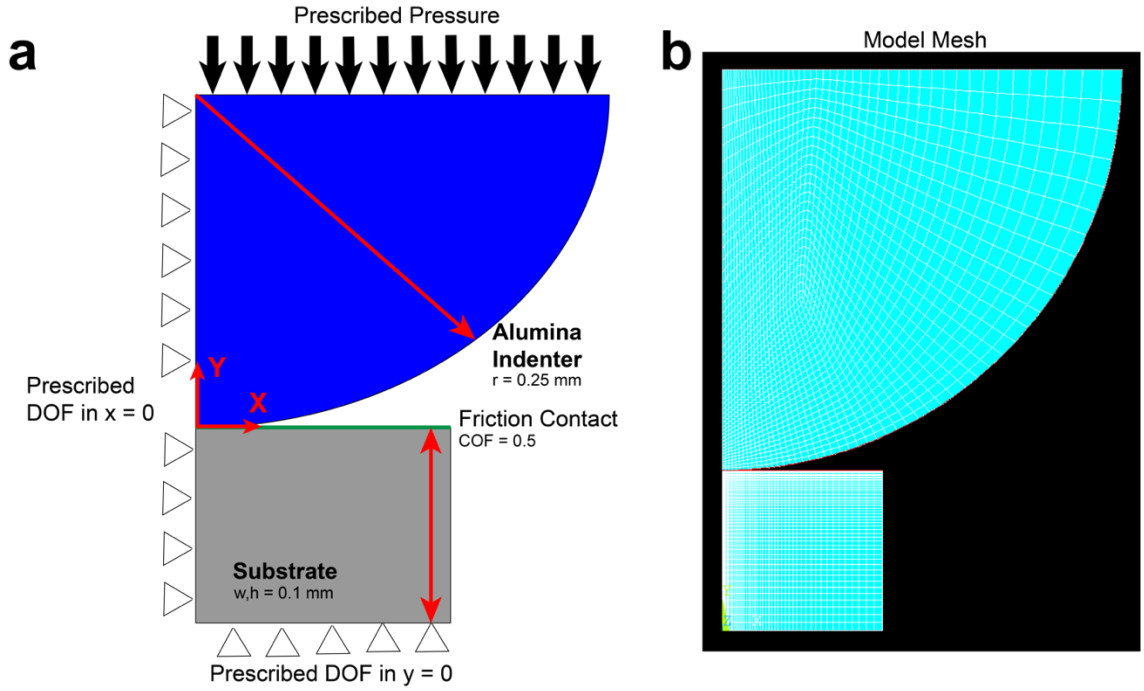

Figure 7.2. (a) Schematic of the ANSYS indentation model with boundary conditions and applied loading. (b) The meshed finite element model, showing the ratio of element sizing toward the contact point between the indenter and the substrate.

The finite element model was sized to capture the accurate proportions of the alumina spherical indenter used in experimental work with a radius of 250 μm. The substrate was sized to a height and width of 100 μm to allow for full indentations matching the largest in experiments and large enough to minimize edge

effects; this size was selected based on the work of Xu and Li [30], in which the authors identified ratios of indentation-to-substrate dimensions to minimize edge effects. The model indenter and substrate were positioned with a single point of contact, representing the point just before the indenter displaces the substrate surface. The model was meshed to concentrate elements near the site of indentation using a 1:10 inside-to-outside element ratio. A prescribed pressure was applied to the top elements of the indenter based on the desired indentation load. Finally, boundary conditions were placed along the inside axis of both the indenter and substrate, restricting lateral movement in the x-direction while a boundary condition was placed along the bottom surface of the substrate to restrict motion in the y-direction (Figure 7.2). Equivalent boundary conditions were commonly reported in similar, axisymmetric indentation simulations found in literature [31,32].

3.3. Development of an Analytical Creep Model

An analytical creep model was assembled to integrate the effects of material heterogeneity rather than directly modeling individual constituents. The foundation of this model was the analytical description of creep described by Equation 7.5; as noted, that equation was applicable to homogeneous, isotropic materials, which the CMC was not. Thus, a new model was necessary to describe the response of the CMC. If Equation 7.5 could be shown to reflect the creep response of individual, homogeneous constituents via indentation of single and polycrystalline silicon and silicon carbide, then it was hypothesized the aggregate response of those constituents may be effectively captured by a rule of mixtures approach.

From a rule of mixtures approach, two types of materials systems were considered: (i) materials in series and (ii) materials in parallel (Figure 7.3). A model based on materials in series assumed the creep response of the aggregate system ε_{cr} was simply the sum of the creep response of individual constituents $\varepsilon_{cr,i}$ as described by:

$$\varepsilon_{cr} = \sum_{i=1} M_i \varepsilon_{cr,i} \text{ where } \sum_{i=1} M_i = 1. \quad (7.6)$$

Here, coefficients of M_i represented the fraction of the material composed of each constituent i. The

creep response of an individual constituent $\varepsilon_{cr,i}$ may be described by Equation 7.5. Such a model may be appropriate for indentation creep purely within the SMI matrix regions, where SiC matrix and Si particulate were mixed randomly, but it was not applicable to any indentation region extended into the fiber tows.

Any creep indentation reflecting the influence of the fiber tows was better described by a parallel rule of mixtures model as follows:

$$\varepsilon_{cr} = \left(\sum_{i=1} \frac{M_i}{\varepsilon_{cr,i}}\right)^{-1} \text{ where } \sum_{i=1} M_i = 1. \tag{7.7}$$

Within the tows, the material was not randomly structured. Instead, fibers ran parallel with each other, forming a highly ordered structure.

To solve the analytical model, the coefficients C_i from Equation 7.5 were identified through a least-squares methodology to fit a curve to the experimental creep data. The material fractions coefficients M_i were determined via an image analysis technique discussed in Section 5.2.

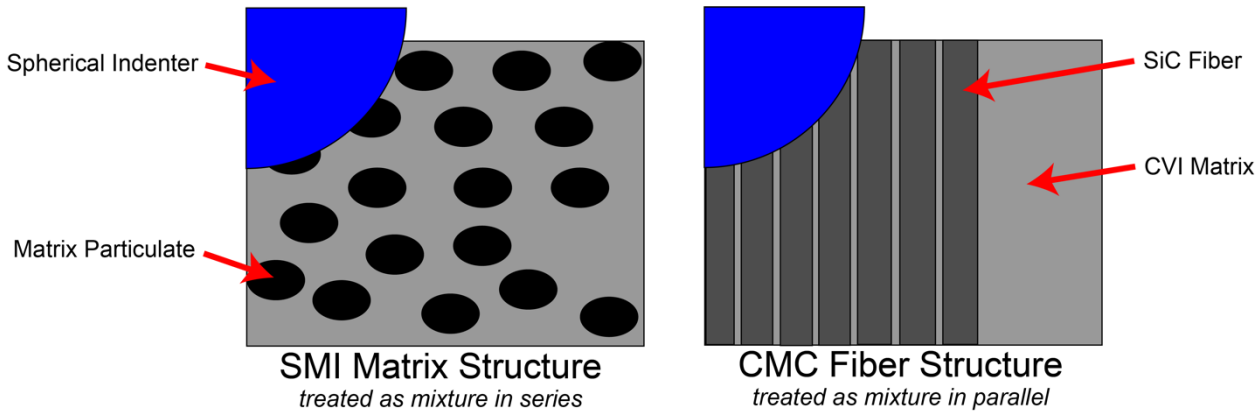

Figure 7.3. Schematic representation of the two primary microstructures considered. The SMI matrix (left) is modeled as a mixture in series while the fiber tow (right) is modeled as a mixture in parallel.

4. Results

Young's modulus was determined via spherical indentation as described by Equation 7.1 and presented in Table 7.1. As expected, modulus values generally indicated excellent thermal stability for each material through 800 °C. However, these modulus values provided experimental validation of the indentation

methodology to identify the material stiffness and deformation; resulting modulus values agreed well with those presented in literature. Expected literature values for the modulus of Si ranged from 124 to 160 GPa depending on crystal orientation [33–36] and for SiC from 390 to 450 GPa depending on SiC grade [37,38].

Indentations on the CMC were targeted to two regions: the fiber/CVI matrix region and the SMI matrix region. Within the fiber/CVI matrix regions, indentations would interact with fibers and the CVI matrix within a single tow. To reduce some of the experimental variation, indentations were only performed where the fiber were oriented perpendicular to the top surface, and the effect of the orientation of the fiber tows was not examined here. It is hypothesized that the orientation effect could still be adequately described by a rule-of-mixtures model; the orientation may however add another parameter to consider beyond the constituent fraction. Within the SMI matrix regions, the indentations would reflect properties of the Si particulate and SiC matrix. The modulus of the CMC varied significantly depending on the specific constituents used, the architecture of tows, and the fiber-matrix interface coating, but typically, the modulus ranged from 240 to 380 GPa [6,39–41].

Table 7.1. Measured Young's modulus via spherical indentation of single crystal (sc) Si and polycrystalline (pc) Si, of sc-SiC and pc-SiC, and of reaction bonded (rb) SiC.

Material	Young's Modulus (GPa)		
	23 °C	300 °C	800 °C
sc-Si	126 ± 2	126 ± 8	121 ± 9
pc-Si	162 ± 5	157 ± 6	152 ± 10
sc-SiC	410 ± 6	395 ± 22	387 ± 31
pc-SiC	399 ± 20	388 ± 21	380 ± 15
rb-SiC	380 ± 12	334 ± 23	347 ± 16
CMC SiC Fiber / CVI Matrix	345 ± 14	342 ± 19	327 ± 20
CMC SMI Matrix	299 ± 16	271 ± 37	267 ± 32

The spherical indentation creep response was also measured over a 60 second period at the max load of 300 mN. Representative creep curves at 800 °C are presented in Figure 7.4 for sc-Si, pc-Si, sc-SiC, pc-SiC, and rb-SiC. Figure 7.5 presents representative creep curves for CMC indentations at 23, 300, and 800 °C. The curves presented in both Figure 7.4 and Figure 7.5 correspond to indentations with an applied load of 300 mN. Several immediate observations were made: (i) The single and polycrystalline materials

exhibited typical creep curves with a clear primary and secondary region. (ii) The rb-SiC and CMC materials exhibited typical creep curves at 23 and 300 °C, but at 800 °C, their creep response was characterized by oscillations.

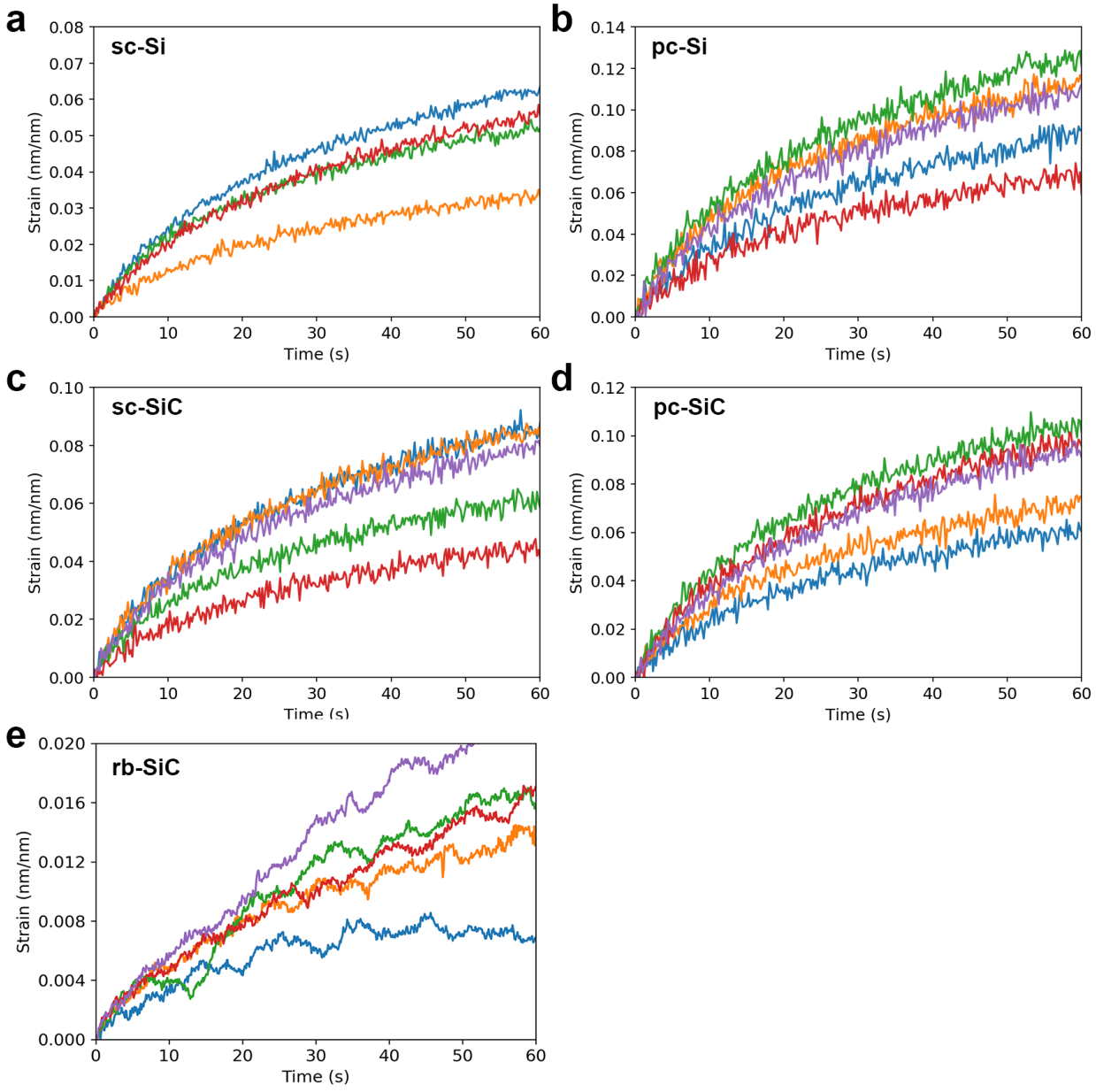

Figure 7.4. Representative indentation creep curves at 800 °C for (a) sc-Si and (b) pc-Si, for (c) sc-SiC and (d) pc-SiC, and (e) rb-SiC. The different colors within each plot represent individual indentations.

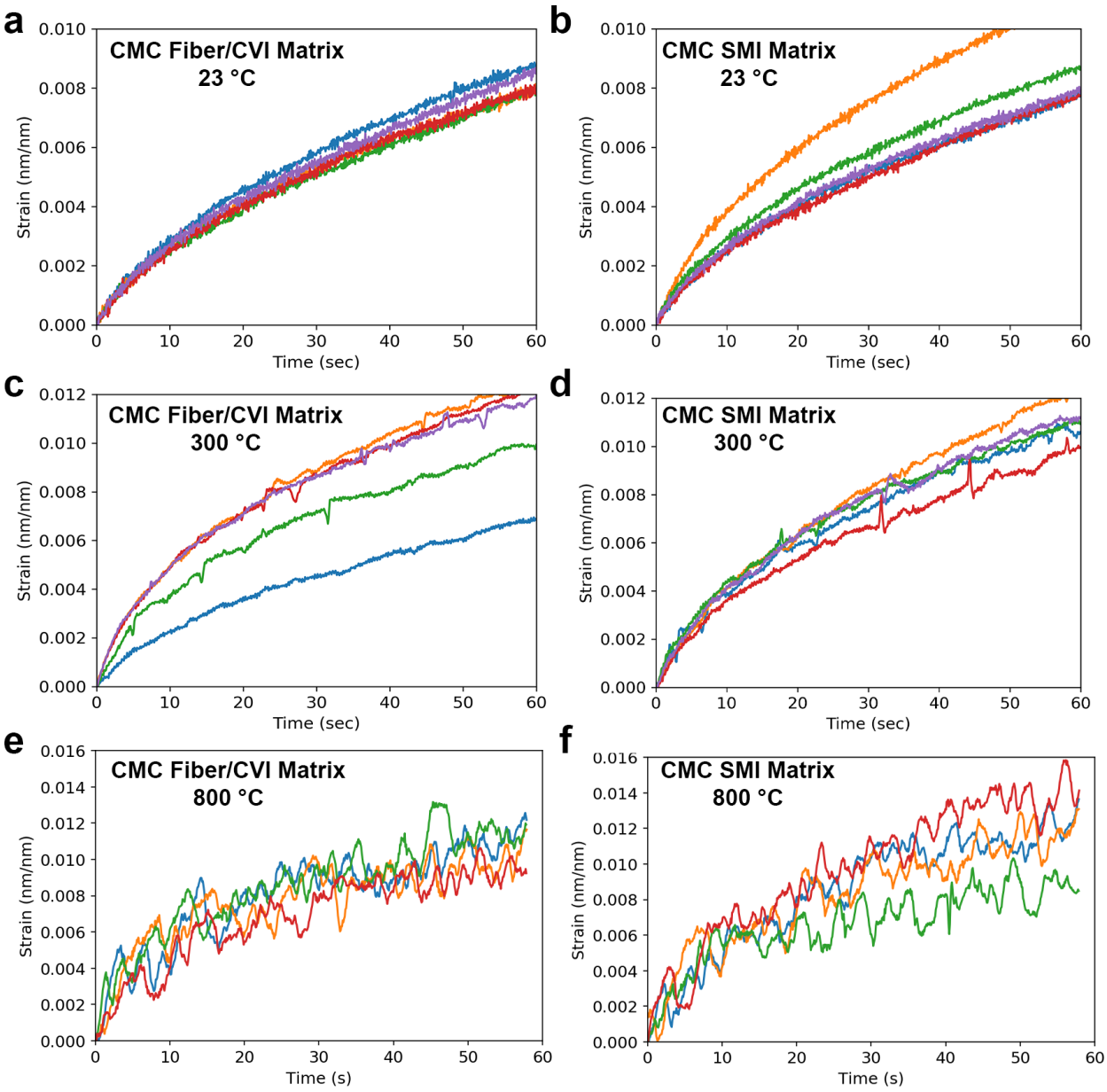

Figure 7.5. Representative indentation creep curves conducted on (left) fiber/CVI matrix and (right) SMI matrix regions of CMC at (a,b) 23°C, (c,d) 300°C, and (e,f) 800 °C. The different colors within each plot represent individual indentations.

5. Discussion

5.1. Characterization of Material Indentation Creep Response

To my knowledge, the oscillations observed in the 800 °C rb-SiC and CMC creep curves have not been documented elsewhere. It was hypothesized these oscillations could be an artifact of physical interactions between material constituents at higher temperatures. These oscillations were observed over multiple sets of indentations; they could not be attributed to a one-time phenomenon. A possible source for the oscillations could be thermal drift between the indenter and specimen; thermal drift would also become more and more pronounced at higher temperatures, which could explain the temperature-dependence of this oscillation phenomenon. Thermal drift was measured for each indentation by tracking how much the probe moved or 'drifted' at a low load, and the average drift for 800 °C indentations are reported in Table 7.2. These drift measurements showed the rb-SiC and CMC indentations experienced no abnormal thermal drift behavior relative to the indentations on single and polycrystalline materials. The oscillations appeared to be superimposed over a typical primary and secondary creep response, so it may be reasonable to still estimate the strain rate by the overall trend during the secondary creep region.

Table 7.2. Measured indenter thermal drift (10^{-3} nm/s) at 800 °C.

Material	Experimental Thermal Drift (10^{-3} nm/s)
sc-Si	251 ± 31
pc-Si	239 ± 31
sc-SiC	161 ± 38
pc-SiC	178 ± 46
rb-SiC	176 ± 41
CMC SiC Fiber / CVI Matrix	223 ± 37
CMC SMI Matrix	187 ± 45

The strain rate was determined via a linear fit of the secondary creep regime. For all tested materials, the secondary creep strain rate increased with temperature (Figure 7.6a). The strain rate of sc-SiC was also larger at all temperatures than sc-Si. Similarly, the strain rate of pc-SiC also generally exceeded that of pc-Si at each temperature. The strain rate of polycrystalline materials was also notably larger than that of the

single crystal, which reflects the influence of vacancy diffusion along grain boundaries [14]. The rb-SiC and CMC materials exhibited generally lower creep rates than the other materials, which was seemingly at odds with the expectation of higher creep rates with greater material complexity.

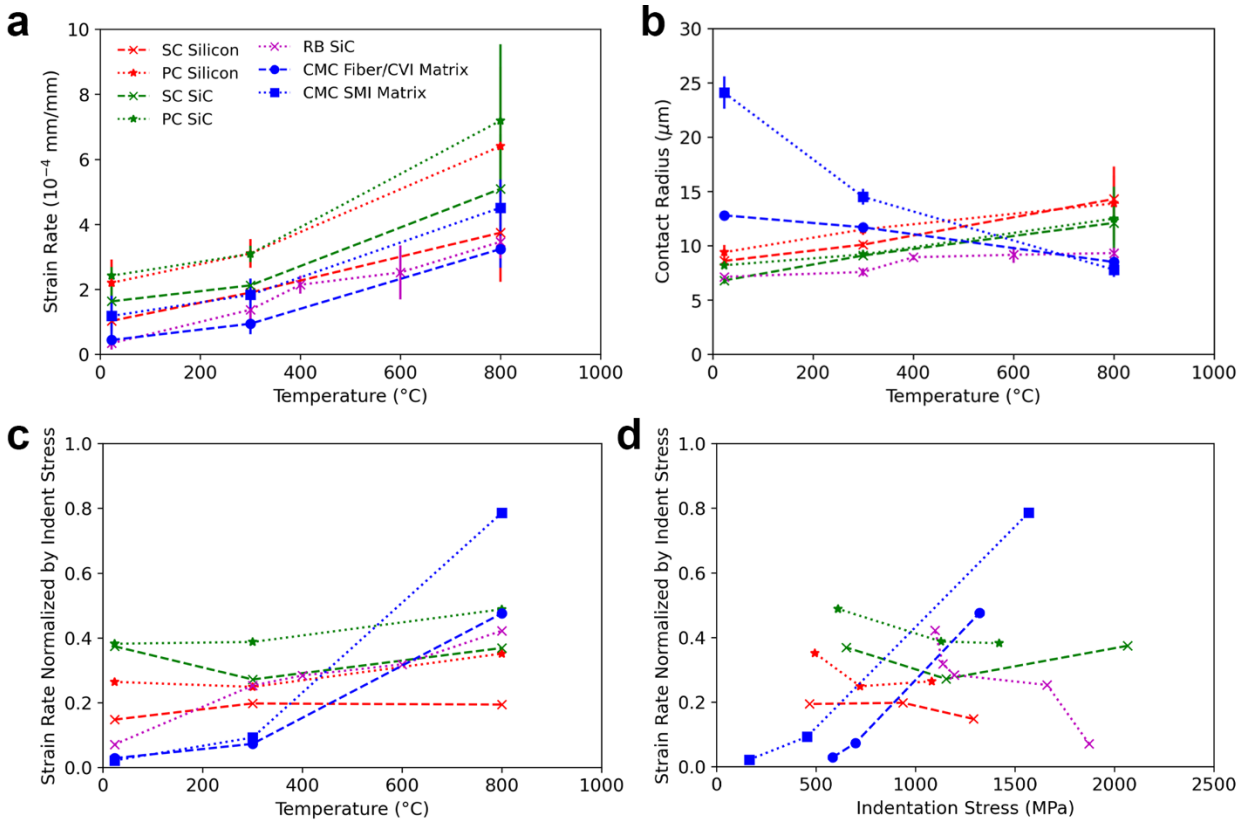

Figure 7.6. The results of spherical indentation are presented for each material. (a) Strain rate during secondary creep. (b) Indentation contact radius R_c at the end of each test ($t = 60\ s$). Strain rate normalized by indentation contact stress plotted against (c) temperature and (d) contact radius.

Many literature sources cite strain rates of 10^{-7} through 10^{-9} mm/mm for Si [42,43] and SiC [44,45]; however, as previously discussed, direct comparisons between indentation creep measurements and bulk creep measurements should not be drawn. Stresses are highly concentrated in indentation testing in contrast to the broad distribution of stress in bulk testing. In order to elucidate the cause of the lower strain rates in the CMC materials, local indentation contact stress was quantified at each indentation as described by

Equation 7.4 from the contact radius R_C (Figure 7.6b), and the measured strain rates were normalized by this contact stress (Figure 7.6c,d). These normalized strain rates indicated the creep of the single and polycrystalline materials was somewhat stable with temperature in contrast with the rb-SiC and CMC materials, which exhibited higher rates of creep with temperature. However, this observation must be paired with an understanding of the local contact area and stress implications. From Figure 7.6b, it was noted that the contact radius moderately increased for the single and polycrystalline materials and rb-SiC with temperature; however, the contact radius significantly decreased for the CMC materials with increasing temperature. The decreasing radius and thus decreasing contact area would result in a higher concentration of contact stress, which would drive a larger strain rate (Figure 7.6d). When normalized by contact stress, the strain rates of rb-SiC were more comparable to pc-SiC strain rates. These plots in Figure 7.6 illustrated the importance of local contact area and stress, as discussed in Section 3.1, when considering the creep response of indentation. In particular, the strain rates of the CMC materials indicated the creep response was highly dependent on the contact conditions. In contrast, the Si and SiC materials showed greater dependence on temperature than contact conditions, which was unsurprising given their lack of structural heterogeneity apart from grain boundaries and grain orientation.

5.2. Predicting the Indentation Zone of Deformation of SiC/SiC CMCs

The indentation experiments provided experimental references for the creep response of various materials, but the extent of the zone of deformation influence, that was the extent of pseudo-plastic and elastic deformation caused by the indentation, was unknown. The ANSYS simulation described in Section 3.2 was used to elucidate the dimensions of this zone. Rather than develop an ANSYS model incorporating the different constituents of the CMC, which would vary with every indentation location and with every CMC sample, the ANSY model only represented a uniform material substrate. It was assumed the zone of CMC deformation would be no larger than that for the SiC materials, given their comparable stiffness. Thus, the CMC material constituents interacting within this zone could be identified. The C_i coefficients from Equation 7.5 were determined via a curve fit of the experimental creep curves for each material (Figure

7.7). The ANSYS finite element model was then run for each material (sc-Si, pc-Si, sc-SiC, pc-SiC, rb-SiC), incorporating the linear elastic deformation and the creep response of each material, as described by Equation 7.5. The resulting displacement of the material surface (Figure 7.8a,b) and the extent of the distribution of stress (Figure 7.8c,d) were exported. These predictions were supported by Hertz contact calculations commonly found in literature [46]. The model-predicted zone of influence extended about 34.2 and 36.5 μm radially from the center point of the indentation at 23 °C and 800 °C, respectively; this radius was determined as the average point when the local stress fell below 5 % of the max substrate indentation stress during an indentation with an applied load of 300 mN.

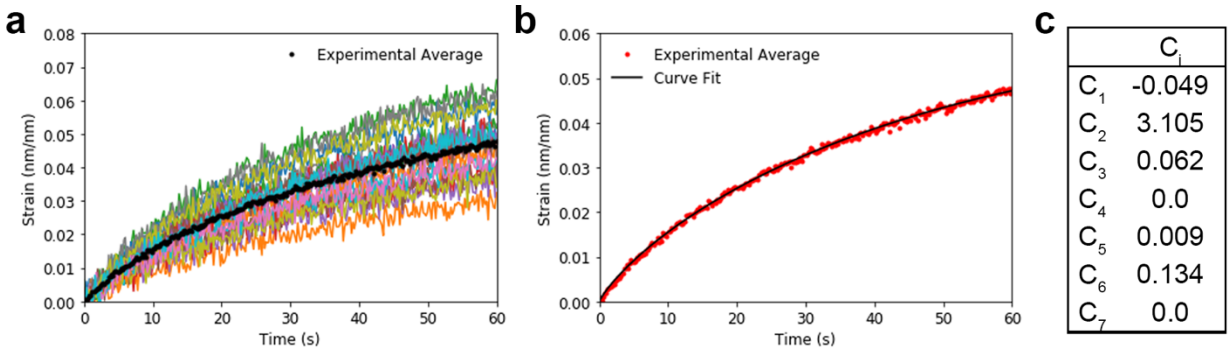

Figure 7.7. A representation of the application of the analytical creep model to single and polycrystalline materials. Shown here, (a) experimental creep curves for pc-Si at 23 °C with a 300 mN applied load were (b) averaged for curve fitting. The averaged curve was fit to solve for the (c) creep coefficients C_i described in Equation 7.5.

Having quantified an upper limit to the zone of deformation, a rule of mixtures model, as represented by Equations 7.6 and 7.7, was applied to incorporate the effects of different CMC material constituents within this zone. Optical micrographs were acquired of the region around every CMC indentation, and the material fraction coefficients M_i were assigned to represent the area proportion corresponding to each CMC constituent within the relevant area of influence around the known indentation location. For each indentation optical micrograph, the different constituents were identified by visual inspection and shaded to provide distinct contrast between constituents. The shaded images could be quickly processed in Python to quantify the number of pixels per constituent and thus approximate the fractional coefficients (Figure

7.9). X-ray tomography was attempted to characterize subsurface material fraction coefficients but lacked sufficient contrast to distinguish the individual constituents. Instead, it was assumed the sub-surface proportions of constituents to be roughly equivalent to the surface fractional coefficients. This assumption was valid for the materials in series model, where the constituents were somewhat randomly distributed, but for more accurate determination of the fractional coefficients, the coefficients should account for the radius of the zone of deformation influence relative to the organization of constituents in the materials in parallel model. The limitations of this assumption would be very small in comparison to the effect of the significant variation of fractional coefficients with indentation location, and the effects on the predictive analytical model would be minor.

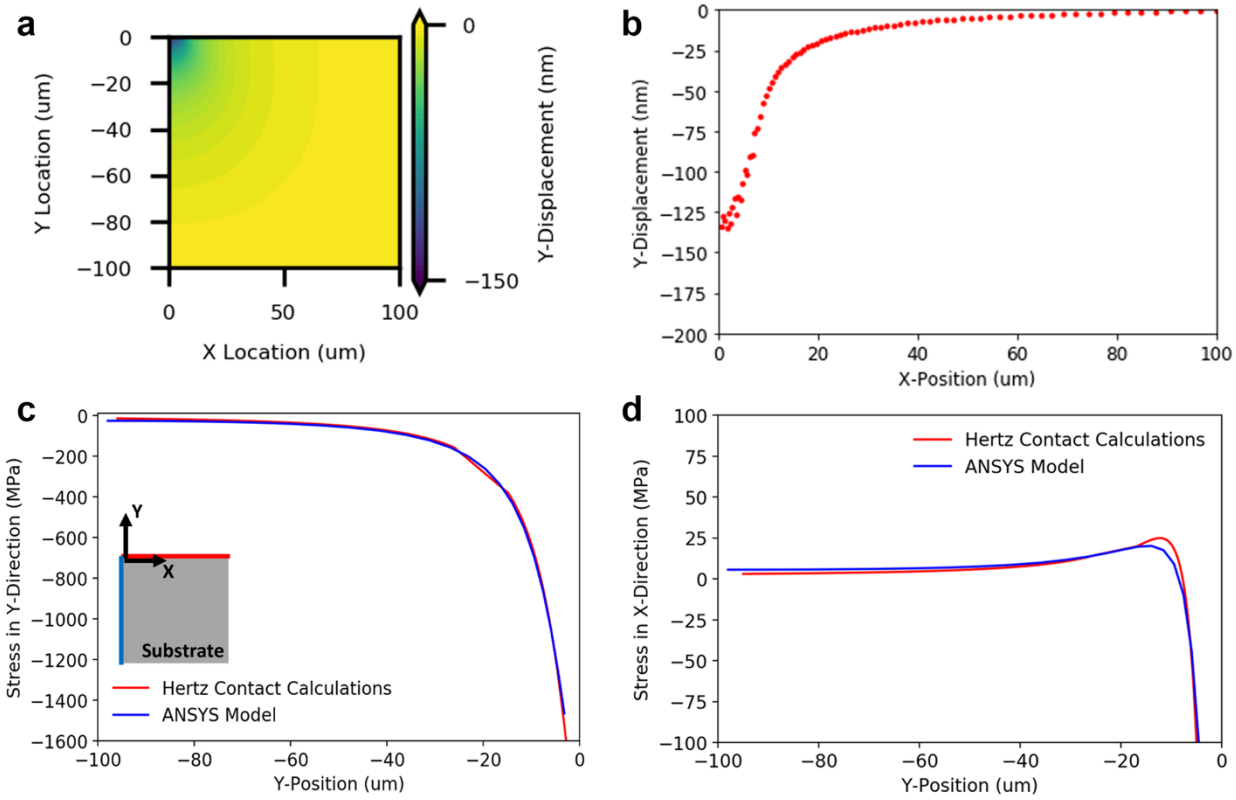

Figure 7.8. Representative finite element model predictions of (a) the substrate y-displacement field and (b) the substrate surface y-displacement. The stress field along the y-axis, directly below the indenter, in the (c) y-direction and (d) x-direction.

The SMI matrix constituents were randomly distributed, so the deformation zones generally encompassed consistent mixes of the SiC matrix and Si particulates. Within the perpendicular fiber/tow regions, the deformation zones were large enough to potentially encompass half a dozen or so fibers (which ranged from 10 to 30 μm in diameter) and surrounding CVI matrix. While these substrate regions could be modeled as materials in series or in parallel, it was often necessary to employ a hybridization as indentations frequently involved large portions of both fiber/tow regions and SMI matrix regions (Figure 7.9), where indentation cross-over between regions would encompass a few fibers, CVI matrix, and SMI matrix. In such instances, the SMI matrix was modeled in series then included as a third region, denoted as M_{SMI}, in parallel with the fiber and CVI matrix.

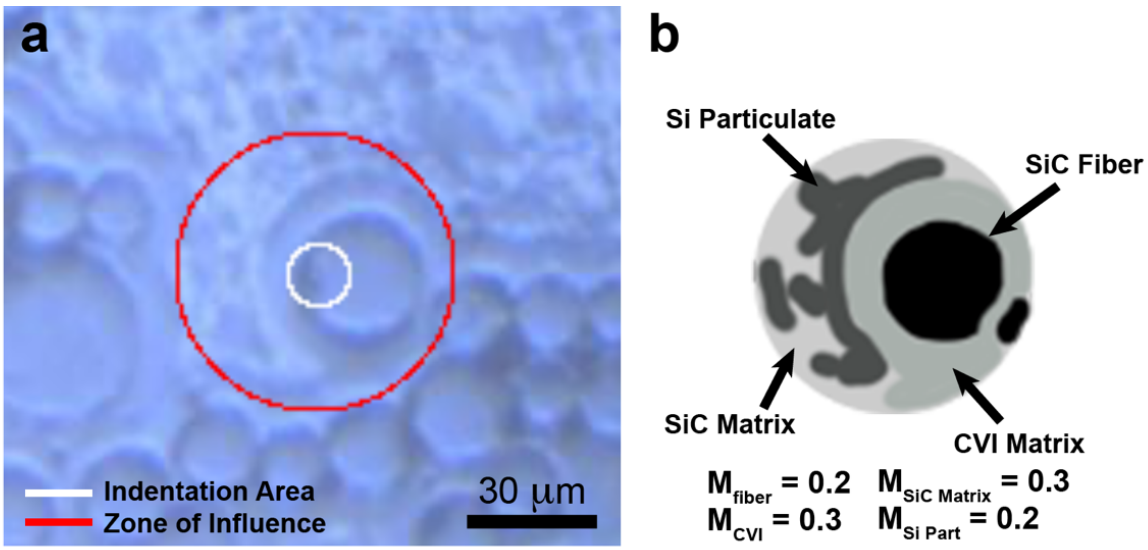

Figure 7.9. CMC image analysis was performed for each individual indentation from an (a) optical micrograph by (b) shading the different CMC constituents. The quantity of pixels of each shade were used to approximate the fraction coefficients.

Furthermore, the analytical model did not directly account for porosity within the CMC. Porosity was only observed within the fiber tows and was quantified as a fractional coefficient of the total zone of influence. However, that portion due to porosity was not fed into the analytical model; instead, the analytical model fit the creep curves based on the remaining M_i fraction coefficients attributed to CMC constituents.

It was important, however, to vary the content of the deformation zones from within the SMI matrix, fiber/tow region, and mixes of both to build a sense of the variation of local creep response of this complex composite.

5.3. Application of the Model to Creep of SiC/SiC CMCs

With the extent of the zone of deformation now approximated and the material constituent fractions known, Equations 7.6 and 7.7 could be applied to predict the creep response of every indentation on the CMC materials. The coefficients of Equation 7.5 were again determined via a curve fit with experimental data. Representative fits are presented in Figure 7.10. This analytical model accurately captured the primary and secondary creep response of the CMC materials at 23 and 315 °C; however, the model did not account for the oscillations present at 800 °C, only the broad trend. From Figure 7.10c,f, the fitted coefficients C_i were observed to vary significantly, indicative of a strong location dependence and any impact of the material fraction coefficient on the final strain performance.

Next, the model was run for a range of temperatures and contact stresses (up to 800 °C and 1500 MPa) to simulate the experimental range as presented in Figure 7.6. The model was run iteratively through multiple combinations of material coefficient parameters M_i. The curve fit parameters C_i would depend on the location and the local material constituents, so the values C_i were prescribed based on the specific M_i values. The resulting trend and standard deviation of resulting strain rates is presented in Figure 7.11, which showed good agreement between the predicted secondary creep strain rate and experimental results. The large standard deviation on the predicted strain rates and the spread of the experimental data, reflected the significant impact of indentation location and resulting proportions of contact between CMC constituents.

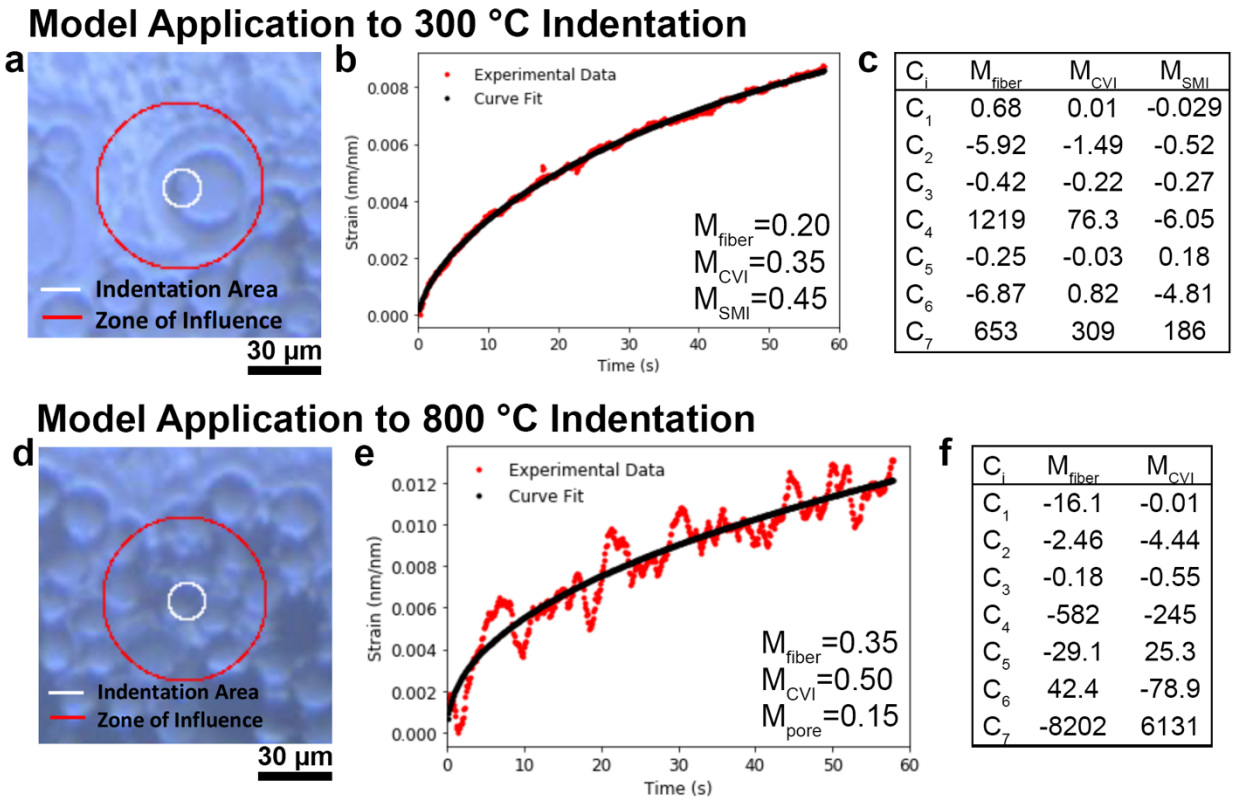

Figure 7. 10. Representative examples of the application of the analytical creep model to CMC indentations performed at (a-c) 300 °C and (d-f) 800 °C. (a,d) Indentation image analysis was used to derive the fractional coefficients M_i such that (b,e) a least-squares curve fit could be used to fit the experimental data and (c,f) determine the C_i creep equation coefficients.

Importantly, this agreement between the predictive analytical creep model and the experiment results demonstrated that despite oscillations in the creep curves and significant location dependence, the local strain rate of CMCs could be predicted and tracked with temperature. Such local predictions of creep are anticipated to be highly important in turbine blade operation where tight tolerances at ultra-high temperatures are critical.

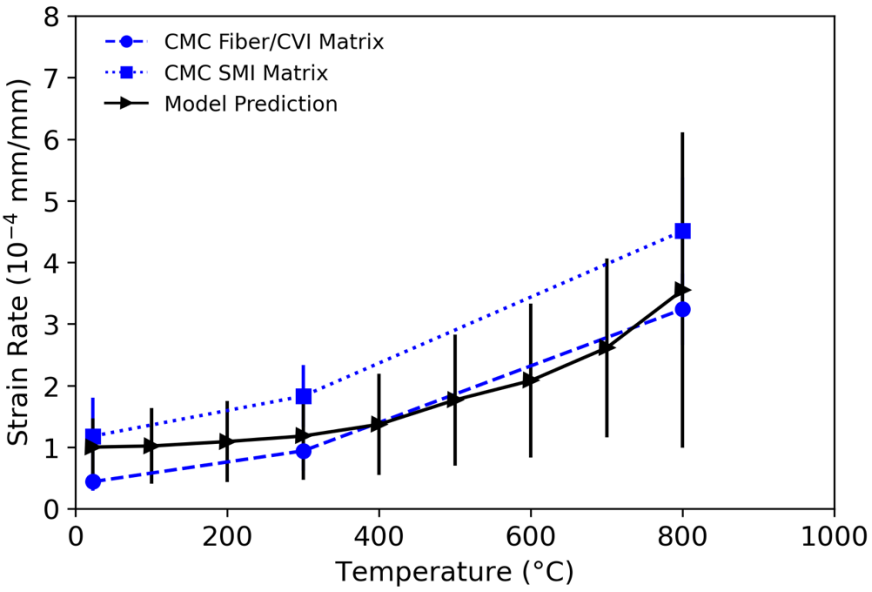

Figure 7.11. The model was run iteratively over multiple combinations of material constituents, temperatures, and contact stresses, which indicated good agreement with experimental results.

6. Conclusions

High temperature spherical indentation was performed to probe the creep response of SiC/SiC ceramic matrix composites to evaluate how the creep mechanisms are governed by the CMC microstructure. The indentation results demonstrated that polycrystalline materials will exhibit slight faster rates of creep than single crystal materials. Comparisons with reaction-bonded SiC and SiC/SiC CMCs were less conclusive; indentation contact stress was the key contributor to creep strain rate and varied significantly across the tests. In general, CMC strain rates were lower than other test Si and SiC materials, but this trend may be attributed to lower contact stresses. Oscillations along the reaction bonded SiC and CMC creep curves at 800 °C were observed for the first time; these oscillations were not observed in either single or polycrystalline Si or SiC, suggesting this effect was unique to the heterogeneous microstructure. It was hypothesized that these oscillations may be attributed to a material thermomechanical interaction effect with the CMC constituents. Future work should probe this effect further and investigate whether this effect is stronger in the fiber tows or matrix regions and evaluate the impact of fiber orientation. Finally, an

analytical creep model was presented based on a rule of mixtures derived by the contact proportions of individual CMC constituents. The model demonstrated good agreement with CMC strain rates up to 800 °C, indicating the rule of mixtures approach can sufficiently account for the heterogeneous CMC microstructure.

7. References

[1] H.M. Yun, J.Z. Gyekenyesi, Y.L. Chen, D.R. Wheeler, J.A. Dicarlo, Tensile behavior of SiC/SiC composites reinforced by treated Sylramic SiC fibers, Ceram. Eng. Sci. Proc. (2001) 521–531. http://onlinelibrary.wiley.com/store/10.1002/9780470294680.ch60/asset/ch60.pdf?v=1&t=ja1et44c&s=ce79b0421089ac5ed8ee192361d317a2f1bcc654 (accessed November 6, 2017).

[2] Y. Zhou, W. Zhou, F. Luo, D. Zhu, Effects of dip-coated BN interphase on mechanical properties of SiCf/SiC composites prepared by CVI process, Trans. Nonferrous Met. Soc. China. 24 (2014) 1400–1406. doi:10.1016/S1003-6326(14)63205-2.

[3] Y. Gowayed, G. Ojard, R. Miller, U. Santhosh, J. Ahmad, R. John, Mechanical Properties of MI SiC/SiC Composites and Their Constituents, 2007. http://oai.dtic.mil/oai/oai?verb=getRecord&metadataPrefix=html&identifier=ADA471472 (accessed May 18, 2016).

[4] T. Ishikawa, Recent developments of the SiC fiber Nicalon and its composites, including properties of the SiC fiber Hi-Nicalon for ultra-high temperature, Compos. Sci. Technol. 51 (1994) 135–144. doi:10.1016/0266-3538(94)90184-8.

[5] C. Droillard, J. Lamon, Fracture toughness of 2-D woven SiC/SiC CVI-composites with multilayered interphases, J. Am. Ceram. Soc. 79 (1996) 849–858. doi:10.1111/j.1151-2916.1996.tb08516.x.

[6] G.N. Morscher, H.M. Yun, J.A. Dicarlo, In-plane cracking behavior and ultimate strength for 2D woven and braided melt-infiltrated SiC/SiC composites tensile loaded in off-axis fiber directions, J. Am. Ceram. Soc. 90 (2007) 3185–3193. doi:10.1111/j.1551-2916.2007.01887.x.

[7] B.F. Sorensen, J.W. Holmes, Effect of loading rate on the monotonic tensile behavior of a continuous-fiber-reinforced glass-ceramic matrix composite, J. Am. Ceram. Soc. 79 (1996) 313–320. doi:10.1111/j.1151-2916.1996.tb08122.x.

[8] G.N. Morscher, Stress-dependent matrix cracking in 2D woven SiC-fiber reinforced melt-infiltrated SiC matrix composites, Compos. Sci. Technol. 64 (2004) 1311–1319. doi:10.1016/j.compscitech.2003.10.022.

[9] J.Z. Gyekenyesi, N.P. Bansal, High Temperature Tensile Properties of Unidirectional Hi-Nicalon/Celsian Composites In Air, 2000. https://ntrs.nasa.gov/archive/nasa/casi.ntrs.nasa.gov/20000085860.pdf (accessed May 25, 2017).

[10] D.J. Bertrand, V. Sabelkin, L. Zawada, S. Mall, Fatigue behavior of sylramic-iBN/BN/CVI SiC ceramic matrix composite in combustion environment, J. Mater. Sci. 50 (2015) 7437–7447. doi:10.1007/s10853-015-9302-8.

[11] R.K. Mishra, C. Beura, Life consumption assessment of a large jet engine, J. Fail. Anal. Prev. 14 (2014) 519–529. doi:10.1007/s11668-014-9842-2.

[12] C.B. Meher-Homji, G. Gabriles, Gas turbine blade failures - causes, avoidance, and troubleshooting, in: Proc. 27th Turbomach. Symp., 1998: pp. 129–179. http://citeseerx.ist.psu.edu/viewdoc/download?doi=10.1.1.462.4970&rep=rep1&type=pdf (accessed May 18, 2016).

[13] N. William D., G. Huajian, W.D. Nix, H. Gao, Indentation size effects in crystalline materials: A law for strain gradient plasticity, J. Mech. Phys. Solids. 46 (1998) 411–425. doi:10.1016/S0022-5096(97)00086-0.

[14] J. Pelleg, Solid Mechanics and Its Applications: Creep in Ceramics, Springer International Publishing, 2017. http://www.springer.com/series/6557.

[15] G.N. Morscher, G. Ojard, R. Miller, Y. Gowayed, U. Santhosh, J. Ahmad, R. John, Tensile creep and fatigue of Sylramic-iBN melt-infiltrated SiC matrix composites: Retained properties, damage development, and failure mechanisms, Compos. Sci. Technol. 68 (2008) 3305–3313. doi:10.1016/j.compscitech.2008.08.028.

[16] S. Zhu, M. Mizuno, Y. Kagawa, Y. Mutoh, Monotonic tension, fatigue and creep behavior of SiC-fiber-reinforced SiC-matrix composites: A review, Compos. Sci. Technol. 59 (1999) 833–851. doi:10.1016/S0266-3538(99)00014-7.

[17] G. Chollon, R. Pailler, R. Naslain, Correlation between microstructure and mechanical behaviour at high temperatures of a SiC fibre with a low oxygen content (Hi-Nicalon), J. Mater. Sci. 32 (1997) 1133–1147.

[18] J.F. Smith, S. Zheng, High temperature nanoscale mechanical property measurements, Surf. Eng. 16 (2000) 143–146. doi:10.1179/026708400101517044.

[19] J.M. Wheeler, D.E.J. Armstrong, W. Heinz, R. Schwaiger, High temperature nanoindentation: The state of the art and future challenges, Curr. Opin. Solid State Mater. Sci. 19 (2015) 354–366. doi:10.1016/j.cossms.2015.02.002.

[20] W.C. Oliver, G.M. Pharr, An improved technique for determining hardness and elastic modulus using load and displacement sensing indentation experiments, J. Mater. Res. 7 (1992) 1564–1583. doi:10.1557/JMR.1992.1564.

[21] W.C. Oliver, G.M. Pharr, Measurement of hardness and elastic modulus by instrumented indentation: Advances in understanding and refinements to methodology, J. Mater. Res. 19 (2004) 3–20. doi:10.1557/jmr.2004.19.1.3.

[22] E.G. Herbert, G.M. Pharr, W.C. Oliver, B.N. Lucas, J.L. Hay, On the measurement of stress–strain curves by spherical indentation, Thin Solid Films. 398–399 (2001) 331–335. https://ac.els-cdn.com/S0040609001014390/1-s2.0-S0040609001014390-main.pdf?_tid=477c58de-0089-11e8-9d79-00000aacb35f&acdnat=1516745205_937785e29b4fdbfe84b157df002eb824 (accessed January 23, 2018).

[23] B. Xu, X. Chen, Determining engineering stress-strain curve directly from the load-depth curve of spherical indentation test, J. Mater. Res. 25 (2010) 2297–2307. doi:10.1557/jmr.2010.0310.

[24] W.D. Nix, H. Gao, Indentation size effects in crystalline materials: a law for strain gradient plasticity, J. Mech. Phys. Solids. 46 (1997) 411–425. doi:0022-5096/98.

[25] X.L. Gao, X.N. Jing, G. Subhash, Two new expanding cavity models for indentation deformations of elastic strain-hardening materials, Int. J. Solids Struct. 43 (2006) 2193–2208. doi:10.1016/j.ijsolstr.2005.03.062.

[26] Y. Huang, F. Zhang, K.C. Hwang, W.D. Nix, G.M. Pharr, G. Feng, A model of size effects in nano-indentation, J. Mech. Phys. Solids. 54 (2006) 1668–1686. doi:10.1016/j.jmps.2006.02.002.

[27] Q. Ma, D.R. Clarke, Size dependent hardness of silver single crystals, J. Mater. Res. 10 (1995) 853–863. doi:10.1557/JMR.1995.0853.

[28] K.W. McElhaney, J.J. Vlassak, W.D. Nix, Determination of indenter tip geometry and indentation contact area for depth-sensing indentation experiments, J. Mater. Res. 13 (1998) 1300–1306. doi:10.1557/JMR.1998.0185.

[29] Structural Analysis Guide - Creep Equations, Mech. APDL Command Ref. (2011). https://www.sharcnet.ca/Software/Fluent14/help/ans_mat/aQy8sq33aldm.html (accessed February 1, 2019).

[30] Z. Xu, X. Li, Sample size effect on nanoindentation of micro-/nanostructures, Acta Mater. 54 (2006) 1699–1703. doi:10.1016/j.actamat.2005.11.043.

[31] H. Takagi, M. Dao, M. Fujiwara, Analysis on pseudo-steady indentation creep, Acta Mech. Solida Sin. 21 (2008). doi:10.1007/s10338-008-0832-3.

[32] J.L. Daly, On comparison of indentation models, University of South Florida, 2007.

[33] A.K. Swarnaker, O. Van der Biest, J. Vanhellemont, Determination of the Si Young's modulus between room and melt temperature using the impulse excitation technique, Phys. Status Solidi C. 11 (2014) 150–155. doi:10.1002/pssc.201.

[34] C.H. Cho, Characterization of Young's modulus of silicon versus temperature using a "beam deflection" method with a four-point bending fixture, Curr. Appl. Phys. 9 (2009) 538–545. doi:10.1016/J.CAP.2008.03.024.

[35] S. Goel, Nanoindentation of polysilicon and single crystal silicon: Molecular dynamics simulation and experimental validation, (2014). doi:10.1088/0022-3727/47/27/275304.

[36] J. Vanhellemont, A.K. Swarnakar, O. Van der Biest, Temperature Dependent Young's Modulus of Si and Ge, ECS Trans. 64 (2014) 283–292. doi:10.1149/06411.0283ecst.

[37] A.A. Wereszczak, W.L. Daloz, K.T. Strong, O.M. Jadaan, Effect of indenter elastic modulus on Hertzian ring crack initiation in silicon carbide, Int. J. Appl. Ceram. Technol. 8 (2011) 885–894. doi:10.1111/j.1744-7402.2010.02522.x.

[38] CoorsTek, Silicon Carbides - SiC - 01024I, 2017.

[39] Y. Katoh, D.F. Wilson, C.W. Forsberg, Assessment of Silicon Carbide Composites for Advanced Salt- Cooled Reactors, Oak Ridge, TN, TN, 2007. http://info.ornl.gov/sites/publications/files/Pub8156.pdf (accessed August 18, 2016).

[40] G.N. Morscher, V. V. Pujar, Creep and Stress-Strain Behavior after Creep for SiC Fiber Reinforced, Melt-Infiltrated SiC Matrix Composites, J. Am. Ceram. Soc. 89 (2006) 1652–1658. doi:10.1111/j.1551-2916.2006.00939.x.

[41] G. Morscher, J. Gyekenyesi, Room temperature tensile behavior and damage accumulation of Hi-Nicalon reinforced SiC matrix composites, 22nd Annu. Conf. Compos. Adv. Ceram. Mater. Struct. (2009). https://ntrs.nasa.gov/archive/nasa/casi.ntrs.nasa.gov/19980237335.pdf (accessed November 9, 2017).

[42] S. Yao, D. Xu, B. Xiong, Y. Wang, The plastic and creep characteristics of silicon microstructure at elevated temperature, Microsyst. Technol. 21 (2015) 1111–1119. doi:10.1007/s00542-014-2184-x.

[43] T.A. Taylor, C.R. Barrett, Creep and recovery of silicon single crystals, Mater. Sci. Eng. 10 (1972) 93–102. doi:10.1016/0025-5416(72)90073-0.

[44] J. Pelleg, Creep in silicon carbide, in: Creep Ceram., 2017: pp. 357–393.

[45] G.S. Corman, Creep of 6H α-silicon carbide single crystals, J. Am. Ceram. Soc. 75 (1992) 3421–3424.

[46] K.L. Johnson, Contact Mechanics, Cambridge University Press, 1985.

CHAPTER 8: SUMMARY & RECOMMENDATIONS

This dissertation has examined the degradation and failure mechanisms of two subcategories of materials for extreme environment energy applications: thermal barrier coatings (TBCs) and silicon carbide fiber / silicon carbide matrix composites (SiC/SiC CMCs). Both materials are of immediate interest for aerospace and nuclear energy applications, where thermal stability, structural performance, and oxidation resistance are mission critical [1–4]. Furthermore, both materials are characterized by complex microstructures, which were shown in this dissertation to correlate with the observed failure mechanisms. These microstructural features, such as pores and interfacial roughness in TBCs and tow cross-over braid structure and spacing in CMCs, may contribute to local stress concentrations and crack initiation. TBC and CMC manufacturers may seek to control and minimize these features to delay crack initiation to achieve enhanced mechanical performance. Specific contributions and recommendations for future research are presented here.

1. Key Contributions

In Chapter 1, the underlying motivation of this dissertation was provided in context with a brief review of the known behavior and properties of TBCs and CMCs. Both materials are characterized by heterogeneous microstructures: in TBCs, a multilayered coating system with pre-existing cracks, pores, and unmolten particles [5,6]; and in CMCs, a braided or woven system of ceramic fibers infiltrated with a ceramic matrix and coated with another ceramic layer [2,7]. The chapters of this dissertation address these materials separately, recognizing the distinct structures and failure mechanisms of these material systems. A brief review of digital image correlation (DIC) techniques was also provided, which the basis for most of the data measurement and analysis in this dissertation. DIC techniques are highly beneficial for their inherent capability to provide full-field displacement and strain measurements in contrast to conventional strain gauge or extensometer measurements [8,9], which provided direct correlation between local microstructural features (pores, interfacial roughness, tow cross-over) and local strain concentrations associated with fracture.

In Chapter 2, experimental wear testing probed the degradation mechanisms of TBCs, which demonstrated a disparity in coating degradation between wear at 23 °C and at 1000 °C. The severity of wear at 1000 °C suggested a temperature-dependent mechanism. Hertz contact and finite element models unveiled a significant thermal stress mismatch between coating layers and sufficient softening of the coating to progress the maximum shear stress deep into the coating. This high temperature stress state quickly met the critical stress intensity factor for fracture initiation, thus initiating severe wear damage. This work illustrated the critical importance of the temperature-dependent stress state to the degradation of these ceramic coatings. This observation was complemented by the thermal cycling experiments in Chapter 4. However, the stresses within the coating layers were determined based on models in the literature for thermal mismatch [10] and for Hertz contact [11]. These calculations did not account for the pre-existing residual stress state of each layer nor the effects of interface geometry, porosity, and other defects on local stresses. Thus, one outcome of the work in Chapter 2 was motivation to implement a methodology to directly quantify the stress state.

In Chapter 3, a methodology to quantify the residual stress state of a multilayer coating system was presented, leveraging *in-situ* 3D-DIC curvature measurements. This methodology relied on the inherent surface texture of the TBC to provide a high contrast speckle pattern instead of applying a paint speckle pattern, which can obscure local structural variations. The accuracy of 3D-DIC measurements was limited by surface roughness and coloration (sufficient contrast), which governed the minimum feature size available for surface profile measurement. With appropriate lighting and camera-sample distances, the 3D-DIC measurements demonstrated spatial accuracy of 22.6 μm or $1/26{,}500^{th}$ of camera-sample distance. Residual stress was calculated from the measured curvature via Euler-Bernoulli beam theory and linear-elastic material models. Experimental curvature measurements up to 900 °C thus yielded residual stress predictions within the top coat, bond coat, and substrate layers. Furthermore, curvature and residual stress were observed to increase at a decreasing rate with successive heat treatments, which was attributed to a phase transformation within the TBC zirconia top coat from tetragonal to monoclinic phases. A key implication of this work was the demonstration of the application of stereoscopic DIC techniques to

correlate the inherent surface texture of these coating system without an applied speckle pattern and with high accuracy.

In Chapter 4, the demonstrated capability to perform DIC on the TBC surface texture was extended to quantify strains and isolate cracking during thermal cycling, where pores, pre-existing cracks, and other microstructural features provided a sufficient, high contrast speckle pattern. Full-field DIC strain maps of cross-sectioned TBCs during thermal cycling up to 1200 °C revealed formation of vertical and horizontal cracks. In-process DIC monitoring tracked the formation of dense vertical cracks and the initiation and propagation of horizontal cracks branching off of vertical cracks. Finite element simulations unveiled that interactions between vertical and horizontal cracks and interfacial geometry produced favorable strain energy release rates for crack propagation along the top coat / bond coat interface. This work thus demonstrated the capability of DIC-enabled, *in-situ* deformation measurements and investigation of microstructure-deformation-failure material relationships. Vertical cracks were observed to originate in regions with a rough, local top coat / bond coat interface and travel from pre-existing voids within the top coat. Coupled with the residual stress model developed in Chapter 3, vertical cracks grew quickly over a few cycles due to tensile stresses in the top coat. Small defects along the vertical crack, including pre-existing lateral cracks between molten particles, unmolten particles, and pores, served as initiation sites for horizontal cracks. These horizontal cracks were observed to propagation along the top coat / bond coat interface, leading to delamination and coating failure.

In Chapter 5, an *in-situ* hermeticity testing apparatus was developed to correlate the mechanical performance and gas tightness of SiC/PyC/SiC CMC tubular components using stereoscopic DIC. This test apparatus was evaluated with characterization of steel, alumina, and borosilicate tubes to establish the limitations on measurements of ductile and brittle materials and correlate *in-situ* DIC deformation data with in-process acoustic emission and leak rate data. The apparatus was then applied to the characterization of the deformation-hermeticity relationship of SiC/SiC CMCs. Analysis of acoustic emissions indicated an onset of matrix microcracking at flexural strains as low as 0.04 %, which coincided with the deviation from linearity, or proportional limit. Loss of gas tightness followed rapidly thereafter as matrix microcracking

created channels through the CMC tube wall. CMC failure was characterized in stages from initial matrix crack initiation, through-thickness matrix crack growth and loss of hermeticity, onset of fiber fracture, and fracture of fiber tows and loss of load-bearing capability. The correlation of DIC deformation data, acoustic emissions, and leak rate began to resolve mechanisms controlling distinct steps in CMC failure, and this methodology and hermetic behavior of these CMC tubes are anticipated to advance the standardization of material evaluation for next generation accident tolerant fuels in nuclear energy applications.

In Chapter 6, the *in-situ*, DIC-enabled mechanical test / hermeticity apparatus was applied to track the progression of fracture of SiC/PyC/SiC CMC tubes. Individual cracks in the composite were isolated as discontinuities in the DIC-measured spatial displacement field and key fracture characteristics (crack opening displacement and spacing) with the CMC flexural strain and leak rate. Multiple specimens were tested after heat treatments to 1200 °C in open air, in vacuum, and in helium to evaluate the environmental effects on the fracture mechanisms of SiC/SiC composites, which indicated CMCs treated in open air underwent a brittle, fast fracture failure mode rather than the multi-stage failure of CMCs without treatment. Energy dispersive X-ray spectroscopy indicated significant oxidation after the open air treatment, and indentation-based fracture toughness measurements decreased by 33 % after the open air treatment compared to a 10 % decrease exhibited by the other treatments. In-process crack opening displacement and spacing measurements, with a resolution of ~ 100 nm, were tracked during flexural testing; crack opening increased linearly through the test while crack spacing stabilized by about 0.2 % flexural strain, indicating a stable number of cracks. Furthermore, it was observed that the cracks occurred at tow cross-over positions, and it was proposed that the diamond braided tows may contribute to the crack propagation by presenting uniform tow cross-over orientations. Instead, CMC manufacturers may consider a regular braided with non-uniform tow cross-over orientations or filament wound tow pattern to delay crack propagation.

In Chapter 7, the local creep response of SiC/BN/SiC ceramic matrix composites was probed via high temperature spherical indentation to examine the contributions of heterogeneous microstructure to creep. Indentations were conducted up to 800 °C in an argon environment on single and polycrystalline Si and SiC, reaction bonded SiC, and the SiC/SiC composite, which indicated that higher creep strain rates of

polycrystalline materials yet comparably lower strain rates of the SiC/SiC composite. Indentation creep rate was instead observed to be highly dependent on contact stresses, and lower contact stresses were related to the low SiC/SiC strain rates. An analytical creep model was presented based on a rule of mixtures approach to incorporate material heterogeneity of the SiC/SiC composite. A finite element model was applied to predict the indentation deformation zone, in which the composite constituents would jointly influence the composite creep response. The heterogeneous microstructure was characterized with optical microscopy to identify the present mixture of constituents. The analytical model was then solved for temperatures up to 800 °C and exhibited good agreement with experimental measurements, demonstrating that a rule-of-mixtures approach can be applied to describe the thermomechanical response of CMC materials. It is anticipated that this model may help to describe and predict the local creep response of CMC materials for aerospace and other high temperature applications.

2. Recommendation for Future Work

This dissertation has developed novel application of DIC techniques to TBCs and CMCs to utilize the inherent surface texture and microstructure for correlation, to unveil degradation and fracture, and to investigate the deformation, strain, and stress states of these materials leading to failure. These techniques have been extended to a diversity of applications from CMC structural variability measurements [12] to residual stress measurements of additively manufactured components [13] to characterization of biomedical implants [14]. In particular, it is envisioned that the *in-situ* residual stress, strain, and crack detection techniques presented here could be readily adapted for smart inline quality control monitoring of many manufacturing processes. As such, there are many avenues of research to develop these techniques for a manufacturing environment or to cater the analysis for specific materials and environments. However, within the context of the research presented in this dissertation, there are several key limitations, which are recommended for future scrutiny.

2.1. Characterization of Sub-Surface Deformation and Fracture

First, the stereoscopic DIC used in this dissertation was limited to surface deformation measurements. In the case of the TBC system, sub-surface deformation was assumed to be uniform, so surface curvature, deformation, and cracking was assumed to represent through-thickness response. It was found that local defects and microstructural features identified on the visible surface of the TBC, like pores, unmolten particles, and interfacial geometry, heavily affected local strain concentrations and crack growth mechanisms. The resulting conclusion that local microstructural features dictate crack growth mechanism, ironically, also raises the specter that some unseen defect just below the surface may yet wield an even greater impact on the surface deformation.

This concern is even more heightened in the CMCs, where braided fiber tows with a chemical vapor infiltrated (CVI) SiC matrix, a chemical vapor deposited (CVD) SiC outer coating, and pores and voids create a constantly varying microstructure. Surface cracks in the CVD SiC were detectable with DIC, but these measurements provided no indication of how those cracks progressed through fiber tows. Leak rate data provided the only confirmation that surface cracks had progressed to through-thickness cracks, and the deviation from linearity in the stress-strain data indicated the point of load transfer from matrix to fibers. In fact, the fracture energy release model presented in Chapter 6 assumed a single crack traveled exclusively through the CVD matrix, but in actuality, this travel path would be interrupted by three plys of tows and pores. The work in Chapters 5 and 6 also focused on braided CMC architectures, but other architectures, such as filament winding, should be considered to continue to investigate the role of microstructure on fracture mechanisms.

In both cases, TBCs and CMCs, it is necessary to collect volumetric deformation data to advance this research further. X-ray computed tomography (XCT) has been demonstrated on many materials [15–17], including CMCs [18], to provide high resolution imaging of the inner constituents and of crack propagation. Immediate next steps could be imaging the CMCs after different stages of flexural loading to visualize crack growth through the matrix and fibers. This high-fidelity characterization of CMC fracture would elucidate the differences in the propagation mechanisms in the heat-treated CMCs as observed in Chapter

6. This inspection should be supplemented with a more detailed look at the extent of oxidation after heat treatment, such as characterization of the fracture surface itself to ascertain channels of oxidation ingression into the CMC.

Similarly, XCT of the TBC systems may unveil how crack growth varies in three dimensions around a defect, like a pore or unmolten particle; how interfacial geometries vary through the thickness of the coated sample; and how fracture growth mechanisms may vary near and away from a free surface. Within Chapter 3, the development of the residual stress state model, the effect of microstructural features, like porosity or dense vertical cracks, was not accounted for in the stress calculations. XCT may help to reveal both the density and distribution of such microstructural features, and with application of volumetric DIC strain measurements, local stress relaxation can be quantified after annealing treatments. Furthermore, it was demonstrated in Chapter 4 that fracture within a TBC system is heavily influenced by the presence of dense vertical cracks and porosity; fracture was observed to account for local stress relaxation. This insight implies there will be a significant effect on the coating stress state, and the effect of the density and distribution of pores, pre-existing cracks, and other defects should be accounted for in future iterations of the residual stress model.

Importantly, for either application, the DIC techniques pioneered in this dissertation are capable of being readily adapted from 2D optical images to 3D X-ray tomographs, where large pseudostrains can be used to track fracture and spatial derivative displacement analysis can quantify crack opening. XCT is also capable of capturing the full field of degradation to TBCs and CMCs after wear or mechanical testing, not just surface degradation, which could reveal sub-surface only cracking or delamination. This insight would be particularly crucial to the CMC studies described here, where it was hypothesized that stress concentrations at tow cross-over locations initiated cracking.

2.2. Characterization of Test Specimen Stress History

To understand the barrier to fracture of TBC and CMC specimens, it is necessary to have an understanding of the residual stress state and stress history. Typically, the residual stress state is built up

during manufacturing from thermal stress mismatch between constituents [19,20], and the orientation of the residual stress can either raise or lower the energy barrier to crack initiation. The residual stress model developed in Chapter 3 was predicated on knowing the thermal gradient, so in order to solve for the residual stress of the coating after thermal spraying, it would be necessary to know the temperature of the molten deposits. This information is obtainable via infrared cameras and thermocouples, but it was not available from the manufacturer in this dissertation research.

An immediate remedy, and the approach taken here, was to anneal the coating samples at high temperature to relieve the pre-existing stress state and establish a new equilibrium. However, a more applicable approach would be to implement the *in-situ* DIC curvature tool in-process during the thermal spray deposition of the TBC, thus providing direct measurement of the change of curvature and residual stress state due to the deposition itself. In such an application, the use of DIC can be directed to simultaneously provide in-process coating thickness measurements to strengthen the operator's understanding of the deposition efficiency. Post deposition characterization as described in Chapters 2-4 may then be repeated to correlate wear and fracture degradation mechanisms with the known residual stress state. Thermal spray deposition parameters, such as flow rates and pressures, may also be varied to investigate coupled processing / residual stress / failure relationships.

Within Chapter 3, it was discussed briefly that the application of a Euler-Bernoulli beam-in-bending model has its limitations. The Euler-Bernoulli beam theory does not account for shear deformation, which limits its application to long, thin beam structures. However, the Timoshenko beam theory does incorporate shear deformation [21–23], which may be better suited to accommodate local shear stresses between individual coating layers due to thermal expansion mismatch. As previously mentioned, this stress model does not account for the effect of microstructural variation, such as that imposed by the presence of dense vertical cracks and inherent porosity; these features were noted in Chapter 4 to impact local stress state and the crack growth mechanisms within the top coat. Such factors, as the shear deformation of individual layers and the effect of porosity, should be revisited to improve the accuracy of the stress predictions from this curvature model.

2.3. *In-situ* Characterization of CMC Mechanical Performance at Elevated Temperatures

In Chapters 5 and 6, mechanical testing of SiC/SiC CMC tubular specimens revealed coupled fracture / hermeticity loss mechanisms, and in Chapter 6, these materials were subjected to pre-experiment heat treatments, which contributed to degradation and loss of fracture toughness. All mechanical testing was still conducted under ambient conditions at 23 °C. However, SiC/SiC CMC fuel claddings would be exposed to temperatures around 300 to 320 °C in a typical light water reactor [24] and to even higher temperatures (up to 1200 °C) in the event of an accident [25]. Thus, it is critical to investigate the fracture / hermeticity loss mechanisms within the reactor operating temperature range and at higher, accident temperatures. While SiC/SiC CMCs are well known for their thermal stability [20,26], there are significant environment-dependent failure mechanisms introduced at temperatures above 500 °C. The pyrolytic carbon interphase layer becomes consumed due to oxidation in an air environment at temperatures around 600 °C, which promotes strong fiber/matrix bonding due to the formation of a silica layer at this interface [27]. This change in the fiber/matrix bonding negates the fracture arresting or deflecting features of the pyrolytic carbon and can enable brittle failure of the CMC.

To investigate these high temperature mechanisms, the same four-point bending / hermeticity tests should be conducted at temperatures stepping through this range of onset of interface oxidation through the formation of the silica-strengthened bonding. Characterization of the TBC specimens (Chapters 3 and 4) has shown that these DIC techniques are just as applicable at high temperatures, so the crack opening analysis can continue to discern changes in the surface fracture patterns with temperature. Post-experiment characterization (X-ray diffraction, energy dispersive X-ray spectroscopy) should also aim to investigate the ingression channels for oxidation to see if certain interfaces, such as the fiber/matrix and CVI SiC / CVD SiC interfaces, are particularly prone to oxidation. Fracture surfaces should also be analyzed to quantify the extent of oxidation and growth of a silica layer. The degree of oxidation and distribution of oxidation among the CMC constituents can then be related to the mechanical performance.

Similarly, the nanoindentation creep experiments (Chapter 7) should also be extended to high temperatures. At present, these experiments only measured the creep response up to 800 °C, which is about the point when oxidation and formation of silica becomes a key factor in the performance of these SiC/SiC materials [28]. However, in aerospace applications, these CMCs will be exposed to temperatures in excess of 1200 °C, so the effects of ultra-high temperatures and oxidation should be investigated. The indentation creep response (Figure 7.11) hinted to a rapidly accelerating creep rate at higher temperatures, so it is also worth investigating at what point this local creep response scales to the bulk material creep response.

In addition to extending the results to higher temperatures, a key question of the creep experiments in Chapter 7 was the role of CMC microstructure; however, these experiments only probed the creep response of CMC fiber tows oriented perpendicular to the surface and did not account for variation of this architecture. Having demonstrated the applicability of a rule-of-mixtures approach, future work should systematically identify the sources of microstructural variation (such as fiber tow orientation, density of fibers, density of matrix particulate, density of pores) and target each source of variation with multiscale indentation. This proposed approach will better elucidate the contributions of individual sources of CMC microstructural variation to the overall indentation creep response. Furthermore, continued creep experiments to higher temperature must also factor the effect of oxidation and growth of a silica layer. As previously mentioned, X-ray diffraction and energy dispersive X-ray spectroscopy techniques should be utilized to characterize the extent of oxidation and identify if oxidation varies across individual constituents or constituent interfaces.

3. References

[1] G.W. Daines, M.P. Short, Evaluation of multilayer silicon carbide composite cladding under loss of coolant accident conditions, 2014. https://dspace.mit.edu/handle/1721.1/103651.

[2] C.P. Deck, G.M. Jacobsen, J. Sheeder, O. Gutierrez, J. Zhang, J. Stone, H.E. Khalifa, C.A. Back, Characterization of SiC-SiC composites for accident tolerant fuel cladding, J. Nucl. Mater. 466 (2015) 1–15. doi:10.1016/j.jnucmat.2015.08.020.

[3] K. Thiruselvam, Thermal barrier coatings in internal combustion engine, J. Chem. Pharm. Sci. (2015) 413–418. www.jchps.com (accessed January 24, 2018).

[4] M. Belmonte, Advanced ceramic materials for high temperature applications, Adv. Eng. Mater. 8 (2006) 693–703. doi:10.1002/adem.200500269.

[5] Y. Niu, X. Zheng, X. Liu, H. Ji, C. Ding, Influence of powder size on characteristics of air plasma sprayed silicon coatings, Ceram. Int. 38 (2012) 5897–5905. doi:10.1016/j.ceramint.2012.03.080.

[6] B.T. Richards, H.N.G. Wadley, Plasma spray deposition of tri-layer environmental barrier coatings, J. Eur. Ceram. Soc. 34 (2014) 3069–3083. doi:10.1016/j.jeurceramsoc.2014.04.027.

[7] T. Koyanagi, Y. Katoh, G. Jacobsen, C. Deck, Handbook of LWR SiC/SiC Cladding Properties-Revision 1, 2018.

[8] M.A. Sutton, J. Yan, X. Deng, C.S. Cheng, P. Zavattieri, Three-dimensional digital image correlation to quantify deformation and crack-opening displacement in ductile aluminum under mixed-mode I/III loading, Opt. Eng. 46 (2007) 051003. doi:10.1117/1.2741279.

[9] H. Schreier, J.J. Orteu, M.A. Sutton, Image correlation for shape, motion and deformation measurements: Basic concepts, theory and applications, Springer US, 2009. doi:10.1007/978-0-387-78747-3.

[10] Y. Song, Z. Lv, Y. Liu, X. Zhuan, T.J. Wang, Effects of coating spray speed and convective heat transfer on transient thermal stress in thermal barrier coating system during the cooling process of fabrication, Appl. Surf. Sci. 324 (2015) 627–633. doi:10.1016/j.apsusc.2014.10.157.

[11] K.L. Johnson, Contact Mechanics, Cambridge University Press, 1985.

[12] F.M. Heim, B.P. Croom, C.H. Bumgardner, X. Li, Scalable measurements of tow architecture variability in braided ceramic composite tubes, J. Am. Ceram. Soc. 101 (2018) 4297–4307. doi:10.1111/jace.15564.

[13] J.L. Bartlett, B.P. Croom, J. Burdick, D. Henkel, X. Li, Revealing mechanisms of residual stress development in additive manufacturing via digital image correlation, Addit. Manuf. 22 (2018) 1–12. doi:10.1016/j.addma.2018.04.025.

[14] V.C. Shen, C.H. Bumgardner, L. Actis, J. Ritz, J. Park, X. Li, 3D digital image correlation evaluation of arthrodesis implants, Clin. Biomech. 71 (2020) 29–36. doi:10.1016/j.clinbiomech.2019.10.011.

[15] B.P. Croom, W.M. Wang, J. Li, X. Li, Unveiling 3D deformations in polymer composites by coupled micro X-ray computed tomography and volumetric digital image correlation, Exp. Mech. 56 (2016) 999–1016. doi:10.1007/s11340-016-0140-7.

[16] M.N. Rossol, J.H. Shaw, H. Bale, R.O. Ritchie, D.B. Marshall, F.W. Zok, Characterizing weave geometry in textile ceramic composites using digital image correlation, J. Am. Ceram. Soc. 96 (2013) 2362–2365. doi:10.1111/jace.12468.

[17] B.P. Croom, H. Jin, B. Mills, J. Carroll, K. Long, J. Brown, X. Li, Damage mechanisms in elastomeric foam composites: Multiscale X-ray computed tomography and finite element analyses, Compos. Sci. Technol. 169 (2019) 195–202. doi:10.1016/j.compscitech.2018.11.025.

[18] B.P. Croom, P. Xu, E.J. Lahoda, C.P. Deck, X. Li, Quantifying the three-dimensional damage and stress redistribution mechanisms of braided SiC/SiC composites by in situ volumetric digital image correlation, Scr. Mater. 130 (2017) 238–241. doi:10.1016/j.scriptamat.2016.12.021.

[19] S. Krämer, S. Faulhaber, M. Chambers, D.R. Clarke, C.G. Levi, J.W. Hutchinson, A.G. Evans, Mechanisms of cracking and delamination within thick thermal barrier systems in aero-engines subject to calcium-magnesium-alumino-silicate (CMAS) penetration, Mater. Sci. Eng. A. 490 (2008) 26–35. doi:10.1016/j.msea.2008.01.006.

[20] Y. Katoh, L.L. Snead, T. Nozawa, T. Hinoki, A. Kohyama, N. Igawa, T. Taguchi, Mechanical properties of chemically vapor-infiltrated silicon carbide structural composites with thin carbon interphases for fusion and advanced fission applications, Mater. Trans. 46 (2005) 527–535.

[21] A. Labuschagne, N.F.J. van Rensburg, A.J. van der Merwe, Comparison of linear beam theories, Math. Comput. Model. 49 (2009) 20–30.

[22] X. Zhang, D. Thompson, X. Sheng, Differences between Euler-Bernoulli and Timoshenko beam formulations for calculating the effects of moving loads on a periodically supported beam, J. Sound Vib. 481 (2020) 115432. doi:10.1016/j.jsv.2020.115432.

[23] O.A.A. Bauchau, J.I.I. Craig, Euler-Bernoulli beam theory, in: Struct. Anal., 2009: pp. 173–221. doi:10.1007/978-90-481-2516-6_5.

[24] S. Ray, S.C. Johnson, E.J. Lahoda, Preliminary Assessment of the Performance of SiC Based Accident Tolerant Fuel in Commercial LWR Systems, Charlotte, NC, 2013.

[25] H. Shah, J. Romero, P. Xu, R. Oelrich, J. Walters, J. Wright, W. Gassmann, Westinghouse-Exelon EnCore ® fuel lead test rod (LTR) program including coated cladding development and advanced pellets, Topfuel. (2018) 1–9.

[26] R.J. Price, Properties of silicon carbide for nuclear fuel particle coatings, Nucl. Technol. 35 (1977) 320–336. doi:10.13182/NT77-A31892.

[27] C.I. Contescu, Initial Assessment of Environmental Effects on SiC/SiC composites in Helium-cooled Nuclear Systems, 2013. http://www.osti.gov/contact.html (accessed October 18, 2018).

[28] R.S. Hay, G.E. Fair, R. Bouffioux, E. Urban, J. Morrow, A. Hart, M. Wilson, Hi-nicalon-S SiC fiber oxidation and scale crystallization kinetics, J. Am. Ceram. Soc. 94 (2011) 3983–3991. doi:10.1111/j.1551-2916.2011.04647.x.